Immunofluorescent Visualisation of Genotoxicity: Characterising DNA Double-Strand Break Kinetics of Experimental Cancer Therapeutics

by

Jake Atkinson

Bachelor of Science (Biomedical Science, Honours)

A thesis submitted for the degree of

Doctor of Philosophy

(Biomaterials Engineering and Nanomedicine)

STEM



University of South Australia

December 2024

Declaration

This thesis presents work carried out by myself and does not incorporate without acknowledgment any material previously submitted for a degree or diploma in any university; to the best of my knowledge it does not contain any materials previously published or written by another person except where due reference is made in the text; and all substantive contributions by others to the work presented, including jointly authored publications, are clearly acknowledged.

Jake Atkinson



17th December 2024

Acknowledgments

I would firstly like to extend the greatest of thanks to my principal supervisor Associate Professor Ivan Kempson, who has been instrumental in the success of my PhD project, as well as my co-supervisors Professor Eva Bezak and Associate Professor Hien Le. Without your guidance throughout the many tumultuous times throughout my project, there is no way I would have made it out (relatively) unscathed. It has been a pleasure to work with such awesome mentors, and I hope to continue to collaborate and build upon the relationships forged over the last four years to make some incredible discoveries together moving forward. I would also like to thank the University of South Australia for supporting my study through the Research Training Program scholarship, and to Tour de Cure for the PhD Scholarship Grant.

To my lab colleagues, Ali Nazarizadeh, Douglas Howard, Luke Roeger, Mahshid Ghasemi, Minh Luu, Quy Le, Sisi Liang, Sonia Sebastian and Tyron Turnbull, thank you all for your support. Many thanks to Alex Cavallaro as well for helping with anything confocal related. You each contributed towards my project in some meaningful way, and it has been great to work alongside such friendly and down to earth people. I'd also like to extend my thanks to everyone who assisted with my work in Taiwan, including Chih-Tsung Yang, I-Chun Cho, Tsi-Chian Chao, Ching-Fang Yu, Zi-Xian Liao, and the many friends I made at Chang Gung University. Thank you all for facilitating the success of this collaboration and for being so welcoming – it definitely won't be my last visit to Taiwan!

Finally, my PhD would not have been possible with the support of my family and friends who stuck by me even when things seemed impossible. Needless to say, many, many thanks to you Mum, Dad, Lenny, and Rusty for carrying me through my academic journey. To my closest friends Hamish, Brandon, Richard, Joel, and my Intrepid Friends Bodie, Jacob, Ting, Minh, Bianca, Nico and Pedro, I appreciate you all. Try as I might to explain the intricacies of molecular biology, or how publishing in Nature is actually a big deal, I am eternally grateful to you all for your unwavering encouragement and belief in me -and in *why* I do this- regardless of understanding *how.*

Contents

Declaration ... ii
Acknowledgments ... iii
Contents ... iv
List of Figures ... viii
List of Tables ... xv
Thesis Outcomes ... xvi
Publications ... xvi
Awards ... xvii
Conferences and Presentations ... xvii
Abstract ... 1
1 Introduction ... 4
1.1 Background ... 4
1.1.1 Role of DNA Damage in Cancer Therapeutics ... 4
1.1.2 DNA Damage and Repair Disparity ... 6
1.1.3 Expanding The Toolbox to Quantify DSB Genotoxicity ... 8
1.1.4 Cancer Radiosensitizers ... 11
1.1.4.1 Gold Nanoparticles ... 11
1.1.4.2 ATM Inhibitor AZD1390 ... 12
1.1.5 Proton and Heavy Ion Therapy ... 13
1.1.6 FLASH-RT: Ultra-High Dose Rate Radiation Therapy ... 16
1.2 Research Goals ... 17
1.2.1 Hypotheses and Aims ... 18
1.3 Thesis Structure ... 19
1.3.1 Chapter 1: Introduction ... 19
1.3.2 Chapter 2: Materials and Methods ... 19
1.3.3 Chapter 3: Literature Review ... 20
1.3.4 Chapter 4: Quantification of DNA Double-Strand Break Damage and Repair Kinetics Using Novel Immunofluorescent Markers ... 20
1.3.5 Chapter 5: Establishment of In Vitro Experiments at the Proton-FLASH Beamline at Chang Gung Memorial Hospital ... 20
1.3.6 Chapter 6: Attenuator Design and Modelling for Adapting High Current Output from Cyclotrons for Proton Irradiation Studies ... 21
1.3.7 Chapter 7: Discussion and Conclusion ... 21
2 Materials and Methods ... 22
2.1 Introduction ... 22
2.2 Cell Culture ... 22

2.3 Clonogenic Assay 23
2.4 *In Vitro* Pre-Treatments 24
2.4.1 Neocarzinostatin 24
2.4.2 Hydrogen Peroxide 24
2.4.3 AZD1390 and AuNPs 24
2.5 Irradiation Parameters and Setup 24
2.5.1 X-ray Irradiation 24
2.5.2 Proton Irradiation 25
2.6 Immunofluorescence Staining 25
2.6.1 STRIDE Assay 25
2.6.2 γH2AX Assay 26
2.6.3 Confocal Imaging: Excitation and Emission Spectra 26
2.6.4 Image Analysis 27
2.6.5 Data Processing and Statistical Analysis 29
2.7 Attenuator Design 30
2.8 Justifications for Approach 31
2.8.1 Cell Selection Rationale 31
2.8.2 Irradiation, ATM Inhibition, and Gold Nanoparticle Dosages 32
3 Literature Review 34
3.1 Introduction 34
3.2 Imaging DNA Double-Strand Breaks, Are We There Yet? 35
3.2.1 Summary 35
3.2.2 Publication 36
3.3 DNA Double Strand Break and Response Fluorescent Assays: Choices and Interpretation 38
3.3.1 Summary 38
3.3.2 Publication 39
3.4 The Current Status of FLASH Particle Therapy: A Systematic Review 66
3.4.1 Summary 66
3.4.2 Publication 67
3.4.3 Updated Systematic Search 99
3.5 Conclusion 101
4 Quantification of DNA double-strand break damage and repair kinetics using novel IHC markers 103
4.1 Introduction 103
4.2 Immunofluorescence Staining Optimisations 103

4.2.1 γH2AX Response to Neocarzinostatin 103
4.2.2 STRIDE Validation in Response to Hydrogen Peroxide 105
4.3 Gold Nanoparticles Cause Radiosensitization in 4T1 Cells by Inhibiting DNA Double Strand Break Repair: Single Cell Comparisons of DSB Formation and γH2AX Expression 112
4.3.1 Summary 112
4.3.2 Publication 113
4.4 Mechanisms of ATM Inhibitor AZD1390-Mediated Radiosensitization by Comparing DNA DSB Formation and Repair in 4T1 Cells 126
4.4.1 Summary 126
4.4.2 Authors and Affiliations 126
4.4.3 Abstract 127
4.4.4 Introduction 127
4.4.5 Methods 131
4.4.5.1 Cell Culture and Pre-treatment 131
4.4.5.2 X-ray Irradiation 131
4.4.5.3 STRIDE Assay 131
4.4.5.4 γH2AX Assay 132
4.4.5.5 Confocal Imaging 132
4.4.5.6 Image Analysis 132
4.4.6 Results and Discussion 133
4.4.6.1 Confocal Imaging 133
4.4.6.2 0 Gy X-rays Negative Controls 134
4.4.6.3 X-ray Irradiation Combined with AZD1390 136
4.4.6.4 Colocalization of STRIDE and γH2AX Foci 139
4.4.7 Conclusion 141
4.4.8 Acknowledgements 142
4.4.9 Supplementary Data 143
5 Establishment of in vitro experiments at the proton-FLASH beamline at Chang Gung Memorial Hospital 154
5.1 Introduction 154
5.2 Experimental Setup 156
5.2.1 Proposed Irradiation Setup 156
5.2.2 Revised Irradiation Setup 158
5.3 Results and Discussion 164
5.3.1 CLAHE Image Enhancement 164
5.3.2 Results 165
5.3.3 Comparisons to Literature 170

5.4 Conclusion 171
6 Attenuator design and modelling for adapting high current output from cyclotrons for preclinical proton irradiation studies 174
6.1 Introduction 174
6.1.1 Material Properties 175
6.1.2 Nuclear Reactions in the Attenuator Material 176
6.2 Attenuator Specifications 179
6.2.1 Dose Rate Calculations 179
6.2.1.1 40 nA Cyclotron Dose Rate 179
6.2.1.2 55 nA Cyclotron Dose Rate 180
6.2.2 Dose Rate Calculations as a Function of Attenuator Pitch 181
6.2.3 SRIM and TRIM 182
6.3 Conclusion 187
7 Discussion and Conclusion 188
7.1 Introduction 188
7.2 Discussion 190
7.2.1 Novel Findings 190
7.2.2 Validity of Findings and Limitations 193
7.2.3 Future Work 195
7.3 Conclusion 199
Reference List 202
Appendices 218
PTCOG 61 Abstract 218

List of Figures

*Does not include figures in publications.

Figure 1: The main two canonical DSB repair pathways in eukaryotic cells. In HR (left) the MRN complex and ATM kinase are recruited to the DSB site, initiating end resection through the BRCA1-Abraxas-RAP80 complex and CtIP. Exo1 and DNA2 generate 3′ single-stranded DNA (ssDNA) overhangs, which are coated by RPA and later replaced by RAD51 with the help of the BRCA1-PALB2-BRCA2 complex. RAD51 mediates strand invasion into a homologous template, enabling accurate DNA repair through synthesis of a new DNA strand and Holliday junction resolution. NHEJ (right) involves the binding of Ku70/80 and the MRN complex to DNA ends, followed by recruitment of DNA-PKcs, which activates Artemis to trim incompatible overhangs. The XRCC4-DNA Ligase IV complex, supported by PAXX and XLF, then ligates the ends, completing this rapid but error-prone repair process. Figure produced with BioRender. 5

Figure 2: Diagram depicting the differences between γH2AX and STRIDE. Histone 2AX phosphorylation at Serine 139 can occur approximately 200 – 400 kilobases (kb) from the site of a DSB [13, 40, 41], an immunofluorescence target of the DDR commonly misrepresented as DSBs. Conversely, STRIDE acts by conjugating BrdU to DSB sites directly, allowing for accurate spatial determination of DSBs. 9

Figure 3: Confocal microscopy capture of a 4T1 cell exposed to 1.93 Gy X-rays, fixed 30 minutes post-irradiation. Immunofluorescence staining was utilised with a combination of DAPI (blue) representing the nucleus, STRIDE (red) showing DSB foci, and γH2AX (green). 10

Figure 4: Brain tumour irradiation simulations (superior view) for X-ray Intensity Modulated Radiation Therapy (IMRT) (left) and proton (right) irradiation. Higher doses of radiation are administered to the tumour site (red, orange, yellow) whilst lower doses of radiation are dispersed throughout normal tissues (green, blue, purple). The dose distribution during proton beam therapy is favourable in this instance, where highly sensitive normal tissue regions are spared on the opposing side of the radiation track. Image courtesy of Mikaela Dell'Oro and Eva Bezak. 13

Figure 5: Graph depicting absorbed dose deposition against dose depth for protons at different initial energies compared to photons [62]. X-rays have an initial peak dose which gradually attenuates through bodily tissue. A proton beam at a set energy is not able to fully irradiate a tumour on its own, since most of its dose is deposited at its Bragg peak, which is relatively narrow compared to the size of the irradiated volume. For the absorbed dose to conform to the entire tumour volume, proton beams of different energies are used, and their Bragg peaks are closely packed to form a spread-out Bragg peak (SOBP). This results in the maximum amount of dose administered throughout the tumour volume, whilst maintaining a negligible entry and exit dose to tissues adjacent to the tumour [62]. Reproduced from Wikipedia user MarkFilipak under the Creative Commons Attribution-Share Alike 3.0 Unported license (https://creativecommons.org/licenses/by-sa/3.0/deed.en). 14

Figure 6: CellProfiler analysis pipeline for the image analysis workflow. A green tick in the checkbox next to the module name indicates each active module in the pipeline. This pipeline processes each image in a batch according to the order of this list, top to bottom. 27

Figure 7: Image segmentation with the IdentifyPrimaryObjects module in CellProfiler. Nuclei were identified based on the blue channel of each RGB image, followed by masking of the green and red channels based on the objects (nuclei) identified. The values of integrated intensity for each channel were then measured for each nucleus with MeasureObjectIntensity. 28

Figure 8: 20x immunofluorescence images of 4T1 cells stained with anti-γH2AX Alexa 488 conjugate (green) representing phosphorylated histone 2AX, and DAPI (blue) representing nuclei. Each condition was treated with varying concentrations of neocarzinostatin for 1 hour and then fixed simultaneously. A.) Negative control, 0 µg/mL NCS., B.) 'Low' dose, 1 µg/mL NCS, and C.) 'High' dose, 10 µg/mL NCS. 104

Figure 9: 4T1 cells stained with DAPI (blue) and STRIDE (red) exposed to 20 mM H_2O_2 for different exposure times and fixed immediately after. Duplicates are represented in each column (top row = first duplicate, bottom row = second duplicate), with negative control (-CTRL) representing no H_2O_2 exposure, and 15, 30 and 60 minutes H_2O_2 exposure times respectively. Images were captured at 20x magnification. 105

Figure 10: 4T1 cells stained with DAPI (blue) and STRIDE (red) exposed to 20 mM H_2O_2 for different exposure times followed by fixation. Cells were either not treated with H_2O_2 as a negative control (-CTRL), negative control and stained with STRIDE without the primary antibodies (-CTRL No Prim Ab), negative control stained with STRIDE without the TUNEL reagents of the STRIDE protocol (-CRL No TUNEL), and treated with H_2O_2 for 15, 30 and 60 minutes. Images were captured at 20x magnification. 106

Figure 11: 4T1 cells stained with DAPI (blue) and STRIDE (red) with no TUNEL (top row, left), no primary antibodies (top row, middle), no mouse primary antibody (bottom row, left), or no rabbit primary antibody (bottom row, middle). Negative and positive control samples of HL-60 were also stained with DAPI (blue) and anti-BrdU antibody (red), represented by TUNEL -CTRL (top row, right) and TUNEL +CTRL (bottom row, right) respectively. Images were captured at 20x magnification. 107

Figure 12: 4T1 cells stained with DAPI (blue) and STRIDE (red), blocked (and antibodies diluted) with either Duolink blocking buffer (top row) or PBST-BSA (bottom row). For either of these blocking buffers, a DAPI only stain was applied (without STRIDE), the secondary antibodies + fluorophore (2ndary Abs Only), -CTRL (0 minutes H_2O_2 exposure), and 30 minutes 20 mM H_2O_2 exposure. Images captured at 20x magnification. 109

Figure 13: PC-3 cells stained with DAPI (blue) and STRIDE (red) washed either three (top row) or five (bottom row) times with wash buffer between STRIDE protocol steps. Cells were also exposed to 20 mM H_2O_2 for 0 (negative control),

15, 30 and 60 minutes and fixed immediately after. Images captured at 20x magnification. 110

Figure 14: U87 cells stained with DAPI (blue) and STRIDE (red) and fixed with either 4% paraformaldehyde (PFA) or 95% EtOH + 5% glacial acetic acid. Cells were either exposed to no H_2O_2 (0 mins H_2O_2) or H_2O_2 for 60 minutes. Images were captured at both 20x and 63x magnification for all conditions. 110

Figure 15: PC-3 cells stained with DAPI (blue), STRIDE (red) and anti-γH2AX Alexa 488 (green). Cells were exposed to either: no ATMi or H_2O_2 (top left), no ATMi and H_2O_2 for 30 minutes (top right), ATM inhibitor and no H_2O_2 (bottom left), and ATM inhibitor and H_2O_2 (bottom right). ATMi AZD1390 was prepared to a final dilution of 30 nM, and H_2O_2 to a final concentration of 20 mM in wells where appropriate. 111

Figure 16: Confocal images at 63x magnification of 4T1 cells irradiated with 1.93 Gy of 160 keV X-rays and fixed 30-minutes post-IR. Cells were co-stained to identify DSBs (red) and γH2AX (green) with STRIDE (Duolink In Situ Detection Reagents FarRed (Cy5)), and anti-phospho-histone H2AX conjugated with Alexa 488 respectively. DAPI was used to label individual nuclei. 133

Figure 17: Negative control condition of 4T1 cells without X-ray or ATM inhibitor AZD1390 treatment (negative control). Integrated intensity values for STRIDE, γH2AX, and DAPI from single cells were measured. STRIDE and γH2AX values were normalised to DAPI. Data show the median value within the 25th and 75th percentile data points (box). Whiskers show the 2.5 - 97.5 percentile, and dots represent data points outside the range represented by whiskers. 134

Figure 18: Non-irradiated 4T1 cells pre-treated with 30 nM AZD1390. Integrated intensity values for STRIDE, γH2AX, and DAPI from single cells were measured. STRIDE and γH2AX values were normalised to DAPI. Data show the median value within the 25th and 75th percentile data points (box). Whiskers show the 2.5 - 97.5 percentile, and dots represent data points outside the range represented by whiskers. 136

Figure 19: 4T1 cells irradiated with X-rays. Integrated intensity values for STRIDE, γH2AX, and DAPI from single cells were measured. STRIDE and γH2AX values were normalised to DAPI. Data show the median value within the 25th and 75th percentile data points (box). Whiskers show the 2.5 - 97.5 percentile, and dots represent data points outside the range represented by whiskers. 137

Figure 20: 4T1 cells irradiated with X-rays and pre-treated with 30 nM AZD1390. Integrated intensity values for STRIDE, γH2AX, and DAPI from single cells were measured. STRIDE and γH2AX values were normalised to DAPI. Data show the median value within the 25th and 75th percentile data points (box). Whiskers show the 2.5 - 97.5 percentile, and dots represent data points outside the range represented by whiskers. 138

Figure 21: 63x magnification images of X-ray irradiated 4T1 cells stained with DAPI (nuclei), STRIDE (red) and anti-γH2AX Alexa 488 conjugate (green), as well as corresponding foci counts at A.) 15-minutes post-IR, B.) 30-minutes post-IR, and C.) 45-minutes post-IR. Each image is representative of an independent

well. D.) 30-minutes post-IR focusing on a single 4T1 cell. Mean + standard error of the mean values of colocalized foci identified across all three fixation timepoints. 140

Figure 22: Mean and standard error of the mean (SEM) values of integrated intensity for STRIDE (red) and γH2AX (green) normalized to DAPI for 4T1 cells under various conditions. Top left: no X-ray irradiation or pre-treatment with AZD1390, top right: exclusively pre-treatment with 30 nM AZD1390, bottom left: exclusively X-ray irradiation, bottom right: X-ray irradiation in combination with 30 nM AZD1390 pre-treatment. Integrated intensity measurements were taken from individual nuclei across different fixation timepoints. 143

Figure 23: No X-rays or AZD1390. Histograms depicting the integrated intensity of DAPI normalized to the intensity of the 2N peak for each fixation timepoint. The gating of the G1 (0.6 – 1.4), S (1.4 – 1.6), and G2/M (1.6 – 2.4) phases are also displayed. Plots produced with Floreada.io. 144

Figure 24: No X-rays + AZD1390. Histograms depicting the integrated intensity of DAPI normalized to the intensity of the 2N peak for each fixation timepoint. The gating of the G1 (0.6 – 1.4), S (1.4 – 1.6), and G2/M (1.6 – 2.4) phases are also displayed. Plots produced with Floreada.io. 145

Figure 25: X-ray irradiation only. Histograms depicting the integrated intensity of DAPI normalized to the intensity of the 2N peak for each fixation timepoint. The gating of the G1 (0.6 – 1.4), S (1.4 – 1.6), and G2/M (1.6 – 2.4) phases are also displayed. Plots produced with Floreada.io. 146

Figure 26: X-ray irradiation + AZD1390. Histograms depicting the integrated intensity of DAPI normalized to the intensity of the 2N peak for each fixation timepoint. The gating of G1 (0.6 – 1.4), S (1.4 – 1.6), and G2/M (1.6 – 2.4) phases are also displayed. Plots produced with Floreada.io. 147

Figure 27: Normalized integrated intensities of STRIDE (x-axis) versus γH2AX (y-axis) for 4T1 cells with no X-ray or AZD1390 treatment. Intensities were gated (Figure 22) to determine the approximate proportion of cells in G1 (blue), S (green) and G2/M (red) phases. 148

Figure 28: Normalized integrated intensities of STRIDE (x-axis) versus γH2AX (y-axis) for 4T1 cells pre-treated with 30 nM AZD1390 only. Intensities were gated (Figure 23) to determine the approximate proportion of cells in G1 (blue), S (green) and G2/M (red) phases. 149

Figure 29: Normalized integrated intensities of STRIDE (x-axis) versus γH2AX (y-axis) for 4T1 cells treated with X-rays only. Intensities were gated (Figure 24) to determine the approximate proportion of cells in G1 (blue), S (green) and G2/M (red) phases. 150

Figure 30: Normalized integrated intensities of STRIDE (x-axis) versus γH2AX (y-axis) for 4T1 cells treated with both X-rays and 30 nM AZD1390. Intensities were gated (Figure 25) to determine the approximate proportion of cells in G1 (blue), S (green) and G2/M (red) phases. 151

Figure 31: Stacked box plots depicting the percentage of 4T1 cells in each cell phase, G1 (blue), S (green), and G2/M (red) across fixation timepoints post-IR. Cells were gated based on the ranges defined in Figure 22-25..... 152

Figure 32: The CGMH Particle Physics and Beam Delivery Core Laboratory. A.) View of experimental beamlines capable of preclinical proton irradiations originating from the 230 MeV Sumitomo Heavy Industries cyclotron. Two discrete beamlines originate from the dipole magnet (blue) with separate beam ports. The longer beamline extending to the left is capable of spread-out Bragg peak (SOBP) irradiations at CONV dose rates, whilst the beamline to the right (highlighted in B) is capable of shoot-through FLASH irradiations in the plateau region. Photos: Jake Atkinson. 155

Figure 33: Outlines of the initial plan for proton irradiations at CGMH utilising SOBP FLASH. Ibidi or Sarstedt 4-well chamber slides (Ibidi, 80426. Sarstedt, 94,6170.402) would be irradiated where the proton beam is incident approximately perpendicular to the longest side of the plate, with the 2 centremost wells (2 and 3) being seeded with cells. The slight incline depicted in the side-on-view ensures the beam is directed to pass through a layer of culture media before reaching the cells to minimise variability in scatter and dose deposition. The Bragg peak is calibrated to deliver maximal dose in the centre of each well, enabling coverage of the dose plateau, Bragg peak, and low/no-dose drop-off regions within each well..... 157

Figure 34: Well plate setup used for proton irradiations. A.) Millicell EZ SLIDE 8-well glass (Merck, PEZGS0896) were seeded with both U87 and OF cell lines and pretreated 2 hours before irradiation with 30 nM AZD1390 or 0.5 nM AuNPs. Immediately prior to irradiation, wells were filled (to capacity) with ~1 mL culture medium containing the appropriate pre-treatments to minimise both scatter and beam attenuation through air. To prevent culture medium from leaking from each plate, Teflon tape was wrapped around the outer walls of each 8-well plate, followed by followed by placing the lid on the well plate and wrapping the entire plate with paraffin. B.) Well plates taped to the HDPE moulds. Underneath each well plate, EBT3 film was adhered for dosimetry purposes to determine what area of each well was irradiated by protons. C.) HDPE mould in position ready for proton irradiation. Four irradiations were performed per run, with each irradiation delivering dose in a 1 cm^2 area to 4 wells. D.) FLASH-irradiated plates with their corresponding EBT3 films. ‘A-D’ marked on the bottom of each film indicates the delivery of each 2 Gy dose, whilst the numbers represent the film’s orientation relative to the well plates, with ‘1’ corresponding to ‘well 1’ in the top left, and ‘8’ to ‘well 8’ in the bottom right of each plate..... 160

Figure 35: Schematic depicting the well plate irradiation setup with the proton-FLASH beamline at Chang Gung Memorial Hospital Proton Centre. Two 1 cm^2 field size proton irradiations were delivered through the underside of each plate, allowing for irradiation of all 8 wells in a single plate. Four irradiations were performed across two plates fields per CONV/FLASH run. 162

Figure 36: Confocal images of U87 cells irradiated with 2 Gy protons and fixed 15 minutes post-irradiation, captured on the ImageXpress Micro Confocal High-Content Imaging System at 40x magnification. The original acquisitions (top row) were enhanced with CLAHE in ImageJ 1.54f (bottom row). 165

Figure 37: U87 cells fixed at 15- and 60-minute timepoints post-irradiation under the following conditions: negative control (-CTRL) cells exposed to 0 Gy protons, or 2 Gy protons delivered at a conventional (CONV) or ultra-high dose rate (FLASH) radiation. Foci counts for STRIDE and γH2AX from single cells were measured. Data show the median value within the 25th and 75th percentile data points (box). Whiskers show the 2.5 - 97.5 percentile, and dots represent data points outside the range represented by whiskers. 167

Figure 38: U87 cells were pretreated with 0.5 nM AuNPs 2 hours prior to irradiation and fixed at 15- and 60-minute timepoints post-irradiation. The irradiation conditions were as follows: negative control (-CTRL) with no radiation exposure + AuNPs, or exposure to 2 Gy protons delivered at either a conventional (CONV) or ultra-high dose rate (FLASH). Foci counts for STRIDE and γH2AX from single cells were measured. Data show the median value within the 25th and 75th percentile data points (box). Whiskers show the 2.5 - 97.5 percentile, and dots represent data points outside the range represented by whiskers. 168

Figure 39: STRIDE normalised integrated intensity values obtained from U87 and oral fibroblast (OF) cells irradiated under three separate conditions. 1. Proton irradiation alone, 2. proton irradiation combined with 30 nM AZD1390, 3. proton irradiation combined with 0.5 nM AuNPs. Treatments were applied 2 hours prior to irradiation, and cells were fixed at 15- and 60-minute time points post-irradiation. The irradiation conditions were as follows: negative control (-CTRL) with no radiation exposure, or exposure to 2 Gy protons delivered at either a conventional (CONV) or ultra-high dose rate (FLASH). Integrated intensity values for STRIDE and DAPI from single cells were measured, with STRIDE values normalised to DAPI. Data show the median value within the 25th and 75th percentile data points (box). Whiskers show the 2.5 - 97.5 percentile, and dots represent data points outside the range represented by whiskers. 169

Figure 40: Dose of neutrons emitted per incident proton (pGy) on the attenuator face for different attenuator setups and materials delivered to a tissue phantom. 235 MeV protons were used, with the thickness for each attenuator listed corresponding to the range of the protons in each material. © Institute of Physics and Engineering in Medicine. Reproduced by permission of IOP Publishing Ltd. All rights reserved [157]. 177

Figure 41: Neutron flux (neutrons/MeV/cm^2/p) from a 6.5 cm thick brass aperture and tungsten multileaf collimator irradiated by 200 MeV protons [158]. The black line perpendicular to the x-axis indicates the operating MeV of the 16.5 MeV GE PETtrace cyclotron, and the red and blue lines perpendicular to the y-axis indicate the neutron flux values of brass and tungsten respectively. © 2011 American Association of Physicists in Medicine. Reproduced by permission of John Wiley and Sons [158]. 178

Figure 42: Graph depicting the exponential decay relationship $y = 10000 \times e(-0.003466)$ between the number of attenuator holes versus attenuator pitch (μm). The three data points displayed: (400, 2500), (800, 625) and (1400, 78) are the hole and pitch combinations to produce dose rates of 3.74 Gy/s, 0.935 Gy/s and 0.117 Gy/s respectively. 181

Figure 43: TRIM calculations representing target depth versus ionisation energy per ion utilising brass (top) and tungsten (bottom) with thicknesses of 650 µm and 400 µm respectively, followed by Lucite with a thickness of 100 µm. Appropriate values of thickness were determined from SRIM. Lucite was also incorporated in TRIM calculations to represent the material of the well plate wall. 184

Figure 44: TRIM simulation output of target depth and individual proton tracks of 1000 16.5 MeV protons passing through 650 µm brass + 100 µm Lucite (top) and 400 µm tungsten + 100 µm Lucite (bottom). 185

Figure 45: Schematic view of A.) Two of the attenuator holes showing the conical shape of the hole, where D1 = 0.1 mm, D2 = 0.15 mm and the 'Pitch' is varied for each of the three attenuators (0.4 mm, 0.8 mm and 1.4 mm respectively) B.) The 16 x 16 mm grid on the attenuator + dimensions of the brass attenuator with a thickness of 0.65 mm (not to scale). © 2019 American Association of Physicists in Medicine. Reproduced by permission of John Wiley and Sons [154]. 186

Figure 46: Plate layout for clonogenic and γH2AX 12-well plate assays under FLASH (40 Gy/s) and CONV (0.61 Gy/s) at different doses (units Gy). Layout replicated 3 times for 4T1, K7M2 and HC11 cell lines. 198

List of Tables

Table 1: Descriptive statistics for each dataset for STRIDE and □H2AX across all timepoints. Values recorded include the number of values in each population (n), mean, median, standard deviation, standard error of the mean, range (defined by Prism as the difference in the minimum and maximum values), and 25th and 75th percentiles. 153

Table 2: Proposed experimental plate setups for SOBP proton-FLASH irradiations at CGMH. Overview of experimental conditions for FLASH and conventional irradiation (CONV) experiments, including variations with ATM inhibitor (ATMi), gold nanoparticles (AuNPs), and control conditions. Each condition specifies the cell type, fixation time, number of wells used, and the number of tests required for immunofluorescence staining (1 cm^2 = 1 test)... 158

Table 3: Arrangement of treatment conditions for each plate of the proton-FLASH irradiations. Each plate was divided into two halves, with pre-treatments repeated at 15-minute and 1-hour fixation timepoints. Each cell of this table that defines a pre-treatment condition: i.e., radiation only (RT), 30 nM AZD1390 (+ATMi), or 0.5 nM gold nanoparticles (+AuNPs), corresponds to a well of the negative control/no radiation (-CTRL), conventional (CONV) and FLASH irradiated samples. For each date, the top row corresponds to wells 1-4, and bottom row wells 5-8 (left to right). 163

Table 4: Summary of U87 and OF proton-FLASH irradiation conditions. Details of the date each irradiation was performed, the dose rate (FLASH vs CONV), cell type, fixation timepoint and EBT3 film position, as well as the dose delivered, pulse duration, and dose rate measured. 163

Table 5: Mechanical properties of both brass [154] and tungsten [155], candidate metals to produce attenuators for FLASH experiments. 176

Table 6: SRIM output for calculating the stopping power of protons of energies up to 16.5 MeV in both brass and tungsten (units: MeV/mm). The projected range and longitudinal straggling of ions were primarily used to calculate optimal attenuator thickness for both metals. 183

Table 7: Specifications of both brass and tungsten, candidate metals to produce attenuators for FLASH experiments, and the specifications for each material. 186

Thesis Outcomes

Publications

1. Atkinson J., Bezak E., and Kempson I., *Imaging DNA double-strand breaks — are we there yet?* Nature Reviews Molecular Cell Biology, 2022. 23(9): p. 579-580.

    - Authoritative perspective on data analysis and interpretation highlighting erroneous interpretation of DNA damage research relevant to molecular biology, cancer therapy and policy development.

2. Atkinson J., Bezak E., Le H., and Kempson I., *DNA Double Strand Break and Response Fluorescent Assays: Choices and Interpretation.* International Journal of Molecular Sciences, 2024. **25**(4): p. 2227.

    - Comprehensive summary of immunofluorescence-based techniques in detecting DNA double-strand breaks and their repair, offering insights into the DNA damage response process and its spatiotemporal kinetics, aiding in marker selection for precise data interpretation.

3. Atkinson J., Bezak E., Le H., and Kempson I., *The current status of FLASH particle therapy: a systematic review.* Physical and Engineering Sciences in Medicine, 2023.

    - Systematic analysis of all literature pertaining to preclinical and clinical proton-FLASH, summary of the mechanisms which underly the normal tissue sparing phenomenon of FLASH, and discussion of contradictory data within the field.

4. Atkinson J., Chopin J., Bezak E., Le H., and Kempson I., *Gold nanoparticles cause radiosensitization in 4T1 cells by inhibiting DNA double strand break repair: Single cell comparisons of DSB formation and γH2AX expression.* ChemPhysChem, 2024.

- Experimental publication comparing STRIDE and γH2AX intensities on a single cell level. Evidence that in vitro X-ray irradiation combined AuNPs exposure induces a delay in DSB repair, and that AuNPs induce DSBs 24-hours post-irradiation.

Awards

1. Research Training Program (RTP) Domestic Stipend - $32,500 AUD p.a.
2. Tour de Cure PhD Scholarship, *FLASH-Proton Therapy: Minimizing Healthy Tissue damage in the Treatment of Solid Tumours* - $10,000
3. FII Director's Awards Student Award 2022
4. ACPSEM Medical Physics Student Paper Night Award 2022
5. ACPSEM Medical Physics Student Paper Night Award 2024

Conferences and Presentations

2021

- **Particle Therapy Co-Operative Group 59 (Attendance),** Online, 4th – 7th June 2021.
- **National Particle Therapy Symposium (Attendance),** SAHMRI, Adelaide, SA, Australia, 7th – 8th October 2021.
- **ACPSEM Medical Physics Student Paper Night (Oral),** Atkinson J., Bezak E., Le H., Kempson I., *FLASH: Synergistic normal tissue sparing with protons and electrons at ultra-high dose rates*, Centre for Cancer Biology, Adelaide, SA, Australia, 27th October 2021.

2022

- **Future Industries Institute HDR Graduate Research Day (Oral),** *FLASH-Proton Therapy Current Status*, Atkinson J., Bezak E., Le H., Kempson I., University of South Australia, Mawson Lakes, SA, Australia, 12th July 2022.
- **ACPSEM Medical Physics Student Paper Night (Oral),** Atkinson J., Bezak E., Le H., Kempson I., *FLASH-Proton Therapy Current Status*,

Darling West Lecture Theatre, University of Adelaide, Adelaide, SA, Australia, 28th September 2022.

- **National Particle Therapy Symposium (Oral),** *FLASH-Proton Therapy Current Status,* Atkinson J., Bezak E., Le H., Kempson I. Westmead Hospital, Sydney, NSW, Australia, 24th – 25th November 2022.

- **FLASH Radiotherapy and Particle Therapy Conference (Poster),** Atkinson J., Bezak E., Le H., Kempson I., *FLASH Particle Therapy: A Systematic Review,* Barcelona, Spain, 30th November – 2nd December 2022.

- **Australian Institute of Physics Congress (Oral),** Atkinson J., Bezak E., Le H., Kempson I., *A Systematic Review of the Proton and Carbon FLASH Effect,* Adelaide Convention Centre, SA, Australia, 11th – 16th December 2022.

2023

- **Particle Therapy Co-Operative Group Asia-Oceania 2023 (Oral),** Atkinson J., Bezak E., Le H., Kempson I., *Illuminating the Mechanisms of FLASH: DNA Damage Assay Approaches,* Taiwan Conference Hall, Linkou, Taoyuan City, Taiwan, 24th – 26th November 2023.

2024

- **Future Industries Institute HDR Seminar (Oral),** Atkinson J., Bezak E., Le H., Kempson I., *Illuminating the Mechanisms of FLASH: DNA Damage Assay Approaches,* University of South Australia, Mawson Lakes, SA, Australia, 5th April 2024.

- **Med Rad Presentation Session (Oral),** Atkinson J., Bezak E., Le H., Kempson I., *Illuminating the Mechanisms of FLASH: DNA Damage Assay Approaches,* University of South Australia, City East Campus, SA, Australia, 29th May 2024.

- **Particle Therapy Co-Operative Group 62 (Poster),** Atkinson J., Bezak E., Le H., Yang C., Liao Z., Yu C., Chao T., Cho I., Kempson I.,

Characterising Proton-FLASH DNA Double-Strand Break Formation and Repair, Suntec, Singapore, 10th – 15th June 2024.

- **ACPSEM Medical Physics Student Paper Night (Oral),** Atkinson J., Bezak E., Le H., Kempson I., *Novel DNA Damage Formation Assessment for DNA Damage Inhibitors*, Centre for Cancer Biology, Adelaide, SA, Australia, SA, Australia, 18th September 2024

- **Future Industries Institute HDR Graduate Research Day (Oral),** *Novel DNA Damage Formation Assessment for DNA Damage Inhibitors*, Atkinson J., Chopin J., Bezak E., Le H., Kempson I., University of South Australia, Mawson Lakes, SA, Australia, 19th November 2024.

Abstract

DNA double-strand breaks (DSBs) are the most lethal forms of DNA damage, playing a key role in determining the effectiveness of cancer therapies. Accurate detection and quantification of DSBs is essential for understanding the biological effects of radiation and novel therapeutic agents. Conventional methods, such as γH2AX staining, have provided valuable information on DNA damage repair. However, endogenous markers associated with DSB repair exhibit limitations in accurately detecting the initial occurrence of DNA DSBs. These markers do not reliably correspond to the presence of DSBs at the time of insult, as their expression reflects DNA damage repair (DDR) processes rather than the DSB itself. This ambiguity leads to discrepancies in quantifying and timing the onset of DNA damage, complicating the assessment of DSB formation dynamics. As such, DDR markers are insufficient to characterise the complexity of DNA damage induced by different treatment modalities. DDR and DSB related assays were thoroughly reviewed, offering insights into methodologies for detecting DNA damage and repair. Of these techniques, this thesis explores the application of the novel DNA damage detection assay STRIDE (SensiTive Recognition of Individual DNA Ends), which offers increased sensitivity and specificity in detecting previously undetectable DSBs. To investigate this, experiments were performed to validate STRIDE and compared foci formation to traditional DNA damage response marker γH2AX. STRIDE was applied to evaluate the mechanisms of action of various cancer therapeutics, particularly focusing on emerging modalities such as gold nanoparticle (AuNP) radiosensitization, ATM inhibition (ATMi) treatment, and ultra-high dose rate proton FLASH radiotherapy. All these experimental techniques are predicted to modulate DNA damage and the DDR. However, without an established method to quantify DSBs, the mechanisms underlying their beneficial therapeutic properties is unclear. While AuNPs have been proposed to amplify radiation dose deposition, this thesis challenges the assumption that their radiosensitizing effects are driven solely by physical dose enhancement. Instead, the intracellular presence of AuNPs substantially modulates the biological regulation of the DDR, contributing to enhanced tumour radiosensitivity through mechanisms that extend beyond physical dose enhancement. Prior to the development of STRIDE, accurately

assessing the effects of ATM inhibition on DSB formation was also challenging due to the limitations of conventional DDR-based assays. γH2AX cannot directly detect DSBs and is suppressed in response to ATMi treatments, making γH2AX characterisation of genotoxicity impossible. STRIDE, with its specificity, overcomes these limitations by directly identifying individual DNA ends, which enabled the detection of DSBs that accumulate in response to ATM inhibition. Preliminary validation of STRIDE was performed with peroxide with PC-3 cells and tested with X-ray irradiations of 4T1 cells in combination with AuNPs and ATMi. Pre-treatment of 4T1 cells with AuNPs or ATMi 2-hours pre-irradiation did not alter the formation of DSBs but influenced the subsequent DNA DSB repair process. STRIDE exhibits kinetics which reflect the presence of DSBs immediately after exposure and the delayed obfuscation of DSBs thereafter. AuNPs were also capable of causing cumulative stress 24-hours post-irradiation, evidenced by DSB formation at this timepoint. These findings demonstrate a complementarity between STRIDE foci formation and γH2AX formation for quantifying DNA damage and subsequent repair, especially where DNA damage response (DDR) is impaired. Conversely, γH2AX foci formation peaks ~60 minutes post-insult but is impeded with DDR inhibition. The complementarity observed between STRIDE foci formation and γH2AX formation underscores the reliability of STRIDE in quantifying DNA damage, particularly in scenarios where the DDR is impaired. Comparative FLASH (~47 Gy/s) and CONV (~0.05 Gy/s) irradiation experiments were also performed on U87 and Human Oral Fibroblast (OF) cell lines at the Chang Gung Memorial Hospital Proton and Radiation Therapy Centre in Linkou, Taiwan. FLASH exhibits equivalent cancer killing capabilities to conventional low dose rate radiotherapy (CONV), but mitigates damage to normal tissues. A systematic review of all existing proton and carbon FLASH studies was also performed, which showed that differences in DNA damage, particularly clustered DSBs under FLASH, may be responsible for this differential response. A workflow was established for in vitro irradiations with their shoot-through FLASH beamline. Preliminary findings indicate that proton-FLASH irradiated U87 cells present fewer γH2AX foci compared to CONV 60 minutes post-irradiation. STRIDE intensities in FLASH-irradiated OF cells were lower than CONV-irradiated cells at 15 minutes post-irradiation. However, when ATMi or AuNPs were applied, it appeared that STRIDE intensities increased for OFs

irradiated by FLASH compared to CONV. An attenuator was also designed and theoretically evaluated to modulate the proton dose rate delivered by a 16.5 MeV PETtrace cyclotron, creating new capacity for radiobiological research in Adelaide using FLASH and CONV dose rate protons. Overall, this thesis highlights the advantages of STRIDE when used alongside complementary DDR factor γH2AX, offering increased sensitivity and specificity in detecting DNA DSBs. This enhanced characterisation of DNA damage furthers understanding of the DSB versus DDR kinetics that drive AuNPs and ATMi radiosensitization, as well as contextualising mechanisms of proton-FLASH radiotherapy. STRIDE facilitates more precise DSB assessment for the development of not only cancer therapeutics, but also broader use in genotoxicity assessment.

1 Introduction

1.1 Background

1.1.1 Role of DNA Damage in Cancer Therapeutics

DNA double-strand breaks (DSBs) are a critical form of DNA damage induced by many cancer therapeutics and can lead to a range of cellular outcomes. The breaking of both strands of the DNA double helix is especially deleterious, destabilising the genome and disrupting essential cellular processes such as transcription and replication. If damage is extensive, unrepaired DSBs can result in compromised genomic integrity through a cascade of genomic translocations, fusions, and deletions, and consequentially, cell death [1]. Their effective repair or misrepair thus plays a central role in determining therapeutic efficacy. Radiotherapy utilises particles or electromagnetic radiation to ionize DNA directly, as well as the surrounding water molecules to produce reactive oxygen species (ROS) that damage DNA indirectly [2]. It is recommended to be included in treatment of 50% of all cancer patients in developed countries worldwide, making it one of the most common modes of treatment available currently. Accounting for only 5% of total cancer therapy costs, as well as being a non-invasive technique, it is appealing in both its low economic burden and practicality [3]. Chemotherapies can also induce DSBs. Alkylating agents like temozolomide methylate DNA at specific sites, leading to replication fork collapse and the formation of DSBs [4]. Radiosensitizers, such as targeted pharmaceuticals or metallic nanoparticles, can perturb the biological processes responsible for cancer cell survival and proliferation during a course of radiotherapy. This includes DNA damage repair inhibitors of poly (ADP-ribose) polymerase (PARP), ataxia-telangiectasia mutated (ATM), phospho-histone 2AX (γH2AX) and DNA-dependent protein kinase (DNA-PKcs) [5, 6]. Each of these proteins play a role in the activation and recruitment of the DNA damage response (DDR), through the two predominant DSB repair pathways (Figure 1), non-homologous end joining (NHEJ) and homologous recombination (HR). The activity of these DSB repair pathways is often dysregulated in cancers due to genetic mutations, epigenetic changes, and selective pressures within the tumour

microenvironment. These alterations, such as mutations in key DDR genes or overexpression of repair proteins, impair accurate DNA repair, promote genomic instability, and contribute to tumourigenesis by enabling cancer cells to survive and proliferate despite accumulating DNA damage [7]. While DDR dysregulation promotes cancer cell survival, it also creates opportunities for targeted therapies that exploit genetic interactions such as synthetic lethality. In this approach, inhibiting two critical genes simultaneously leads to cell death, selectively affecting cancer cells that possess only one functional copy of the gene, while sparing healthy tissues that retain both functional copies [8]. By leveraging this vulnerability, DDR inhibitors can sensitize cancerous tissues whilst allowing healthy tissues to survive. Nanoparticle-based approaches are also capable of impeding DSB repair processes, with the presence of gold nanoparticles (AuNPs) within cancerous cells bottlenecking DNA synthesis [9], and altering expression of the DNA damage response [10].

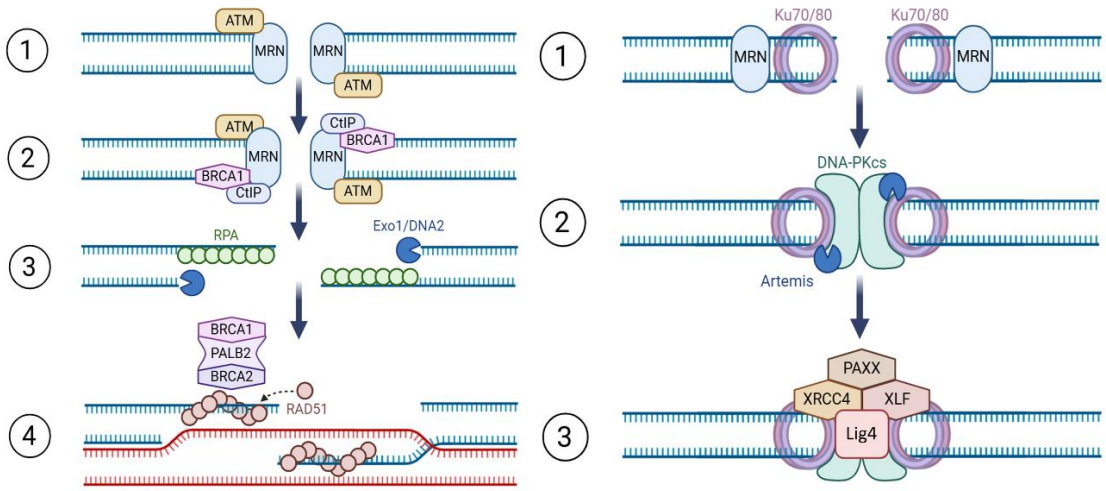


Figure 1: The main two canonical DSB repair pathways in eukaryotic cells. In HR (left) the MRN complex and ATM kinase are recruited to the DSB site, initiating end resection through the BRCA1-Abraxas-RAP80 complex and CtIP. Exo1 and DNA2 generate 3′ single-stranded DNA (ssDNA) overhangs, which are coated by RPA and later replaced by RAD51 with the help of the BRCA1-PALB2-BRCA2 complex. RAD51 mediates strand invasion into a homologous template, enabling accurate DNA repair through synthesis of a new DNA strand and Holliday junction resolution. NHEJ (right) involves the binding of Ku70/80 and the MRN complex to DNA ends, followed by recruitment of DNA-PKcs, which activates Artemis to trim incompatible overhangs. The XRCC4-DNA Ligase IV complex, supported by PAXX and XLF, then ligates the ends, completing this rapid but error-prone repair process. Figure produced with BioRender.

While manipulation of these molecular mechanisms is central to therapeutic strategies, clinical success also relies on minimising damage to normal tissues. There are significant advantages to utilising conventional X-ray radiation therapy, however it has the potential for causing detrimental effects to healthy tissue and organs at risk, inherent in radiation treatment. Reducing healthy tissue exposure to radiation is therefore crucial since normal tissue complications limit dose delivery. Clinicians refer to the therapeutic window as the optimal range of dose which maximises the curative probability of a therapeutic whilst simultaneously minimising damage to normal tissues. Identifying strategies which broaden the therapeutic window allows for a lower incidence of negative side effects in patients, and even allow for greater doses to improve the probability of tumour control [11]. Regarding this, adjuvant therapeutics have been discovered that improve the effectiveness of radiotherapies by making cancerous cells more vulnerable to radiation. However, despite the therapeutic potential of DSB induction in both radiotherapy and chemotherapy, and the ability to exploit DDR dysregulation for selective cancer cell killing, accurate quantification of DSBs remains a significant challenge.

1.1.2 DNA Damage and Repair Disparity

Immunofluorescence microscopy offers the advantage of enabling single-cell analysis and imaging within complex tissues, with the potential for quantifying individual DSBs, regardless of their origin. However, despite its capabilities, historically it has often been limited to using markers of DNA damage repair rather than directly detecting DSBs themselves. Notably, γH2AX [12-14], ATM [15-17], and 53BP1 [18-20] have been correlated with DSB formation, as have other components of the DDR [21, 22]. The γH2AX assay is the most widely used for this purpose, with multiple publications have misrepresenting its relevance, often equating the detection of DDR factors to the proportional presence of DSBs [23-25]. However, they are prone to inconsistencies because of numerous confounding factors. Radiation may result in variability in gene regulation, and hence variable expression and activation of these repair factors, if the damage occurs to a gene that expresses a DDR protein [26]. The activation of these factors may also differ between cell types, making direct comparison between normal and cancerous cell types inconclusive [27]. Therefore, although they work

as a guide and may be correlated with the presence of DSBs under specific circumstances, they cannot directly detect DSB presence. This is a pertinent issue in quantifying and characterising genotoxicity currently, as this places limits on the interpretation of the mechanisms of various cancer therapies [6].

The challenges and limitations of using DDR factors to quantify DSBs has been highlighted in multiple studies. Notably, this issue has been discussed in publications establishing quantitative DSB sequencing and analysing γH2AX repair dynamics [28-30]. Similar issues arise with other assays that rely on markers of endogenous damage response. Combining assays has been proposed as a potential solution, though this is still typically limited to γH2AX and 53BP1. While combining assays may offer more accurate data in some cases, the co-localisation of markers can invalidate the 1:1 correlation between foci and DSBs [30]. This is particularly true of techniques such as the DNA Damage In Situ Ligation Followed by Proximity Ligation Assay (DI-PLA) which marks DSBs with biotinylated oligonucleotides but relies upon an endogenous partner protein for successful staining [31]. While it is possible that fluorescently labeled DDR foci correlate one-to-one with DSBs in specific circumstances, this remains an assumption rather than a universally applicable fact.

The confounding effects of genotoxicity, as well as cellular heterogeneity, on DDR factor expression means that DSB accumulation cannot be properly measured with immunofluorescent tagging of DDR proteins. The presence of DSB repair factors does not necessarily indicate the presence of DSBs [32-35] , and endogenous factors are susceptible to inhibition or variation in activity, rendering them unreliable for characterising genotoxicity [6, 36]. The question remains: how can the mechanisms by which cancer therapeutics damage DNA be interpreted when there isn’t yet an established measure for DSB induced genotoxicity? Currently, it is a matter of measuring the downstream effect of radiosensitizers, i.e., DDR perturbation, whilst being blind to diagnosing the root cause. This ambiguity could be eliminated through using a direct microscopy-based assay to directly mark and accurately quantify DSBs.

1.1.3 Expanding The Toolbox to Quantify DSB Genotoxicity

Although DSB repair in response to radiation and chemo-pharmaceuticals is well understood, the ability to observe and quantify DSBs accurately is not. As per an extensive literature search by the author at the time of writing, there are currently no studies that comprehensively characterize DNA DSBs in response to genotoxic insults. Understanding DSB formation is critical as they are a key factor in determining the effectiveness of cancer therapies. Despite the importance of DSBs in treatment response, their detection and the subsequent repair pathways have been difficult to characterise with existing methodologies, often opting to correlate DSBs with repair proxies such as γH2AX. Recently developed immunofluorescence-based assays are capable of visualising sites of DNA damage and repair factors in situ. Some are even capable of resolving individual DSBs on a single-cell level. SensiTive Recognition of Individual DNA Ends (STRIDE) by Kordon et al. 2020 is one such technique, which uses a combination of BrdU conjugation, anti-BrdU antibodies, and a proximity ligation assay to mark DSB ends [37]. This technique is uniquely capable of binding to free DSB ends throughout an entire cell, offering a comprehensive view of where and when DSBs are occurring post-insult [37]. The ability to precisely track DSBs on a single-cell level is a major advantage when studying the effects of experimental treatment modalities, as it allows for accurate tracking of the physical damage without a reliance on ambiguous endogenous markers. Although there are other similar DSB detection techniques available, including DI-PLA [31] and TUDEL [38], STRIDE was selected for use in the studies detailed in this thesis due to being the most thoroughly validated as of 2021 when experiments commenced.

The STRIDE method employs a multi-step molecular process to ensure precise binding and amplification of a fluorescence signal at DSB sites. It begins with the enzymatic conjugation of bromodeoxyuridine (BrdU), a synthetic nucleoside analogue, at the ends of DSBs via terminal deoxynucleotidyl transferase (TdT). Primary anti-BrdU antibodies are then introduced and bind to the BrdU-labelled DSBs, followed by addition of secondary Duolink antibodies which bind to the anti-BrdU primary antibodies. These secondary antibodies contain oligonucleotides which facilitate a rolling circle amplification (RCA) reaction, with the resulting concatemeric DNA sequence providing binding sites for

fluorescently labeled probes. This generates a highly amplified fluorescence signal at locations where DSBs are present, making it easier to visualize individual DSBs with high sensitivity. This multi-step process is particularly useful in detecting subtle differences in DNA damage across different treatments and doses. In conjunction with STRIDE, γH2AX was also employed as a complementary marker. γH2AX is a phosphorylated histone variant that is activated in response to DSB formation, typically reaching peak phosphorylation 30 – 60 minutes post-insult [39]. By comparing the STRIDE signal with γH2AX, both the presence of physical DSBs and the subsequent biological repair responses can be measured, allowing for simultaneous analysis of their spatiotemporal kinetics on a single-cell level and across multiple timepoints (Figure 2).

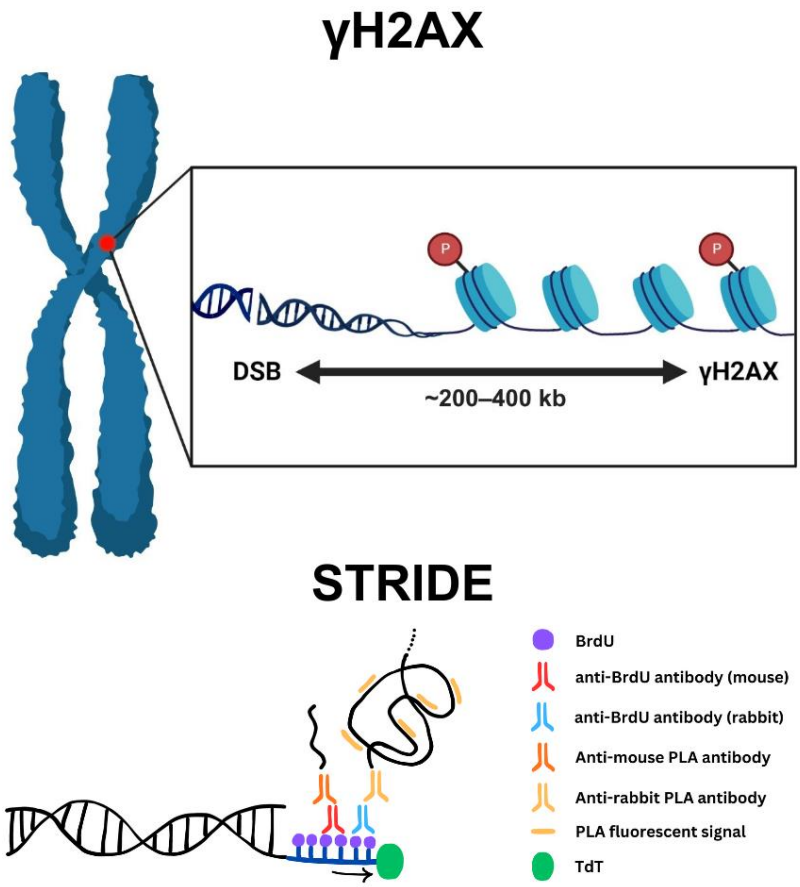


Figure 2: Diagram depicting the differences between γH2AX and STRIDE. Histone 2AX phosphorylation at Serine 139 can occur approximately 200 – 400 kilobases (kb) from the site of a DSB [13, 40, 41], an immunofluorescence target of the DDR commonly misrepresented as DSBs. Conversely, STRIDE acts by conjugating BrdU to DSB sites directly, allowing for accurate spatial determination of DSBs.

By analysing the formation of DSBs with STRIDE and pairing this with co-stain for a marker of DSB repair activation, it is possible to compare DSB formation with repair factor kinetics. This is invaluable as it provides new insight into the mechanisms of DSB formation underlying unique radiobiological phenomena that remain difficult to interpret, and enables investigation of DSB formation and repair mechanisms in response to multiple types of insults (Figure 3). X-rays and particle therapies are widely used in clinical settings, making it important to map their damage profiles. This offers new opportunities in quantifying effects of radiotherapy modalities and when radiation is used in conjunction with emerging radiosensitizers.

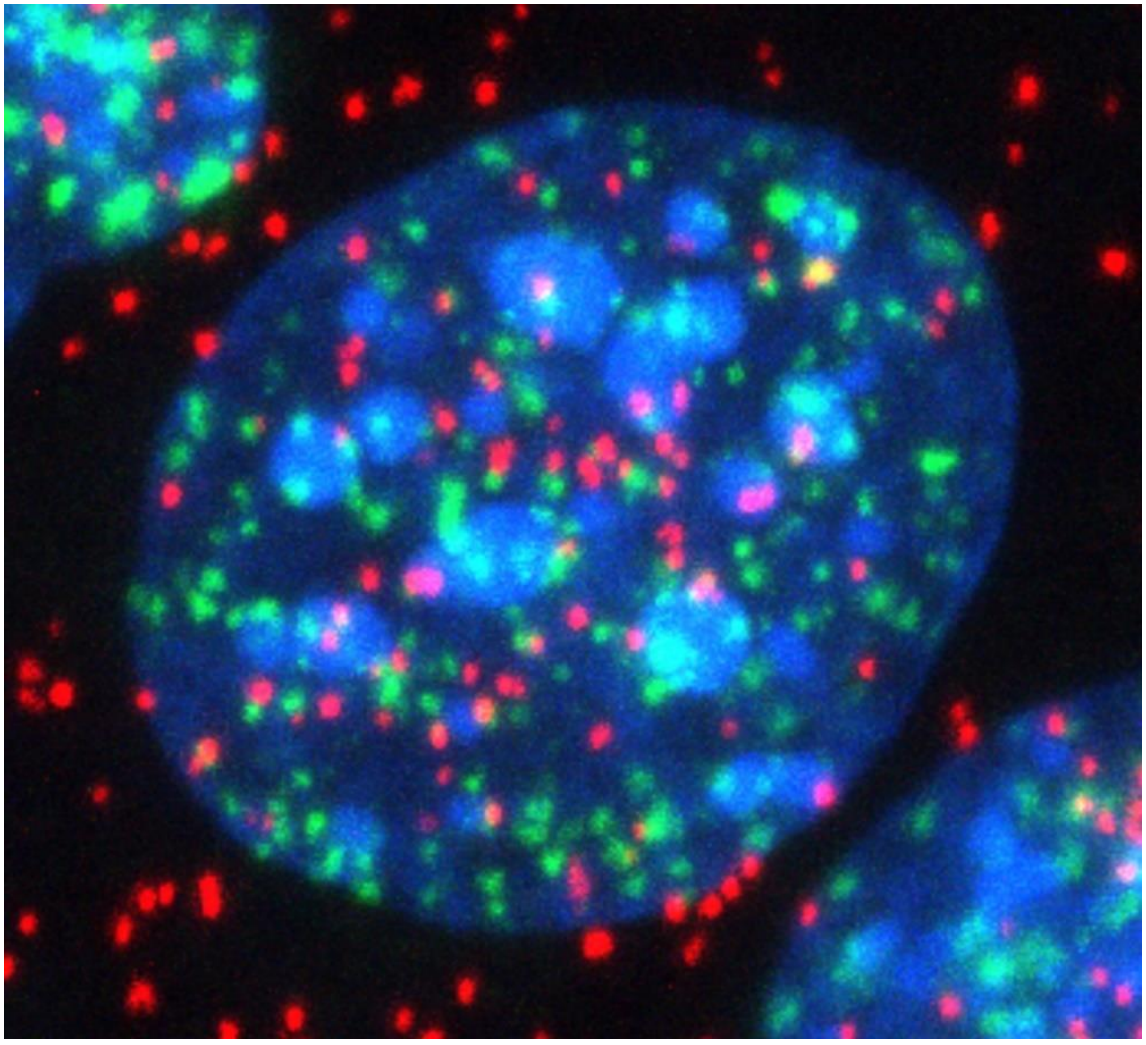


Figure 3: Confocal microscopy capture of a 4T1 cell exposed to 1.93 Gy X-rays, fixed 30 minutes post-irradiation. Immunofluorescence staining was utilised with a combination of DAPI (blue) representing the nucleus, STRIDE (red) showing DSB foci, and γH2AX (green).

1.1.4 Cancer Radiosensitizers

Complimentary to radiotherapy, pharmaceutical and nanomedical radiosensitization approaches are being developed to improve patient treatment outcomes. As radiosensitizers aim to reduce the threshold radiation dose above which cancers cannot recover, it increases the probability that the same total dose will eliminate a tumour than without radiosensitization. Therefore, if normal tissue complications are a limiting factor to successfully treat a tumour, particularly if located in proximity to sensitive areas such as the brain and spinal cord, radiosensitizers can allow for a reduced total dose to be administered whilst minimising damage to peripheral healthy tissues. This can allow previously radioresistant, untreatable cancers to be vulnerable enough to kill, thereby broadening the therapeutic window and allowing for successful treatment.

1.1.4.1 Gold Nanoparticles

Metal nanoparticles have been developed for clinical use as radiosensitizers [42-44]. Hypotheses exist based upon the physical mechanisms of radiosensitization, for instance, increasing the total dose deposition through increased absorption of radiation by high-z materials [45]. These include the photoelectric effect and pair production, which were previously thought to predominantly account for the sensitization effect when nanoparticles are internalised [42, 46]. However, recent studies have shown that the physical or physico-chemical interactions between the imparted radiation and the nanoparticles are not necessarily the primary drivers of radiosensitization, but rather the mere presence of nanoparticles within tumourigenic cells inducing a biological response [42]. Turnbull et al. 2019 highlighted that AuNPs sensitize cells preferentially by impeding the enzyme thymidylate synthase, as well as displaying that the correlation between AuNP uptake and γH2AX foci was highest in S-phase cells [9]. Responsible for catalysing the production of deoxyuridine monophosphate to deoxythymidine monophosphate, thymidylate synthase is essential for production of thymidine nucleotides, a rate limiting step in DNA repair and a target of anti-cancer pharmaceuticals [47]. Therefore, this alludes to a mechanism by which sensitization occurs due to a biological interaction between internalised nanoparticles and processes that regulate DNA damage repair, preventing cells from synthesising new DNA and proliferating, and thus enhancing the effect of

radiation. A challenge in definitively confirming the underlying mechanisms has been the limitation in being able to measure physical DNA damage independently of the subsequent biological DDR.

1.1.4.2 ATM Inhibitor AZD1390

Ataxia-telangiectasia mutated (ATM) inhibitors hold great potential in targeting radio- and chemo-resistant tumours by interrupting DNA damage response (DDR) processes, and thus interrupting cell recovery post-insult. ATM is a key signalling molecule within the DDR, being recruited to DNA breakage sites by the DSB tethering MRE11-RAD50-NBS1 (MRN) complex, and subsequently undergoing autophosphorylation at Ser1981. This active form of ATM then phosphorylates Ser139 of histone variant H2AX (γH2AX), which allows for widespread chromatin remodelling and the recruitment of numerous downstream DNA DSB repair factors [48]. The production of DNA double-strand breaks is one of the principal modes of causing cell death during radiotherapy [49]. DNA repair factors such as γH2AX and ATM are activated in response to these lesions and have been used as markers indicating the severity of genotoxicity. The inhibition of ATM prevents signalling of γH2AX, thereby impeding the accumulation of repair proteins to DSBs. As well as interfering with DNA repair, ATMi KU55933 has been shown to prevent Akt-mediated glucose uptake and metabolism in aggressive cancers, resulting in apoptosis [50]. AstraZeneca ATMi AZD1390 was developed to treat glioblastomas, with preclinical in vivo studies establishing it as capable of passing the blood brain barrier [48], a protective membrane which prevents permeation of 98% of small-molecule biopharmaceuticals currently available [51]. Thus, this inhibitor is particularly clinically relevant, with phase 1 trials NCT03215381, NCT03423628 and NCT03215381 [52] being conducted to determine its efficacy and safety in humans. As for AuNPs, conventional detection assays alone are not informative enough to determine the impact of ATMi on the DDR or on DSB formation. As ATMi directly inhibit pathways responsible for DSB repair (Figure 1), marking of factors such as γH2AX is inherently unreliable due to their suppression. γH2AX signals are also suppressed when ATMi are utilised [53], and hence the extent DNA damage cannot be inferred. Thus, use of a marker that acts independently of DDR

pathways such as STRIDE can enable the detection of DNA damage and compare this to the extent of DDR suppression by ATMi.

1.1.5 Proton and Heavy Ion Therapy

Particle therapy employs the use of ions, including protons and carbon, to irradiate tumour volumes with minimal exit dosage compared to X-ray photons, preventing significant irradiation of the surrounding healthy tissues (Figure 3, right). In megavoltage X-ray beams, the dose initially increases with depth due to the build-up of secondary electrons until electronic equilibrium is established, typically around the depth of maximum dose (Dmax). Beyond this point, the dose attenuates exponentially as the beam continues to lose energy through scattering and absorption. Due to the exponential absorbed dose deposition profile of X-ray photons, normal tissues are exposed to radiation prior to entering, and upon exiting, a treatment volume (Figure 4, left).

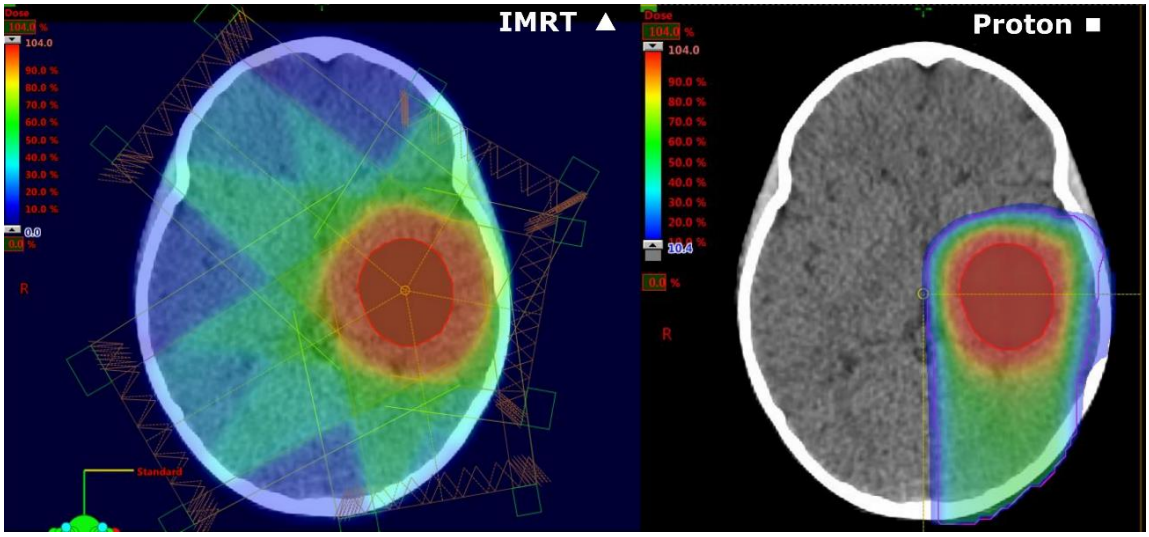


Figure 4: Brain tumour irradiation simulations (superior view) for X-ray Intensity Modulated Radiation Therapy (IMRT) (left) and proton (right) irradiation. Higher doses of radiation are administered to the tumour site (red, orange, yellow) whilst lower doses of radiation are dispersed throughout normal tissues (green, blue, purple). The dose distribution during proton beam therapy is favourable in this instance, where highly sensitive normal tissue regions are spared on the opposing side of the radiation track. Image courtesy of Mikaela Dell'Oro and Eva Bezak.

Conversely, particles have a low degree of energy deposition upon entry and deposit their maximum dose at a sharp peak towards the end of their track. The rate of energy loss of a particle is inversely proportional to the square of its

velocity, thus when its velocity nears zero, it will reach its maximum rate of energy loss, known as the ‘Bragg peak’ [54]. In clinical treatments, particles of multiple different energies are delivered so that a ‘spread-out Bragg peak’ (Figure 5) is produced to irradiate the entire tumour volume.

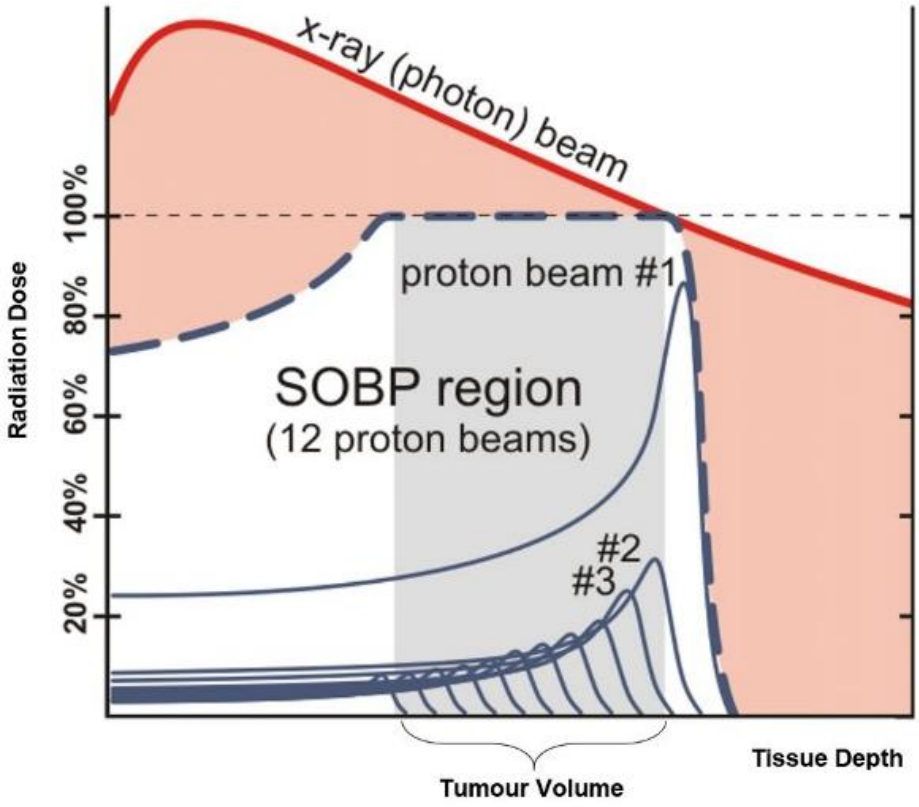


Figure 5: Graph depicting absorbed dose deposition against dose depth for protons at different initial energies compared to photons [55]. X-rays have an initial peak dose which gradually attenuates through bodily tissue. A proton beam at a set energy is not able to fully irradiate a tumour on its own, since most of its dose is deposited at its Bragg peak, which is relatively narrow compared to the size of the irradiated volume. For the absorbed dose to conform to the entire tumour volume, proton beams of different energies are used, and their Bragg peaks are closely packed to form a spread-out Bragg peak (SOBP). This results in the maximum amount of dose administered throughout the tumour volume, whilst maintaining a negligible entry and exit dose to tissues adjacent to the tumour [55]. Reproduced from Wikipedia user MarkFilipak under the Creative Commons Attribution-Share Alike 3.0 Unported license (https://creativecommons.org/licenses/by-sa/3.0/deed.en).

Particle therapy offers significant advantages in minimising dose to surrounding normal tissues due to its distinct dose deposition profile. However, toxicity can still arise in adjacent healthy structures, resulting in a range of treatment-related side effects. Cancers such as those of the brain and central nervous system

(CNS), head and neck, lungs, breast, and prostate, can be incredibly difficult to treat successfully whilst mitigating damage to highly radiosensitive peripheral normal tissues [56]. Radiation-induced optic neuropathy, in which external cranial irradiation results in late onset necrosis of the anterior visual pathways, has been reported for doses below reported safe thresholds (<55 Gy) [57]. The potential normal tissue complications that can result from lung irradiation include early onset pneumonitis, late onset fibrosis (occurring in 5-20% of patients), and risks of heart or spine irradiation depending upon tumour location [58]. The risks that these complications are amplified in paediatric patients, as they have a substantially longer lifetime after treatment for late symptoms to manifest and negatively impact quality of life. When treating for medulloblastoma, a decline in both the intelligence quotient and cognitive performance of paediatric patients has been observed when compared to their healthy peers [59]. Additionally, hypothalamic-pituitary unit irradiation is associated with growth impediment throughout childhood; radiation induced hypothalamic-pituitary dysfunction produces deficiencies in growth hormones, insulin-like growth factor-1, and thyroid stimulating hormone production [60]. Whilst these are amongst the most extreme and uncommon cases of radiation induced damage, striving to reduce these potential risks, particularly through modalities like proton therapy, will improve cancer patients' quality of life after treatment considerably.

To mitigate such adverse effects, recent advancements in radiotherapy have focused on enhancing precision and minimising collateral damage to healthy tissues. Modern particle beam centres are now employing intensity modulated therapies, otherwise known as pencil beam scanning, which targets tumours in layers of irradiation spots at differing doses, depths, and positions [61]. The benefits of such treatment include better dose conformation, minimisation of damage to healthy tissues and an increased total dose that can be administered [62]. Particles such as protons and carbon are being utilised for this purpose. In Australia, the Australian Bragg Centre for Proton Therapy in Adelaide's biomedical precinct is anticipated to be Australia's first proton therapy facility. As these technologies become more accessible, they are expected to play an essential role in expanding treatment options for paediatric and those with

tumours near critical structures, while advancing the broader goal of achieving more effective, personalised cancer care with fewer side effects.

1.1.6 FLASH-RT: Ultra-High Dose Rate Radiation Therapy

Despite the development of radiosensitizers, and hence the overall enhancement of radiotherapies against tumourigenic tissues, there is still demand for new and innovative treatment modalities that reduce damage caused to radiation sensitive healthy tissues. The resurgence of studies involving irradiation of tissue at ultra-high dose rates, also known as FLASH radiation therapy (FLASH-RT), and widespread development of heavy ion therapy, may be pivotal steps in further improving the therapeutic efficacy of radiotherapy. FLASH-RT typically delivers dose rates greater than 40 Gy/s to irradiate tumours in very small timeframes (< 1 s), as opposed to conventional dose rates (CONV, < 0.03 Gy/s) which are normally fractionated and delivered over the course of minutes [63]. There is substantial evidence that the utilisation of this technique, even with photon or electron beam therapies, results in a radioprotective effect in normal tissues, which reduces tissue toxicity compared to CONV. The differential tissue sparing effects of both proton therapy and FLASH may prove to be highly beneficial when utilised in combination. Taking advantage of the proton beam's characteristics, including conforming the Bragg peak to the tumour volume, its relatively low entry and minimal exit dose, alongside the normal tissue sparing properties afforded by FLASH, has the potential to synergistically reduce healthy tissue toxicity.

Although there are multiple studies outlining the outcomes of the FLASH effect, there are few studies exploring the mechanistic radiobiological implications of ultra-high dose rates**.** Multiple mechanisms have been hypothesised to explain this phenomenon, including cellular oxygen depletion and preventing toxic reactive oxygen species (ROS) production in normal tissues [64], immune response modulation [65], and alterations to the DNA damage repair pathway, including DNA damage complexity. However, the radiobiological process by which these mechanisms occur during FLASH-RT is not well understood. All these factors are thought to contribute towards the unique sparing effect of FLASH-RT, which has been previously demonstrated in vitro and in vivo for photons, electrons, and heavy ions (see Chapter 3.4). Considering DSBs are the

primary mode of action of radiotherapy, the FLASH effect could be driven by the ability of FLASH to form DSBs of different complexity to CONV and induce an altered DNA damage repair response [65]. Compared to isolated DSBs, clustered DSBs are difficult for cells to repair successfully [66]. Current literature shows that there are minimal differences in γH2AX or 53BP1 foci formation between FLASH and CONV dose rates at early timepoints post-irradiation [67-70]. However, as only earlier timepoints are presented in these studies (30 minutes), these trends may not extend to longer timepoints post-irradiation. The kinetics of DDR factor accumulation have not been thoroughly explored, in addition to an absence of accurate DSB quantification. Insights into this mechanism may be attained by using STRIDE, providing an explanation for the radiobiological benefits FLASH displays in preclinical studies and clinical trials. To achieve this, this thesis examines how FLASH and CONV delivery modalities, particularly in the context of proton therapy, may influence DSB damage and repair kinetics, highlighting the role of STRIDE in characterising the mechanisms that lead to possible therapeutic advantages observed with FLASH compared to CONV. This work was conducted at Chang Gung Memorial Hospital Proton and Radiation Therapy Centre in Linkou, Taiwan, establishing an international collaboration between Chang Gung University and The University of South Australia, and a protocol for *in vitro* proton-FLASH at their facility. Finally, design of an attenuator to modify the current non-clinical cyclotron setup at the South Australian Health and Medical Research Institute (SAHMRI) to enable proton-FLASH work in Adelaide was also explored. This would allow for preclinical experiments to be performed locally, increasing Australia's capacity for radiobiological research.

1.2 Research Goals

The overall aim of this research was to provide new understanding of the nature of DNA damage and repair under a range of irradiation conditions currently undergoing pre-clinical and clinical translation. The project specifically focused on comparing the novel DNA damage marker STRIDE with γH2AX to provide new insights into the mechanistic effects of AuNPs, ATM inhibitors, and ultra-high dose rate protons in promoting advantageous radiobiological responses for cancer treatment. AuNPs are hypothesised to enhance physical radiation dose deposition, potentially amplifying DNA damage in tumour cells. STRIDE was

used to evaluate whether reported radiosensitization effects of AuNPs is driven by a physical dose enhancement, and whether this translates to measurable biological effects on DNA damage and repair. By analysing the impact of AuNPs on DNA damage signalling and repair dynamics, this research sought to clarify their action as radiosensitizers and identify their impacts on the DDR. STRIDE was also employed to characterise DNA damage induced by ATM inhibitors in combination with radiation previously undetectable with immunofluorescent techniques. ATM inhibitors suppress the DDR by blocking the activation of key repair pathways, resulting in persistent DNA damage that sensitizes cancer cells to radiation. Using STRIDE, this project aimed to quantify these effects in greater detail, providing a direct evaluation of how ATM inhibitors influence DSB formation and persistence over time, as well as delays in repair kinetics. Additionally, the project aimed to validate a preclinical proton-FLASH irradiation setup at Chang Gung Memorial Hospital (CGMH) in Taiwan. STRIDE was utilised to investigate differences in DSB formation between FLASH and CONV proton delivery methods. Finally, an attenuator was designed to enable potential preclinical proton-FLASH experiments in Adelaide, facilitating future research in this emerging field. The specific hypotheses and aims were as follows:

1.2.1 Hypotheses and Aims

1. **Hypothesis:** AuNPs enhance the radiosensitivity of tumours by interfering with the DDR rather than by enhancing the physical dose of radiotherapy.

   Aim: Investigate whether the radiosensitization effects of AuNPs are due to physical dose enhancement using STRIDE, and to evaluate their potential impacts on the DDR with γH2AX, thereby validating part of their radiosensitization mechanism.

2. **Hypothesis:** ATM inhibitors increase radiosensitivity by inducing persistent DSBs that are otherwise undetectable by conventional assays and delay the activation of DDR pathways.

   Aim: Quantify previously undetectable DSBs with STRIDE and assess how ATM inhibitors impact DDR kinetics, providing a clearer understanding of their mechanistic role in radiosensitization.

3. **Hypothesis:** Proton-FLASH irradiation results in different patterns of DNA damage complexity compared to conventional dose rates, which contribute to its therapeutic advantages by enhancing tumour radiosensitivity while sparing normal tissues.

   Aim: Contextualise the role of DNA damage complexity as a potential mechanism of proton-FLASH radiobiology, via 1.) a systematic review to determine the extent of literature that identifies mechanisms of FLASH, especially relating to DSB formation and repair, and 2.) *in vitro* proton-FLASH experiments at CGMH to establish a practical capability to clarify competing theories surrounding these underlying mechanisms.

4. **Aim:** Design an attenuator to enable radiobiological proton-FLASH research to be conducted in Adelaide at the GE PETtrace 16.5 MeV cyclotron.

1.3 Thesis Structure

1.3.1 Chapter 1: Introduction

A primer for the content of the thesis, this Chapter provides an overview of the relevance of DNA DSBs in the context of cancer therapeutics. This includes a summary of the key hurdles in quantifying DSBs historically, how novel DSB detection assay STRIDE can overcome this, and the emerging treatment modalities it can be applied to. This highlights how the mechanisms of radiosensitizers, particularly AuNPs and ATM inhibitors, can be characterised with this technology. Moreover, it emphasises how the underlying cause of the normal tissue sparing effect conferred by FLASH may be identified, while also outlining future directions for proton-FLASH research in Adelaide with design of an attenuator. It provides background, context, and the research goals and professional outcomes of this PhD project.

1.3.2 Chapter 2: Materials and Methods

Experimental methods that were utilised throughout the project and the rationale for using them. It explains the STRIDE and γH2AX immunofluorescence assay protocols and emphasises their significance in investigating experimental cancer

therapeutics. This includes proton therapy and its potential improvements through ultra-high dose rate FLASH irradiation, as well as adjuvants such as DNA repair inhibitors and nanoparticles. It also delves into the specific motivations for what biological models were used, aiming to inform future preclinical research.

1.3.3 Chapter 3: Literature Review

Comprising three publications, this Chapter offers a comprehensive examination of existing literature. This chapter synthesizes relevant studies and findings related to DNA double-strand break damage and repair mechanisms and FLASH proton and carbon therapy. It sets the stage for the subsequent chapters by providing a foundation of prior research and current understanding, including a commentary about imaging DSBs, and a narrative review highlighting DSB and DDR immunofluorescent techniques, and a systematic review on particle-FLASH.

1.3.4 Chapter 4: Quantification of DNA Double-Strand Break Damage and Repair Kinetics Using Novel Immunofluorescent Markers

Establishment, optimisation, and utilisation of novel immunofluorescence assay STRIDE to quantify DNA double-stranded breaks. It starts with optimisation of the STRIDE methodology and testing efficacy with 4T1 cells exposed to hydrogen peroxide. This was then utilised for a kinetics-based study utilising ~ 2 Gy X-ray irradiation of 4T1 cells pretreated with ATM inhibitor AZD1390, AuNPs, or radiation alone resulting in two publications (one in print and one submitted at the time of writing). Cells were fixed incrementally over a 24-hour period to analyse DSB formation and repair kinetics quantified with STRIDE and γH2AX stains respectively.

1.3.5 *Chapter 5: Establishment of In Vitro Experiments at the Proton-FLASH Beamline at Chang Gung Memorial Hospital*

This chapter presents proton-FLASH experiments conducted at the Chang Gung Memorial Hospital Beamline. U87 glioblastoma and human oral fibroblast cell lines were irradiated at FLASH (~47 Gy/s) and CONV (0.53 Gy/s) and treated with radiation only, AZD1390, and AuNPs. This chapter discusses the setup, execution, and results of these *in vitro* experiments, comparing the DNA damage and repair and the potential benefits of ultra-high dose rate proton irradiation.

1.3.6 *Chapter 6: Attenuator Design and Modelling for Adapting High Current Output from Cyclotrons for Proton Irradiation Studies*

Preparation of future work, this chapter delves into the engineering aspects of attenuator manufacture and modelling. It describes the utilisation of SRIM and TRIM modelling software in designing an attenuator for use in SAHMRI's 16.5 MeV GE PETtrace cyclotron, facilitating comparative FLASH and CONV dose rate irradiations. This attenuator design will enable future preclinical proton-FLASH work in Adelaide using this infrastructure.

1.3.7 Chapter 7: Discussion and Conclusion

The discussion of results and their implications in a radiobiological context, and the key conclusions drawn from them. This chapter provides a summary of the entire thesis content, novelty of the experiments performed, and directions for future experimental work to be conducted from these findings.

2 Materials and Methods

2.1 Introduction

The methods employed throughout the experimental portions of this project used *in vitro* cancerous and non-cancerous cell cultures, which were exposed to a variety of genotoxic insults. The methods used for the systematic review and other manuscripts (published or prepared for publication), are outlined in their respective chapters. For validation purposes in preliminary experiments, this included neocarzinostatin (NCS) to confirm the reliability of γH2AX immunofluorescent staining, and hydrogen peroxide (H_2O_2) to optimise the STRIDE protocol. This informed more complex experiments where STRIDE and γH2AX stains were used in combination, and where cells were exposed to approximately 2 Gy of X-rays (Chapter 4) or protons (Chapter 5). To obtain quantitative data from these immunofluorescent stains, confocal imaging of stained cells and subsequent computational analysis of these images was performed. The content of this chapter provides a detailed overview of all the methodologies used for the experiments detailed within the remainer of this thesis, as well as the rationale behind the selection of each specific protocol.

2.2 Cell Culture

All cell lines were cultured in a 37°C incubator at 95% relative humidity and 5% CO_2. Mouse derived 4T1 (American Type Culture Collection, CRL-2539) and PC-3 (American Type Culture Collection, CRL-1435) cells were cultured with RPMI (Thermo Fisher: 11875093). Human U-87 MG (American Type Culture Collection, HTB-14) cells were cultured with DMEM (Thermo-Fisher: 10564011), and primary Human Gingival Fibroblast (HGF-1) (American Type Culture Collection, CRL-2014) cells were cultured with Fibroblast Basal Media (American Type Culture Collection, PCS-201-030), prepared with the Fibroblast Growth Kit Low Serum Kit as per the manufacturer's instructions (American Type Culture Collection, PCS-201-041). 24 hours before exposure to genotoxic insult, cells were seeded into Ibidi µ-Slide 8 Well chambered coverslips (Ibidi, 80826) at a density of 30000 - 40000 cells per well (NCS, H_2O_2, X-rays) or Millipore 8-well

detachable chamber slides (Merck, PEZGS0896) at a density of 15,000 cells per well (protons).

2.3 Clonogenic Assay

4T1 cells were seeded at a density of approximately 1 x 10^5 cells per well into four wells of a 6-well plate, with each well containing 1.5 mL RPMI, and allowed to adhere overnight at 37°C. A series of hydrogen peroxide (H_2O_2, Chem-Supply, HA154-500M) dilutions in PBS were prepared from a 10 M stock as follows: 100 mM (0.1 mL of 10 M H_2O_2 in 9.9 mL PBS), 1 mM (0.1 mL of 100 mM H_2O_2 in 9.9 mL PBS, labeled as the High concentration), 100 µM (1:10 dilution of the 1 mM solution, labeled as Medium), and 10 µM (1:10 dilution of the 100 µM solution, labeled as Low). Following incubation, RPMI medium was removed from each well and 500 µL of the respective H_2O_2 was added to wells at the following concentrations for 3 hours. Well 1: 0 µM (Control), Well 4: 10 µM (Low), Well 5: 100 µM (Medium), Well 6: 1000 µM (High). H_2O_2 was then removed from each well and cells were washed three times with PBS, followed by replacement of 1.5 mL fresh RPMI medium. Cells were allowed to recover for 1 hour before washing once with PBS and incubating with 300 µL trypsin for 5 minutes and addition of 700 µL RPMI. Cell suspensions were transferred to sterile 15 mL centrifuge tubes, and a 1:10 dilution of each cell suspension was prepared by adding 1 mL of cell suspension to 9 mL RPMI medium in a new tube for cell counting. 50 µL of each diluted suspension was added to a 1.5 mL Eppendorf tube and counted using a hemocytometer. Following cell counts, each suspension was further diluted to a final concentration of 2000 cells/mL. The following concentrations and volumes of each cell suspension were then seeded into 6-well plates: 0 µM (Control): 200 cells/well, 100 µL; 10 µM (Low): 300 cells/well, 150 µL; 100 µM (High): 500 cells/well, 250 µL; 1000 µM: 1000 cells/well, 500 µL. Each condition was then topped up to 1.5 mL RPMI per well and incubated overnight at 37°C. Cultures were maintained for approximately 7 - 8 days until colonies 25 - 50 cells in size (5 - 6 divisions) were formed, after which all cells were washed with PBS, fixed, and stained with 0.5% crystal violet in methanol for 10 minutes. After staining, each well was briefly immersed in water and left to dry. Finally, images were taken of the underside of the 6-well plate for colony counting in ImageJ.

2.4 *In Vitro* Pre-Treatments

2.4.1 Neocarzinostatin

4T1 cells seeded into Ibidi 8 well µ-slides were exposed to 0 µg/mL (Control), 1 µg/mL (labelled 'Low' dose), 10 µg/mL (labelled 'High' dose) of NCS, which was introduced into the cell media for 1 hour at 37°C. After exposure, medium containing NCS was aspirated and cells washed thoroughly with PBS, followed by fixation with 95% EtOH + 5% glacial acetic acid on ice.

2.4.2 Hydrogen Peroxide

Cells seeded into Ibidi 8 well µ-slides were exposed to 200 µL H_2O_2 mixture for 0 (Control), 15, 30, or 60 minutes at 20 mM in RPMI. Following exposure, cells were washed with PBS and fixed with 4% paraformaldehyde or 95% EtOH + 5% glacial acetic acid on ice.

2.4.3 AZD1390 and AuNPs

Cells were exposed to three different conditions: no pre-treatment, pre-treatment with 30 nM ATM inhibitor AZD1390 (MedChemExpress, HY-109566), or pre-treatment with 0.5 nM (protons) or 1 nM (X-rays) AuNPs. AuNPs of size 16 – 18 nm were synthesised with the Turkevich method [71], which were consequently PEGylated and functionalised with transferrin as reported previously [9, 10, 72]. 2 hours prior to irradiation, stocks AZD1390 and AuNPs were diluted to working concentrations in either DMEM or Fibroblast Basal Media from a stock of 1 mM to 30 nM, and AuNPs from a stock of 87nM to 0.5 nM (protons) or 1 nM (X-rays). 2 hours before irradiation, culture media was replaced with the appropriate solutions of 30 nM AZD1390 or 0.5/1 nM AuNPs. For proton irradiations, each well was filled without airgaps to prevent scatter.

2.5 Irradiation Parameters and Setup

2.5.1 X-ray Irradiation

X-ray irradiations were performed with a 160 kV RadSource 2000 Small Animal Irradiator located at the South Australian Health and Medical Research Institute (SAHMRI), Adelaide, Australia. Cells were irradiated for 45 seconds with a total dose delivered of approximately ~1.93 Gy (0.0429 Gy/s). Cells were fixed

incrementally at 0 (pre-irradiation), 15-, 30-, 45-, 60-, 120-, 240-, and 1440-minutes post-irradiation with 4% paraformaldehyde for 10 minutes at room temperature.

2.5.2 Proton Irradiation

Proton irradiations were performed with the 230 MeV Sumitomo Heavy Industries cyclotron located at Linkou Chang Gung Memorial Hospital, Taoyuan City, Taiwan. Cells were irradiated with 2 Gy protons with FLASH for 43.03 ms with an average dose rate of 47.815 ± 0.860 Gy/s, and CONV for 40 s with an average dose rate of 0.53 Gy/s. The rationale for using a lower dose was to allow direct comparison to conventional radiotherapy dose regimens and to isolate dose rate-dependent differences in DNA damage and repair foci formation without confounding by overwhelming cytotoxicity which would prevent foci resolution. Although a 2 Gy dose may not produce the full spectrum of FLASH tissue sparing effects reported at higher doses, it provides valuable mechanistic insight into the potential biological underpinnings of the FLASH response. Two well plates were irradiated for each dose rate condition, with a field size of $1cm^2$ covering two positions on each 8-well plate (4 radiation doses delivered total). HDPE moulds were utilised to align the well plates vertically and perpendicular to the proton beam, with EBT3 Gafchromic film adhered to the bottom of each well-plate to determine the field of dose deposition. Cells were fixed at 15- and 60-minutes post-irradiation for each condition with 4% paraformaldehyde for 10 minutes at room temperature.

2.6 Immunofluorescence Staining

2.6.1 STRIDE Assay

Following fixation, cells were permeabilised in PBS/0.5%Triton X-100 for 10 min and subsequently incubated with 0.5-10mM EDTA/PBS for 10 min at RT. Cells washed with 100 µL of TUNEL kit Wash Buffer at RT. BrdUTP conjugation to DSB ends was performed with the APO-BrdU Kit (BD Biosciences, Cat No. 556405). A master mix of TdT enzyme, TdT reaction buffer, BrdUTP and ddH_2O was made according to the manufacturer's instructions. 50uL of the BrdUTP conjugation master mix was added per well and incubated for 1 hour at 37°C in

a humidified incubator, followed by a wash with 100 µL of Rinse Buffer at RT. Each well was then blocked with 200µL 3% BSA for 1 hour at 37°C, then incubated with 40 µL of both Mouse MoBu-1 anti-BrdU (Abcam, 8039, 1:500) and Rabbit Polyclonal anti-BrdU (Abcam, ab152095, 1:200) antibodies in 3% BSA overnight at 4˚C. Wells were then thoroughly washed with Duolink® In Situ Wash Buffers, Fluorescence, 1X Wash Buffer A (Sigma Aldrich, DUO82049) and incubated with 40 µL of Duolink® In Situ PLA® Probe Anti-Rabbit PLUS (Sigma Aldrich, DUO92002-100RXN) and Anti-Mouse MINUS (Sigma Aldrich, DUO92004-100RXN) master mixed in 3% BSA for 1 h in a 37˚C humidified incubator. Wells were then washed with 1X Wash Buffer A and incubated with 40 µL of ligation mix (Sigma Aldrich, DUO92013) for 30 minutes at 37˚C. Wells were washed with 1X Wash Buffer A and subsequently incubated with 40 µL polymerase mix (Sigma Aldrich, DUO92013) for 100 minutes at 37˚C. Finally, wells were washed for 10 minutes with 1X Wash Buffer B (Sigma Aldrich, DUO82049) at RT, and then 0.01X Wash Buffer B for 1 min.

2.6.2 γH2AX Assay

Cells were blocked with 3% BSA for 1 hour at 37°C, followed by incubation with anti-phospho-histone H2A.X (Ser139) (20E3) Rabbit mAb conjugated with Alexa Fluor 488 (Cell Signalling Technology, #9719). Finally, nuclear staining of the cells was performed with 1 mg/mL DAPI solution (Thermo Fisher, Cat No. 62248).

2.6.3 Confocal Imaging: Excitation and Emission Spectra

Peroxide and X-rays: The Zeiss LSM 710 and LSM 980 laser scanning confocal microscopes (Carl Zeiss, Germany) were used to acquire fluorescent images of cells at 20x magnification. Sets of laser excitation and emission spectra are as below:

- DAPI: λex 350 nm; λem 470 nm
- γH2AX: λex 488 nm; λem 496 nm (Alexa 488)
- STRIDE: λex 644 nm; λem 669 nm (Cyanine 5, Zeiss Filter set 50)

Protons: The ImageXpress® Micro Confocal High Content Imaging System was used at 40x magnification across 3 excitation filters:

- DAPI: λex 377/50 nm; λem 470 nm
- γH2AX: λex 475/34 nm; λem 496 nm (FITC)
- STRIDE: λex 560/32 nm; λem 624 nm (Texas Red)

2.6.4 Image Analysis

Images were processed with CellProfiler Version 4.2.6. It is an open-source analysis package which allows for high-throughput tools to define and quantify cellular features. CellProfiler has several modules that perform different operations on a set of input images. When ordered in the fashion below (Figure 6), this is called an 'analysis pipeline'.

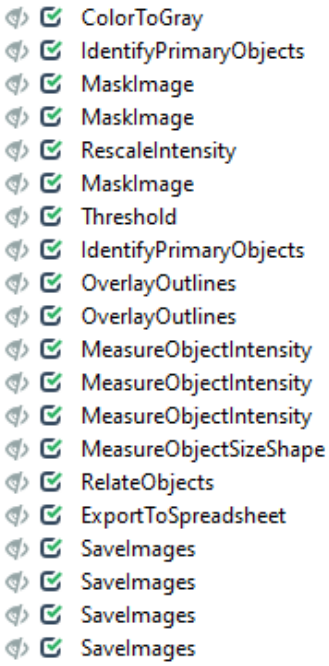
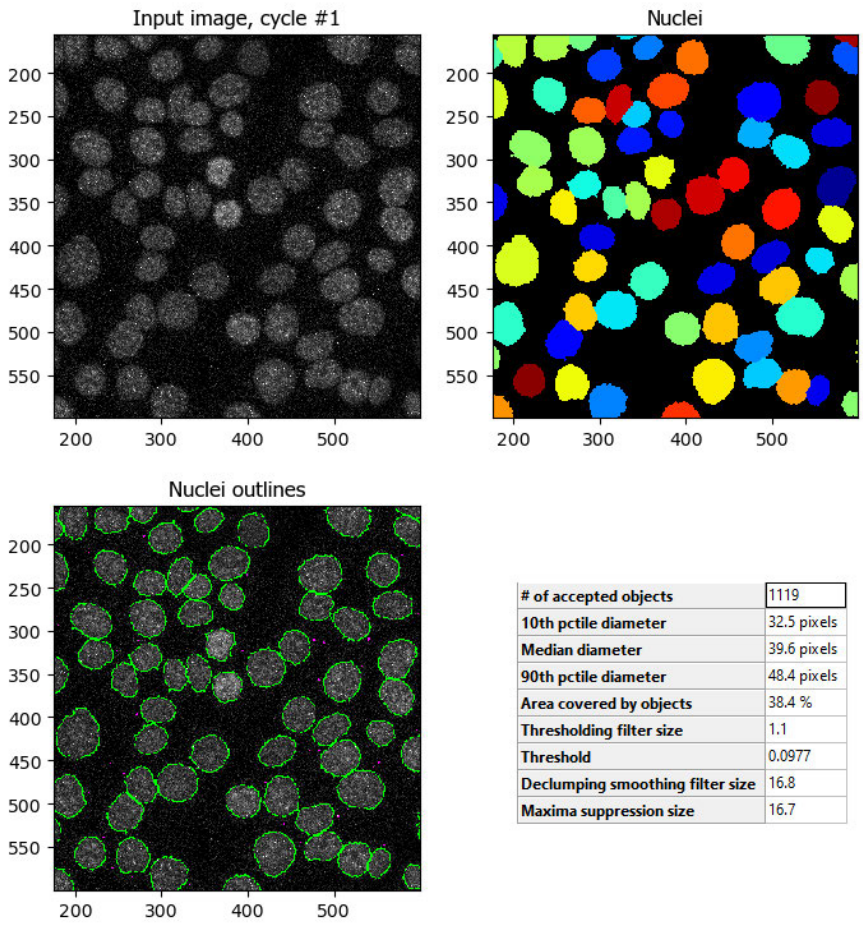


Figure 6: CellProfiler analysis pipeline for the image analysis workflow. A green tick in the checkbox next to the module name indicates each active module in the pipeline. This pipeline processes each image in a batch according to the order of this list, top to bottom.

Modules can be added, removed, or re-ordered depending on the needs of each experimental run. The process to identify objects within nuclei follow the general format of splitting each RGB image into their grayscale counterparts, classifying and identifying nuclei, and then further classifying and identifying the red and green foci within each nucleus. Data is then exported to a spreadsheet for further graphing and statistical analysis. IdentifyPrimaryObjects was used to produce

outlines of objects within images based on predefined parameters. For the sake of biological analysis, this is usually first applied to the nuclei of cells, with a size threshold and method typical for nuclei identification (e.g., Otsu). In this analysis pipeline it has been applied to the blue channel of each image to outline the nucleus of each cell (Figure 7).



# of accepted objects	1119
10th pctile diameter	32.5 pixels
Median diameter	39.6 pixels
90th pctile diameter	48.4 pixels
Area covered by objects	38.4 %
Thresholding filter size	1.1
Threshold	0.0977
Declumping smoothing filter size	16.8
Maxima suppression size	16.7

Figure 7: Image segmentation with the IdentifyPrimaryObjects module in CellProfiler. Nuclei were identified based on the blue channel of each RGB image, followed by masking of the green and red channels based on the objects (nuclei) identified. The values of integrated intensity for each channel were then measured for each nucleus with MeasureObjectIntensity. Reproduced by permission of John Wiley and Sons [73].

After identifying which objects were nuclei, MaskImage was then used to remove all signal surrounding each nucleus. This was also repeated for the red and green channels. This is to ensure that the IdentifyPrimaryObjects module for STRIDE and γH2AX only counts objects that reside within the nucleus. STRIDE and γH2AX foci counts were also quantified through use of IdentifyPrimaryObjects to

the red and green channels respectively, and then assigned to each nucleus with the RelateObjects module. A quality assurance step to ensure the IdentifyPrimaryObjects module is outlining objects correctly is the OverlayOutlines module. This allows for a ‘sanity check’ to be performed where the outlines produced from IdentifyPrimaryObjects can be overlayed on top of the red, green, or blue channel of the image. This ensures that the IdentifyObjectsModule is outlining STRIDE, γH2AX and nuclei consistently. In cases where low or high intensity foci make it difficult to identify foci consistently, the Threshold module was used. Producing a binary image, it is typically based on lower and upper bounds of pixel brightness (0 – 255, black to white) that define a feature that should be included for downstream processing. This thresholding step was applied to identify clusters of STRIDE within the nucleus of high intensity, as for some images, particularly for the proton images acquired in Taiwan, STRIDE did not present as discrete foci, but as a pan-signal throughout the entire nucleus. Instead of quantifying individual foci counts within each nucleus, the brightness of the signal within each nucleus, or the integrated intensity with MeasureObjectIntensity, was quantified. Blue, red, and green channels were measured in this module, providing the sum of pixel intensities for DAPI, STRIDE and γH2AX signals respectively.

2.6.5 Data Processing and Statistical Analysis

Once the image processing process was complete, single cell data was exported with ExportToSpreadsheet, which produces an Excel spreadsheet containing all raw data values from the modules used in the CellProfiler pipeline. This data is arranged with each row representing an identified nucleus and each column representing a variable measured for that nucleus, including the values of integrated intensity for DAPI, STRIDE and γH2AX. These values are then organised in a separate spreadsheet, where normalization calculations are performed by dividing the integrated intensity of STRIDE or γH2AX by the corresponding DAPI integrated intensity value. Following normalization, data was transferred from Excel to GraphPad Prism to produce box and whisker plots, scatter plots, and histograms, as well as summary statistics for each condition. Since this data is non-parametric, a Mann-Whitney U test was performed to assess the differences between two independent conditions at a single fixation

timepoint. This test compares the ranked values between two independent groups to assess whether their distributions differ. It ranks all the data points from both groups together, and then compares the sum of ranks for each group. Instead of comparing means as per a t-test, it determines whether the values in one group tend to be larger or smaller than the values in the other, making it suitable for this non-parametric dataset. For example, this test was used to compare the normalized integrated intensity of STRIDE during X-ray radiation alone to X-rays in combination with gold nanoparticles.

After analysing the STRIDE and γH2AX signals from each cell, the correlation between these signals and cell phase was determined. Firstly, a histogram was plotted to depict the frequency distribution of integrated intensity values from the DAPI channel. These values were then normalized to the most frequent intensity value for each histogram plot, representing the G_1 phase peak. This provided a frequency distribution that approximated the total DNA content in a cell across phases (1 = 2N, 2 = 4N). The G_1 phase was categorised as 0.6 – 1.4, S as 1.4 – 1.6, and G_2/M as 1.6 – 2.4. These plots were then gated per these arbitrary normalized DAPI units in Floreada.io, allowing for the plotting of STRIDE versus γH2AX signal at each timepoint with each phase represented in blue (G_1), red (G_2/M), and green (S).

2.7 Attenuator Design

The attenuator design involved two materials: Brass with a thickness of 0.65 mm and Tungsten with a thickness of 0.40 mm. Stopping and Range of Ions in Matter (SRIM) and Transport of Ions in Matter (TRIM) by Ziegler et al. [74] Monte Carlo packages were used to determine the minimum thickness of attenuator material required to stop the protons. Both materials were configured as a 25 x 25 mm area containing a 16 x 16 hexagonal array of holes with diameters of 100 µm (D1) and 150 µm (D2). The array was designed with varying pitches of 400 µm, 800 µm, and 1400 µm, resulting in 2500, 625, and 78 holes respectively. These configurations theoretically resulted in corresponding dose rates of 3.74 Gy/s, 0.935 Gy/s, and 0.117 Gy/s, calculated from dosimetry measurements from Asp et al. 2019 [75] using the GE PETtrace 16.5 MeV cyclotron.

2.8 Justifications for Approach

2.8.1 Cell Selection Rationale

The cell lines utilised throughout these experiments have an emphasis upon clinical translation. Proton therapies are highly beneficial for treating paediatric cancers and preventing latent side-effects in normal tissues. The characteristic Bragg Peak allows for highly localised dose delivery to the tumour while minimizing radiation exposure to critical surrounding structures [76]. Rare and aggressive cancers of the brain and spinal cord, including glioblastoma, gliosarcoma and medulloblastoma, are all considerations for experimental models *in vitro* and xenograft models in vivo. For radioresistant cancers in critical areas (e.g., chordoma in the base of the skull) dose escalation, and consequently the extent of tumour control, depends on the sensitivity of the organs surrounding it. Brain tissue is particularly radiation-sensitive due to the complexity of its structure and the detrimental effects radiation has on its function, which can lead to long-term neurological impairments [77]. Blindness or neurocognitive development delay are serious collateral side-effects in the treatment of radioresistant tumours, that which ultra-high dose rate proton therapy could potentially alleviate [78, 79]. The total dose threshold would consequently be improved, allowing for higher dose administration throughout treatment and greater tumour control. Conversely, some tumours may not be highly radiation resistant, yet grow in areas which include highly radiosensitive normal tissues; such is the case for some breast cancers and lung metastases. The focus of treating such cancers is shifted more-so on identifying the minimum dose threshold at which tumour control is achieved. Minimising the total dose administered to the radiation sensitive surrounding tissues is therefore the priority, rather than in a radioresistant tumour where treatment aims for the maximum dose threshold before damage to surrounding tissues becomes too severe. X-ray radiotherapy is often prescribed in breast cancer treatments, [80] particularly after lumpectomy or mastectomy to target residual cancer cells in areas surrounding the former tumour site. Therefore, the murine-derived 4T1 cell line was selected for x-ray irradiations, and the human-derived Uppsala 87 Malignant Glioma (U87 or U87-MG) and oral fibroblast (OF) cell lines were selected for proton irradiations. 4T1 cells are often used as a model of triple-

negative breast cancer for in vivo studies [81], and thus use of this cell line allows us to reflect clinical treatments and to progress this work to animals in future studies. U87 and OF cells were selected as they represent a glioma, commonly treated with proton therapy [76, 82], and a representative normal tissue of the oral cavity which can be irradiated during treatments of head and neck cancers [83]. Using these two cell types during proton irradiations allows for comparing differential effects of dose rate on DNA damage and repair foci formation between cancerous and normal cells, with a focus on investigating the DNA damage mechanisms of the FLASH effect. Although OFs are not derived from brain tissue, they provide a relevant normal cell type for assessing different biological responses to FLASH irradiation. Normal cells may exhibit less damage and recover quicker compared to cancerous cells under FLASH dose rates compared to CONV [84]. This would explain how FLASH-RT can minimise normal tissue damage whilst maintaining cancer killing efficacy, thereby enabling the assessment of whether differences in DSB formation and repair contribute to this proposed differential response.

2.8.2 Irradiation, ATM Inhibition, and Gold Nanoparticle Dosages

The rationale for selecting 2 Gy as a dose for X-ray and proton irradiations is grounded in its clinical relevance and the biological response it induces. Regarding cell survival, previous clonogenic assays showed that a 2 Gy dose results in a survival fraction of approximately 50%, enabling observation of cellular responses without excessive cell death (data unpublished). In the remaining cell population that can be observed after fixation, it is estimated that there are approximately 20 - 40 DSBs per Gy of X-ray radiation [18], however this is assumed from correlating the number of 53BP1 or γH2AX foci with DSBs. A dose of 2 Gy therefore causes around ~40 – 80 DSBs per cell, thereby inducing a sufficient degree of DNA damage whilst preventing the complete saturation of the nucleus with STRIDE and γH2AX foci. This is to ensure that when quantifying these foci with an automated detection method such as CellProfiler, that it was capable of segmenting foci more accurately by minimising the number that cluster and overlap. In the context of FLASH experiments, the use of 2 Gy enabled mechanistic comparisons between FLASH and conventional dose rates at a clinically relevant fraction size, whilst simultaneously avoiding foci oversaturation.

As well as this, STRIDE/γH2AX foci within each nucleus remained at manageable levels of brightness to allow for precise measurements of integrated intensity. This dosage was therefore beneficial when acquiring confocal images, decreasing the total number of pan-stained nuclei, and thereby streamlining downstream quantification.

Our experiments also involve the testing of adjuvant therapies. This involved pre-treatment of cells with either 0.5/1 nM gold nanoparticles (AuNPs) or 30 nM ATM inhibitor (ATMi) AZD1390. Multiple clinical trials have been conducted with AuNPs to study their therapeutic (NCT04626921, NCT03815916), drug delivery (NCT02837094, NCT03020017, NCT00356980) and photothermal therapy (NCT04240639, NCT02680535) capabilities [85]. Although not yet FDA approved, they have also been trialed against solid tumours (NCT00356980, NCT00436410) [43]. AZD1390 also has two ongoing clinical trials to determine its tolerability in treatment of brain metastases (NCT05182905, NCT03423628) [86]. Both therapeutics have been employed to improve the efficacy of current cancer therapies, however their mechanisms of action, especially regarding DSB formation, have yet to be fully characterized. Akin to determining optimal X-ray dose, clonogenicity experiments were also performed to determine AuNP dose. 4T1 cell survival in response to AuNPs at concentrations ranging from 0 to 5.76 nM was previously evaluated. After 24 hours of AuNP exposure, cell survival rates were approximately 58 to 90% for doses between 0.36 and 1.44 nM, assessed 48 hours post-exposure (data unpublished). Therefore, 0.5 and 1 nM AuNPs were deemed suitable for inducing cytotoxicity without causing excessive cell death, whilst still allowing for effective measurement using STRIDE and γH2AX. Conversely, a previous study with analogous ATM inhibitor AZD0156 (also developed by AstraZeneca), displayed a reduction in γH2AX levels in FaDu cells at a dose of 30 nM following 5 Gy irradiation [53]. As the active form of ATM phosphorylates γH2AX, its inhibition, via AZD0156 or AZD1390, consequently decreases γH2AX phosphorylation. Given that AZD1390 is highly selective for ATM, with an IC50 of 0.78 nM, and the dose employed is substantially higher than this (30 nM), near-complete suppression of the γH2AX signal was also anticipated.

3 Literature Review

3.1 Introduction

Current immunofluorescent techniques have proven to be invaluable tools in the study of genotoxicity through characterisation of the DNA damage response (DDR). A key limitation of these assays is their inability to directly detect DNA double-strand breaks (DSBs), the most lethal form of DNA damage. This limitation highlights the need for more accurate methods to directly assess DSBs, particularly in the context of therapeutic research and the development of novel cancer treatments. To address this gap in detection capabilities, two comprehensive reviews were conducted to examine all current novel and conventionally used assays for detecting both DSBs and DDR factors. The first of these reviews was a Comment published in *Nature Reviews Molecular Cell Biology*, which explored the emerging technologies in DSB detection and the need for improved methodologies. The second review, a narrative article in the *International Journal of Molecular Sciences*, expanded on these ideas, providing a more detailed summary of the techniques available for detecting DDR factors and their activation timelines in response to DNA damage. From the findings of these reviews, this PhD project sought to advance the detection of DSBs by employing the SensiTive Recognition of Individual DNA Ends (STRIDE) assay, which was selected for its ability to directly measure DSBs *in vitro*. STRIDE was then applied to characterise the effects of experimental cancer therapeutics, including gold nanoparticles (AuNPs) and ATM inhibitors (ATMi) as radiotherapy adjuvants and ultra-high dose rate FLASH radiotherapy. Despite FLASH's growing relevance, no comprehensive reviews existed at the time that systematically summarised the literature on particle-FLASH, or the mechanisms of DNA damage and repair in this context. This led to the creation of a particle-FLASH systematic review, which provided a thorough analysis of the existing research on FLASH radiotherapy and its impact on DNA repair mechanisms. The findings from the *Nature* Comment, the IJMS narrative review, and the particle-FLASH systematic review were then integrated to inform the experimental design and approach of this PhD project. These reviews not only provided a thorough

understanding of current methodologies but also highlighted key gaps and opportunities for advancing research in DNA damage detection and radiotherapy, guiding the experimental work undertaken throughout the project.

3.2 Imaging DNA Double-Strand Breaks, Are We There Yet?

3.2.1 Summary

The ability to detect and quantify DSBs is essential to advancing understanding of cellular responses to genotoxic stress and the mechanisms underlying DNA repair. The *Nature* commentary was written to address a critical gap in the field by emphasising the importance of accurate and reproducible DSB detection methodologies. Traditional detection methods, while widespread, lack the sensitivity or specificity required to capture subtle variations in DNA damage, instead quantifying DNA repair. The commentary sought to highlight emerging technologies that have significantly enhanced DSB detection capabilities, specifically new immunofluorescence-based techniques. These advancements provide researchers with tools to better characterise DSB repair dynamics, identify novel therapeutic targets, and evaluate the efficacy of treatments including radio- and chemo-therapeutics. By showing both the need for these methodologies and the recent innovations in the field, the commentary aimed to stimulate further development and application of cutting-edge DSB detection assays and challenge the current paradigm of quantifying genotoxicity. This is pertinent for not only radiation, but radio- and chemo-pharmaceuticals, nanoparticles, and gene editing technologies. Its relevance in characterising a broad range of therapies makes the development of these novel DSB detecting assays very important to measure unexplained phenomena including the FLASH effect and nanoparticle radiosensitisation.

Check for updates

Imaging DNA double-strand breaks — are we there yet?

Jake Atkinson[1], *Eva Bezak*[2,3] *and Ivan Kempson*[1] ✉

DNA double-strand breaks (DSBs) are fundamental to cell biology, from evolution to the latest gene-editing technologies. Yet, does an assay exist that truly quantitatively visualizes DSBs? Over-reliance on DSB detection by proxies can misguide interpretation of conventional assays, and more faithful DSB representatives await development.

DNA double-strand breaks (DSBs) can arise spontaneously from nuclease activities or through insults from reactive species, radiation and cytotoxic agents. DSBs are the most deleterious form of DNA damage, causing genome instability and chromosomal aberrations; DSB repair responses are thus rapid and stringently regulated[1]. By contrast, prescribed cleavage of DNA at targeted loci facilitates gene-editing technologies such as CRISPR–Cas.

Quantifying DSBs is essential for identifying relationships between DNA cleavage and repair, which are pertinent to ageing, mutagenesis, genotoxicity and therapeutics, both established (chemo- and radio-therapies) and emerging (gene editing, particle and FLASH radiotherapy, and so on). Currently, our most powerful tools to spatially observe DSBs rely on immunofluorescence labelling of DNA damage response (DDR) proteins or histone modifications such as 53BP1 and γH2AX, respectively. These well-established markers typify the DDR[2]. However, interpretation of these downstream proxies is often extended upstream, through a range of assumptions, to DSB formation in a directly proportional, quantitative manner. These interpretations can be problematic: repair can be partial, thereby skewing the proportionality between DSBs and 53BP1 or γH2AX 'repair' foci; initiation of the repair response does not equal repair completion; and 'repair' foci can exist in the absence of DSBs[3]. Thus, detecting DSBs with a high degree of reliability is still challenging, and more sensitive markers are required for accurate DSB quantification. In this commentary, we discuss sources of potential DSB misinterpretation using common assays, and propose to reshape our approach to measuring DSBs.

Endogenous markers of DSBs

DSB sensors, including PARP1, the MRE11–RAD50–NBS1 complex, the Ku70–Ku80 complex and SIRT6 detect DSBs and initiate the DDR[2,4]. H2AX phosphorylation (γH2AX) is a pivotal early step in the repair process, allowing the remodelling of chromatin surrounding DSBs and the recruitment of repair proteins[2]. One such protein is 53BP1, which recruits additional DSB repair proteins and regulates repair-pathway choice. Through immunofluorescence, 53BP1 and γH2AX are widely used, often dogmatically, as DSB markers, as they form discrete foci at or in proximity to DSBs.

Biases of current assays

The only conventional method for in situ DSB detection is terminal deoxynucleotidyl transferase dUTP nick-end labelling (TUNEL), but it does not quantify discrete DSB foci. Consequently, other markers are used, but considering many reports in the literature, it is necessary to remember that DDR markers generally reflect repair, not DSBs. An excellent example is perturbation of the DDR with a TGFβ inhibitor prior to DNA insult. Consequently, fewer γH2AX foci are detected compared with control, which correlates with decreasing clonogenicity, that is, repair is impaired, leading to reduced proliferative capacity[5]. This highlights the crux of assays based on DDR factors: they are ambiguous. Do foci correlate with DSB accumulation, increased repair capacity and/or efficiency, or expression of DDR factors? Other misconceptions when using DDR proteins as DSB markers may arise.

Regarding γH2AX, it is generally true that DDR induces H2AX phosphorylation, but H2AX phosphorylation is not always correlated with DNA damage (REF.[3] and references therein). Although γH2AX is an excellent tool, especially for monitoring DDR kinetics, quantifying the relationship between γH2AX foci production and DSBs is challenging, especially owing to the rapid progression of the DDR. Highly variable repair kinetics and H2AX phosphorylation at sites other than where DSB repair is occurring complicate the picture. For example, loss of shelterin complex functionality at short telomeres leads to chromosomal ends also being recognized by DDR machinery[6]. Regarding 53BP1, biases lie in its dominance in the G1 phase of the cell cycle, where it mediates recruitment of non-homologous end-joining factors; inversely, homologous recombination dominates DSB repair in other cell cycle phases.

[1]*Future Industries Institute, University of South Australia, Adelaide, Australia.*

[2]*Allied Health and Human Performance, University of South Australia, Adelaide, Australia.*

[3]*Department of Physics, University of Adelaide, Adelaide, Australia.*

✉*e-mail: Ivan.Kempson@unisa.edu.au*

https://doi.org/10.1038/s41580-022-00513-7

Novel assays

A few novel techniques to overcome the lack of highly specific diagnostic biomarkers of DSBs are emerging. For example, the DSB-binding protein Gam, derived from bacteriophage Mu, was fused to GFP[7]. Gam's normal function is to inhibit host exonucleases by binding to exposed ends of linear phage DNA, thereby preventing its degradation. GamGFP is capable of binding to DSBs, thereby allowing the observation of discrete DSB foci. A major drawback of this technique is that the efficiency of GamGFP binding to DSB sites in mammalian cells is challenged by its orthology with Ku[7]. Thus, although GamGFP is useful in specifically marking DSBs, its competition with Ku to bind to DSBs makes it difficult to utilize quantitatively without first knocking-out Ku.

Similar to GamGFP, a fluorescently conjugated SIRT6 was used to validate SIRT6 function in DSB detection[4]. One of its key attributes is its ability to localize to DSB sites independently of PARP1, MRE11 and Ku80 and initiate the DDR. It is believed that SIRT6 binds open-ended DNA as a homodimer, and its dimerization was suggested to be cooperative with binding[4]. Although there is evidence supporting SIRT6's capacity to bind to DSBs, it is also predicted that the SIRT6 monomer is capable of binding to single-stranded DNA breaks. Additionally, SIRT6 is involved in other processes including cellular metabolism and inflammation[8]. Thus, use of SIRT6 for DSB detection is likely to produce substantial off-target background signalling, complicating its establishment as a DSB-specific biomarker. GamGFP and SIRT6 highlight the challenges in using fluorescently tagged proteins, which may compete with DDR machinery or possess multiple functions that reduce foci specificity to DSBs. Exogenous markers are likely to be less ambiguous.

A technique more specific for DSB detection is sensitive recognition of individual DNA ends (STRIDE)[9]. In STRIDE, the nucleotide analogue BrdU is enzymatically conjugated to free 3′-OH DNA ends, thereby facilitating recognition through two sets of primary and secondary antibodies, with each secondary antibody being conjugated with its own set of oligonucleotides. Amplification of the fluorescence signal is then performed through rolling circle amplification (RCA). Labelling was demonstrated for DSBs induced by Cas9, chemical and biological agents, ionizing radiation and spontaneous formation[9].

At the other end of the DDR, persistent repair foci are uniquely identified by DNA damage in situ ligation followed by proximity ligation assay (DI-PLA)[10]. DI-PLA, which has broad utility and can be applied also to DDR factors, involves the blunting of DSB ends, ligation of biotinylated oligonucleotides, and incubation with antibodies against biotin and against a protein of interest, and is also followed by RCA. Able to discriminate between persistent DSBs and active repair or other chromatin modifications, DI-PLA provides an accurate measure of foci resistant to repair machinery, which threaten chromosome integrity.

Although further use of these cutting-edge techniques is required to properly assess their practicality and efficacy compared with conventional and other novel techniques, STRIDE and DI-PLA vastly improve fluorescent targeting of DSBs, in a bid to eliminate the ambiguity conferred by labelling of the currently used endogenous protein proxies.

Conclusion

The development of new and innovative fluorescence-based DSB detection techniques is pushing the envelope in the quantification of DSBs. A long road lies ahead of establishing these newer methodologies, which have the potential to eliminate the reliance on using endogenous DDR factors as DSB proxies. Owing to their relative novelty, information on their reliability is sparse, and they require additional refinement, optimization and improved affordability prior to widespread use. Continual development of accurate DSB detectors is essential to improving our understanding of mutagenesis, cancer and ageing-related diseases and for the development of suitable therapies.

1. Scully, R. et al. DNA double-strand break repair-pathway choice in somatic mammalian cells. *Nat. Rev. Mol. Cell Biol.* **20**, 698–714 (2019).
2. Mah, L. J. et al. γH2AX: a sensitive molecular marker of DNA damage and repair. *Leukemia* **24**, 679–686 (2010).
3. Rybak, P. et al. Low level phosphorylation of histone H2AX on serine 139 (γH2AX) is not associated with DNA double-strand breaks. *Oncotarget* **7**, 49574–49587 (2016).
4. Onn, L. et al. SIRT6 is a DNA double-strand break sensor. *eLife* **9**, e51636 (2020).
5. Bouquet, F. et al. TGFbeta1 inhibition increases the radiosensitivity of breast cancer cells in vitro and promotes tumor control by radiation in vivo. *Clin. Cancer Res.* **17**, 6754–6765 (2011).
6. Maciejowski, J. & de Lange, T. Telomeres in cancer: tumour suppression and genome instability. *Nat. Rev. Mol. Cell Biol.* **18**, 175–186 (2017).
7. Shee, C. et al. Engineered proteins detect spontaneous DNA breakage in human and bacterial cells. *eLife* **2**, e01222 (2013).
8. Yang, X. et al. Roles of SIRT6 in kidney disease: a novel therapeutic target. *Cell Mol. Life Sci.* **79**, 53 (2021).
9. Kordon, M. M. et al. STRIDE — a fluorescence method for direct, specific in situ detection of individual single- or double-strand DNA breaks in fixed cells. *Nucleic Acids Res.* **48**, e14-e14 (2019).
10. Galbiati, A. et al. A novel single-cell method provides direct evidence of persistent DNA damage in senescent cells and aged mammalian tissues. *Aging Cell* **16**, 422–427 (2017).

Competing interests
The authors declare no competing interests.

Peer review information
Nature Reviews Molecular Cell Biology thanks the anonymous reviewers for their contribution to the peer review of this work.

3.3 DNA Double Strand Break and Response Fluorescent Assays: Choices and Interpretation

3.3.1 Summary

DSBs initiate a highly coordinated cellular response involving the activation and recruitment of DDR factors, which are essential for maintaining genomic stability. Building upon the concepts outlined in the *Nature* commentary, the *International Journal of Molecular Sciences* publication expanded the discussion to provide a comprehensive review of DSB detection methodologies and their role in monitoring DDR factor activation. This work aimed to provide a detailed guide on how to detect key DDR proteins, such as γH2AX and 53BP1, and to map their spatiotemporal kinetics following DNA damage. This includes a chronological timeline of protein activation from DSB formation to its repair, as well as what fluorescent markers are relevant at each stage of the repair process. The timescales presented are on the order of minutes to hours post-insult. It also details the intricacies of each DDR protein and their relation to the wider network of DSB repair factors, which factors they regulate (and are regulated by), and whether suppression of related DDR factors will affect how it presents fluorescent foci during microscopy. Common limitations were also addressed such as variability in staining protocols and resolution constraints, while offering recommendations for optimising detection accuracy. This publication serves as a resource for advancing research on DNA damage and repair mechanisms, particularly in informing therapeutic development.

International Journal of
Molecular Sciences

MDPI

Review

DNA Double Strand Break and Response Fluorescent Assays: Choices and Interpretation

Jake Atkinson [1], Eva Bezak [2,3], Hien Le [2,4] and Ivan Kempson [1,*]

[1] Future Industries Institute, University of South Australia, Mawson Lakes, SA 5095, Australia; jake.atkinson@mymail.unisa.edu.au
[2] UniSA Allied Health and Human Performance, University of South Australia, Adelaide, SA 5095, Australia; eva.bezak@unisa.edu.au (E.B.)
[3] Department of Physics, University of Adelaide, North Terrace, Adelaide, SA 5005, Australia
[4] Department of Radiation Oncology, Royal Adelaide Hospital, Adelaide, SA 5000, Australia
* Correspondence: ivan.kempson@unisa.edu.au

Abstract: Accurately characterizing DNA double-stranded breaks (DSBs) and understanding the DNA damage response (DDR) is crucial for assessing cellular genotoxicity, maintaining genomic integrity, and advancing gene editing technologies. Immunofluorescence-based techniques have proven to be invaluable for quantifying and visualizing DSB repair, providing valuable insights into cellular repair processes. However, the selection of appropriate markers for analysis can be challenging due to the intricate nature of DSB repair mechanisms, often leading to ambiguous interpretations. This comprehensively summarizes the significance of immunofluorescence-based techniques, with their capacity for spatiotemporal visualization, in elucidating complex DDR processes. By evaluating the strengths and limitations of different markers, we identify where they are most relevant chronologically from DSB detection to repair, better contextualizing what each assay represents at a molecular level. This is valuable for identifying biases associated with each assay and facilitates accurate data interpretation. This review aims to improve the precision of DSB quantification, deepen the understanding of DDR processes, assay biases, and pathway choices, and provide practical guidance on marker selection. Each assay offers a unique perspective of the underlying processes, underscoring the need to select markers that are best suited to specific research objectives.

Keywords: microscopy; non-homologous end joining (NHEJ); homologous-recombination (HR); γH2AX; p53 Binding Protein 1 (53BP1); foci; pathway choice; repair

check for updates

Citation: Atkinson, J.; Bezak, E.; Le, H.; Kempson, I. DNA Double Strand Break and Response Fluorescent Assays: Choices and Interpretation. *Int. J. Mol. Sci.* **2024**, *25*, 2227. https://doi.org/10.3390/ijms25042227

Academic Editors: Volkmar Lessmann, Arkadiusz Matwijczuk, Mariusz Gagoś and Beata Podkościelna

Received: 22 December 2023
Revised: 7 February 2024
Accepted: 8 February 2024
Published: 13 February 2024

Copyright: © 2024 by the authors. Licensee MDPI, Basel, Switzerland. This article is an open access article distributed under the terms and conditions of the Creative Commons Attribution (CC BY) license (https://creativecommons.org/licenses/by/4.0/).

1. Introduction

Double-stranded breaks are one of the most harmful forms of DNA damage that cells can sustain. They are characterized by breakage of the sugar-phosphate backbone on opposing strands of a DNA molecule, occurring within a proximity of ~10–20 base pairs [1]. The cellular response to this form of damage is rapid and prone to stringent regulation, as the presence of DSBs results in a variety of degradative effects that severely impact cell survival. These effects include the destabilization of genomic DNA via chromosomal translocations, inversions, and deletions [2]. Although these may result in cell death, some deleterious mutations may confer beneficial clonal advantages, resulting in the uncontrolled regulation of cell growth and progression to cancerous phenotypes. Tumorigenic cells can thus withstand a higher frequency of DSBs due to the overexpression of oncogenes and contain mutations within key factors of the DNA damage response [3]. In contrast, normal cell apoptosis can be triggered with just one unrepaired DSB if an essential locus is disrupted [4].

There are a variety of genotoxic factors that pose a threat to DNA integrity, both natural and artificial. For instance, radiation exposure comes from terrestrial sources, including naturally occurring radioisotopes in soil and water, and from bioaccumulation within the

ecosystem's flora and fauna. The inhalation of radon, a naturally occurring radioactive gas, contributes towards approximately 50% of the annual background radiation exposure for the global population [5,6]. Ultraviolet-B wavelengths in sunlight, which have health benefits in facilitating the production of endorphins and vitamin D, are also the principal risk factor for developing skin cancer [7]. With the advent of interplanetary and commercial space travel, understanding the impact of cosmic radiation is crucial for the wellbeing of astronauts during long missions [8,9]. On the other hand, manmade genotoxic sources include pesticides, alcohol, tobacco smoke, and certain medications. Despite the potential harm posed by radiation, it is a crucial tool in the medical field for both diagnosing and treating illness. This includes providing detailed images of the body through X-ray imaging and computed tomography and treating cancer through radiation therapy, which over 50% of patients in developed countries undergo [10]. Given that people are constantly exposed to genotoxic sources through their lifetime, it is crucial to accurately characterize and assess the damage caused and how cells act in response.

The repair of DNA DSBs occurs via a number of pathways, each comprising the intricate timing of sensing damage, recruiting appropriate repair machinery to the breakage site, and ultimately repair. Several variables determine the pathway responsible for repairing DSBs. Cellular conditions, including the cell cycle phase, availability of DNA repair proteins, and severity of damage, all contribute towards which factors are utilized to repair DNA lesions [1]. To validate the presence of DSBs experimentally, many current studies utilize immunofluorescence techniques to target DDR proteins that are activated in response to DSB presence. Established markers, including the commonly used γH2AX and 53BP1, typify the early steps in the initiation of the DDR and are often assumed to be reliable indications of DSB presence [11]. However, fluorescence signals generated by these markers are not a direct indication of DSBs themselves. Rather, the presence of these markers signifies the initiation of DSB repair and not the presence of the actual breakage sites [12]. Tagging these proteins is an indirect method of DSB detection [13], but it is still extremely useful for identifying relationships among damage formation, repair efficacy, and repair kinetics. However, detecting actual DSBs, rather than markers of their repair, with a high degree of reliability is still challenging. As DSB repair is complex and prone to error [1], its detection assays are influenced by multiple factors. These include missing DSBs that have already been repaired by the DDR, competition for binding with endogenous DDR factors [14], and a lack of sensitivity, all of which can produce false negatives. Conversely, issues also arise with techniques that lack specificity. For instance, the terminal transferase dUTP nick end-labeling (TUNEL) assay is commonly used to assess the extent of DNA fragmentation to identify cells undergoing apoptotic cell death [15]. This includes the labeling of DSBs, to which fluorescently labeled nucleotides are conjugated to free 3′-OH DNA ends at breakage sites. However, it is limited in its specificity as it is also capable of binding single-strand DNA (ssDNA) nicks or single-stranded breaks (SSBs), which occur at a frequency of ~10,000 breakages per day per cell [16]. This results in pan-nuclear staining, which is incapable of resolving discrete DSB foci, but useful in the binary determination of whether cells are apoptotic/necrotic. This can also occur when staining cells exposed to very high radiation doses [17], which is another important consideration when performing immunofluorescence assays.

Other classic methods of DNA damage detection include the comet assay, where fragmented DNA is separated from intact DNA through gel electrophoresis. The greater the extent of DNA fragmentation within a cell, the greater the proportion DNA that will reside within the comet "tail" formed versus the intact DNA "head" [18]. The alkaline-halo assay similarly measures the ratio of fragmentated DNA, but instead damaged DNA will spread outwards to form a halo structure around the nuclear cage, whereas intact DNA will not diffuse [19,20]. These techniques have also been combined with Fluorescence In-Situ Hybridization (FISH). Notably, DBD-FISH utilizes a whole-genome probe in combination with comet to simultaneously detect SSBs and DSBs, with Fernandez et al. proposing that the average FISH probe intensity and comet area correlate with the presence of each lesion, respectively [21]. Akin to

TUNEL, these techniques are limited as although they can quantify the proportion of DNA fragmentation that occurs on a single-cell level, they lack the ability to visualize individual DSB sites or repair factors and thus will not be discussed in this review.

Ultimately, different markers are required for assays depending on the specific research question being investigated. Knowing the correct context and circumstances for which specific markers should be used is critical in drawing accurate conclusions from DDR data. Therefore, characterizing double-stranded breaks allows us to better evaluate multiple forms of genotoxicity and the impact they have on cell genomic integrity and to obtain a more reliable gauge of the severity they present to cellular function. The intrinsic links among DSB and DDR factor accumulation, the cell cycle, cell death, and the biological impact of genotoxic insults, means that characterizing DSBs not only allows us to better understand the extent of genotoxic insults, but also in accurately understanding the mechanisms responsible for DSB repair. Thus, this review considers the formation of a DSB and then in chronological order steps through the DSB detection and repair pathways with respect to fluorescence-based assays that can identify specific aspects of the DNA damage formation and response (Figure 1). By doing so, the review identifies what individual assays technically represent at a molecular level. This is valuable for identifying biases associated with each assay and facilitates accurate data interpretation (Table 1). It also enables decision making for conducting the best assays aimed at specific research questions. The assays included here encompass both common and novel fluorescence-based techniques and the advantages and disadvantages each present in identifying DSB repair or DSBs specifically. The aim of this review is to provide researchers with the tools required to make informed decisions about which assays are best suited to their specific needs, leading to more insightful and reliable data.

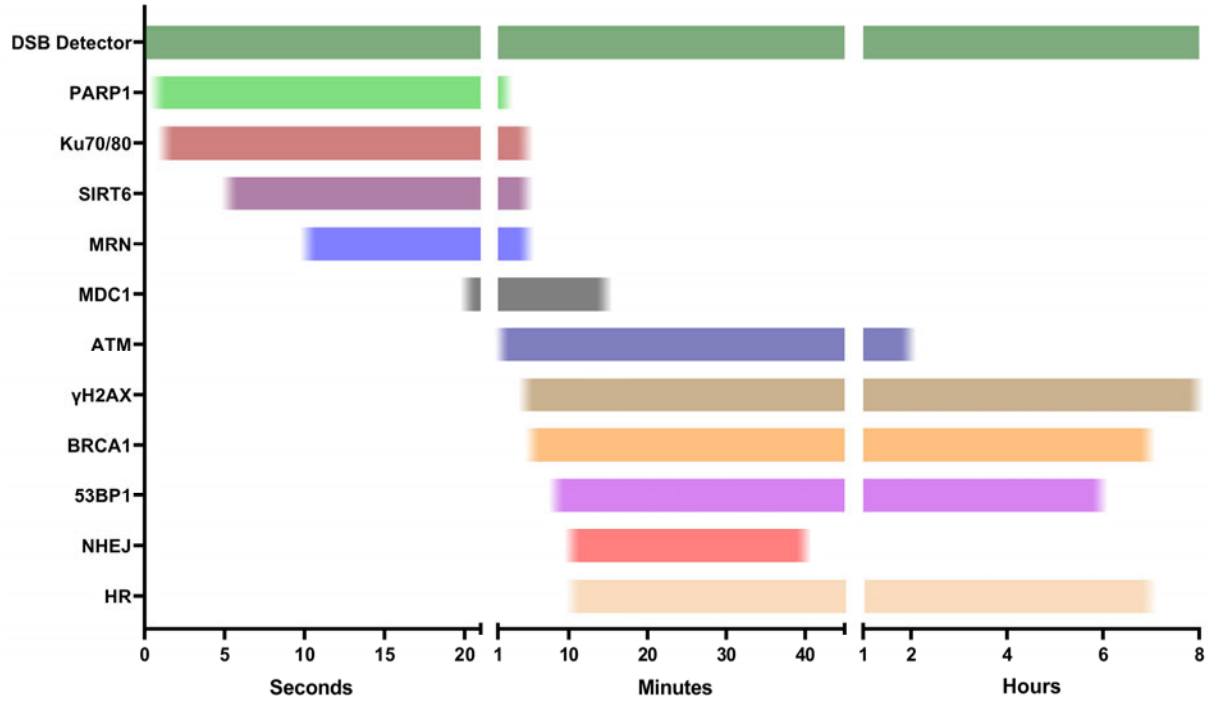


Figure 1. Timescale depicting the temporal kinetics of DSB detectors and key DDR proteins at peak activity throughout the DSB repair process after genotoxic exposures, based upon previous fluorescence imaging studies. DSB detectors utilizing exogenous factors are theoretically capable of DSB detection across all timepoints where DSBs are present (see DSB detector assays). Endogenous markers are sequentially recruited to the breakage site in a signaling cascade, resulting in the accumulation of repair factors to the DSB site. Some factors bind transiently over the course of minutes (PARP1 [22], Ku70/80 [23], SIRT6 [23], MRN [22], MDC1 [24]), whilst others persist and remain detectable hours post-insult (ATM [25,26], γH2AX [27], BRCA1 [28], 53BP1 [29,30], NHEJ/HR [31]).

Table 1. Summary of the DNA damage and repair assays reviewed. Stars ★ indicate the relative level of complexity of each assay, with five stars being the most complex.

DDR Stage	Marker	Complexity	Uses	Challenges
DSB Detector Assays	GamGFP	★★★☆☆	Binds specifically to DSBs. Simple protocol compared to other DSB assays.	Competition with endogenous Ku in mammalian cells. Optimizing transfection efficiency.
	DNA damage In situ ligation followed by Proximity Ligation Assay (DI-PLA)	★★★★★	Identifies DDR proteins proximal to DSB sites.	May not target all DSBs due to changes in DDR activity.
	SensiTive Recognition of Individual DNA Ends (STRIDE)	★★★★★	Highly sensitive. Detects single CRISPR/Cas9 nicks.	TdT enzyme may result in non-specificity (SSBs, cytosolic DNA, mitochondrial DNA)
	TdT-UTP DSB End Labeling (TUDEL)	★★★★☆	High sensitivity.	
First Responders	Poly (ADP-ribose) Polymerase-1 (PARP1)	★★★☆☆	Active 0.5 s post-insult. Recruits multiple DDR factors.	Can reside at intracellular locations distinct from DSBs.
	Ku70/80	★★☆☆☆	Active 1 s post-insult. Involved in canonical-NHEJ (c-NHEJ).	Displaced from DSBs during S/G2 phases and HR.
	Sirtun 6 (SIRT6)	★★★☆☆	Active 5 s post-insult. Binds to DSBs independently of other DDR factors.	Binds to SSBs. FRET to identify dimer pairs at DSB sites.
	MRN	★★☆☆☆	Active 10 s post insult. Involved in HR.	Involved in c-NHEJ and alternative-NHEJ (a-NHEJ), role not yet established.
DDR Activators	Ataxia-Telangiectasia Mutated (ATM)	★★☆☆☆	Key DDR regulator. Phosphorylates H2AX.	Activity is cell-cycle-dependent. Non-DSB damage can activate ATM, do not form discrete foci.
	γH2AX	★★☆☆☆	Well-established DDR marker. Activated to promote DSB repair molecules.	Foci do not always indicate the presence or proximity of DSBs. Activation kinetics vary.
	Mediator of DNA Damage Checkpoint protein 1 (MDC1)	★★☆☆☆	Enhances signaling of damage. Regulates multiple molecules across most stages of repair.	Damage kinetics can be inconsistent across cell types due to regulating multiple proteins.
Repair Pathway Specific Assays	Breast Cancer 1 (BRCA1)	★★★☆☆	Regulates HR initiation.	BRCA1 and 53BP1 antagonism. Repair kinetics altered in different cell types (e.g., cancers).
	p53 Binding Protein 1 (53BP1)	★★★☆☆	Regulates NHEJ initiation.	

2. DSB Detector Assays

A DSB detector can be defined as a biomolecular marker utilized to identify and quantify DSBs. These are often exogenous molecules that function by binding to one or both ends of a DSB and generate a signal that can be visualized via fluorescence microscopy when successfully bound. Currently, there are two main methods. The first is by utilizing proteins that typically possess DSB-end binding capabilities, conjugated with a fluorescent protein. The other is to incorporate oligonucleotides at the 3′-OH ends of a DSB, which can be tagged with probes that emit fluorescence signals when in proximity. Assessing DSBs via methods mentioned in this section allow for the direct quantification of breaks, without reliance on marking endogenous DDR factors. This allows for the number of breaks to be determined without the multitude of factors that can influence DDR factor expression, thereby providing an unambiguous understanding of the extent of genotoxic damage in cells.

2.1. GamGFP

In 2013, Shee et al. reported a new fluorescent marker to identify DSBs, desiring a direct method of detection [14]. They produced a doxycycline-inducible plasmid containing

DSB binding protein "Gam", derived from bacteriophage Mu, bound to green fluorescent protein (GFP). This protein is an ortholog to the NHEJ Ku proteins used in both bacterial and mammalian cells [32], but its function when used by phage Mu differs substantially from its DDR roots. Upon phage infection, Gam's role is to prevent the action of cellular exonucleases by binding to the ends of linear phage DNA, thereby protecting it from degradation. Mu Gam is capable of binding to either blunt- or sticky-ended DSBs [33], making it a prime candidate for a DSB marker. GamGFP binds directly to the site of the DSB lesion, allowing for the observation of discrete GFP foci where DSB ends are present. According to their study, GamGFP foci appear to co-localize with γH2AX, but not extensively with 53BP1. Using Ku80-deficient mouse embryonic fibroblasts (MEFs) after laser micro-irradiation, co-localization between Gam and 53BP1 was 31%. Note that although laser-microirradiation does induce DSBs, a variety of other genomic lesions are also formed, which may cause DSB repair factors to accumulate due to other types of DNA lesions [34]. Shee et al. suggest that this is due to GamGFP detecting DSBs with higher speed and specificity compared to 53BP1. However, one major drawback to this technique is that the efficiency of binding GamGFP to damage sites within mammalian cells is lowered due to competition with endogenous Ku. A 2-fold increase in GamGFP foci was observed in Ku−/− MEFs when compared to a Ku+/− knockout (Figure 2A) [14].

Therefore, whilst this marker is useful in specifically marking DSBs, its competition to bind to DSBs with Ku means it underestimates the total number of DSBs, and it is difficult to utilize without first producing Ku knockouts prior to experimentation. In terms of complexity, this assay involves production of a GamGFP fusion gene in an inducible plasmid and then transfection or transformation into a mammalian or bacterial cell line of interest, respectively. Issues may arise in optimizing transfection efficiency, with different cell lines varying greatly in this regard [35]. However, compared to other techniques listed in this review herein, the concept of utilizing GamGFP as a DSB marker is relatively simple and reliable, most effective for use in bacterial studies, but under-represents DSBs in mammalian models. An example of the type of experiment where this assay would be appropriate is Nath et al., who previously utilized GamGFP to evaluate DSB formation in *Escherichia coli* (*E. coli*) in response to fluoroquinolone antibiotic treatment [36].

Kotlajich et al. also sought to produce a similar DSB end-labeling GFP fusion protein to Gam-GFP [37]. They utilized the N protein of phage Mu, which has been previously reported to bind Mu phage DNA non-covalently in a circular complex, and thus investigated whether this protein might possess DSB ending properties. Foci formation was compared between N- and Gam-GFP in *E. coli* exposed to either phleomycin (a radiomimetic agent), enzymatic cleavage, or X-rays. The proportion of cells with N-GFP foci in response to phleomycin treatment was approximately half that of Gam-GFP, and 4-to-6 times fewer in response to I-SceI restriction enzyme digestion or X-rays (Figure 2B).

Although they found that N-GFP was capable of binding to DSB sites, data from the phleomycin treatments also suggested it could label "non-DSB" DNA damage. Unlabeled Gam was also produced via an expression vector to determine whether the binding of N-GFP was competitively inhibited by Gam occupying DSB ends. N-GFP foci formation was found to remain consistent regardless of Gam production, implying that N-GFP identifies DNA damage distinct from DSBs (presumably SSBs) [37].

2.2. DI-PLA

In labeling DSB ends, three similar techniques have been produced, which rely upon three basic steps ensuring the specific labeling of double stranded breaks. These being the conjugation of a nucleotide analogue to mark free DNA ends, labeling of these DSB end-bound analogues with fluorescent marker-bound antibodies, and production of a fluorescent signal when these antibodies are in proximity to each other. The first of these techniques was reported in 2017 by Galbiati et al., termed the "DNA damage In situ ligation followed by Proximity Ligation Assay" (DI-PLA) [38]. Cells are first paraformaldehyde-fixed and permeabilized, followed by treatment with T4 DNA polymerase to blunt the

DSB DNA ends. These DNA ends are then tagged by biotinylated nucleotides using T4 ligase at the site of a break. Following this, primary antibodies against both the biotinylated nucleotides and a proximal complex (e.g., γH2AX, core histone) are added. As the presence of an individual biotin molecule does not produce a sufficiently strong signal, a proximity ligation assay is performed. Secondary antibodies, directed against each primary antibody, contain conjugated oligonucleotides to facilitate a rolling circle amplification reaction that initiates when the biotin-tagged DSB and proximal DDR protein are within range (approx. 40 nm). This produces a strong fluorescent signal and distinct foci when observed via immunofluorescence microscopy (Figure 3A) [38].

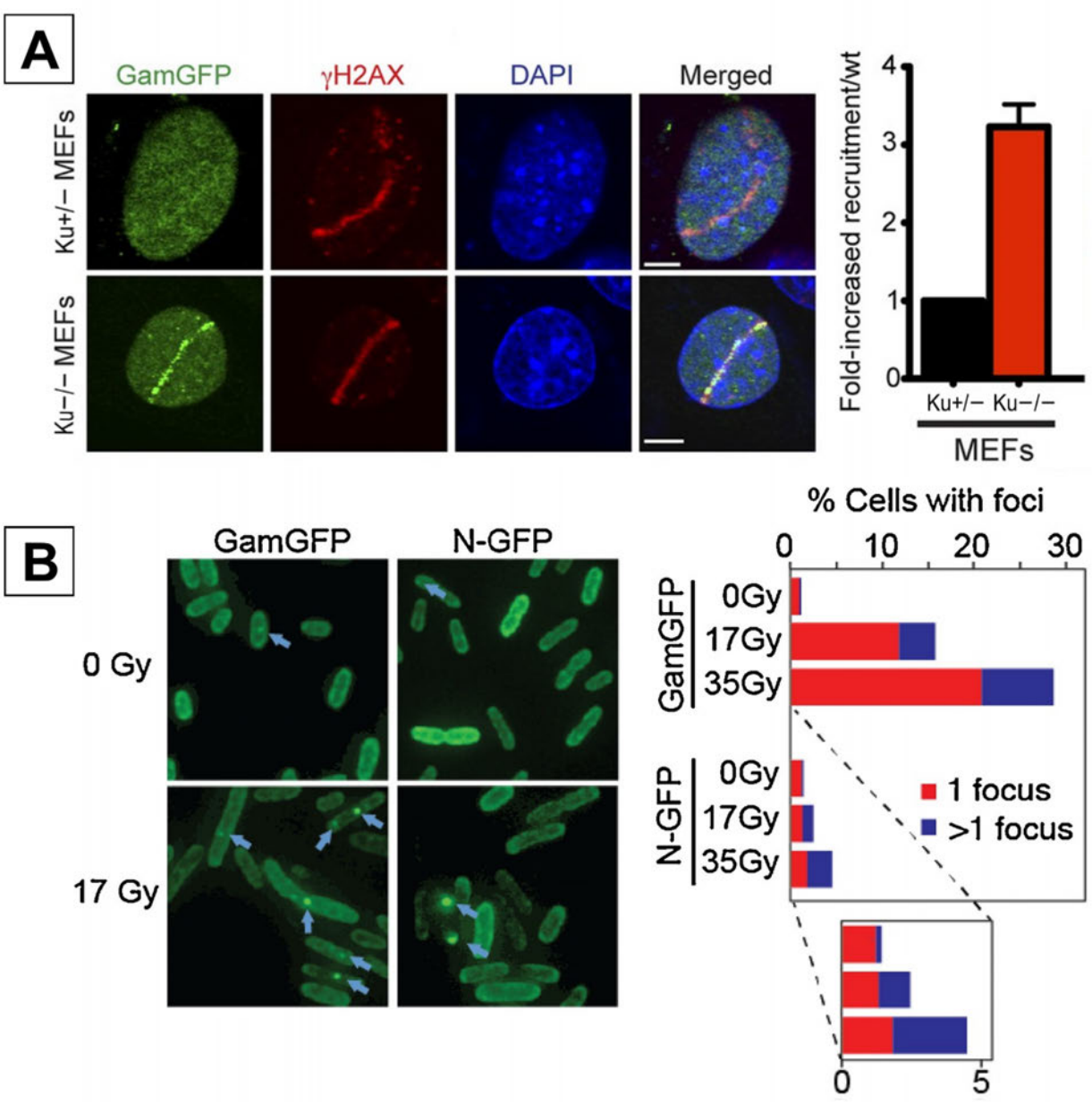


Figure 2. (**A**) Co-localization of GamGFP with the DDR marker γH2AX after laser-induced damage in either Ku+/− or Ku−/− MEFs. A marked reduction in GamGFP foci is observed in Ku+/− MEFs, where Ku acts as a competitive inhibitor of GamGFP [14]. Reprinted with permission from Ref. [14]. 2013, eLife under the CC BY 4.0 Deed | Attribution 4.0 International | Creative Commons. (**B**) Comparison of GamGFP and N-GFP foci formation in *E. coli* cells after exposure to 0, 17, or 35 Gy X-rays. Approximately 30% of GamGFP cells presented foci at 35 Gy compared to 5% for N-GFP [37]. Reprinted with permission from [37]. 2018, DNA Repair | Vol 72, Pages 1–116 | ScienceDirect.com by Elsevier.

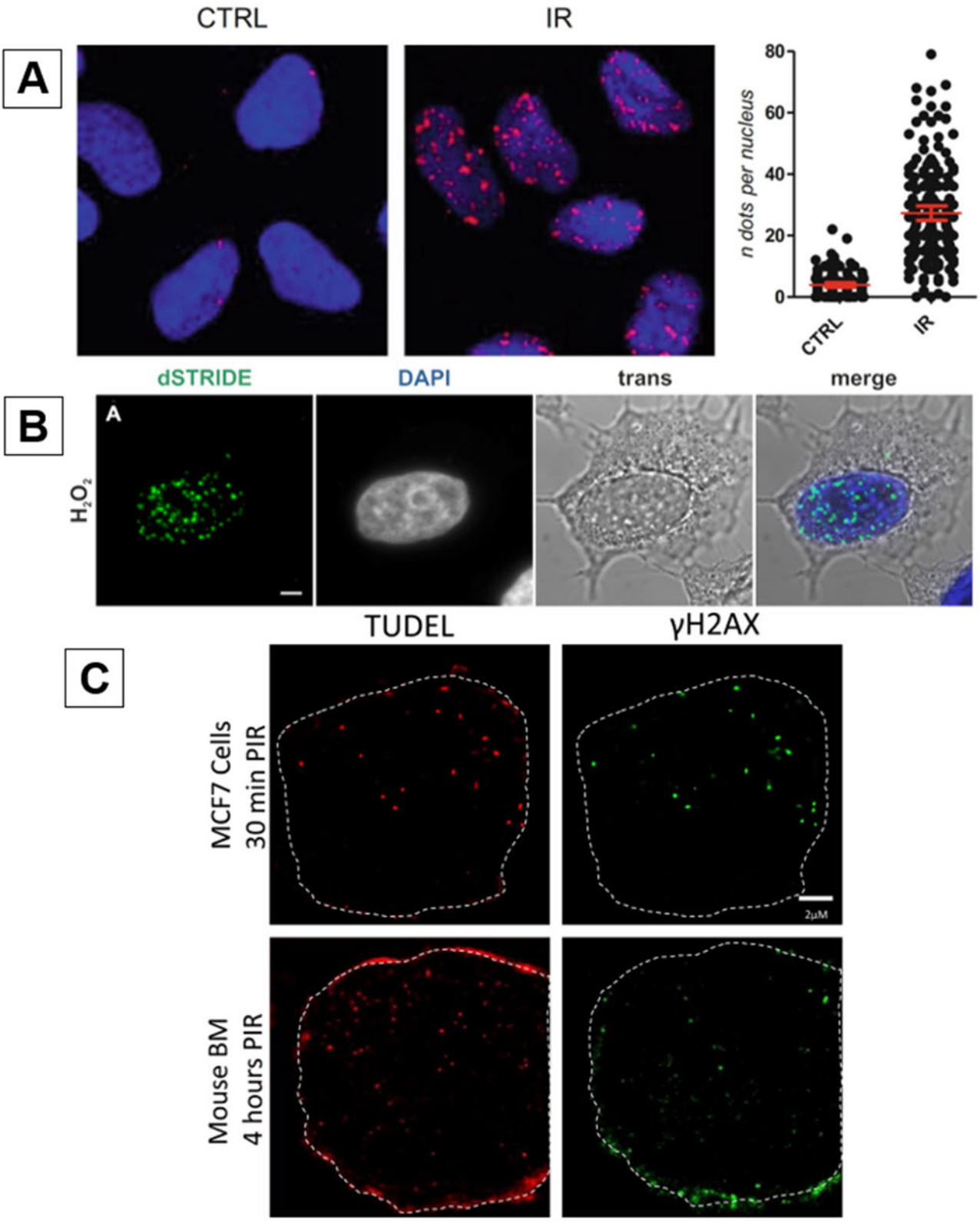


Figure 3. *Cont.*

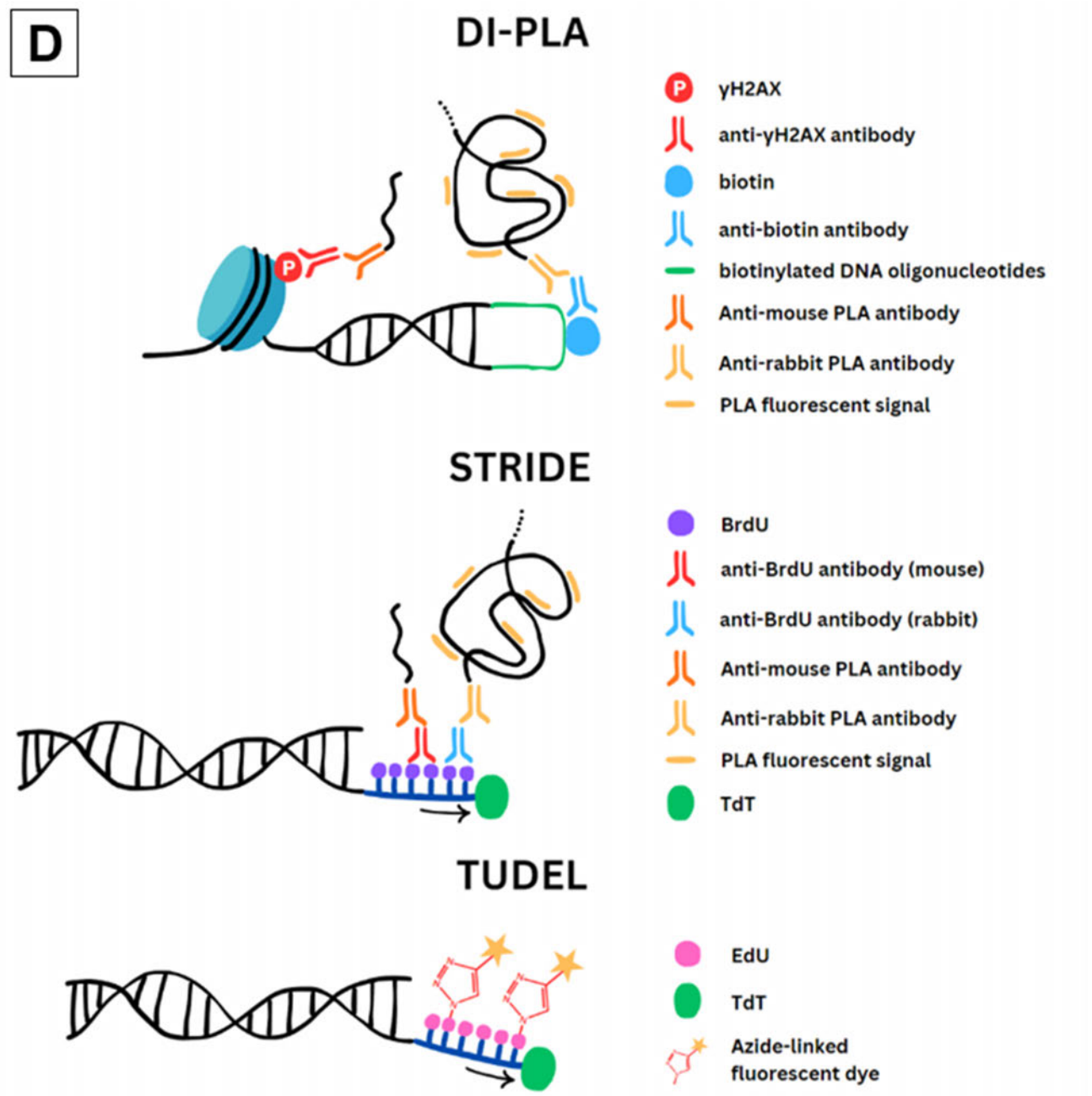


Figure 3. (**A**) U2OS cells treated with or without an inducible restriction enzyme (AsiSI). DI-PLA (yellow) was employed with antibodies against biotin (biotinylated linker nucleotides) and γH2AX. Nuclear DNA counterstained with DAPI (blue) [38,39]. Reprinted with permission from Refs. [38,39]. 2017, Springer Nature. (**B**) HeLa cells exposed to 4 mM hydrogen peroxide and stained with dSTRIDE (green) and DAPI (blue). dSTRIDE foci are representative of the tagging of free 3′-OH DNA ends within both the nucleus and the cytoplasm by [40]. Reprinted with permission from Ref. [40]. 2019, Oxford University Press on behalf of Nucleic Acids Research. (**C**) MCF7 cells exposed to 6 Gy from a Cs-137 source, fixed 30 min post-irradiation (PIR). Cells were stained with TUDEL and anti-γH2AX antibodies. TUDEL (red) co-localizes with γH2AX foci (green) within the nucleus (dotted line represents approximate border) [41]. Reproduced with permission from Ref. [41]. 2022, Springer Nature. (**D**) Diagrammatic representation of the differences among the DI-PLA, STRIDE, and TUDEL DSB detection assays. DI-PLA and STRIDE share similarities in employing a proximity ligation assay (PLA) reaction to produce fluorescence, whereas STRIDE and TUDEL share similarity in utilizing TdT to incorporate the oligonucleotide analogues 5-bromo-2′-deoxyuridine (BrdU) and ethynyl-dUTP (EdU), respectively.

In addition to identifying DSBs in proximity to DDR factors, this technique could also be adapted to identify breakages in proximity to other proteins, such as centromeres or telomeres, to further increase the specificity of where damage is identified. This is potentially problematic when concerning DDR factors, such as γH2AX, where changes in DDR activity will influence the number of DSBs detected, decreasing the accuracy of DSB quantification. Further discussion and comparison with STRIDE and TUDEL are provided at the end of this section.

2.3. STRIDE

In 2020, Kordon et al. published a new fluorescence-based technique for detecting DSBs called SensiTive Recognition of Individual DNA Ends (STRIDE), which when modified allows for the in situ detection of either single or double-strand breaks [40]. The initial steps of the STRIDE DSB detection method share similarities to the TUNEL assay [42]. First, the nucleotide analogue 5-bromo-2′-deoxyuridine (BrdU) is conjugated to free 3′-OH DNA ends enzymatically via terminal deoxynucleotide transferase (TdT). Two primary antibodies, derived from separate hosts and specific to BrdU, are then bound. Subsequently, two secondary antibodies, each specific to one of the primary antibodies, are also attached. Each secondary antibody is conjugated with its own set of oligonucleotides, which are then ligated to hybridizing connector oligonucleotides, forming a circular DNA template. Akin to DI-PLA, a rolling circle amplification reaction takes place, with one of the secondary antibody's attached oligonucleotides acting as a primer for DNA polymerase. This newly synthesized concatemeric sequence allows for the hybridization of fluorescently labeled probes to these sequences, producing a strong amplified signal where DSBs are present (Figure 3B) [43].

The practicalities of the STRIDE technique include its ability to tag all double-strand break DNA breakages throughout the cell. Often when characterizing genotoxicity, measurement of the nuclear response is used as a measure of damage severity. Mitochondrial DSBs also cause stress through the triggering of p21/p53 cell cycle arrest, resulting in impaired proliferation [44]. As STRIDE is capable of labeling 3′-OH DNA ends, STRIDE can also identify mitochondrial DNA damage, present as discrete foci within the cytoplasm. One caveat this presents is that incorporation may occur with free cytoplasmic DNA fragments that are not damage-associated, decreasing specificity.

2.4. TUDEL

Building on the principles of the TUNEL assay and sharing aspects of both STRIDE and DI-PLA is the TdT-UTP DSB End Labeling (TUDEL) assay developed by Lutze et al. [41]. Like DI-PLA, the TUDEL labeling process begins via cell fixation and the application of T4 DNA polymerase blunting. However, instead of using BrdU as a nucleoside analogue and rolling circle amplification to produce a fluorescent signal, as per STRIDE, ethynyl-dUTP (EdU) is incorporated to blunted 3′-OH DNA ends and Huisgen cycloaddition (click chemistry) is used to produce a fluorescent signal. The incorporated EdU molecules contain reactive alkyne groups, which allow for the production of covalent bonds between EdU and a fluorescent dye (Figure 3C) [41].

While the TUDEL, STRIDE, and DI-PLA methodologies share some similarities, there are notable differences in their strengths, shortcomings, and validation. These assays all possess the ability for the direct in situ detection of DSBs in the nuclei of single cells, providing more accurate localization of breakage sites. Particularly, the DI-PLA and STRIDE techniques possess higher sensitivity compared to other DNA damage response markers due to incorporating rolling circle amplification reactions. This is best exemplified in the study that introduced STRIDE, where Kordon et al. were able to detect and precisely locate site-specific DSBs induced by CRISPR/Cas9 in the nucleus, demonstrating its ability to accurately assess even low levels of DNA damage [40]. Because of this, STRIDE is the most thoroughly validated of these assays, also supported by its comprehensive testing against various genotoxic agents, including doxorubicin, ultraviolet and laser micro-irradiation,

hydrogen peroxide, and age-related and spontaneous DNA damage [40]. The establishment of DI-PLA and TUDEL was also compelling, both displaying the colocalization of γH2AX and 53BP1 with their DSB detectors post-irradiation [38,41].

Another notable difference is the use of T4 DNA polymerase in both DI-PLA and TUDEL, but not STRIDE (Table 2). As previously mentioned, T4 DNA polymerase is capable of filling in exposed 3′-OH ends of single-strand breaks and performing a 3′ overhang resection at sites of double-stranded breaks. In the case of DI-PLA, the purpose of end-blunting is to ligate biotinylated nucleotides at breakage sites via T4 ligase [38], and for TUDEL, to reduce non-specific background fluorescence by filling in single-strand breaks, thus reducing recognition by TdT [41]. TdT is capable of catalyzing oligonucleotides at the 3′-OH ends of either single- or double-strand breaks; however, it will preferentially bind to 3′-OH overhangs of the latter because of its catalytic characteristics [45–49]. According to Lutze et al., although SSBs are not an ideal substrate for TdT to conjugate oligonucleotides (DNA polymerase 1 is utilized in STRIDE when detecting SSBs for this reason [40]), substantial background fluorescence may be present, particularly at early timepoints after DNA damage induction [41]. This caveat would mainly affect STRIDE and TUDEL, both with a reliance upon TdT incorporation to detect DSBs, contributing to a lower signal-to-noise ratio when analyzing fluorescent foci. Moreover, the 3′-OH binding capacity of TdT means that there is also the ability for cytosolic DNA fragments and mitochondrial DNA breakages to be marked by STRIDE and TUDEL. Although DI-PLA utilizes proximal endogenous DDR markers that are associated with breakage sites to avoid these issues, the downregulation of repair machinery may lead to fewer detected breakage sites resulting in false negatives. Overall, the main limitations of these protocols are that although they can more accurately characterize DSBs, they are also prone to a degree of non-specificity and are susceptible to variation due to their complexity. Furthermore, the procedures to achieve such stains are elaborate (Figure 3D), making it difficult to troubleshoot and interpret results if issues arise.

Table 2. Comparative table highlighting the key differences among the DI-PLA, STRIDE, and TUDEL DSB detection assays. It outlines the main steps of each protocol in chronological order, left to right, from whether cells are treated with T4 DNA polymerase through to fluorescence-based detection.

Technique	T4 Pol Blunting	Incorporation Reagent	DSB End Conjugate	Antibody Pair	Signal Amplification	Fluorescent Signal
DI-PLA	Yes	T4 Ligase	Biotin linker	Biotin + proximal DDR marker	Yes	Proximity Ligation Assay
STRIDE	No	TdT	BrdU	BrdU + BrdU	Yes	Proximity Ligation Assay
TUDEL	Yes	TdT	EdU	None	No	Azide-linked Fluorophore

As these DSB detection techniques are relatively cutting-edge, complex, and costly, there are not many published studies utilizing them for the quantification of DSBs. A 2021 thesis successfully reproduced the STRIDE technique to detect DSBs in both an adenocarcinoma line, MCF-7, and spermatozoa, after exposure to either ultraviolet light or hydrogen peroxide [50]. To date, no other publications cite the usage of DI-PLA or TUDEL experimentally. As it stands currently, the further use of these techniques is required to properly comment on their practicality and efficacy compared to other conventional and novel techniques alike. Regardless, the development of DI-PLA, STRIDE, and TUDEL comprises steps in the right direction for vastly improving the targeting of fluorescent foci to DSBs, in a bid to eliminate the ambiguity conferred by labeling endogenous factors, and to accurately study the mechanisms of DNA damage.

3. First Responders

First responder proteins are classified as proteins that arrive at the very first stages of DSB detection. These include proteins that are in the well-established conventional DDR, such as the MRN complex (composed of MRE11, RAD50, and NBS1) and Ku70/80,

which promote HR and NHEJ repair, respectively, and members of the Sirtuin and poly (ADP-ribose) polymerase (PARP) families, which lie upstream of these pathways and act in promoting DNA repair. After the binding of this class of proteins to a DSB site, a cascade of DDR activation occurs (detailed in the "DDR Activators" subsection). Although they act via binding to the ends of DSBs akin to the exogenous DSB detectors, first responders are endogenous molecules and typically initiate or assist in the repair of DSBs, whereas DSB detectors do not. First responder proteins are ideal targets for visualization in instances where the initiation of DDR repair is concerned, as they are essential in both identifying DSB sites and amplifying downstream DDR factors. The rapid recruitment to sites of damage within seconds of an insult establishes them as DNA damage first responders, meaning early DDR kinetics can be observed by targeting these proteins.

3.1. PARP1

One of the first responders is PARP1, a member of the ADP-ribosyl transferase family responsible for initiating DNA damage repair. After a genotoxic insult, PARP1 rapidly localizes to DSBs within 0.5 s [22] and aids in the initiation of the DDR, capable of binding to DSBs via its zinc finger and tryptophan-glycine-arginine rich (WGR) domains [51]. Following this, it utilizes ADP-ribosyl enzymatic activity to remodel chromatin and recruit early DDR signaling proteins such as MRE11 and ATM to the breakage site, as well as PARP1-dependent transcription factors [52]. PARP1 binding motifs are also present within key HR genes, regulating proteins including breast cancer 1 (BRCA1) and 2 (BRCA2) [53,54], TOPBP1, which is involved in the recovery of stalled replication forks and ATR signaling [55], and OBFC2B and SSBIP1, which are components of the SOSS complex that participates in ATM signaling [56]. As such, PARP1 is a key promoter of the HR pathway in the S/G2 phase where it has been shown to remove Ku70/80 from DSBs [23].

Given its crucial role in DNA maintenance, there are several ways PARP1 can be detected. The first paper to document the association of PARP1 with MRE11, and by extension the MRN complex, was Haince et al. in 2008. Akin to the aforementioned Gam-GFP [14], they produced a PARP1-GFP vector to analyze the spatiotemporal accumulation of PARP1 in response to laser micro-irradiation in live cells [22]. Interestingly, they showed that PARP1 was necessary for the rapid recruitment of MRE11 and NBS1, where the recruitment of these factors was inhibited in PARP1-deficient cells. Additionally, transfection of the PARP1-GFP plasmid in PARP1-deficient cells increased the number of detectable 53BP1 foci post-insult, showing that cells expressing functional PARP1-GFP can recover DDR recruitment and downstream signaling [22]. More recently, Yang et al. established GFP vectors of PARP1 and various DDR factors, including the previously mentioned NBS1 within the MRN complex, Ku70/80, and SIRT6. From this, they could also determine the spatiotemporal recruitment kinetics of PARP1, where foci appeared 1 s after microirradiation (Figure 4) [23].

Although possessing multifaceted roles in the regulation of DSB repair, the sensitivity of PARP1 is not limited to DSBs. There is evidence that PARP1 can modulate the repair of SSBs including being implicated in the base excision repair pathway [57,58]. This includes the regulation of gene transcription [59], cell death [60–62], pro-inflammatory cytokines [63,64], and viral immunity [65]. It is a therapeutic target for cancer treatment due to this, with multiple PARP inhibitors currently approved for treatment of BRCA1/2 mutated breast, ovarian, prostate, and pancreatic cancers because of their tumoricidal properties [66,67]. There is also evidence that PARP1 is capable of activation via SIRT6 during oxidative stress [68], suggesting that its accumulation at damage sites is regulated depending upon specific cellular stresses. In a study conducted by Wang et al. utilizing immunofluorescence staining against PARP1, they demonstrated that PARP1 was capable of translocation into the cytoplasm following infection with herpes simplex virus type 1 (HSV-1) in HeLa cells [61]. When in some cases researchers might utilize this protein as an indication of DSB presence or repair initiation i.e., in response to chemical [69] or ionizing-radiation [70] induced DSBs, this is evidence of PARP1's capacity to reside at

intracellular locations distinct from DSBs. These factors may have unpredictable effects upon the localization of PARP1 foci, highlighting the need for careful interpretation of its presence at DNA damage sites or association with targets outside of the DDR.

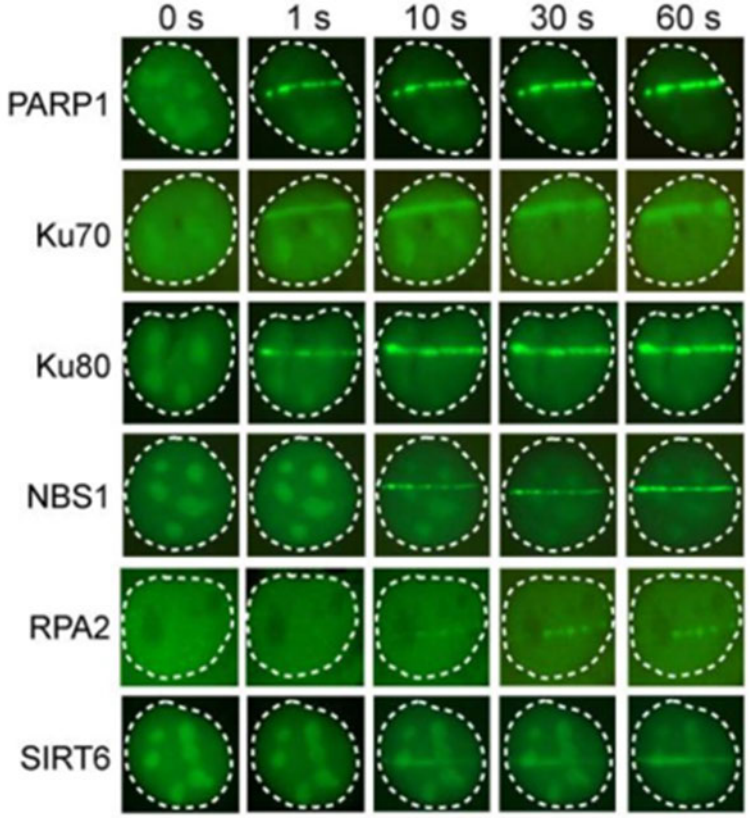


Figure 4. U2OS cells exposed to microirradiation, and kinetics monitored via live cell imaging. DDR proteins were tracked via transfecting GFP fusions of target proteins (i.e., PARP1-GFP, Ku70-GFP etc.) prior to the insult [23]. Reprinted with permission from Ref. [23]. 2018, Oxford University Press on behalf of the International Journal of Molecular Sciences.

3.2. Ku70/80 and MRN

The MRN complex and Ku70/80 play critical roles in the repair of DSBs. That is, they are amongst the first proteins recruited to the site of a break, with there being evidence for them arriving at the site of damage within 10 s in the case of MRN [22,71], and 1 s for Ku70/80 [23]. The Ku70/80 complex is a heterodimeric protein that also binds to the DNA ends of DSBs but is predominantly involved in c-NHEJ. Binding the DSB in a ring-like structure that encapsulates duplex DNA [72], Ku mediates recruitment of the DNA-dependent protein kinase catalytic subunit (DNA-PKcs), which enables the synapsis of DSB ends and further recruitment of downstream c-NHEJ effector proteins [73]. The Ku complex also plays a role in telomere maintenance by protecting chromosome ends from degradation and recombination, localizing to telomeres through its affinity for the TRF1 shelterin protein, and ensuring genomic stability [74,75].

In contrast, the MRN complex consists of three subunits: MRE11, RAD50, and NBS1. MRE11 possesses endonuclease activity and processes DSBs by resecting the 5′ ends of the DSB, forming 3′ ssDNA overhangs on either side of the break to facilitate HR [76]. It is important to note that end resection is suppressed in the G1 phase of the cell cycle to promote NHEJ, while the converse is true within the S/G2 phases [77]. Prior to DNA replication in the early S phase, HR cannot engage as there is no sister chromatid from which complementary strands can be synthesized. Under these conditions, MRN also plays a role in canonical-NHEJ (c-NHEJ) and alternative-NHEJ (a-NHEJ) pathways [78], affecting

mechanisms in lymphocytes including V(D)J [79] and class switch recombination [80]. Although its role is not yet clearly defined, producing mutations in the dimerization region of MRN has been shown to hinder NHEJ repair [81], where under normal conditions it is predicted to aid in the tethering of free DSB ends to facilitate c-NHEJ protein accumulation [82]. The RAD50 component facilitates the tethering of DNA ends through a zinc hook domain that stabilizes sister chromatids during HR and aligns broken ends during NHEJ [83], whilst NBS1 serves as a scaffold protein that recruits other repair factors to the DSB [84]. MRN also regulates the activity of telomerase [85,86], and activates ATM kinase [87], a key regulator of the DDR.

Immunofluorescence assays are a common method for the detection of the MRN and Ku70/80 complexes. For MRN complex detection, antibodies against MRE11, RAD50, and NBS1 can be used to label DSB ends, and co-localization with downstream repair signals, such as γH2AX, a histone modification that is activated in response to DNA damage, can be used to further validate the recruitment of MRN to the breakage site. Similarly, antibodies against Ku70/80 can be used in conjunction with NHEJ repair factors, such as 53BP1, to validate its recruitment. Examples from previous studies include Mirzoeva et al., who applied the indirect immunofluorescent marking of MRE11 after cells were exposed to gamma irradiation [88], and Britton et al., who applied the same technique for Ku70 in response to laser micro-irradiation [89]. An alternative fluorescence detection method is by producing vectors that encode the MRN or Ku fused with fluorescent proteins for transfection, Yang et al. using this technique to analyze their repair kinetics alongside PARP1 [23]. It should be noted that even though both MRN and Ku70/80 are regarded as sensors of DSBs and are capable of binding to DSB ends, there are instances where they may not bind to all breaks present within a cell. For example, in situations where Ku70/80 is displaced during HR, particularly in the S/G2 phases of the cell cycle, foci will not be resolved at each DSB end if only Ku is utilized as a quantifier of DSB ends. Therefore, although MRN and Ku70/80 predominantly play important roles in DSB recognition and repair, their functions differ in terms of the specific repair pathways they promote and in which they are involved. For instance, there is evidence of both MRE11 [90] and Ku80 [91] present within mitochondria. As mitochondrial DNA undergoes distinct DSB repair processes when compared to nuclear DNA, in addition to HR and c-NHEJ [92], this can ultimately complicate the interpretation of immunofluorescence data. Nuclear foci may thus provide more meaningful interpretations when trying to interpret cellular responses to genotoxicity. Factors that promote the accumulation of MRN and Ku70/80 to DSBs (e.g., PARP1) also have the potential to influence their kinetics. This limits their usage as a one-to-one marker of DSBs due to this degree of endogenous variability, but they are extremely useful in understanding which proteins associate with or regulate their accumulation at breakage sites. Regardless, immunofluorescence or GFP-fusion proteins can be used to detect and analyze the recruitment and dynamics of both complexes in response to damage, which can provide valuable insights into their functions in DSB detection and repair.

3.3. SIRT6

Sirtuins are a family of regulatory proteins responsible for maintaining genomic stability. They possess a variety of signaling capabilities, including cell cycle control, epigenetic chromatin modification, mitochondrial metabolism, and the DDR. As such, dysfunctions in Sirtuin class proteins are responsible for a variety of diseases related to aging, obesity, and cancer progression [93]. The downregulation of SIRT6 has been implicated in increased rates of neurodegeneration, aging, cancers, and tissue degradation due to its importance in recognizing DNA damage [94–96]. Onn et al. were the first to report SIRT6 as a DSB sensor in 2020, establishing its role in the initiation of the DDR. To explore this, they produced multiple SIRT6 plasmids, including SIRT6-GFP and -RFP, to validate its involvement in the DDR [97]. One of the unique attributes that they discovered is its ability to rapidly localize to DSB sites independently from DNA damage sensors within the DDR pathway (Figure 5). SIRT6 was previously reported, by Toiber et al., to

accumulate at DSBs within 5 s of a DSB, with its accumulation plateauing at 30 s post-insult [96]. Inhibiting key factors of the DDR pathway, including γH2AX or 53BP1, had no impact on SIRT6 initiating the repair response [97].

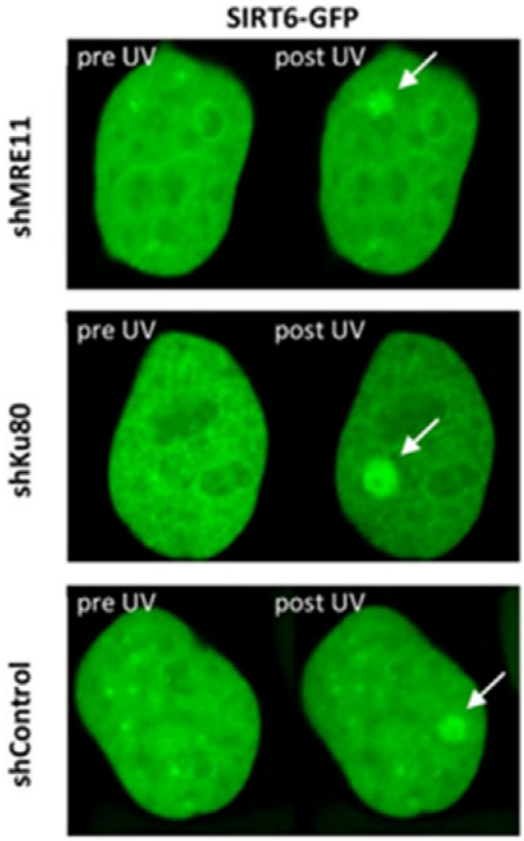


Figure 5. HeLa cells exposed to UV laser irradiation and recruitment kinetics of SIRT6-GFP monitored via live cell imaging. Prior to irradiation, key DDR proteins were silenced, including MRE11 (shMRE11) and Ku80 (shKu80), and compared to HeLa cells without silencing (shControl). This evidence supports that SIRT6 activation is not dependent on DSB detectors within the DDR [97]. Reprinted with permission from Ref. [97]. 2020, eLife under the CC BY 4.0 Deed | Attribution 4.0 International | Creative Commons.

SIRT6 contains a core DNA-binding domain that binds to SSBs via a tunnel-like tertiary structure, surrounding broken DNA strands to prevent further DNA damage, and facilitate the recruitment of DDR factors. This core DNA-binding domain is conserved amongst Sirtuin family proteins, sharing the DNA-binding capability of SIRT6, albeit with decreasing affinity. In addition to binding to SSBs, electrophoretic mobility shift assay results suggest that cooperative binding allows SIRT6 to bind to open-ended DSBs in a dimer conformation. Silencing SIRT6 appears to affect the expression of downstream signaling factors within the DDR pathway, including the phosphorylation of H2AX and recruitment of ATM, Ku70/80, BRCA1, and 53BP1, thus suppressing the initiation of both HR and NHEJ pathways [97]. In using SIRT6 as a DSB detector, the development of vectors expressing fluorescent SIRT6 that emit distinct signals upon dimerization, including Förster resonance energy transfer (FRET) fluorophores [98], may be a viable solution to increase foci specificity. This would effectively eliminate the off-target binding of SIRT6 to SSBs and produce foci specific to DSBs, given the assumption that SIRT6 exclusively binds to DSBs in a dimer configuration.

4. DDR Activators

DDR activators are proteins that propagate the cellular response to DNA damage, downstream of the first responder molecules that accumulate at DSB sites. After the MRN

complex detects a DNA lesion, autophosphorylated ATM monomers are recruited to the breakage site [76]. Chromatin-based DSB signaling is then initiated, with ATM rapidly phosphorylating Ser-139 on histone variant H2AX, resulting in the formation of γH2AX. The phosphorylation of this subunit acts as an epigenetic signal indicative of the presence of DSBs, which is recognized by mediator of DNA damage checkpoint protein 1 (MDC1). The constitutive phosphorylation of MDC1 by casein kinase 2 (CK2) and chromatin-bound ATM initiates a positive feedback loop, whereby additional MRN and ATM are recruited to damage sites [99]. Phosphorylated MDC1 then recruits the E3 ubiquitin ligases RING finger 8 (RNF8) and RNF168, which ubiquitylate chromatin surrounding the break [100]. This promotes remodeling that facilitates access of scaffolding and repair proteins to the DSB site, in addition to providing binding sites for downstream repair machinery [101,102]. After this point, the pathway diverges into the two predominant DSB repair pathways: HR and NHEJ (Figure 6) [11,103,104].

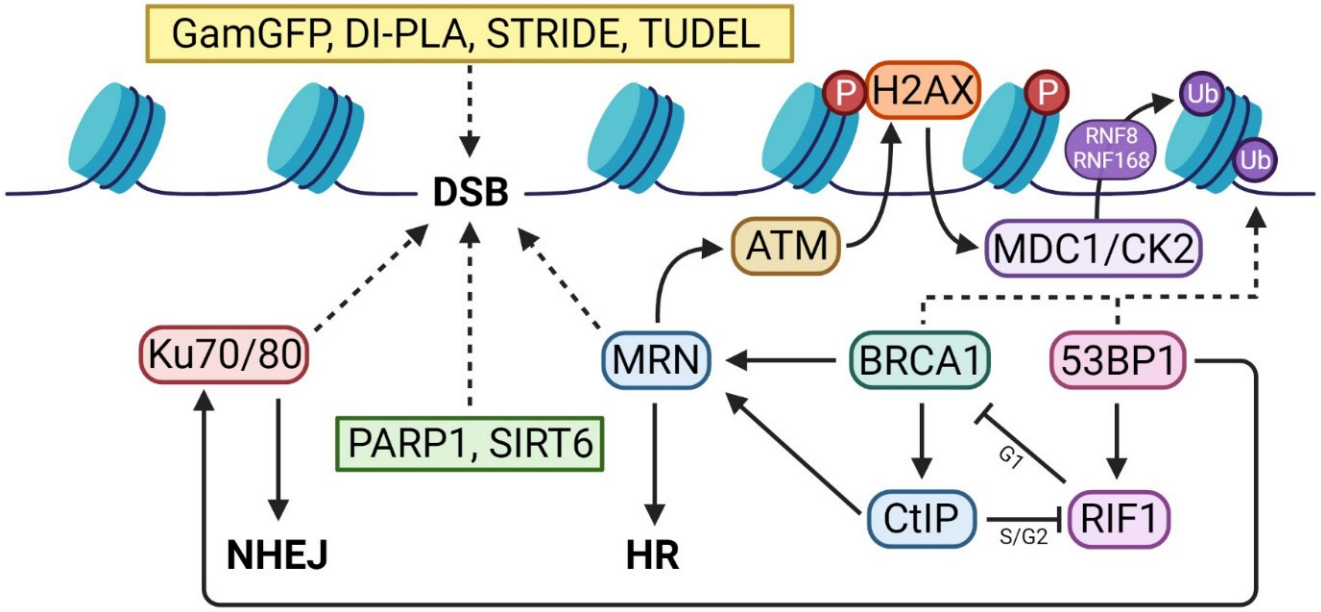


Figure 6. Protein interaction chart of DSB detectors and repair pathway decision process. Immunofluorescent markers of DSBs, including DI-PLA, STRIDE, and TUDEL, act independently of the DSB repair process when binding to breakage sites. SIRT6 and PARP1 are also capable of arriving at breaks independently of DDR activators. Decision-making between HR and NHEJ is driven by antagonism between BRCA1 and 53BP1 depending on cell cycle phase.

Currently, the most widely adopted markers used to quantify DSB insults are the aforementioned DSB activators, the most popular of these being γH2AX. With the phosphorylation of histone variant H2AX being one of the cells earliest steps in initiating the DDR after the induction of DSBs, it has been widely utilized as a cellular marker of the presence of these lesions via immunofluorescent labeling, with discrete foci at or in proximity to DSBs. This allows for the visualization and quantification of DDR activation, caused by ionizing radiation or chemical agents, by using fluorescence microscopy. As ATM and MDC1 function in the initiation of the DDR, they may also be used as effective stains alongside the well-established γH2AX as markers for the activation of DSB repair. However, out of all DDR activators, γH2AX has been favored due to its convenience, efficacy, and sensitivity [105].

4.1. ATM

ATM, a member of the PI3K-like protein kinase family, plays a vital role in various cellular functions, such as cell-cycle regulation, chromosome condensation, and DNA maintenance. Its key function involves transmitting signals after the recognition of DSBs, thus propagating the cascade of damage recognition and facilitating the recruitment of DDR proteins to the DSB site. Under conditions where the cell is not under stress, ATM exists in an inactive homodimeric conformation [106]. However, upon exposure to genotoxic stress, ATM dissociates from its dimeric structure through autophosphorylation at several sites, including Ser367, Ser1893, Ser1981, and Ser2996, in addition to acetylation on Lys3016. From here, it regulates multiple canonical (HR/NHEJ) and non-canonical repair pathways, which encompasses hundreds of downstream effector molecules within the DDR [107].

Fluorescence assays utilized in the detection of ATM employ similar techniques to the marking of upstream DDR factors mentioned previously. Davis et al. used ATM tagged with yellow fluorescent protein (YFP-ATM) to determine the real-time recruitment and kinetics of ATM in response to laser micro-irradiation in live cells [26]. A vector containing the YFP-ATM fusion protein was transiently expressed in AT5 cells, which were then exposed to laser micro-irradiation. The accumulation of ATM at damage sites was recorded at multiple time points over 2 h, with a peak relative fluorescence intensity at 20 min post-insult [26]. Ray et al. sought to discover additional proteins that promote ATM recruitment in response to UV-irradiation-induced damage. Using immunofluorescence, they found that ATM is regulated by nucleotide excision repair proteins during G1, but not during the S phase [108], emphasizing the importance of the cell cycle for DDR factor activation.

There are situations where ATM can localize differently in response to various cellular stressors. When ATM is activated by DSB formation, it results in the localization of activated ATM, which appears as individual fluorescence foci within the nucleus and is associated with DNA damage repair machinery [109]. However, in a study conducted by Bakkenist et al. in 2003, it was found that ATM was still capable of phosphorylation even after cells were exposed to stressors that did not cause DSBs [106]. In the case of non-DSB-inducing stressors, including topoisomerase inhibitor and hypotonic buffers, the activated ATM appears as phosphorylated ATM-Ser1981 scattered throughout the nucleus in a diffuse pattern without forming discrete foci (Figure 7A) [109–111]. It has been proposed that this is because ATM activation is not strictly dependent upon the direct binding of ATM to DSBs or the MRN complex [112]. This should be considered prior to the analysis of ATM via fluorescence-based techniques, as it will ultimately influence its intracellular distribution when observed via microscopy.

4.2. γH2AX

In response to a DSB, numerous chromatin modifications occur to initiate repair, rapidly and meticulously. One of the most important of these is the phosphorylation of histone variant H2AX at Ser-139 by ATM (as well as DNA-PKcs and ATR) to form γH2AX [104]. This promotes the recruitment of downstream DSB repair molecules, in addition to ensuring genomic stability [118]. However, there are common misconceptions when utilizing proteins within the DDR as markers for DSBs, as they are only an indication of whether DNA repair has been initiated, and not markers of where DSBs are located specifically [12]. Regarding γH2AX, it is generally true that the presence of DSBs induces the phosphorylation of H2AX. Yet this is often misinterpreted in the reverse case, with the assumption that all γH2AX foci represent DSBs. Although γH2AX has been cited for its reliability, many inconsistencies have been reported regarding the quantitative relationship between γH2AX foci production and DSBs [13]. These include the time taken to detect the maximum number of γH2AX foci via microscopy being 15–30 min post-irradiation [103], the phosphorylation of H2AX at sites other than where DSB repair is occurring [119] (Figure 7B), and the clustering of repair foci [120].

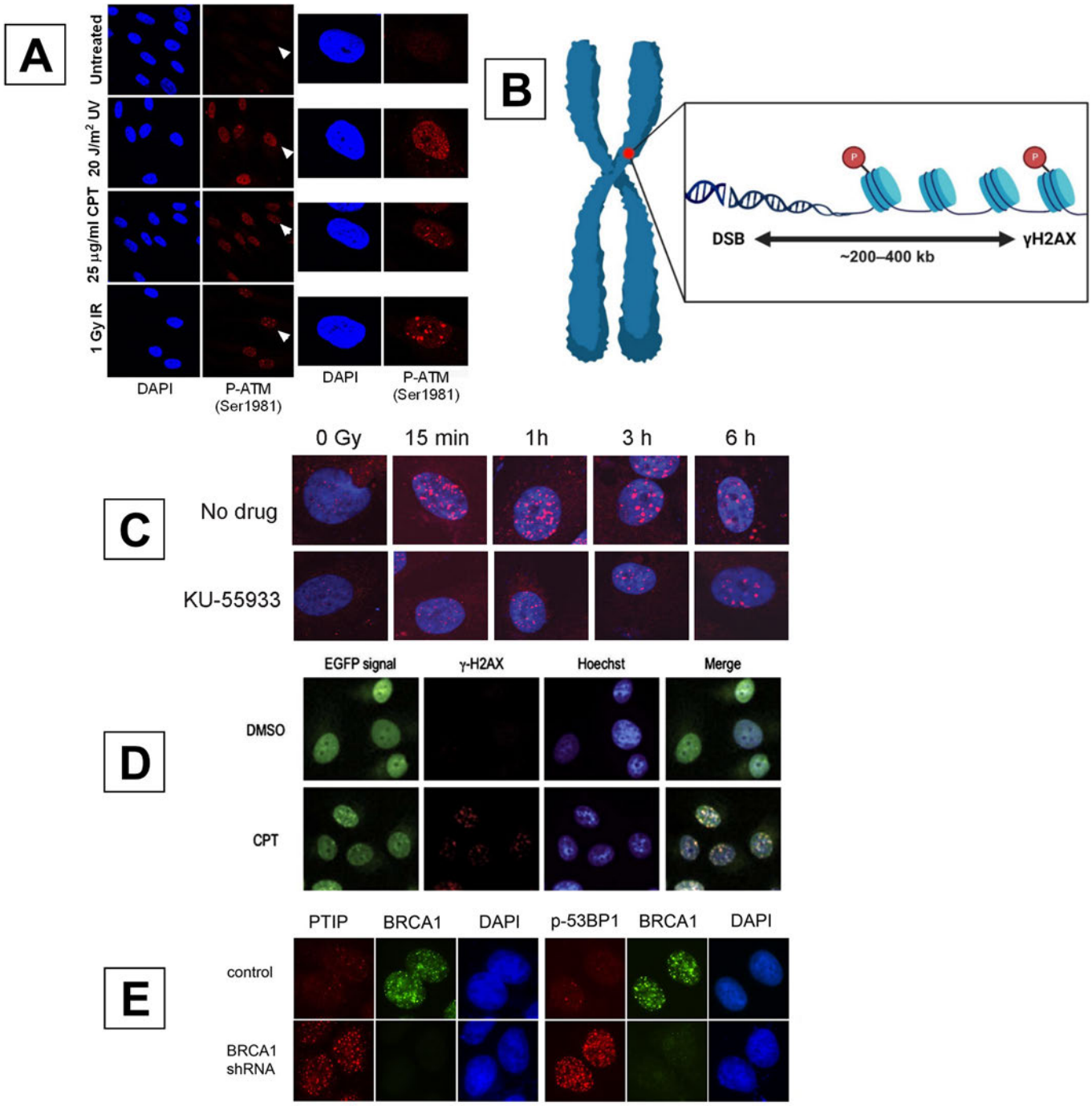


Figure 7. (**A**) Immunofluorescence images of quiescent human dermal fibroblasts 1 h after exposure to UVC, camptothecin, or 1 Gy ionizing radiation (source not mentioned). Cells were stained with an anti-phospho-ATM (1981) antibody (red) and DAPI (blue) [111]. Reprinted with permission from Ref. [111]. 2015, Springer Nature. (**B**) Visual representation of the spatial arrangement of γH2AX foci relative to DSB sites (not to scale). Occurring proximally to beaks within the initial stages of detection, thousands of H2AX phosphorylation sites can rapidly spread to up to 200–400 kb from the site of a DSB [27,113,114]. Because of this, foci are capable of being resolved at nuclear locations distinct from DSBs during immunofluorescent visualization. (**C**) Adams et al. highlight the dependence of H2AX phosphorylation on ATM through the use of the ATM inhibitor KU-55933. Immunofluorescence images of astrocytes pre-treated with 10 μM KU-55933 for 1 h, followed by 2 Gy radiation. The reduced foci count indicates reduced DSB repair and not a reduction in the formation of DSBs. Cells were fixed after the radiation insult and stained with an anti-γH2AX antibody (red) and DAPI

(blue) [115]. Reprinted with permission from Ref. [115]. 2010, PLoS One under the CC BY 4.0 Deed | Attribution 4.0 International | Creative Commons. (**D**) EGFP-MDC1-expressing MCF7 cells exposed to either 0.1% (*v*/*v*) DMSO or 10 μM calprotectin (CPT) for 1 h. After treatment, cells were fixed and stained with an anti-γH2AX antibody (red) and Hoechst (blue), alongside the expression of EGFP-MDC1 (green). Co-localization between EGFP-MDC1 and γH2AX is depicted in yellow (Merge) [116]. Reprinted with permission from Ref. [116]. 2014, Genes and Environment under the CC BY 4.0 Deed | Attribution 4.0 International | Creative Commons. (**E**) HeLa cells synchronized in the S/G2 phase via double-thymidine block irradiated with 10 Gy γ-radiation and infected with control or BRCA1 short hairpin RNA (shRNA). Cells were fixed 2 h post-irradiation. Left: stained with anti-PTIP (red) and anti-BRCA1 antibodies (green) and counterstained with DAPI. Suppression of BRCA1 in the S/G2 phase restored the expression of PTIP. Right: stained with anti-p53BP1 (red) and anti-BRCA1 (green) antibodies, counterstained with DAPI. The presence of BRCA1 inhibits the formation of 53BP1 foci, and the suppression of BRCA1 through shRNA restores 53BP1 foci formation [117]. Reproduced with permission from Ref. [117]. 2015, Springer Nature under the CC BY 4.0 Deed | Attribution 4.0 International | Creative Commons.

In mitotic cells, there also appears to be the damage-independent phosphorylation of H2AX, suggesting that γH2AX performs functions outside of signaling DSB repair [121]. Finally, the loss of γH2AX foci is assumed to be the result of complete DSB repair. Whether this is triggered by ligation of the sugar-phosphate backbone and the re-annealing of DNA strands or by chromatin reverting to its normal conformation is unclear. However, Bouquet et al. highlight that there are still questions surrounding the disappearance of γH2AX foci and its linearity to the degree of the genotoxic insult [122,123]. Exposure to severe insults may result in a persistent, saturated γH2AX signal, allowing for the continued detection of γH2AX foci after DSBs have been fully repaired [122]. They also show that TGFβ inhibition prior to radiation treatment reduces γH2AX foci formation [123], highlighting that impeding the pathways that regulate DDR activation has a substantial impact on foci formation. All of these factors may alter the total counts of γH2AX foci and therefore misrepresent the true number of DSBs present. For example, if DSB sensors or upstream repair activators, such as ATM are inhibited (Figure 7C) or downregulated, γH2AX will not form to its fullest extent despite the existence of DSBs. However, this does not discredit the value in conducting these types of assays in other contexts. For instance, γH2AX is extremely valuable in assessing the extent of DDR activation (or inhibition) in a pathway-independent fashion, which is essential for understanding how regulation of the DDR may be affected in response to a genotoxic insult. This also allows for comparisons to be drawn between the number of DSBs produced by a genotoxic insult and the extent that the DDR is activated in response to these breakages. Making this distinction is pivotal to prevent misinterpretation of radiobiological data: that these DDR activators should be utilized as markers in the analysis of DDR activation kinetics, and not in the quantification of either DNA breakage formation at the DNA level or complete repair.

4.3. MDC1

Another key regulator within the DDR, MDC1, is activated within 20–30 s of DNA damage [24]. It achieves this through ATM-dependent-phosphorylation, as well as specific recognition of γH2AX's C-terminus via its BRCA1 carboxy-terminal (BRCT) tandem domains [124,125]. One of the main roles of MDC1 within the cellular response to DSBs is to amplify the phosphorylation of γH2AX proximal to breakage sites [113]. MDC1 also facilitates the binding of the ubiquitin ligase RNF8 to chromatin, allowing for ubiquitylation and the recruitment and turnover of downstream effectors that regulate DSB repair and pathway choice [126]. These include associations with MRE11 and NBS1 within the MRN complex [24], RAD51 [127], PALB2 [126], and the repair choice mediators BRCA1 and 53BP1 [124]. Described as a "master regulator" of the DDR, MDC1 promptly recruits a variety of factors to DBSs. This facilitates efficient HR and NHEJ repair and enhances the

signaling of damage to neighboring chromatin, thereby ensuring genomic stability [128]. Lee et al. established a link between inhibitor of DNA-binding 3 (ID3) and MDC1, finding that there is an ID3–MDC1-dependent interaction required for MDC1 accumulation at sites of DSB repair. The depletion of ID3 resulted in impaired MDC1 recruitment at DSB sites, also resulting in a reduction in γH2AX-bound MDC1 foci and cellular sensitization to radiation [128]. This has broad implications when choosing MDC1 as a candidate marker, as its expression modulates the accumulation of DDR proteins at DSB sites.

Plasmids encoding fluorescent MDC1 have been produced to analyze its recruitment dynamics and association with endogenous DDR factors. Matsuda et al. utilized a vector containing enhanced green fluorescent protein (EGFP)-fused to MDC1 to visualized its accumulation within MCF7 cells exposed to multiple mutagens, including camptothecin, cisplatin, and DNA-adduct-forming compounds. To validate whether the normal function of MDC1 was compromised when fused to EGFP, the nuclear location of EGFP-MDC1 foci was compared to the staining of MDC1 with anti-MDC1 and anti-γH2AX antibodies. After EGFP-MDC1/MCF7 cells were exposed to 10μM camptothecin treatment for 1 h, fluorescence imaging revealed that the localization of EGFP foci overlapped with both anti-MDC1 and anti-γH2AX signals, suggesting that EGFP-MDC1 maintained its functional capability to associate with DSB sites after exposure to DNA damage (Figure 7D) [116].

One notable limitation in this experimental protocol was that the proportion of EGFP-MDC1-expressing cells was 1%, meaning that, in this instance, high-throughput analysis would present difficulties [116] Moreover, there appears to be a high background level of EGFP, resulting in poor sensitivity and preventing the detection of low levels of MDC1. Similarly, Lukas et al. produced GFP and YFP fusion proteins of MDC1. They discovered that NBS1 recruitment at DSB sites was heavily reliant upon the presence of MDC1. In cells exposed to MDC1-targeting siRNAs, NBS1 exhibited a reduced affinity to bind and remain at damaged chromatin [24]. Although acting chronologically after the binding of MRN to DSBs or is considered "downstream" of DSB sensing, MDC1 acts in assisting nearly every stage of the response to DNA damage. Because MDC1 regulates a variety of DDR proteins, it is an ideal marker for a wholistic overview of repair recruitment. However, contrasting γH2AX, its damage kinetics do not possess a defined relationship amongst all cell types and all pathways of DSB repair [129], limiting its utility in the quantification of genotoxicity.

5. Repair Pathway Specific Assays

The progression towards either HR or NHEJ is controlled by several factors. The error-free DNA repair process HR is the predominant mechanism of repairing DSBs, but only in the S and G2 phases of the cell cycle. It is capable of fully restoring damaged genomic sequences; however, it requires sister chromatids to utilize as a template for replication. In contrast, NHEJ repair is error-prone as it is performed with no regard to homology, yet it is the most frequently utilized DSB repair mechanism in eukaryotes. While predominantly employed in the G0, G1, and early S phase, NHEJ can occur during any time in the cell cycle. HR is characterized by extensive end resection at DSB sites; in contrast, end protection typifies the selection of NHEJ [130], ultimately influencing the set of proteins present at each DSB site depending on which pathway will proceed. Changes in cell cycle distribution consequently change the portion of cells undergoing either HR or NHEJ repair and thus affect the proportion of proteins expressed in either of these pathways.

BRCA1 and 53BP1

In conjunction with cell cycle dependence and end resection, one model posits that the choice between HR and NHEJ pathways is determined by the action of two key proteins after chromatin ubiquitylation [131], these being the recruitment of either BRCA1 to promote HR [132,133] or 53BP1 for NHEJ [134,135]. BRCA1 and 53BP1 interact antagonistically, with the activation of one inhibiting the other's ability to associate with damaged chromatin, making them important for determining which DSB repair pathway will proceed [131,136].

After RNF8- and RNF168-induced chromatin ubiquitylation, the progression towards NHEJ is initiated through the subsequent ubiquitylation of H2AK15, which promotes the recruitment of 53BP1 and the exposure of H4K20me2 residues [102,135]. 53BP1 possesses various functions in the recruitment of additional DSB-repair proteins, checkpoint signaling, and NHEJ initiation [102,135,137]. Another potential substrate of RNF8 and RNF168 is the BRCA1–Abraxas–RAP80 complex, with RAP80-containing ubiquitin-interaction domains. This allows BRCA1 to form the RING heterodimer [138], and consequently associates with C-terminal binding protein-interacting protein (CtIP) and the MRN complex to promote 5′ resection at the DSB ends, forming 3′ ssDNA overhangs on either side of the break [139–141]. To prevent progression towards NHEJ during S and G2 phases, studies indicate that BRCA1 is capable of displacing 53BP1 and its associated effector protein, RAP1-interacting factor 1 (RIF1), from damaged chromatin [142–144]. The mechanism of action responsible for this is unclear; however, the result is extensive end-resection that drives the recruitment of downstream HR factors [145]. During G1, the opposite occurs, and the end-resection-promoting activity of BRCA1 is inhibited by the 53BP1–RIF1 complex, limiting the accumulation of BRCA1 at DSB sites, as well as the association with the CtIP-MRN complex. 53BP1's mechanism of action includes blocking end-resection via recruitment of the Shieldin (SHLD) complex [146], as well as localized fill-in DNA synthesis through CTC1–STN1–TEN1 (CST) and DNA polymerase α (Pol α) to reduce the extent of resected DSBs [147]. This allows for the predomination of NHEJ, as end resection is severely impeded.

Feng et al. used antibodies against 53BP1 to analyze its association with the downstream effectors RIF1 and Pax transactivation domain-interacting protein (PTIP) [117]. They produced a highly specific PTIP antibody that recognized it as a pan-nuclear protein in undamaged HeLa cells. However, after exposure to γ-irradiation, PTIP could form discrete foci. Interestingly, an analysis of cells irradiated at different stages of the cell cycle revealed that PTIP and BRCA1 exhibited a mutually exclusive relationship when forming foci and that both ATM-dependent 53BP1 phosphorylation and PTIP and RIF1 accumulation at DSB sites is limited to the G1 phase [117], suggesting that PTIP contributes to the inhibition of HR (Figure 7E).

Another study by Wei et al. utilized GFP-fused BRCA1 to analyze its in situ response to microirradiation, revealing that the N-terminal domain of BRCA1 is associated with Ku80, in addition to showing that missense mutations within cancer cell lines substantially altered the repair kinetics of BRCA1 [28]. This highlights that the recruitment of pathway-specific factors is not only limited to the cell phase, but also cell type, which is pertinent to consider when making conclusions about their interactions with other key DDR components.

As the interactions by which BRCA1/53BP1 antagonism occurs have not yet been thoroughly validated, leaving some ambiguity in the steps that precede the DSB repair pathway choice, an analysis of proteins at this stage can provide information into the time and duration that these proteins associate with breakage sites and the extent of their activation, in addition to identifying proteins of interest that they may co-localize with. Therefore, they are prime candidates for immunofluorescence imaging to determine cellular progression towards resolving DSBs through HR or NHEJ, enabling a quantitative foci comparison to upstream DSB detectors, DDR activators, and downstream HR and NHEJ factors. Moreover, they can be utilized alongside other techniques, such as the Single Molecule Analysis of Resection Tracks (SMART) assay, to determine the extent of end-resection during the repair of DSBs through HR works [148]. SMART functions by incorporating nucleotide analogues (such as 5-Ido-2′-deoxyuridine, IdU) to cells during the S-phase, followed by cell lysis and the stretching of DNA fibers on a microscope slide. Immunofluorescence staining is then used to stain the nucleotide analogues incorporated into the stretched 3′ single-stranded DNA strands. Fluorescence microscopy and image analysis packages can then be used to determine the lengths of these DNA strands. This is useful in measuring the extent of DNA end-resection in response to a genotoxic insult and, by extension, the efficacy of end-resection machinery [148]. This can allow for clearer relationships to be

identified between the activation/inhibition of the DDR (e.g., PARP1 inhibitors) [139], how BRCA1 and 53BP1 expression is affected by changes in repair regulation, and if this results in cells preferring one DSB repair mechanism over another.

6. Conclusions

The appearance of a wide variety of new and innovative fluorescence-based DSB detection techniques is promising, continually pushing the envelope in improving characterization of DNA damage and responses. Moreover, there are a variety of targets to selectively analyze the regulation of specific stages of the DSB-induced DDR. Fluorescently conjugated proteins, such as Gam-GFP and SIRT6-GFP, are prime examples of simple, single-step biomolecular markers for DSBs. The interference between Gam-GFP and endogenous Ku proteins and the ability of PARP1 and SIRT6 to also bind to SSBs are issues that must be overcome for these proteins to be established as robust DSB markers. STRIDE, TUDEL, and DI-PLA also appear to present these shortcomings, yet due to the relative novelty of these methodologies, information on their reliability is sparse. More widespread utilization and optimization of these new methodologies is required before establishing them as "best-in-class: DSB detectors. Endogenous factors responsible for signaling the accumulation of DSB repair machinery, including PARP1, MRN, ATM, and the commonly utilized γH2AX, are invaluable markers in providing an overview of widespread DSB repair activation. This can be applied when comparing DSB and DDR markers, particularly in studies contrasting the kinetics of DSB formation versus repair activation. Although the mechanism of action by which HR/NHEJ promotion has not yet been fully established, BRCA1 and 53BP1 stand out as proteins that bias each pathway, respectively, and indicate the DSB repair pathway choice. Overall, due to the complexity of the DDR, careful consideration is required to select the correct target for the stage of DSB repair being studied, also accounting for multifunctional proteins that are not confined to operating within DSB detection and repair alone. Utilizing each of these DSB-DDR targets in a wide variety of cell lines and insults, whilst drawing comparisons between them, is the only way to ascertain which are most valuable in characterizing each stage of DSB repair. The continual development of accurate markers for each repair stage is essential not only in providing more accurate data in response to cytotoxic damage, but also in gaining a greater understanding of the mechanisms that define the DNA damage response overall.

Author Contributions: Conceptualization, J.A. and I.K.; investigation, J.A.; resources, I.K.; data curation, J.A.; writing—original draft preparation, J.A.; writing—review and editing, I.K., E.B. and H.L.; visualization, J.A.; supervision, I.K., E.B. and H.L.; project administration, I.K.; funding acquisition, J.A. and I.K. All authors have read and agreed to the published version of the manuscript.

Funding: This research was funded by the Tour de Cure PhD Scholarship, grant ID number RSP-641-FY2023.

Institutional Review Board Statement: Not applicable.

Data Availability Statement: Data sharing not applicable. No new data were created or analyzed in this study. Data sharing is not applicable to this article.

Acknowledgments: We acknowledge Tour de Cure's contribution towards the preparation of this manuscript through the Tour de Cure Scholarship Grant and appreciate their continued support in endorsing this work. Figures were reproduced under the Creative Commons (CC) CC BY 3.0 (https://creativecommons.org/licenses/by/3.0/, accessed on 5 February 2024) and CC BY-NC-ND 4.0 (https://creativecommons.org/licenses/by-nc-nd/4.0/, accessed on 5 February 2024) licenses respectively.

Conflicts of Interest: The authors declare no conflicts of interest.

References

1. Schipler, A.; Iliakis, G. DNA double-strand-break complexity levels and their possible contributions to the probability for error-prone processing and repair pathway choice. *Nucleic Acids Res.* **2013**, *41*, 7589–7605. [CrossRef]
2. Varga, T.; Aplan, P.D. Chromosomal aberrations induced by double strand DNA breaks. *DNA Repair* **2005**, *4*, 1038–1046. [CrossRef]
3. Aparicio, T.; Baer, R.; Gautier, J. DNA double-strand break repair pathway choice and cancer. *DNA Repair* **2014**, *19*, 169–175. [CrossRef]
4. Trenner, A.; Sartori, A.A. Harnessing DNA Double-Strand Break Repair for Cancer Treatment. *Front. Oncol.* **2019**, *9*, 1388. [CrossRef]
5. Kang, J.-K.; Seo, S.; Jin, Y.W. Health Effects of Radon Exposure. *Yonsei Med. J.* **2019**, *60*, 597–603. [CrossRef]
6. Bhaskaran, R.; Damodaran, R.C.; Kumar, V.A.; Panakal John, J.; Bangaru, D.; Natarajan, C.; Sathiamurthy, B.S.; Mundiyanikal Thomas, J.; Mishra, R. Inhalation Dose and Source Term Studies in a Tribal Area of Wayanad, Kerala, India. *J. Environ. Public Health* **2017**, *2017*, 1930787. [CrossRef]
7. Angelo, G.; Lorena, C.; Marta, G.; Antonella, C. Biochemical Composition and Antioxidant Properties of Lavandula angustifolia Miller Essential Oil are Shielded by Propolis Against UV Radiations. *Photochem. Photobiol.* **2014**, *90*, 702–708. [CrossRef]
8. Durante, M.; Cucinotta, F.A. Physical basis of radiation protection in space travel. *Rev. Mod. Phys.* **2011**, *83*, 1245–1281. [CrossRef]
9. Mishra, B.; Luderer, U. Reproductive hazards of space travel in women and men. *Nat. Rev. Endocrinol.* **2019**, *15*, 713–730. [CrossRef]
10. Baskar, R.; Lee, K.A.; Yeo, R.; Yeoh, K.-W. Cancer and Radiation Therapy: Current Advances and Future Directions. *Int. J. Mol. Sci.* **2012**, *9*, 193–199. [CrossRef]
11. Kuo, L.J.; Yang, L.X. Gamma-H2AX–A novel biomarker for DNA double-strand breaks. *In Vivo* **2008**, *22*, 305–309.
12. Atkinson, J.; Bezak, E.; Kempson, I. Imaging DNA double-strand breaks—Are we there yet? *Nat. Rev. Mol. Cell Biol.* **2022**, *23*, 579–580. [CrossRef]
13. Cleaver, J.E.; Feeney, L.; Revet, I. Phosphorylated H2Ax is not an unambiguous marker for DNA double-strand breaks. *Cell Cycle* **2014**, *10*, 3223–3224. [CrossRef]
14. Shee, C.; Cox, B.D.; Gu, F.; Luengas, E.M.; Joshi, M.C.; Chiu, L.Y.; Magnan, D.; Halliday, J.A.; Frisch, R.L.; Gibson, J.L.; et al. Engineered proteins detect spontaneous DNA breakage in human and bacterial cells. *Elife* **2013**, *2*, e01222. [CrossRef]
15. Kyrylkova, K.; Kyryachenko, S.; Leid, M.; Kioussi, C. Detection of apoptosis by TUNEL assay. *Methods Mol. Biol.* **2012**, *887*, 41–47.
16. Hossain, M.A.; Lin, Y.; Yan, S. Single-Strand Break End Resection in Genome Integrity: Mechanism and Regulation by APE2. *Int. J. Mol. Sci.* **2018**, *19*, 2389. [CrossRef]
17. Ahmed, E.A.; Agay, D.; Schrock, G.; Drouet, M.; Meineke, V.; Scherthan, H. Persistent DNA damage after high dose in vivo gamma exposure of minipig skin. *PLoS ONE* **2012**, *7*, e39521. [CrossRef]
18. Olive, P.L.; Banáth, J.P. The comet assay: A method to measure DNA damage in individual cells. *Nat. Protoc.* **2006**, *1*, 23–29. [CrossRef]
19. Sestili, P.; Cantoni, O. Osmotically driven radial diffusion of single-stranded DNA fragments on an agarose bed as a convenient measure of DNA strand scission. *Free Radic. Biol. Med.* **1999**, *26*, 1019–1026. [CrossRef]
20. Sestili, P.; Calcabrini, C.; Diaz, A.R.; Fimognari, C.; Stocchi, V. The Fast-Halo Assay for the Detection of DNA Damage. In *Fast Detection of DNA Damage: Methods and Protocols*; Didenko, V.V., Ed.; Springer: New York, NY, USA, 2017; pp. 75–93.
21. Fernández, J.L.; Vázquez-Gundín, F.; Rivero, M.T.; Genescá, A.; Gosálvez, J.; Goyanes, V. DBD-fish on neutral comets: Simultaneous analysis of DNA single- and double-strand breaks in individual cells. *Exp. Cell Res.* **2001**, *270*, 102–109. [CrossRef]
22. Haince, J.-F.; McDonald, D.; Rodrigue, A.; Déry, U.; Masson, J.-Y.; Hendzel, M.J.; Poirier, G.G. PARP1-dependent Kinetics of Recruitment of MRE11 and NBS1 Proteins to Multiple DNA Damage Sites. *J. Biol. Chem.* **2008**, *283*, 1197–1208. [CrossRef]
23. Yang, G.; Liu, C.; Chen, S.-H.; Kassab, M.A.; Hoff, J.D.; Walter, N.G.; Yu, X. Super-resolution imaging identifies PARP1 and the Ku complex acting as DNA double-strand break sensors. *Nucleic Acids Res.* **2018**, *46*, 3446–3457. [CrossRef]
24. Lukas, C.; Melander, F.; Stucki, M.; Falck, J.; Bekker-Jensen, S.; Goldberg, M.; Lerenthal, Y.; Jackson, S.P.; Bartek, J.; Lukas, J. Mdc1 couples DNA double-strand break recognition by Nbs1 with its H2AX-dependent chromatin retention. *EMBO J.* **2004**, *23*, 2674–2683. [CrossRef]
25. Jakob, B.; Taucher-Scholz, G. Live Cell Imaging to Study Real-Time ATM-Mediated Recruitment of DNA Repair Complexes to Sites of Ionizing Radiation-Induced DNA Damage. In *ATM Kinase: Methods and Protocols*; Kozlov, S.V., Ed.; Springer: New York, NY, USA, 2017; pp. 287–302.
26. Davis, A.J.; Wang, S.Y.; Chen, D.J.; Chen, B.P.C. Imaging of Fluorescently Tagged ATM Kinase at the Sites of DNA Double Strand Breaks. *Methods Mol. Biol.* **2017**, *1599*, 277–285.
27. Rogakou, E.P.; Boon, C.; Redon, C.; Bonner, W.M. Megabase chromatin domains involved in DNA double-strand breaks in vivo. *J. Cell Biol.* **1999**, *146*, 905–916. [CrossRef]
28. Wei, L.; Lan, L.; Hong, Z.; Yasui, A.; Ishioka, C.; Chiba, N. Rapid recruitment of BRCA1 to DNA double-strand breaks is dependent on its association with Ku80. *Mol. Cell Biol.* **2008**, *28*, 7380–7393. [CrossRef]
29. Suchánková, J.; Kozubek, S.; Legartová, S.; Sehnalová, P.; Küntziger, T.; Bártová, E. Distinct kinetics of DNA repair protein accumulation at DNA lesions and cell cycle-dependent formation of γH2AX- and NBS1-positive repair foci. *Biol. Cell* **2015**, *107*, 440–454. [CrossRef]

30. Bekker-Jensen, S.; Lukas, C.; Melander, F.; Bartek, J.; Lukas, J. Dynamic assembly and sustained retention of 53BP1 at the sites of DNA damage are controlled by Mdc1/NFBD1. *J. Cell Biol.* **2005**, *170*, 201–211. [CrossRef]
31. Mao, Z.; Bozzella, M.; Seluanov, A.; Gorbunova, V. Comparison of nonhomologous end joining and homologous recombination in human cells. *DNA Repair* **2008**, *7*, 1765–1771. [CrossRef]
32. Bhattacharyya, S.; Soniat, M.M.; Walker, D.; Jang, S.; Finkelstein, I.J.; Harshey, R.M. Phage Mu Gam protein promotes NHEJ in concert withEscherichia coliligase. *Proc. Natl. Acad. Sci. USA* **2018**, *115*, E11614–E11622. [CrossRef]
33. Abraham, Z.H.; Symonds, N. Purification of overexpressed gam gene protein from bacteriophage Mu by denaturation-renaturation techniques and a study of its DNA-binding properties. *Biochem. J.* **1990**, *269*, 679–684. [CrossRef]
34. Williams, E.S.; Stap, J.; Essers, J.; Ponnaiya, B.; Luijsterburg, M.S.; Krawczyk, P.M.; Ullrich, R.L.; Aten, J.A.; Bailey, S.M. DNA double-strand breaks are not sufficient to initiate recruitment of TRF2. *Nat. Genet.* **2007**, *39*, 696–698. [CrossRef]
35. Horibe, T.; Torisawa, A.; Akiyoshi, R.; Hatta-Ohashi, Y.; Suzuki, H.; Kawakami, K. Transfection efficiency of normal and cancer cell lines and monitoring of promoter activity by single-cell bioluminescence imaging. *Luminescence* **2014**, *29*, 96–100. [CrossRef] [PubMed]
36. Nath, A.; Roizman, D.; Pachaimuthu, N.; Blázquez, J.; Rolff, J.; Rodríguez-Rojas, A. Antibiotic-induced recombination in bacteria requires the formation of double-strand breaks. *bioRxiv* **2022**, 2022.03.08.483535. [CrossRef]
37. Kotlajich, M.V.; Xia, J.; Zhai, Y.; Lin, H.-Y.; Bradley, C.C.; Shen, X.; Mei, Q.; Wang, A.Z.; Lynn, E.J.; Shee, C.; et al. Fluorescent fusions of the N protein of phage Mu label DNA damage in living cells. *DNA Repair* **2018**, *72*, 86–92. [CrossRef] [PubMed]
38. Galbiati, A.; Beauséjour, C.; d'Adda di Fagagna, F. A novel single-cell method provides direct evidence of persistent DNA damage in senescent cells and aged mammalian tissues. *Aging Cell* **2017**, *16*, 422–427. [CrossRef] [PubMed]
39. Galbiati, A.; d'Adda di Fagagna, F. DNA Damage In Situ Ligation Followed by Proximity Ligation Assay (DI-PLA). In *Cellular Senescence: Methods and Protocols*; Demaria, M., Ed.; Springer: New York, NY, USA, 2019; pp. 11–20.
40. Kordon, M.M.; Zarębski, M.; Solarczyk, K.; Ma, H.; Pederson, T.; Dobrucki, J.W. STRIDE—A fluorescence method for direct, specific in situ detection of individual single- or double-strand DNA breaks in fixed cells. *Nucleic Acids Res.* **2019**, *48*, e14. [CrossRef]
41. Lutze, J.; Warrington, S.E.; Kron, S.J. TdT-dUTP DSB End Labeling (TUDEL), for Specific, Direct In Situ Labeling of DNA Double Strand Breaks. In *Biomedical Engineering Technologies*; Rasooly, A., Baker, H., Ossandon, M.R., Eds.; Springer: New York, NY, USA, 2022; pp. 299–317.
42. Darzynkiewicz, Z.; Zhao, H. Detection of DNA strand breaks in apoptotic cells by flow- and image-cytometry. *Methods Mol. Biol.* **2011**, *682*, 91–101.
43. Banér, J.; Nilsson, M.; Mendel-Hartvig, M.; Landegren, U. Signal amplification of padlock probes by rolling circle replication. *Nucleic Acids Res.* **1998**, *26*, 5073–5078. [CrossRef]
44. Pinto, M.; Pickrell, A.M.; Wang, X.; Bacman, S.R.; Yu, A.; Hida, A.; Dillon, L.M.; Morton, P.D.; Malek, T.R.; Williams, S.L.; et al. Transient mitochondrial DNA double strand breaks in mice cause accelerated aging phenotypes in a ROS-dependent but p53/p21-independent manner. *Cell Death Differ.* **2017**, *24*, 288–299. [CrossRef]
45. Didier, M.; Bursztajn, S.; Adamec, E.; Passani, L.; Nixon, R.A.; Coyle, J.T.; Wei, J.Y.; Berman, S.A. DNA strand breaks induced by sustained glutamate excitotoxicity in primary neuronal cultures. *J. Neurosci.* **1996**, *16*, 2238–2250. [CrossRef]
46. Chen, J.; Jin, K.; Chen, M.; Pei, W.; Kawaguchi, K.; Greenberg, D.A.; Simon, R.P. Early Detection of DNA Strand Breaks in the Brain After Transient Focal Ischemia: Implications for the Role of DNA Damage in Apoptosis and Neuronal Cell Death. *J. Neurochem.* **1997**, *69*, 232–245. [CrossRef]
47. Honda, S.; Sugita, I.; Miki, K.; Saito, I. The Semi-quantitative Comparison of Oxidative Stress Mediated DNA Single and Double Strand Breaks using Terminal Deoxynucleotidyl Transferase Mediated End Labeling Combined with a Slot Blot Technique. *Free Radic. Res.* **2004**, *38*, 481–485. [CrossRef]
48. Leduc, F.; Faucher, D.; Bikond Nkoma, G.; Grégoire, M.-C.; Arguin, M.; Wellinger, R.J.; Boissonneault, G. Genome-Wide Mapping of DNA Strand Breaks. *PLoS ONE* **2011**, *6*, e17353. [CrossRef] [PubMed]
49. Yamadori, I.; Yoshino, T.; Kondo, E.; Cao, L.; Akagi, T.; Matsuo, Y.; Minowada, J. Comparison of Two Methods of Staining Apoptotic Cells of Leukemia Cell Lines: Terminal Deoxynucleotidyl Transferase and DNA Polymerase I Reactions. *J. Histochem. Cytochem.* **1998**, *46*, 85–90. [CrossRef] [PubMed]
50. Halvorsen, P.S. *Establishment of a new quantitative method for in situ detection of DNA breaks in human spermatozoa*; Oslo Metropolitan University: Oslo, Norway, 2021.
51. Pandey, N.; Black, B.E. Rapid Detection and Signaling of DNA Damage by PARP-1. *Trends Biochem. Sci.* **2021**, *46*, 744–757. [CrossRef]
52. Izhar, L.; Adamson, B.; Ciccia, A.; Lewis, J.; Pontano-Vaites, L.; Leng, Y.; Liang, A.C.; Westbrook, T.F.; Harper, J.W.; Elledge, S.J. A Systematic Analysis of Factors Localized to Damaged Chromatin Reveals PARP-Dependent Recruitment of Transcription Factors. *Cell Rep.* **2015**, *11*, 1486–1500. [CrossRef]
53. Roy, R.; Chun, J.; Powell, S.N. BRCA1 and BRCA2: Different roles in a common pathway of genome protection. *Nat. Rev. Cancer* **2012**, *12*, 68–78. [CrossRef]
54. Thorslund, T.; West, S.C. BRCA2: A universal recombinase regulator. *Oncogene* **2007**, *26*, 7720–7730. [CrossRef] [PubMed]
55. Navadgi-Patil, V.M.; Burgers, P.M. A tale of two tails: Activation of DNA damage checkpoint kinase Mec1/ATR by the 9–1–1 clamp and by Dpb11/TopBP1. *DNA Repair* **2009**, *8*, 996–1003. [CrossRef]

56. Huang, J.; Gong, Z.; Ghosal, G.; Chen, J. SOSS complexes participate in the maintenance of genomic stability. *Mol. Cell* **2009**, *35*, 384–393. [CrossRef]
57. Ko, H.L.; Ren, E.C. Functional Aspects of PARP1 in DNA Repair and Transcription. *Biomolecules* **2012**, *2*, 524–548. [CrossRef]
58. Sefer, A.; Kallis, E.; Eilert, T.; Röcker, C.; Kolesnikova, O.; Neuhaus, D.; Eustermann, S.; Michaelis, J. Structural dynamics of DNA strand break sensing by PARP-1 at a single-molecule level. *Nat. Commun.* **2022**, *13*, 6569. [CrossRef] [PubMed]
59. Ogino, H.; Nozaki, T.; Gunji, A.; Maeda, M.; Suzuki, H.; Ohta, T.; Murakami, Y.; Nakagama, H.; Sugimura, T.; Masutani, M. Loss of Parp-1 affects gene expression profile in a genome-wide manner in ES cells and liver cells. *BMC Genom.* **2007**, *8*, 41.
60. Virág, L.; Robaszkiewicz, A.; Rodriguez-Vargas, J.M.; Oliver, F.J. Poly(ADP-ribose) signaling in cell death. *Mol. Asp. Med.* **2013**, *34*, 1153–1167. [CrossRef]
61. Wang, F.; Zhao, M.; Chang, B.; Zhou, Y.; Wu, X.; Ma, M.; Liu, S.; Cao, Y.; Zheng, M.; Dang, Y.; et al. Cytoplasmic PARP1 links the genome instability to the inhibition of antiviral immunity through PARylating cGAS. *Mol. Cell* **2022**, *82*, 2032–2049.e7. [CrossRef]
62. Wang, Y.; Kim, N.S.; Haince, J.-F.; Kang, H.C.; David, K.K.; Andrabi, S.A.; Poirier, G.G.; Dawson, V.L.; Dawson, T.M. Poly(ADP-Ribose) (PAR) Binding to Apoptosis-Inducing Factor Is Critical for PAR Polymerase-1-Dependent Cell Death (Parthanatos). *Sci. Signal.* **2011**, *4*, ra20. [CrossRef]
63. Haddad, M.; Rhinn, H.; Bloquel, C.; Coqueran, B.; Szabó, C.; Plotkine, M.; Scherman, D.; Margaill, I. Anti-inflammatory effects of PJ34, a poly(ADP-ribose) polymerase inhibitor, in transient focal cerebral ischemia in mice. *Br. J. Pharmacol.* **2006**, *149*, 23–30. [CrossRef] [PubMed]
64. Pazzaglia, S.; Pioli, C. Multifaceted Role of PARP-1 in DNA Repair and Inflammation: Pathological and Therapeutic Implications in Cancer and Non-Cancer Diseases. *Cells* **2019**, *9*, 41. [CrossRef] [PubMed]
65. Zhu, H.; Tang, Y.-D.; Zhan, G.; Su, C.; Zheng, C. The Critical Role of PARPs in Regulating Innate Immune Responses. *Front. Immunol.* **2021**, *12*, 712556. [CrossRef]
66. Rose, M.; Burgess, J.T.; O'Byrne, K.; Richard, D.J.; Bolderson, E. PARP Inhibitors: Clinical Relevance, Mechanisms of Action and Tumor Resistance. *Front. Cell Dev. Biol.* **2020**, *8*, 564601. [CrossRef]
67. Ratanaphan, A. A DNA Repair BRCA1 Estrogen Receptor and Targeted Therapy in Breast Cancer. *Int. J. Med. Sci.* **2012**, *13*, 14898–14916. [CrossRef]
68. Mao, Z.; Hine, C.; Tian, X.; Van Meter, M.; Au, M.; Vaidya, A.; Seluanov, A.; Gorbunova, V. SIRT6 promotes DNA repair under stress by activating PARP1. *Science* **2011**, *332*, 1443–1446. [CrossRef]
69. Ryabokon, N.I.; Goncharova, R.I.; Duburs, G.; Hancock, R.; Rzeszowska-Wolny, J. Changes in poly(ADP-ribose) level modulate the kinetics of DNA strand break rejoining. *Mutat. Res./Fundam. Mol. Mech. Mutagen.* **2008**, *637*, 173–181. [CrossRef]
70. Shao, Z.; Lee, B.J.; Rouleau-Turcotte, É.; Langelier, M.F.; Lin, X.; Estes, V.M.; Pascal, J.M.; Zha, S. Clinical PARP inhibitors do not abrogate PARP1 exchange at DNA damage sites in vivo. *Nucleic Acids Res.* **2020**, *48*, 9694–9709. [CrossRef] [PubMed]
71. Li, M.; Lu, L.Y.; Yang, C.Y.; Wang, S.; Yu, X. The FHA and BRCT domains recognize ADP-ribosylation during DNA damage response. *Genes Dev.* **2013**, *27*, 1752–1768. [CrossRef] [PubMed]
72. Walker, J.R.; Corpina, R.A.; Goldberg, J. Structure of the Ku heterodimer bound to DNA and its implications for double-strand break repair. *Nature* **2001**, *412*, 607–614. [CrossRef] [PubMed]
73. Zhao, B.; Rothenberg, E.; Ramsden, D.A.; Lieber, M.R. The molecular basis and disease relevance of non-homologous DNA end joining. *Nat. Rev. Mol. Cell Biol.* **2020**, *21*, 765–781. [CrossRef] [PubMed]
74. Zahid, S.; Seif El Dahan, M.; Iehl, F.; Fernandez-Varela, P.; Le Du, M.-H.; Ropars, V.; Charbonnier, J.B. The Multifaceted Roles of Ku70/80. *Int. J. Med. Sci.* **2021**, *22*, 4134. [CrossRef]
75. Li, B.; Reddy, S.; Comai, L. Depletion of Ku70/80 reduces the levels of extrachromosomal telomeric circles and inhibits proliferation of ALT cells. *Aging (Albany NY)* **2011**, *3*, 395–406. [CrossRef]
76. Qiu, S.; Huang, J. MRN complex is an essential effector of DNA damage repair. *J. Zhejiang Univ. Sci. B* **2021**, *22*, 31–37. [CrossRef] [PubMed]
77. Lamarche, B.J.; Orazio, N.I.; Weitzman, M.D. The MRN complex in double-strand break repair and telomere maintenance. *FEBS Lett.* **2010**, *584*, 3682–3695. [CrossRef]
78. Rass, E.; Grabarz, A.; Plo, I.; Gautier, J.; Bertrand, P.; Lopez, B.S. Role of Mre11 in chromosomal nonhomologous end joining in mammalian cells. *Nat. Struct. Mol. Biol.* **2009**, *16*, 819–824. [CrossRef] [PubMed]
79. Deriano, L.; Stracker, T.H.; Baker, A.; Petrini, J.H.J.; Roth, D.B. Roles for NBS1 in Alternative Nonhomologous End-Joining of V(D)J Recombination Intermediates. *Mol. Cell* **2009**, *34*, 13–25. [CrossRef] [PubMed]
80. Dinkelmann, M.; Spehalski, E.; Stoneham, T.; Buis, J.; Wu, Y.; Sekiguchi, J.M.; Ferguson, D.O. Multiple functions of MRN in end-joining pathways during isotype class switching. *Nat. Struct. Mol. Biol.* **2009**, *16*, 808–813. [CrossRef]
81. Li, Y.; Wang, J.; Zhou, G.; Lajeunesse, M.; Le, N.; Stawicki, B.N.; Corcino, Y.L.; Berkner, K.L.; Runge, K.W. Nonhomologous End-Joining with Minimal Sequence Loss Is Promoted by the Mre11-Rad50-Nbs1-Ctp1 Complex in Schizosaccharomyces pombe. *Genetics* **2017**, *206*, 481–496. [CrossRef]
82. Williams, R.S.; Moncalian, G.; Williams, J.S.; Yamada, Y.; Limbo, O.; Shin, D.S.; Groocock, L.M.; Cahill, D.; Hitomi, C.; Guenther, G.; et al. Mre11 Dimers Coordinate DNA End Bridging and Nuclease Processing in Double-Strand-Break Repair. *Cell* **2008**, *135*, 97–109. [CrossRef]
83. Bian, L.; Meng, Y.; Zhang, M.; Li, D. MRE11-RAD50-NBS1 complex alterations and DNA damage response: Implications for cancer treatment. *Mol. Cancer* **2019**, *18*, 169. [CrossRef]

84. Williams, R.S.; Dodson, G.E.; Limbo, O.; Yamada, Y.; Williams, J.S.; Guenther, G.; Classen, S.; Glover, J.N.; Iwasaki, H.; Russell, P.; et al. Nbs1 flexibly tethers Ctp1 and Mre11-Rad50 to coordinate DNA double-strand break processing and repair. *Cell* **2009**, *139*, 87–99. [CrossRef]
85. Wu, Y.; Xiao, S.; Zhu, X.D. MRE11-RAD50-NBS1 and ATM function as co-mediators of TRF1 in telomere length control. *Nat. Struct. Mol. Biol.* **2007**, *14*, 832–840. [CrossRef]
86. Khayat, F.; Cannavo, E.; Alshmery, M.; Foster, W.R.; Chahwan, C.; Maddalena, M.; Smith, C.; Oliver, A.W.; Watson, A.T.; Carr, A.M.; et al. Inhibition of MRN activity by a telomere protein motif. *Nat. Commun.* **2021**, *12*, 3856. [CrossRef] [PubMed]
87. Warren, C.; Pavletich, N.P. Structure of the human ATM kinase and mechanism of Nbs1 binding. *eLife* **2022**, *11*, e74218. [CrossRef] [PubMed]
88. Mirzoeva, O.K.; Petrini, J.H. DNA damage-dependent nuclear dynamics of the Mre11 complex. *Mol. Cell Biol.* **2001**, *21*, 281–288. [CrossRef] [PubMed]
89. Britton, S.; Coates, J.; Jackson, S.P. A new method for high-resolution imaging of Ku foci to decipher mechanisms of DNA double-strand break repair. *J. Cell Biol.* **2013**, *202*, 579–595. [CrossRef] [PubMed]
90. Dmitrieva, N.I.; Malide, D.; Burg, M.B. Mre11 is expressed in mammalian mitochondria where it binds to mitochondrial DNA. *Am. J. Physiol. Regul. Integr. Comp. Physiol.* **2011**, *301*, R632–R640. [CrossRef] [PubMed]
91. Coffey, G.; Lakshmipathy, U.; Campbell, C. Mammalian mitochondrial extracts possess DNA end-binding activity. *Nucleic Acids Res.* **1999**, *27*, 3348–3354. [CrossRef]
92. Alexeyev, M.; Shokolenko, I.; Wilson, G.; LeDoux, S. The maintenance of mitochondrial DNA integrity—Critical analysis and update. *Cold Spring Harb. Perspect. Biol.* **2013**, *5*, a012641. [CrossRef]
93. Bosch-Presegué, L.; Vaquero, A. Sirtuins in stress response: Guardians of the genome. *Oncogene* **2014**, *33*, 3764–3775. [CrossRef]
94. Li, X.; Liu, L.; Li, T.; Liu, M.; Wang, Y.; Ma, H.; Mu, N.; Wang, H. SIRT6 in Senescence and Aging-Related Cardiovascular Diseases. *Front. Cell Dev. Biol.* **2021**, *9*, 641315. [CrossRef]
95. Tian, X.; Firsanov, D.; Zhang, Z.; Cheng, Y.; Luo, L.; Tombline, G.; Tan, R.; Simon, M.; Henderson, S.; Steffan, J.; et al. SIRT6 Is Responsible for More Efficient DNA Double-Strand Break Repair in Long-Lived Species. *Cell* **2019**, *177*, 622–638.e22. [CrossRef]
96. Toiber, D.; Erdel, F.; Bouazoune, K.; Silberman, D.M.; Zhong, L.; Mulligan, P.; Sebastian, C.; Cosentino, C.; Martinez-Pastor, B.; Giacosa, S.; et al. SIRT6 recruits SNF2H to DNA break sites, preventing genomic instability through chromatin remodeling. *Mol. Cell* **2013**, *51*, 454–468. [CrossRef]
97. Onn, L.; Portillo, M.; Ilic, S.; Cleitman, G.; Stein, D.; Kaluski, S.; Shirat, I.; Slobodnik, Z.; Einav, M.; Erdel, F.; et al. SIRT6 is a DNA double-strand break sensor. *eLife* **2020**, *9*, e51636. [CrossRef]
98. Sekar, R.B.; Periasamy, A. Fluorescence resonance energy transfer (FRET) microscopy imaging of live cell protein localizations. *J. Cell Biol.* **2003**, *160*, 629–633. [CrossRef] [PubMed]
99. Chapman, J.R.; Jackson, S.P. Phospho-dependent interactions between NBS1 and MDC1 mediate chromatin retention of the MRN complex at sites of DNA damage. *EMBO Rep.* **2008**, *9*, 795–801. [CrossRef] [PubMed]
100. Daley, J.M.; Sung, P. 53BP1, BRCA1, and the choice between recombination and end joining at DNA double-strand breaks. *Mol. Cell Biol.* **2014**, *34*, 1380–1388. [CrossRef] [PubMed]
101. Mailand, N.; Bekker-Jensen, S.; Faustrup, H.; Melander, F.; Bartek, J.; Lukas, C.; Lukas, J. RNF8 Ubiquitylates Histones at DNA Double-Strand Breaks and Promotes Assembly of Repair Proteins. *Cell* **2007**, *131*, 887–900. [CrossRef] [PubMed]
102. Panier, S.; Boulton, S.J. Double-strand break repair: 53BP1 comes into focus. *Nat. Rev. Mol. Cell Biol.* **2014**, *15*, 7–18. [CrossRef] [PubMed]
103. Kinner, A.; Wu, W.; Staudt, C.; Iliakis, G. Gamma-H2AX in recognition and signaling of DNA double-strand breaks in the context of chromatin. *Nucleic Acids Res.* **2008**, *36*, 5678–5694. [CrossRef]
104. Mah, L.J.; El-Osta, A.; Karagiannis, T.C. γH2AX: A sensitive molecular marker of DNA damage and repair. *Leukemia* **2010**, *24*, 679–686. [CrossRef] [PubMed]
105. Rothkamm, K.; Löbrich, M. Evidence for a lack of DNA double-strand break repair in human cells exposed to very low x-ray doses. *Proc. Natl. Acad. Sci. USA* **2003**, *100*, 5057–5062. [CrossRef]
106. Bakkenist, C.J.; Kastan, M.B. DNA damage activates ATM through intermolecular autophosphorylation and dimer dissociation. *Nature* **2003**, *421*, 499–506. [CrossRef] [PubMed]
107. Phan, L.M.; Rezaeian, A.H. ATM: Main Features, Signaling Pathways, and Its Diverse Roles in DNA Damage Response, Tumor Suppression, and Cancer Development. *Genes* **2021**, *12*, 845. [CrossRef] [PubMed]
108. Ray, A.; Blevins, C.; Wani, G.; Wani, A.A. ATR- and ATM-Mediated DNA Damage Response Is Dependent on Excision Repair Assembly during G1 but Not in S Phase of Cell Cycle. *PLoS ONE* **2016**, *11*, e0159344. [CrossRef] [PubMed]
109. Kitagawa, R.; Kastan, M.B. The ATM-dependent DNA damage signaling pathway. *Cold Spring Harb. Symp. Quant. Biol.* **2005**, *70*, 99–109. [CrossRef] [PubMed]
110. Tanaka, T.; Huang, X.; Halicka, H.D.; Zhao, H.; Traganos, F.; Albino, A.P.; Dai, W.; Darzynkiewicz, Z. Cytometry of ATM activation and histone H2AX phosphorylation to estimate extent of DNA damage induced by exogenous agents. *Cytometry A* **2007**, *71*, 648–661. [CrossRef] [PubMed]
111. Tresini, M.; Warmerdam, D.O.; Kolovos, P.; Snijder, L.; Vrouwe, M.G.; Demmers, J.A.A.; van Ijcken, W.F.J.; Grosveld, F.G.; Medema, R.H.; Hoeijmakers, J.H.J.; et al. The core spliceosome as target and effector of non-canonical ATM signalling. *Nature* **2015**, *523*, 53–58. [CrossRef] [PubMed]

112. Shibata, A.; Jeggo, P.A. ATM's Role in the Repair of DNA Double-Strand Breaks. *Genes* **2021**, *12*, 1370. [CrossRef]
113. Savic, V.; Yin, B.; Maas, N.L.; Bredemeyer, A.L.; Carpenter, A.C.; Helmink, B.A.; Yang-Iott, K.S.; Sleckman, B.P.; Bassing, C.H. Formation of Dynamic γ-H2AX Domains along Broken DNA Strands Is Distinctly Regulated by ATM and MDC1 and Dependent upon H2AX Densities in Chromatin. *Mol. Cell* **2009**, *34*, 298–310. [CrossRef]
114. Shroff, R.; Arbel-Eden, A.; Pilch, D.; Ira, G.; Bonner, W.M.; Petrini, J.H.; Haber, J.E.; Lichten, M. Distribution and dynamics of chromatin modification induced by a defined DNA double-strand break. *Curr. Biol.* **2004**, *14*, 1703–1711. [CrossRef]
115. Adams, B.R.; Golding, S.E.; Rao, R.R.; Valerie, K. Dynamic Dependence on ATR and ATM for Double-Strand Break Repair in Human Embryonic Stem Cells and Neural Descendants. *PLoS ONE* **2010**, *5*, e10001. [CrossRef] [PubMed]
116. Matsuda, S.; Matsuda, R.; Matsuda, Y.; Yanagisawa, S.-y.; Ikura, M.; Ikura, T.; Matsuda, T. An Easy-to-use Genotoxicity Assay Using EGFP-MDC1-expressing Human Cells. *Genes Environ.* **2014**, *36*, 17–28. [CrossRef]
117. Feng, L.; Li, N.; Li, Y.; Wang, J.; Gao, M.; Wang, W.; Chen, J. Cell cycle-dependent inhibition of 53BP1 signaling by BRCA1. *Cell Discov.* **2015**, *1*, 15019. [CrossRef] [PubMed]
118. Celeste, A.; Petersen, S.; Romanienko, P.J.; Fernandez-Capetillo, O.; Chen, H.T.; Sedelnikova, O.A.; Reina-San-Martin, B.; Coppola, V.; Meffre, E.; Difilippantonio, M.J.; et al. Genomic instability in mice lacking histone H2AX. *Science* **2002**, *296*, 922–927. [CrossRef] [PubMed]
119. Rybak, P.; Hoang, A.; Bujnowicz, L.; Bernas, T.; Berniak, K.; Zarębski, M.; Darzynkiewicz, Z.; Dobrucki, J. Low level phosphorylation of histone H2AX on serine 139 (γH2AX) is not associated with DNA double-strand breaks. *Oncotarget* **2016**, *7*, 49574–49587. [CrossRef] [PubMed]
120. Meyer, B.; Voss, K.-O.; Tobias, F.; Jakob, B.; Durante, M.; Taucher-Scholz, G. Clustered DNA damage induces pan-nuclear H2AX phosphorylation mediated by ATM and DNA–PK. *Nucleic Acids Res.* **2013**, *41*, 6109–6118. [CrossRef] [PubMed]
121. Tu, W.-Z.; Li, B.; Huang, B.; Wang, Y.; Liu, X.-D.; Guan, H.; Zhang, S.-M.; Tang, Y.; Rang, W.-Q.; Zhou, P.-K. γH2AX foci formation in the absence of DNA damage: Mitotic H2AX phosphorylation is mediated by the DNA-PKcs/CHK2 pathway. *FEBS Lett.* **2013**, *587*, 3437–3443. [CrossRef]
122. Bouquet, F.; Muller, C.; Salles, B. The Loss of gammaH2AX Signal is a Marker of DNA Double Strand Breaks Repair Only at Low Levels of DNA Damage. *Cell Cycle* **2006**, *5*, 1116–1122. [CrossRef]
123. Bouquet, F.; Pal, A.; Pilones, K.A.; Demaria, S.; Hann, B.; Akhurst, R.J.; Babb, J.S.; Lonning, S.M.; DeWyngaert, J.K.; Formenti, S.C.; et al. TGFβ1 inhibition increases the radiosensitivity of breast cancer cells in vitro and promotes tumor control by radiation in vivo. *Clin. Cancer Res.* **2011**, *17*, 6754–6765. [CrossRef]
124. Goldberg, M.; Stucki, M.; Falck, J.; D'Amours, D.; Rahman, D.; Pappin, D.; Bartek, J.; Jackson, S.P. MDC1 is required for the intra-S-phase DNA damage checkpoint. *Nature* **2003**, *421*, 952–956. [CrossRef]
125. Kolas, N.K.; Chapman, J.R.; Nakada, S.; Ylanko, J.; Chahwan, R.; Sweeney, F.D.; Panier, S.; Mendez, M.; Wildenhain, J.; Thomson, T.M.; et al. Orchestration of the DNA-damage response by the RNF8 ubiquitin ligase. *Science* **2007**, *318*, 1637–1640. [CrossRef]
126. Zhang, F.; Bick, G.; Park, J.Y.; Andreassen, P.R. MDC1 and RNF8 function in a pathway that directs BRCA1-dependent localization of PALB2 required for homologous recombination. *J. Cell Sci.* **2012**, *125*, 6049–6057. [CrossRef] [PubMed]
127. Zhang, J.; Ma, Z.; Treszezamsky, A.; Powell, S.N. MDC1 interacts with Rad51 and facilitates homologous recombination. *Nat. Struct. Mol. Biol.* **2005**, *12*, 902–909. [CrossRef] [PubMed]
128. Lee, J.-H.; Park, S.-J.; Hariharasudhan, G.; Kim, M.-J.; Jung, S.M.; Jeong, S.-Y.; Chang, I.-Y.; Kim, C.; Kim, E.; Yu, J.; et al. ID3 regulates the MDC1-mediated DNA damage response in order to maintain genome stability. *Nat. Commun.* **2017**, *8*, 903. [CrossRef] [PubMed]
129. Wang, H.; Adhikari, S.; Butler, B.E.; Pandita, T.K.; Mitra, S.; Hegde, M.L. A Perspective on Chromosomal Double Strand Break Markers in Mammalian Cells. *Jacobs J. Radiat. Oncol.* **2014**, *1*, 3.
130. Zhao, F.; Kim, W.; Kloeber, J.A.; Lou, Z. DNA end resection and its role in DNA replication and DSB repair choice in mammalian cells. *Exp. Mol. Med.* **2020**, *52*, 1705–1714. [CrossRef] [PubMed]
131. Escribano-Díaz, C.; Orthwein, A.; Fradet-Turcotte, A.; Xing, M.; Young, J.T.F.; Tkáč, J.; Cook, M.A.; Rosebrock, A.P.; Munro, M.; Canny, M.D.; et al. A Cell Cycle-Dependent Regulatory Circuit Composed of 53BP1-RIF1 and BRCA1-CtIP Controls DNA Repair Pathway Choice. *Mol. Cell* **2013**, *49*, 872–883. [CrossRef]
132. Chen, L.; Nievera, C.J.; Lee, A.Y.-L.; Wu, X. Cell Cycle-dependent Complex Formation of BRCA1·CtIP·MRN Is Important for DNA Double-strand Break Repair. *J. Biol. Chem.* **2008**, *283*, 7713–7720. [CrossRef]
133. Yun, M.H.; Hiom, K. CtIP-BRCA1 modulates the choice of DNA double-strand-break repair pathway throughout the cell cycle. *Nature* **2009**, *459*, 460–463. [CrossRef]
134. Bunting, S.F.; Callén, E.; Wong, N.; Chen, H.-T.; Polato, F.; Gunn, A.; Bothmer, A.; Feldhahn, N.; Fernandez-Capetillo, O.; Cao, L.; et al. 53BP1 Inhibits Homologous Recombination in Brca1-Deficient Cells by Blocking Resection of DNA Breaks. *Cell* **2010**, *141*, 243–254. [CrossRef]
135. Dimitrova, N.; Chen, Y.-C.M.; Spector, D.L.; de Lange, T. 53BP1 promotes non-homologous end joining of telomeres by increasing chromatin mobility. *Nature* **2008**, *456*, 524–528. [CrossRef]
136. Bouwman, P.; Aly, A.; Escandell, J.M.; Pieterse, M.; Bartkova, J.; van der Gulden, H.; Hiddingh, S.; Thanasoula, M.; Kulkarni, A.; Yang, Q.; et al. 53BP1 loss rescues BRCA1 deficiency and is associated with triple-negative and BRCA-mutated breast cancers. *Nat. Struct. Mol. Biol.* **2010**, *17*, 688–695. [CrossRef]
137. Mirman, Z.; de Lange, T. 53BP1: A DSB escort. *Genes Dev.* **2020**, *34*, 7–23. [CrossRef]

138. Christou, C.M.; Kyriacou, K. BRCA1 and Its Network of Interacting Partners. *Biology* **2013**, *2*, 40–63. [CrossRef]
139. Walsh, C.S. Two decades beyond BRCA1/2: Homologous recombination, hereditary cancer risk and a target for ovarian cancer therapy. *Gynecol. Oncol.* **2015**, *137*, 343–350. [CrossRef] [PubMed]
140. Polato, F.; Callen, E.; Wong, N.; Faryabi, R.; Bunting, S.; Chen, H.-T.; Kozak, M.; Kruhlak, M.J.; Reczek, C.R.; Lee, W.-H.; et al. CtIP-mediated resection is essential for viability and can operate independently of BRCA1. *J. Exp. Med.* **2014**, *211*, 1027–1036. [CrossRef]
141. Liu, Y.; Lu, L.-Y. BRCA1 and homologous recombination: Implications from mouse embryonic development. *Cell Biosci.* **2020**, *10*, 49. [CrossRef] [PubMed]
142. Chapman, J.R.; Sossick, A.J.; Boulton, S.J.; Jackson, S.P. BRCA1-associated exclusion of 53BP1 from DNA damage sites underlies temporal control of DNA repair. *J. Cell Sci.* **2012**, *125*, 3529–3534. [CrossRef]
143. Nakamura, K.; Saredi, G.; Becker, J.R.; Foster, B.M.; Nguyen, N.V.; Beyer, T.E.; Cesa, L.C.; Faull, P.A.; Lukauskas, S.; Frimurer, T.; et al. H4K20me0 recognition by BRCA1–BARD1 directs homologous recombination to sister chromatids. *Nat. Cell Biol.* **2019**, *21*, 311–318. [CrossRef]
144. Michelena, J.; Pellegrino, S.; Spegg, V.; Altmeyer, M. Replicated chromatin curtails 53BP1 recruitment in BRCA1-proficient and BRCA1-deficient cells. *Life Sci. Alliance* **2021**, *4*, e202101023. [CrossRef]
145. Paiano, J.; Zolnerowich, N.; Wu, W.; Pavani, R.; Wang, C.; Li, H.; Zheng, L.; Shen, B.; Sleckman, B.P.; Chen, B.R.; et al. Role of 53BP1 in end protection and DNA synthesis at DNA breaks. *Genes Dev.* **2021**, *35*, 1356–1367. [CrossRef] [PubMed]
146. Shibata, A.; Jeggo, P.A. Roles for 53BP1 in the repair of radiation-induced DNA double strand breaks. *DNA Repair* **2020**, *93*, 102915. [CrossRef] [PubMed]
147. Lyu, X.; Lei, K.-H.; Biak Sang, P.; Shiva, O.; Chastain, M.; Chi, P.; Chai, W. Human CST complex protects stalled replication forks by directly blocking MRE11 degradation of nascent-strand DNA. *EMBO J.* **2021**, *40*, e103654. [CrossRef] [PubMed]
148. Altieri, A.; Dell'Aquila, M.; Pentimalli, F.; Giordano, A.; Luigi, A. SMART (Single Molecule Analysis of Resection Tracks) Technique for Assessing DNA end-Resection in Response to DNA Damage. *Bio Protoc.* **2020**, *10*, e3701. [CrossRef] [PubMed]

Disclaimer/Publisher's Note: The statements, opinions and data contained in all publications are solely those of the individual author(s) and contributor(s) and not of MDPI and/or the editor(s). MDPI and/or the editor(s) disclaim responsibility for any injury to people or property resulting from any ideas, methods, instructions or products referred to in the content.

3.4 The Current Status of FLASH Particle Therapy: A Systematic Review

3.4.1 Summary

At the time of writing this thesis, construction of the Australian Bragg Centre for Proton Therapy has currently been completed and is awaiting installation of a clinical proton beamline, with an emphasis on treating paediatrics with solid tumours. It is the very first proton therapy centre in Australia, with construction of another proton therapy unit at the Queensland Cancer Centre also announced at the end of 2023. Although proton therapy is now becoming highly relevant in Australia currently, the progress of preclinical research utilising protons within Australia does not reflect this. This was a contributing factor towards shaping the research aims of this PhD project, particularly in beginning proton therapy research in Australia and validating experimental treatment modalities. Prior to commencement of FLASH experiments, a review of all proton- and carbon-FLASH therapy literature was performed to gain insights into the current state of research. Specifically, it provides a comprehensive summary using a systematic methodology to identify key literature. This method is reproducible to allow for identification of any new publications in this field when this process is repeated. It details the shortcomings of FLASH experiments thus far, including the lack of stringent dosimetry and use of the Bragg peak for *in vivo* tumour models. It also consolidated publications based on mechanisms of the normal tissue sparing phenomenon known as the FLASH effect. Of these mechanisms, literature concerning the complexity of DNA damage was of interest continuing from the *Nature* Comment and narrative reviews about DSB detectors.

Physical and Engineering Sciences in Medicine (2023) 46:529–560
https://doi.org/10.1007/s13246-023-01266-z

SYSTEMATIC REVIEW

The current status of FLASH particle therapy: a systematic review

Jake Atkinson[1] · Eva Bezak[2,3] · Hien Le[4] · Ivan Kempson[1]

Received: 30 December 2022 / Accepted: 20 April 2023 / Published online: 9 May 2023
© The Author(s) 2023

Abstract

Particle therapies are becoming increasingly available clinically due to their beneficial energy deposition profile, sparing healthy tissues. This may be further promoted with ultra-high dose rates, termed FLASH. This review comprehensively summarises current knowledge based on studies relevant to proton- and carbon-FLASH therapy. As electron-FLASH literature presents important radiobiological findings that form the basis of proton and carbon-based FLASH studies, a summary of key electron-FLASH papers is also included. Preclinical data suggest three key mechanisms by which proton and carbon-FLASH are able to reduce normal tissue toxicities compared to conventional dose rates, with equipotent, or enhanced, tumour kill efficacy. However, a degree of caution is needed in clinically translating these findings as: most studies use transmission and do not conform the Bragg peak to tumour volume; mechanistic understanding is still in its infancy; stringent verification of dosimetry is rarely provided; biological assays are prone to limitations which need greater acknowledgement.

Keywords FLASH radiotherapy · Ultra-high dose rate · Proton therapy · Carbon therapy · Normal tissue sparing · Biological mechanisms · Cancer treatment

Introduction

It is recommended that X-ray radiation therapy (RT) be included in the treatment of 50% of all cancer patients in developed countries worldwide, making it one of the most common modes of treatment available currently [1]. Accounting for only 5% of total cancer therapy costs, as well as being a non-invasive technique, it is appealing in both its low economic burden and practicality [2]. Although there are significant advantages to utilising conventional X-ray RT, this modality has the potential to cause detrimental off-target effects, inherent in the physics involved. Due to exponential absorbed dose by an X-ray beam, normal tissues are exposed to radiation prior to entering, and upon exiting, a tumour site. This may produce severe, negative side effects in patients if highly sensitive tissues lie within the radiation track [3]. For instance, the potential tissue complications that can result from lung irradiation include early onset pneumonitis, late onset fibrosis (occurring in 5–20% of patients), and risks of heart or spine irradiation depending upon tumour location [4]. The risks that RT complications present are amplified in paediatric patients. Brain irradiation presents risk of cognitive decline and growth hormone deficiencies in paediatric patients compared to their healthy peers [5, 6]. Second malignancy induction is also a prominent issue in the paediatric and young adult population due to their longer survivorship period [7]. Therefore, limiting the degree of normal tissue damage, and consequent accumulation of toxicity, is pivotal in preventing late effects from occurring. Despite success of RT to date, there is still demand for new and innovative treatment modalities to mitigate radiation damage to peripheral normal tissues, with advances being essential for improving both the rate of cancer survival and the quality of life of patients after treatment. Identifying irradiation techniques which broaden the therapeutic window by minimising normal tissue damage

✉ Ivan Kempson
Ivan.Kempson@unisa.edu.au

1 Future Industries Institute, University of South Australia, Mawson Lakes, South Australia 5095, Australia

2 Cancer Research Institute, University of South Australia, Adelaide, South Australia 5000, Australia

3 Department of Physics, University of Adelaide, North Terrace, Adelaide, South Australia 5000, Australia

4 Department of Radiation Oncology, Royal Adelaide Hospital, Adelaide 5000, Australia

will allow for a lower incidence of negative side effects in patients, and even allow for greater radiation doses to be delivered to improve the probability of tumour control [8].

Particle therapy is one such modality that is continually being developed and currently being employed clinically for this reason. It employs the use of high Linear Energy Transfer (LET) particles to irradiate treatment volumes with minimal exit dosage compared to X-ray photons (low LET), reducing irradiation of surrounding healthy tissues. X-rays deliver their maximum dose at the point of electronic equilibrium and then attenuate exponentially as they pass through the remaining tissue, prior to and upon exiting the tumour. Conversely high LET particles, including protons or carbon ions, have low energy deposition upon entry and maximum deposition at the Bragg Peak towards the end of their track. Particle therapy centres are now employing intensity modulated and pencil beam scanning techniques, which target tumours in layers of irradiation spots at differing doses, depths, and positions [9]. The benefits of such treatment include better dose conformation, minimisation of damage to healthy tissues and an increased total dose that can be administered [10]. Use of high LET particles, particularly carbon ions, allows for efficient treatment of radioresistant tumours localised within critical organs where X-ray or proton beam therapies would be ineffective.

The resurgence of studies involving irradiation of tissue at ultra-high dose rates, also known as FLASH radiation therapy (FLASH-RT), alongside development of proton and carbon ion therapies, are steps towards further improving the therapeutic efficacy of RT. FLASH-RT typically delivers absorbed dose rates greater than 40 Gy/s to irradiate tumours in very small timeframes (< 1 s), as opposed to conventional dose rates (CONV, < 0.1 Gy/s) which are normally fractionated and delivered over the course of minutes [11]. There is some evidence that the utilisation of FLASH technique, even with photon or electron beams, results in a radioprotective effect in normal tissues, which reduces toxicity compared to CONV. Multiple mechanisms have been hypothesised to explain this phenomenon, including rapid intracellular oxygen depletion preventing indirect DNA damage via reactive oxygen species (ROS) [12], alterations to the nature of DNA damage and DNA repair pathways, and immune response modulation [13]. However, the radiobiological processes by which these mechanisms occur during FLASH-RT are not well understood. All these factors are thought to contribute towards the unique normal tissue sparing effect of FLASH-RT, which has been previously demonstrated in vivo for photons, electrons, and heavy ions.

Incorporating the differential tissue response of the FLASH concept with the normal tissue sparing of particle therapy may prove to be beneficial when utilised in combination. Taking advantage of proton or carbon ion beam's characteristics - particularly their minimal exit dose - alongside the normal tissue sparing properties afforded by FLASH, there is the potential to synergistically minimise healthy tissue toxicities. Although there are multiple studies outlining the biological outcomes of the FLASH effect with electrons and X-ray photons [14–16], few studies have explored the implications of using proton or carbon ions at ultra-high dose rates in vitro and in vivo. This systematic review summarises available literature detailing FLASH-RT's discovery, its implementation in electron, proton and carbon ion-based studies, as well as discussion of conflicting data concerning the various hypotheses that form the basis of these studies. Overviews of theoretical, in vitro, and in vivo particle beam studies relevant to ultra-high dose rates, and their effect upon normal and cancer cell biology, are the primary focus with the aim of understanding current state of knowledge on mechanistic benefits that could further improve particle therapy outcomes in the future. From literature captured by the systematic search strategy, this review provides: a brief history of electron FLASH experiments; its recent resurgence in the literature in terms of in vitro, in vivo, and even clinical application; and the current state of research into FLASH delivery of protons and carbon ions.

Methodology

Systematic review process

To produce an accurate overview of the biological mechanisms of the FLASH effect, a systematic review of all literature pertaining specifically to particle-FLASH (excluding electrons) has been compiled. Since electron-FLASH publications were amongst the most prevalent throughout initial FLASH searches, the key electron-FLASH studies were included in a non-systematic manner in this manuscript to provide background and context to the particle-FLASH studies identified throughout the systematic process. The progression of the electron-FLASH field has been essential in providing preliminary data that will aid in translation into the particle-FLASH field.

The inclusion criteria for literature within review include:

- Scientific articles. Conference abstracts and reviews were excluded.
- Findings only pertaining to the radiobiological effect of ultra-high dose irradiation on normal and cancerous cellular function and response. Technical developments pertaining to proton and carbon-ion delivery were excluded.
- *In silico*, in vitro, in vivo, and clinical studies.

- Studies utilising ultra-high dose rates, defined as an average dose rate of greater or equal to 40 Gy/s.
- Articles published between the years 2009–2022.
- Language restricted to English (translations also accepted).

In completing this process systematically, multiple search criteria were utilised with increasing degrees of complexity (additional search terms, higher search specificity). Table 1 below outlines the set of search criteria used to identify proton and carbon-FLASH literature performed on the 8th December, 2022.

Studies from search #4 of Table 1 were added to the studies found in the initial literature searches. In addition to utilising Scopus and Medline to compile resources, other articles were found via selecting relevant citations from systematically identified literature (pearling). Finally, additional sources were identified via grey literature searching with Google Scholar. This resulted in the culmination of 110 publications, which were then screened by IK to validate their relevance, followed by EB to resolve any disagreement in relevance between IK and JA. The final number of systematically identified proton and carbon therapy papers was 34. A diagrammatic summary of the PRISMA search strategy utilised for this systematic review is displayed in Fig. 1. PRISMA guidelines were followed in the literature identification and exclusion process [17]. Relevant electron-FLASH papers identified in a non-systematic manner were summarised in table format (Table 2), with systematically identified particle-FLASH literature being summarised in the same manner (Table 3), listing year of publication, particle type, irradiation source and mode, model (e.g., *in vitro, in vivo)*, particle energy (MeV), doses (Gy), delivery time, pulse/burst count and rate, FLASH average and instantaneous dose rate per fraction (Gy/s), comparative low or CONV dose rate, (Gy/s) and key experimental conclusions. Throughout the text, average dose rates are discussed unless specified.

History of FLASH radiotherapy

Although the first publications that cite the use of radiation at ultra-high dose rates did not initially quote the term 'FLASH' irradiation, coined by Favaudon et al. in 2014 [18], interest in the field was motivated earlier by exploring the relationship between radiation dose rate and biological response. In 1958, Kirby-Smith and Dolphin published one of the first papers that suggests a dose rate dependent effect on DNA lesion formation, showing that in a *Tradescantia* (spiderwort plant) model, the total number of chromosome aberrations was reduced when electrons were administered at higher dose rates of up to 4×10^6 Gy/s [19]. The effect of cellular oxygenation on cellular radiosensitivity was also topical, and in 1959 Dewey and Boag presented a radiobiological relationship between dose rate, cellular oxygenation, and cellular survival. They aimed to observe the effect of dose rate on the surviving fraction of *Serratia marcescens* bacteria, whilst modifying both total irradiation dose and the concentration of dissolved oxygen. Bacteria were irradiated in the presence of both CONV X-rays (0.1 Gy/s) and ultra-high dose rate electrons (5×10^7 – 10×10^8 Gy/s) with total absorbed doses ranging between 0 and 200 Gy, and also varying oxygen concentrations (100% O_2, 1% O_2 in N_2 and 100% N_2). The proportion of surviving bacteria was higher at the ultra-high dose rate irradiation, which was comparable to the radioprotection afforded under anaerobic conditions at the conventional dose rate [20]. This was theorised to be a result of the initial absorbed dose of radiation 'consuming' the oxygen dissolved within the irradiated bacterium, thus preventing the production of harmful reactive oxygen species that would usually result in cytotoxic DNA damage and apoptosis. Also lending to the theory, the authors suggested that the irradiation timeframe was so minute, that even if dissolved oxygen was not completely removed from the extracellular environment, it would not be able to re-enter the cell rapidly enough for the radiation pulse to dissociate it. This theory, termed the 'oxygen effect', would consequently form part of the hypothesis behind the healthy tissue sparing effects of FLASH irradiation. Similar publications around this time held interest in the relationship

Table 1 Search strategy for proton- and carbon-FLASH articles, utilising an expanded set of FLASH, proton, and carbon therapy search terms. A total of 62 experimental studies were yielded from Scopus and Medline searches after duplicates were removed

Search #	Search Terms	Scopus	Medline
1	"FLASH-RT" OR "FLASH radiation therapy" OR "FLASH radiotherapy*" OR "FLASH effect*" OR "FLASH irradiation" OR "Ultra-high dose rate*"	662	396
2	"Proton therapy" OR "Proton beam therapy" OR "Proton radiation therapy" OR "Proton radiotherapy" OR "Proton beam irradiation"	12,562	8,447
3	"Heavy ion radiotherapy" OR "Heavy ion radiation therapy" OR "Carbon ion therapy" OR "Carbon ion irradiation" OR "Carbon ion radiotherapy" OR "Carbon ion radiation therapy" OR "Carbon beam therapy"	2,468	2,090
4	FLASH **AND** (Proton therapy **OR** Heavy ion/Carbon therapy) (#1 AND (#2 OR #3))	78	37

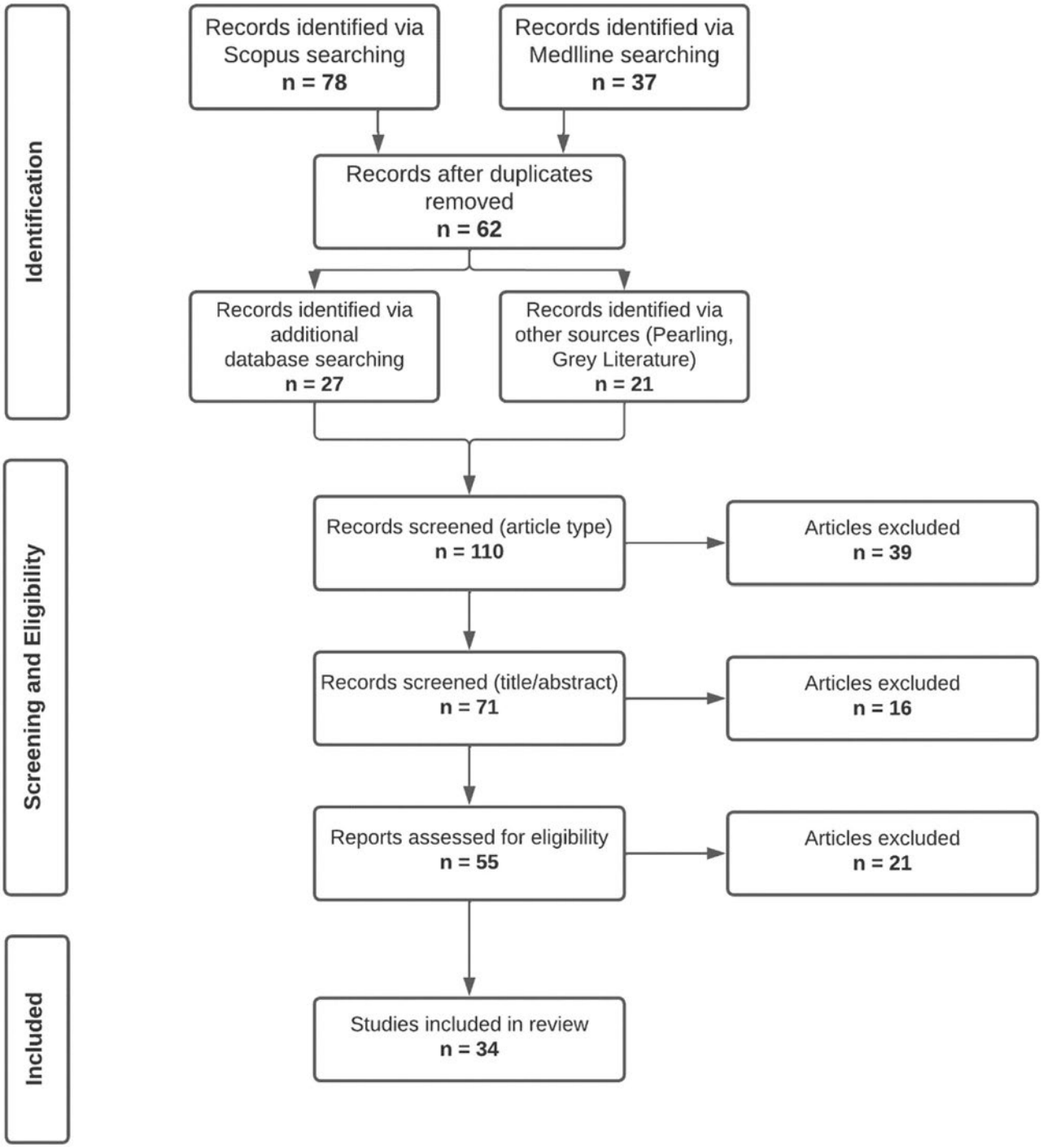


Fig. 1 PRISMA flowchart summary of the search strategy employed in this systematic review. Search terms were filtered through either Scopus or Medline databases and then excluded based upon their relevance to the radiobiological effect of FLASH and ultra-high dose rates. Additional terms were then added from keywords or terminology discovered whilst reading through relevant literature and searches repeated in both databases. Sources were then reviewed by co-authors of this review and categorised. 34 proton- and carbon-FLASH studies are incorporated into the final review

between dose rate and ROS concentration [21], and if there were analogous FLASH effects in *E. coli* [22].

Further work looking into the dose rate effect in the survival of mammalian cells was conducted by C.D. Town in 1967. Using 3.5×10^7 Gy/s electrons, experiments were conducted comparing HeLa cell survival as a function of radiation dose, between single and double pulses of radiation. When cells were exposed to doses higher than 10 Gy, there was an apparent sparing of tissues; cells treated with doses administered in a single burst of radiation had a higher survival fraction compared to irradiation over two pulses. To validate whether this tissue sparing was related to the oxygen effect, an additional test, wherein cell suspensions were exposed to either nitrogen or air, was performed. Single pulse irradiations under aerated conditions resulted in similar cell survival curves to that of irradiation under anaerobic conditions (at doses exceeding 10 Gy) [23]. These findings, similar to Dewey and Boag's *S. marcescens* experiments, supported that the 'oxygen effect' is not limited to bacterial cells; indeed, there was sufficient evidence alluding to its role in mammalian cell protection. In the present day, the definition of the 'FLASH effect' phenomenon has formed as the sparing effect ultra-high dose rates have upon healthy, but not cancerous, tissues in vivo, whereas this was not the primary aim of these initial studies. Nevertheless, they highlight the discovery of dose-rate dependent radiobiological responses, and paved the way for FLASH's re-emergence as a potential cutting-edge treatment modality decades later.

Electron FLASH

Resurgence of FLASH

Studies concerning ultra-high dose rate irradiation faded into obscurity for some 30 years until its sudden resurgence in the 2010s. Although in previous publications in vitro experiments predominated, more recent work aimed to identify how ultra-high dose rates benefited normal tissues *in vivo.* Radiation-induced pulmonary fibrosis is a side effect [24] with the potential for treatment-related death following external beam irradiation [25]. As such, multiple in vivo studies have been performed to determine whether utilising ultra-high dose rates may elicit a greater differential response between normal and tumour tissue damage compared to current clinical dose rates. A summary of the experimental results of these electron-FLASH papers is presented in Table 2 below.

In vivo studies of tumour treatment

Favaudon et al. (2014) demonstrated a sparing effect in mice after bilateral thorax exposure to single pulse, FLASH dose rate electrons (60 Gy/s, 4.5 MeV). Mice exposed to a total dose of 17 Gy at 0.03 Gy/s, representative of a conventional clinical dose rate, exhibited fibrogenesis initiation at 8 weeks post-irradiation, and progressing to intraparenchymal fibrosis at 34 weeks. Conversely, exposure to 60 Gy/s electron-FLASH (same total dose) did not develop pulmonary fibrosis after treatment. Activation of the Transforming Growth Factor Beta (TGFβ) cascade, a characteristic pathway in fibrosis pathogenesis, was also prevented. In subsequent dose escalation experiments, 30 Gy absorbed electron dose was the minimum required dose to induce fibrosis at FLASH dose rates. The relative biological effectiveness of both dose rates was comparable; growth of HBCx-12 A and HEp2 tumour xenografts was inhibited irrespective of FLASH or CONV dose rates, although FLASH irradiated mice exhibited a skin sparing effect [18].

Zebrafish studies

Montay Gruel et al. (2019) displayed a FLASH sparing effect in zebrafish embryos [36]. In this study, alterations to the length of FLASH irradiated zebrafish embryos was significantly less than CONV irradiated embryos 5 days postfertilization, where irradiations occurred at 4 h postfertilization. When zebrafish were preincubated with an antioxidant, FLASH exhibited no further sparing effect, whilst the embryos were spared from CONV induced radiation damage [36]. Another zebrafish embryo model was used by Pawelke et al. (2021) to validate whether the pulse dose rate and oxygen levels used during irradiations masked a potential FLASH effect. 26 Gy of 20 MeV electrons at a continuous, conventional dose rate of 0.1116 Gy/s were compared to FLASH with a mean dose rate of 1×10^5 Gy/s, and zebrafish embryos were irradiated within vessels at differing pO_2 levels. A sparing effect was observed in this study at pO_2 levels below atmospheric oxygen levels (< 148 mmHg) with a greater degree of protection afforded at < 5 mmHg (hypoxic conditions). Whilst FLASH-RT appeared to have a mild protective effect over CONV-RT at both pO_2 levels, at high pO_2 levels, FLASH and CONV-RT zebrafish morphologies exhibited minimal differences, whereas the effect was more substantial at low pO_2 [48]. This included preventing the reduction of embryo length and eye diameter by 4%, as well as a 20% reduced rate of PE and SC in comparison to low dose rate, quasi-continuous irradiation.

Table 2 Summary table of key electron-FLASH literature identified non-systematically. For FLASH irradiations, delivery time, pulse count and rate, average dose rate per fraction, instantaneous dose rate (within one pulse), and comparative CONV dose rate are provided. Data listed in bold have been calculated from information provided in the text

Ref.	Year	Model	Energy (MeV)	Dose (Gy)	Delivery Time (s)	Pulse Count	Pulse Rate (Hz)	FLASH Average Dose Rate (Gy/s)	FLASH Instantaneous Dose Rate (Gy/s)	Low or CONV Dose Rate (Gy/s)	Outcome
[26]	1971	Random bred TO strain mice	7	**8–40**	NM*	NM*	400	**16–83**	$\mathbf{>2\times10^{4}}$	**1, 2.5**	The LD_{50} of mice 4–5 days post irradiation was increased for whole body irradiation at dose rates of 16–83 Gy/s compared to 1 Gy/s when breathing oxygen. N_2 breathing mice had comparable LD_{50} to the oxygen breathing mice at high dose rates, with the prediction that a reduction in oxygen tension was responsible.
[27]	1974	Rat, hind leg	7	**20–80**	< 0.5	NM*	NM*	**66.7–83.3**	NM*	**0.03**	Decreased level of skin damage with increasing dose rate under aerobic conditions. Break away response at 20 Gy, where skin irradiation of hindlegs was comparable to anoxic conditions (reduced radiosensitivity). Suggests oxygen depletion is responsible for radioprotection at high dose rates.
[28]	1977	Human lymphocytes, blood taken from adult male donor	15	**0.44–7.64**	1×10^{-6}	1	Single - Pulse	$\mathbf{5.3\times10^{5}}$–$\mathbf{7.64\times10^{6}}$	$\mathbf{5.3\times10^{5}}$–$\mathbf{7.64\times10^{6}}$	**1**	Absence of dose-dependent effect on chromosomal aberration yield for 0.44–7.64 Gy doses in vitro. Dose-response relationship using electrons is comparable to previous X-ray and gamma-ray irradiation studies.
[18]	2014	C57BL/6J mice, bilateral thorax irradiation, HBCx-12a, HEp-2 tumour xenografts, TC-1 Luc^{+} orthotopic lung carcinoma	4.5	7.5, 17, 30	> 0.1	4–6	100–500	60	1×10^{6}	0.03	No complications were observed in mice after thoracic irradiation at FLASH dose rates below 23 Gy. Pulmonary fibrosis, TGFβ cascade induced in CONV irradiation at 17 Gy, 30 Gy FLASH required to induce same effects. FLASH also prevented acute apoptosis in bronchial epithelia, smooth muscle, and vasculature. The tumour killing efficacy of FLASH was comparable to CONV irradiations at equivalent doses.
[29]	2015	Human squamous cell carcinoma: FaDu and SKX.	20	1–10	$\leq1\times10^{-3}$	**~13,000**	1.3×10^{7}	$\mathbf{9\times10^{4}}$	$\mathbf{1.67\times10^{8}}$	**0.006, 0.067**	No appreciable difference between different ELBE** beam pulse regimes and resulting mean dose rates, including clonogenic survival response and the number of residual γH2AX or 53BP1 foci present 24 h post irradiation.
[30]	2016	Normal tissue mammary gland breast epithelium 184A1, normal neonatal foreskin-derived dermal fibroblasts HDF	20	4, 8	$\leq1\times10^{-3}$	**~13,000**	1.3×10^{7}	$\mathbf{9\times10^{4}}$	$\mathbf{1.67\times10^{8}}$	**0.006, 0.067**	No radiobiological difference in clonogenic survival or DNA DSB*** between cells irradiated at CONV or FLASH dose rates for 184A1 and HDF cell lines. Additionally, there appeared to be no discernible difference in γH2AX or 53BP1 foci formation between either dose rate used 24 h post irradiation.

Table 2 (continued)

Ref.	Year	Model	Energy (MeV)	Dose (Gy)	Delivery Time (s)	Pulse Count	Pulse Rate (Hz)	FLASH Average Dose Rate (Gy/s)	FLASH Instantaneous Dose Rate (Gy/s)	Low or CONV Dose Rate (Gy/s)	Outcome
[31]	2017	C57BL/6J mice, whole brain irradiation	6	10	1.8×10^{-6} – 0.3	1–10	100	60–5.6×10^{6}	1.9×10^{5} – 5.6×10^{6}	0.1–30	FLASH whole brain irradiations appeared to spare hippocampal neurogenesis, evidenced by increased BrdU positive neural clusters in 10 Gy FLASH irradiated mice compared to CONV. No substantial difference in Recognition Ratio between FLASH (75.9 ± 4.0%) and non-irradiated (78.3 ± 2.6%) mice (CONV = 53.0 ± 1.7%). Loss of a neuroprotective effect was observed at dose rates < 30 Gy, however a memory preserving effect was regained at dose rates > 100 Gy/s.
[32]	2017	C57BL/6 mice, total abdominal irradiation	20	10–22	NM*	NM*	NM*	70, 210	NM*	0.05	Mice exposed to 13–19 Gy whole abdomen radiation exposure exhibited a survival rate of 29% in the CONV group, and 90% survival for those administered FLASH 20 days post-irradiation. The LD_{50} were 14.7 Gy for CONV irradiation and 17.5 Gy for FLASH.
[33]	2019	Pig model, skin irradiations, cat patients, T2/T3N0M0 squamous cell carcinoma (nasal)	4.5, 6	25–41	0.09–0.1	9–10	100	> 277	**0.5×10^{6}–1.8×10^{6}**	**0.083**	Mini Pigs: FLASH irradiations of pig skin had greatly reduced tissue toxicities compared to CONV, including preservation of hair follicles and $CD34^{+}$ cells, and the prevention of erythema, moist desquamation and fibronecrosis. Cats: FLASH patients exhibited permanent depilation, mild mucositis/dermatitis, and no late toxicities. Progression-free survival 16 months post-treatment was 84% versus 50–60% 12 months post treatment at CONV dose rates.
[34]	2019	75-year-old human male, CD30 + T-cell cutaneous lymphoma	5.6	15	0.09	10	100	**158**	**1.5×10^{6}**	NM*	Epidermal thickness and basal membrane unaltered. Grade 1 epithelitis and transient grade 1 oedema observed 3 weeks post irradiation. Complete and rapid tumour response.
[35]	2019	C57BL/6 mice, BALB/c mice, murine pancreatic cancer cell lines KPC and Panc02, human peripheral blood mononuclear cells (PBMCs)	20	0–16	NM*	NM*	180	32.6, 38.8	NM*	0.1	FLASH induces higher rates of clonogenic cell death and apoptosis in pancreatic cancer cell lines. Comparable lymphocyte killing capacity to CONV. FLASH did not preserve immune cells irradiated via either cardiac or splenic tissues, induced higher degree of gastrointestinal toxicity than CONV in vivo.

Table 2 (continued)

Ref.	Year	Model	Energy (MeV)	Dose (Gy)	Delivery Time (s)	Pulse Count	Pulse Rate (Hz)	FLASH Average Dose Rate (Gy/s)	FLASH Instantaneous Dose Rate (Gy/s)	Low or CONV Dose Rate (Gy/s)	Outcome
[36]	2019	C57BL/6J mice, whole brain irradiation,	6	10, 12, 14	1.8×10^{-6}	1	100	**5.6×10^{6}–7.8×10^{6}**	**5.6×10^{6}–7.8×10^{6}**	**0.09–0.16**	Neurocognitive dysfunction was not induced in FLASH irradiated mice, evidenced by novel object recognition, object in place, temporal order, elevated plus maze, light-dark box and fear memory tests being comparable to non-irradiated controls. Increasing pO_2 levels in the brain with carbogen breathing resulted in a loss of neurocognitive sparing during FLASH. FLASH also had lower levels of gliosis markers compared to CONV. FLASH irradiated zebrafish embryos exhibited a lower degree of morphological changes versus CONV.
		Zebrafish embryos		8	1.49×10^{-6}	1	200	**5.4×10^{6}**	**5.4×10^{6}**	**0.06**	
[37]	2019	C57BL6/J mice, whole brain irradiation	16, 20	30	0.1–0.16	18	106, 180	200, 300	8.75×10^{5}	0.13	Neurocognitive deficits were not observed in mice 10-weeks post irradiation. FLASH mice exhibited preservation of hippocampal dendritic spines, reduced microglial inflammation and reduced expression of inflammation mediator cytokines. Novel object recognition and object location were not impaired in FLASH mice.
[38]	2020	C57BL/6J mice, whole brain irradiation	6	8	1.8×10^{6}	1	100	4.4×10^{6}	4.4×10^{6}	0.1	FLASH and low dose rate mice lacked memory recall 2 months-post treatment. At 4-months, FLASH mice regained memory recall/update ability. FLASH irradiation also preserved novel object recognition and social interaction capabilities similar to control mice.
[39]	2020	C57BL/6J mice, whole brain irradiation	6	10	1.8×10^{-6}	1	100	5.6×10^{6}	5.6×10^{6}	0.1	In FLASH irradiated mice, the expression of astrogliosis factors was reduced compared to CONV irradiation, including toll-like receptor 4 (TLR4) and glial fibrillary acidic protein (GFAP). However, expression of complements C1q and C3 were elevated under both FLASH and CONV conditions.
[40]	2020	Prostate cancer cell line DU145	10	0–25	**0.005–0.03**	**1–6**	200	600	NM*	**0.23**	Negligible difference between FLASH and CONV under normoxic conditions, however a higher proportion of cells survived under hypoxic conditions. Under different relative partial O_2 pressures, FLASH had higher surviving fractions of cells for 1.6%, 2.7% and 4.4% pO_2.
[41]	2020	C57BL/6J mice, whole brain irradiation	6	10, 25	0.01, 1.8×10^{-6}	1, 2	100	2.5×10^{3}, 5.6×10^{6}	5.6×10^{6}, 6.9×10^{6}	0.09	FLASH reduced apoptosis in neurogenic brain regions 1-day post irradiation. Vascular dilation and downregulation of tight junction proteins occurred 1–4 weeks after CONV treatment but was minimal in FLASH mice, thereby preserving vasculature integrity in the brain.
[11]	2020	C57BL/6 mice, skin irradiation	16	10, 40	**0.056–0.22**	**5–20**	90	180	4.0×10^{5}	0.075	FLASH irradiations of mice skin resulted in a lower incidence of ulceration in combination with reduced skin toxicities compared to CONV. 30 and 40 Gy hemithoracic irradiations also resulted in reduced mortality in FLASH irradiated mice (median survival > 180 days, both doses) versus CONV (median survival = 100 days at 30 Gy, 52 days at 40 Gy).

Table 2 (continued)

Ref.	Year	Model	Energy (MeV)	Dose (Gy)	Delivery Time (s)	Pulse Count	Pulse Rate (Hz)	FLASH Average Dose Rate (Gy/s)	FLASH Instantaneous Dose Rate (Gy/s)	Low or CONV Dose Rate (Gy/s)	Outcome
[42]	2020	Monte-Carlo simulation, EGSnrc, paediatric whole brain irradiation simulation	40	3	NM*	NM*	1000	115	NM*	NM*	In the treatment of paediatric brain tumours, there is theoretically less homogeneity in dose distribution of 40 MeV FLASH dose rate electrons compared to 6 MeV CONV photons due to electron scattering.
[43]	2020	C57BL/6 mice, total abdominal irradiation, ID8 ovarian cancer cells	16	12, 14, 16	**0.056–0.074**	**6, 7, 8**	108	216	NM*	0.079	Sparing of lethal intestinal injury and preservation of intestinal function was observed in normal and tumour-bearing mice. FLASH tumour killing effectiveness matched CONV in the treatment of ID8 ovarian cancer.
[44]	2020	C57BL/6J wild type and $Terc^{-/-}$ mice, bilateral thorax irradiation, human lung fibroblast MRC5 and IMR-90 cells, human lung epithelial carcinoma A-549, pulmonary bronchial epithelial cells	4.5	2, 4, 5.2, 17	0.033–0.11	5–11	100–150	135–600	8×10^5 – 3.2×10^6	0.03	30 min post irradiation, significantly fewer 53BP1 foci in fibroblast cell lines, whereas γH2AX showed minimal variation compared to CONV dose rate. FLASH irradiated lung tissue exhibits fewer 53BP1 foci compared to CONV, and partially prevents the onset of fibrosis. Half the number SA-β-gal^+ senescent clusters were produced under FLASH compared to CONV at 4 months post treatment.
[45]	2021	Human T-ALL M106 cell xenografts, hematopoietic stem cell progenitor cells, $CD34^+$ cells, BRγc-/- mice	6	4	0.02	3	100	200	7.4×10^5	0.072	Total body irradiation at FLASH dose rates controlled the propagation of T-ALL cases with similar genetic abnormalities. FLASH preserved hematopoietic stem cell progenitor and $CD34^+$functionality.

Table 2 (continued)

Ref.	Year	Model	Energy (MeV)	Dose (Gy)	Delivery Time (s)	Pulse Count	Pulse Rate (Hz)	FLASH Average Dose Rate (Gy/s)	FLASH Instantaneous Dose Rate (Gy/s)	Low or CONV Dose Rate (Gy/s)	Outcome
[46]	2021	Bovine serum albumin solutions (5%), nude mice, MDA-MB-231 tumour model	10	20	**0.074–0.22**	**15–17**	120, 240, 360	50–300	2.14×10^5, 2.38×10^5	0.1	In vitro model: greater decrease in oxygen concentration observed in response to CONV vs. FLASH. High level O_2: CONV = 3.8 mm Hg decrease in pO_2, FLASH = 3.1 mm Hg decrease in pO_2. Low level O_2: CONV = 4.2 mm Hg decrease, FLASH = 3.4 mm Hg FLASH decrease. In vivo model: FLASH depleted oxygen to a higher degree in normal tissues than tumour tissues, maintained at dose rates of 90, 180, 270 Gy/s and no statistically significant difference in O_2 depleted between dose rates.
[47]	2021	$NU_{(Ico)}$-$Foxn1^{nu}$ female nude mice, brain irradiation, H454 orthotopic murine GBM model, U87 orthotopic murine GBM model	6	10, 14, 4×3.5, 2×7, 25, 3×10	1.8×10^6, 0.01	1, 2	100	1.9×10^6 – 7.8×10^6	1.9×10^6 – 7.8×10^6	0.1	Antitumour efficacy of irradiations was not affected by use of hypofractionated regimens; FLASH and CONV irradiations were equipotent in the delay of GBM tumour growth in mice. The discrimination index of mice exposed to FLASH irradiations in the 10 Gy, 2×7 Gy, and 3×10 Gy groups showed no significant difference to unirradiated controls.

* NM = Not mentioned, ** ELBE = electron linac for beams with high brilliance and low emittance, *** DSB = double-strand breaks **** GBM = glioblastoma.

Mice brain studies

With the prospect of FLASH minimising healthy tissue damage, its effectiveness in the treatment of brain tumours is of extreme relevance clinically, particularly in paediatrics. In this respect, in vivo whole brain irradiation electron-FLASH studies are prevalent. Alaghband et al. (2020) displayed an apparent radioprotective effect in brain tissue of mice following FLASH irradiation. After exposure to 8 Gy, 6 MeV electron irradiation at 4.4×10^6 Gy/s (FLASH), neurocognitive test results were indistinguishable from the control group, whereas conventional irradiation at 0.077 Gy/s with 6 MeV electrons caused substantial cognitive detriment. The benefit of FLASH, when utilised in the brain, was reduced neurocognitive impairment, attributed to the preservation of neurogenetic niche and neurogenesis. Mice irradiated at conventional dose rates observed a lower proportion of mature and immature neurons 4 months after irradiation. Additionally, a two-fold reduction in plasma growth hormone expression was also observed a week post treatment in comparison to controls, suggesting conventional irradiation also impairs pituitary gland function. These side effects were not observed in FLASH-irradiated mice [38]. Other whole brain irradiation studies displayed similar findings at and exceeding 100 Gy/s [32], including but not limited to: 200 Gy/s, 300 Gy/s [37], 2.5×10^3 and 5.6×10^6 Gy/s [39, 41].

Higher order animal models

Demonstration of the electron FLASH effect is not limited to in vivo mice experiments, with implications in both mini-pig test animals and cat patients. Mini-pig irradiation at 300 Gy/s compared to 0.083 Gy/s markedly reduced damage to skin tissues, avoiding signs of acute toxicity including inflammation, ulcer formation and hair follicle destruction [33]. Additionally, late skin fibronecrosis was limited to CONV irradiated pigs, with FLASH experiencing no tissue complications at 36 weeks after 28–34 Gy irradiations. Six cat patients diagnosed with squamous cell carcinoma of the nasal planum were also FLASH treated, resulting in a progression free survival (PFS) of 84% at 16 months [33]. Side effects were limited to acute mucositis in half of the patients, and depilation across all cat patients. Although the sample size of this study is limited, it is some of the first evidence displaying no notable toxicity of FLASH in higher mammal models. One key limitation is that there are no experimental groups within this study irradiated at conventional dose rates; only retrospective data are referred to in drawing conclusions in this aspect. PFS ranged from 50 to 80% within other conventional dose rate trials [49]. This is promising in its potential applications in human patients, with regards to increasing total dosages (thereby improving tumour control) whilst also mitigating side effects.

Recently, a similar in vivo study by Kondradsson et al. (2021) attempted to identify potential adverse effects and treatment procedures required to administer electron-FLASH in canines with microscopic residual disease and spontaneous superficial solid tumours. Ten patients were prescribed doses ranging from 15 to 35 Gy, with average dose rates ranging between 400 and 500 Gy/s. 11 out of 13 irradiated tumours presented with either a complete response, partial response, or stable disease. Out of the 10 patients, only one experienced a grade 3 adverse skin event after a 35 Gy dose to the nasal planum, characterised by moist desquamation. Other adverse events appeared to be mild during follow up examinations 3–6 months post-treatment, including alopecia, dry desquamation, and erythema [50]. Akin to the feline-based study conducted by Vozenin et al., the key limitation to this preclinical trial was no comparative conventional dose rate group to compare adverse effects and disease response efficacy. It would be greatly beneficial for future in vivo work with canine and feline models to include conventional dose rate groups so that more accurate comparisons may be drawn. However, the feasibility in completing comparative experiments such as these may be difficult due to ethics considerations.

First-In-Human case study

The first-in-human case study of FLASH irradiation was reported in 2019 on a 75-year-old male with a multi-resistant cutaneous lymphoma, which had metastasised to multiple sites across his skin's surface [34]. The patient had experienced unfavourable side effects from the previous treatment of approximately 110 tumour sites with either MV/kV X-rays or low energy electrons. Regardless of the relatively low radiation doses and fractionation regimens employed (20 Gy in 10 fractions or 21 Gy in 6 fractions), skin continued to respond poorly, requiring up to 4 months to heal damage at irradiation sites 3–4 cm in diameter. FLASH was therefore administered due to its previous implications in the sparing of healthy tissues whilst maintaining tumour control efficacy comparable to that of conventional dose rates. In this trial study, 5.6 MeV electrons at a dose rate of 167 Gy/s and dose of 15 Gy was administered to one of the patient's most progressive ulcero-infiltrating tumours 3.5 cm in diameter. A 5 mm bolus was utilised, resulting in a 90% isodose coverage depth of 1.3 cm. Grade 1 epithelitis presented at 3 weeks post-FLASH, however 5 months after therapy almost all trace of negative skin reactions from treatment had receded (Figs. 2, [34]).

This study presents some valuable qualitative results depicting the temporal evolution of the treated area to



Fig. 2 Temporal evolution of the treated lesion: (a) before treatment; the limits of the PTV are delineated in black; (b) at 3 weeks, at the peak of skin reactions (grade 1 epithelitis NCI-CTCAE v 5.0); (c) at 5 months. Reprinted from Bourhis et al. 2019 [34], Copyright (2019), with permission from Elsevier

provide comparisons between healthy and irradiated tissue. The fact that this is the first clinical study using FLASH dose rates is also substantial. However, it is limited in that they exclusively analysed the short-term effect of FLASH on cancerous skin tissue alone; the effect that electron FLASH would have on other organs of different tissue depths and morphologies based on this data is unknown. Regardless, this result bodes well for further clinical translation, as limiting inflammation is still greatly beneficial for patients experiencing radiation induced skin complications. Further translation clearly requires additional indications to display the benefits of this treatment modality, (e.g., irradiation of brain, lung, or liver tumours) would represent more complicated anatomy where improvement in outcomes is needed. Additionally, there were no conventional dose rate irradiations conducted within this study to directly compare the FLASH treatment to; all irradiations were FLASH only [34].

Proton-FLASH

In vitro studies

Although proton-FLASH studies are not as widespread as those conducted with electrons or X-ray photons, many of these models also reinforce the relationship between ultra-high dose rates and normal tissue protection. It is of note that save for proof-of-concept dosimetry planning by Wei et al. [51] and 6 experimental studies [52][53–57], herein to our knowledge, that no other papers either explicitly state or utilise the high LET Bragg peak region for proton-FLASH irradiations.

Buonanno et al. (2019) presented one of the first studies to analyse the long-term radiobiological effects of FLASH proton irradiation in vitro, particularly in non-cancerous human cells. At three different instantaneous dose rates: 0.05 Gy/s, 100 Gy/s or 1000 Gy/s, IMR90 lung fibroblast cells were irradiated with 0–10 Gy of 4.5 MeV protons and a colony forming assay conducted. Altering dose rate did not appear to have a dramatic impact upon cell survival, with no significant difference between the fraction of surviving cells across all dose rates and total doses administered. This aligns with previous studies observing the effect of proton dose rate on cellular survival, with dose rates exceeding 10^9 Gy/s having no effect on colony formation compared to conventional dose rates for Human umbilical vein endothelial cells (HUVEC) [58], V-79 Chinese Hamster cells [59], or human-hamster hybrid cells (A_L) [60]. Interestingly, this effect carries over into cancer cell clonogenicity, with human derived cervical cancer cell line HeLa [61, 62] exhibiting no dose rate dependence upon cellular survival post irradiation.

In quantifying DNA damage, exposure to 20 Gy absorbed proton dose delivered at a FLASH instantaneous dose rate of 1000 Gy/s displayed a statistically significant reduction in γH2AX fluorescence 30-minutes post-irradiation compared to both 0.05 Gy/s and 100 Gy/s protons [63]. Although this finding initially appears promising, it is limited by the immunolabelling techniques used to acquire data. Specifically, the resolution at which microscopy was performed (40x) and an apparent plateau of γH2AX fluorescence for doses ≥ 10 Gy suggests that accurate distinction of foci could not be obtained due to saturation above this threshold. At a dose of 20 Gy, approximately 700 double-strand breaks (DSBs) could be expected considering the formation roughly 35 DSBs/1 Gy [64]. One may assume that such a high number of γH2AX foci would prevent definitive resolution of the true number of DSBs formed, and thus lead to the saturation observed ≥ 10 Gy. This is a factor that needs to be taken into serious consideration in future work, as this will determine the doses at which the FLASH effect maximally prevents normal tissue DNA damage. Additionally, these results seem to contradict other studies analysing dose rate effects on DSB production via γH2AX [65–67] and 53BP1 [66, 68] immunofluorescence, which show a non-significant induction of these foci between FLASH and CONV dose rates.

Further tests to quantify markers of cellular senescence and inflammation (at 20 Gy, 1000 Gy/s) also showed reduced proportions of β-galactosidase positive cells 1-month post-irradiation (40% fewer vs. CONV) and TGFβ1 induction 24 h and 1-month (4.4-fold and 4.3-fold

decrease respectively) post-irradiation [63]. At 100 Gy/s, the only significant difference was ~20% fewer β-gal positive cells compared to CONV, which may suggest that higher dose rates more effectively mitigate long-term cellular senescence.

These data scratch the surface of which factors modulate the proton-FLASH effect, illustrating that tissue protection may be more heavily reliant upon modifying gene expression in response to radiation exposure, especially concerning inflammatory and senescent cellular pathways. A summary table outlining all systematically identified proton and carbon-FLASH publications is presented in Table 3.

In vivo studies

One of the first papers to demonstrate in vivo FLASH radioprotection using protons was published in 2020 by Diffenderfer et al. [72]. A 230 MeV proton beamline with dose rates of 78 Gy/s for FLASH and 0.9 Gy/s for conventional irradiation were utilised in 15 Gy whole abdominal irradiations of C57BL/6J mice. Akin to studies performed with electron irradiation, FLASH irradiated mice exhibited greatly reduced levels of acute intestinal damage, defined by an increased number of EdU positive cells within abdominal crypts and increased crypt regeneration compared to the conventional dose rate. Moreover, where symptoms of fibrosis were severe in conventionally irradiated mice, FLASH irradiated tissues displayed intestinal morphology similar to that of non-irradiated tissues 8-weeks post irradiation. In a follow up experiment testing for tumour growth and control probability in a flank injection, murine pancreatic cancer model, no difference was observed between either dose rate used and doses of 12 and 18 Gy [72]. This aligns with previous claims that proton-FLASH has comparable tumour kill efficiency to conventional dose rates. Yet, this data is exemplary in highlighting the favourability of ultra-high dose rates to both mitigate the inflammatory response and maintain cellular proliferation after exposure. A murine model conducted by Cunningham et al. also supports this, wherein equivalent tumour control was maintained in a squamous cell carcinoma FLASH irradiation compared to CONV [74]. Additionally, when FLASH irradiating normal hind leg tissue, there were decreased levels of TGFβ1 24- and 96- hours post irradiation, as well as a higher G-CSF to GM-CSF ratio, both indicative of reduced inflammation compared to CONV [74].

Similar experiments were performed by Zhang et al. (2020) utilising an experimental beamline for whole abdominal irradiations of mice, with average dose rates of 120 Gy/s and 0.05 Gy/s for proton-FLASH and CONV respectively. Mice survived doses of 13 Gy at either dose rate and died within 15 days of 19 and 22 Gy irradiation. However, an apparent differential effect was observed for 16 Gy irradiations, with 100% of FLASH mice surviving versus ~40% at the CONV dose rate. In addition, FLASH mice exhibited better weight retention 9 days post-irradiation. Hematoxylin and eosin stains were also performed to observe late effects 90 days post-irradiation. Both dose rates showed mild signs of inflammation with inflammatory cells infiltrating intestinal villi. Remarkably, FLASH irradiated intestines appeared to exhibit reduced signs of inflammation compared to CONV protons, evidenced by a lower proportion of infiltrating inflammatory cells and thinner layer of hyperplastic submucosa and muscularis [73]. In syngeneic mice models, there is evidence that proton-FLASH produces an improved tumorigenic response due to increased recruitment and infiltration of CD3 + T cells within the tumour microenvironment [70]. These findings may be reflective of the ability of FLASH to minimise interference with, or perhaps aid in stimulating, the immune response.

Similar to the previously described electron-FLASH experiment conducted by Pawelke et al. [48], Beyreuther et al. [69] also performed zebrafish embryo irradiations, but with 224 MeV protons at a CONV dose rate of 0.08 Gy/s and FLASH at 100 Gy/s. The endpoints of this study were relative embryonic survival and the rate at which morphological changes occurred, including pericardial edema (PE) and spinal curvature (SC). Only 23 Gy irradiation appeared to exhibit statistically significant differences between CONV and FLASH embryos with PE at 3- and 4-days post-irradiation; dose rate did not appear to have a substantial effect upon any other endpoints or at other doses [69]. Akin to in vitro studies, the Bragg peak is not reported to conform to targeted tissues throughout these experiments.

First-In-Human clinical trial

In December of 2020, recruitment began for the first proton-FLASH clinical investigation, conducted at Cincinnati Children's Proton Therapy Center [83]. The focus of this study was to assess the workflow of a palliative FLASH treatment for bone metastases in the extremities of 10 patients aged 18 years or older. FLASH treatments were delivered at a dose rate of 51–61 Gy/s, with single dose regimen of 8 Gy being utilised on a total of 12 metastatic sites across all patients. This was followed by assessment of radiation related normal tissue toxicities and adverse side effects in addition to pain response, use of pain relief and pain flare [84]. Key results from the study include 6 out of the 12 treated sites experiencing a complete pain relief response, 2 of 12 sites reporting partial pain relief, and 4 of 12 sites experiencing pain flare following treatment. Twelve adverse events were reported within this patient group, with eleven of these being classed as grade 1 including skin hyperpigmentation,

Table 3 Summary table of systematically identified particle-FLASH literature. For FLASH irradiations, delivery time, pulse or bunch count and rate for synchrotrons and cyclotrons respectively (or either for linear accelerators, (LINAC) or laser-accelerated protons (LAP)), average dose rate per fraction, instantaneous dose rate (within one pulse or bunch), and comparative CONV dose rate are provided. Data listed in bold have been calculated from information provided in the text. Only in vitro and in vivo works are listed. *In silico* and preclinical studies are summarised throughout the Proton-FLASH, Carbon-FLASH and Discussion sections

Ref.	Year	Particle Type, Source, Delivery Mode	Model	Energy (MeV)	Dose (Gy)	Delivery Time (s)	Pulse/ Bunch Count	Pulse/ Bunch Rate (Hz)	FLASH Dose Rate Average (Gy/s)	FLASH Instantaneous Dose Rate (Gy/s)	Low or CONV (Gy/s)	Outcome
[62]	2009	Proton, LAP pulsed and continuous	Human derived cervical cancer cell line HeLa	20	3	1×10^{-9}	1	3.9×10^{4}	$\mathbf{3\times10^{9}}$	$\mathbf{3\times10^{9}}$	**30**	Pulsed FLASH (3×10^{8} Gy/s) RBE** was not significantly different than continuous (30 Gy/s) CONV irradiation. Additionally, there were also no substantial differences in the production of micronuclei observed between FLASH or CONV dose rates.
[61]	2011	Proton LAP pulsed and continuous	Human derived cervical cancer cell line (HeLa)	20	0–5	1×10^{-9}	1	100	$\mathbf{1\times10^{9}}$	$\mathbf{1\times10^{9}}$	**30**	Reduced number of cells accumulated in the G_2 phase of the cell cycle 10 h post-FLASH compared to post-CONV. No differences in HeLa cell clonogenicity were observed when comparing FLASH and CONV dose rates.
[60]	2011	Proton, LAP, pulsed and continuous	Human-hamster hybrid cells (A_L)	20, 23, 25	3.6	1×10^{-9}	1	3.9×10^{4}	$\mathbf{3.6\times10^{9}}$	$\mathbf{3.6\times10^{9}}$	**36**	RBE** showed no significance between pulsed (FLASH) and continuous (CONV) modes. Higher proportion of dicentric, centric rings and excess acentrics chromosome aberrations in CONV mode compared to FLASH.
[59]	2012	Proton, LAP, pulsed and continuous	Chinese hamster cells (V-79)	1–5	0.8–5	7×10^{-13}	1	NM*	1×10^{9}	1×10^{9}	NM*	Laser accelerated protons at FLASH dose rates appear to show no substantial difference in RBE (1.4 ± 0.2) in terms of clonogenicity when compared to previous studies utilising protons at CONV dose rates.
[67]	2012	Proton, LAP, pulsed and continuous	Human derived cervical cancer cell line HeLa	20	1, 5	1×10^{-9}	1	3.9×10^{4}	$\mathbf{1\times10^{9}}$, $\mathbf{5\times10^{9}}$	$\mathbf{1\times10^{9}}$, $\mathbf{5\times10^{9}}$	**10, 50**	No significant difference observed between FLASH (pulsed) and CONV (continuous) proton irradiation of HeLa cells regarding both the formation and time-dependent loss of γH2AX foci.

Table 3 (continued)

Ref.	Year	Particle Type, Source, Delivery Mode	Model	Energy (MeV)	Dose (Gy)	Delivery Time (s)	Pulse/ Bunch Count	Pulse/ Bunch Rate (Hz)	FLASH Dose Rate Average (Gy/s)	FLASH Instantaneous Dose Rate (Gy/s)	Low or CONV (Gy/s)	Outcome
[54]	2014	Proton LAP, pulsed and continuous	NMRI (nu/nu) mice model, FaDu tumour xenograft	23	20	2100	1	3.9×10^{4}	**0.009**	$\mathbf{2\times10^{10}}$	**0.002**	In the treatment of human tumour xenografts, FLASH and CONV dose rate protons appeared to have comparable measures of both tumour growth delay and RBE (1.22 ± 0.19 and 1.10 ± 0.18 respectively). Note that although instantaneous dose rates differ greatly, average dose rates are similar due to the 35 min required to irradiate tumour volumes.
[66]	2016	Proton, LAP: pulsed LINAC: continuous	Human lung cancer cell line A549	0–2.2	0, 0.25, 0.5, 1, 2	NM*	NM*	NM*	NM*	1×10^{8}	0.01	Laser and conventionally accelerated protons induce γH2AX and 53BP1 foci with similar efficacy. Induction of 3-nitrotyrosine, a marker for nitroxidative stress, was 2-3-fold lower in laser accelerated protons compared to conventionally accelerated protons, with similar induction compared to X-rays at 1 Gy.
[58]	2017	Proton, LAP: pulsed and continuous	Human umbilical vein endothelial (HUVEC) cells	6–14	0–4.5	$\mathbf{1.5\times10^{-9}}$–$\mathbf{4.5\times10^{-9}}$	NM*	NM*	$\mathbf{>1\times10^{9}}$	$\mathbf{>1\times10^{9}}$	NM*	No statistically significant difference in HUVEC clonogenic survival between laser-accelerated protons, conventionally accelerated protons and X-rays. Conversely, laser-accelerated protons saw higher proportions of senescent cells at 7 and 14 days after 0.5 Gy, and from 2–28 days after 1.5 Gy irradiations. No significant effect on senescence for 4.5 Gy.

Table 3 (continued)

Ref.	Year	Particle Type, Source, Delivery Mode	Model	Energy (MeV)	Dose (Gy)	Delivery Time (s)	Pulse/ Bunch Count	Pulse/ Bunch Rate (Hz)	FLASH Dose Rate Average (Gy/s)	FLASH Instantaneous Dose Rate (Gy/s)	Low or CONV (Gy/s)	Outcome
[68]	2019	Proton, LAP: pulsed, cyclotron: continuous	Human skin fibroblasts (AG01522B)	10	1–2	1×10^{-9}	1	NM*	1×10^{9}	1×10^{9}	**0.067**	Non-significant differences between 53BP1 foci induction, foci size, and fraction of repaired DSBs between FLASH laser-accelerated protons and 225 kVp X-rays. However, protons appeared to have greater yields of 10–14 foci per cell at 6 and 24 h post irradiation. Track structures (foci/cell/track) of laser-accelerated protons were also similar to cyclotron-accelerated protons.
[63]	2019	Proton, LINAC: pulsed	Normal human lung fibroblasts (IMR90)	4.5	0–20	NM*	NM*	NM*	*NM	100, 1000	0.05	For colony formation assay, Clonogenic cellular survival was not affected by proton dose rate regardless of dose administered. Decrease in γH2AX foci at 20 Gy for 1000 Gy/s, 100 Gy/s FLASH foci formation comparable to 0.05 Gy/s CONV. Cell senescence and expression of TGFβ1 decreased with increasing dose rate (statistically significant).
[65]	2019	Proton, LAP: pulsed, cyclotron: continuous	Glioblastoma cell lines SF763 and U87-MG, human colon carcinoma (HCT116)	20	0–10	NM*	0–12	0.5	NM*	1.5×10^{8}	**0.021**	Laser driven protons (LDP) induce numbers of γH2AX foci similarly to conventional, continuous proton beams and X-rays. Modification of the LDP repetition rate altered the survival of both WT and $p53^{-/-}$ HCT116 cells. Survival was a non-monotonic function of time between pulses. Inhibition of PARP1 protein reversed this effect.

Table 3 (continued)

Ref.	Year	Particle Type, Source, Delivery Mode	Model	Energy (MeV)	Dose (Gy)	Delivery Time (s)	Pulse/ Bunch Count	Pulse/ Bunch Rate (Hz)	FLASH Dose Rate Average (Gy/s)	FLASH Instantaneous Dose Rate (Gy/s)	Low or CONV (Gy/s)	Outcome
[69]	2019	Proton, cyclotron: quasi-continuous	Zebrafish embryos	224	0–45	**0.1–0.45**	NM*	NM*	100	5×10^4	0.08	Statistically significant difference between FLASH and CONV protons at 25 Gy, with a lower incidence of pericardial edema for FLASH irradiated embryos. Dose rate did not influence relative survival or spinal curvature as a function of total dose.
[70]	2019	Proton, NM*	C57BL/6J mice model, Lewis lung carcinoma	NM*	18	NM*	NM*	NM*	40	NM*	NM*	Recruitment of CD3+, CD4 + and CD8 + T-lymphocytes from the tumour periphery to inside the tumour volume was increased under FLASH irradiation. Tumours were significantly smaller in the FLASH or pulsed-FLASH groups compared to CONV-RT.
[71]	2019	Proton	C57BL/6 mice model, thorax irradiation	NM*	15, 17.5, 20	0.375–0.5	NM*	NM*	40	NM*	0.5	Female mice irradiated with FLASH exhibited improved overall survival, breathing ability, and reduced incidence of dermatitis compared to CONV irradiations at doses of 17.5 and 20 Gy. There was minimal difference between FLASH and CONV in male mice. Mode of cell death was also affected between a pulse-FLASH mode, FLASH and CONV irradiations, regardless of mice gender.
[72]	2020	Proton, cyclotron, quasi-continuous	C57BL/6J mice, abdominal irradiation, MH641905 mouse pancreatic tumour cells	230	12, 15, 18	**0.16–0.29**	18–20	1.06×10^8	63, 94	**~300**	0.71, 0.74, 0.94	Whole abdominal 15 Gy FLASH irradiations substantially prevented the loss of proliferating cells (higher proportion of EdU + cells) within intestinal crypts compared to CONV irradiation. Conversely, 12 and 18 Gy FLASH irradiation of tumours did not exhibit a tissue sparing effect.

Table 3 (continued)

Ref.	Year	Particle Type, Source, Delivery Mode	Model	Energy (MeV)	Dose (Gy)	Delivery Time (s)	Pulse/ Bunch Count	Pulse/ Bunch Rate (Hz)	FLASH Dose Rate Average (Gy/s)	FLASH Instantaneous Dose Rate (Gy/s)	Low or CONV (Gy/s)	Outcome
[73]	2020	Proton, cyclotron: quasi-continuous	C57BL/6J mice model, partial abdominal irradiation	225.5	13, 16, 19, 22	**0.096–0.181**	NM*	1.06×10^8	106–137.88	NM*	< 0.745	Mice exposed to 16 Gy FLASH exhibited higher overall survival 21 days post-irradiation (100%) compared to CONV (40%). At 19 and 22 Gy doses regardless of dose rate, all mice died by 12 days post irradiation. FLASH mice also showed improved weight retention following irradiation compared to CONV. Chronic inflammatory cell infiltration and thickening of submucosa and muscularis was observed at 16 Gy under both FLASH or CONV conditions.
[74]	2021	Proton, cyclotron: continuous	C57BL/6J mice model, toxicity model: hind leg irradiation, tumour model: murine derived squamous cell carcinoma (MOC1/MOC2)	250	15, 35	0.24–0.61	NM*	7.2×10^7	61.8, 62.2, 115.1	206.3, 207.6, 385	1	In immunocompetent mice, equivalent tumour control observed between FLASH and CONV-RT. Decreased TGFβ1 production in FLASH irradiated mice 24- and 96-hours post-irradiation. G-CSF, and GM-CSF cytokine ratio higher in FLASH mice than CONV, indicative of reduced toxicity.

Table 3 (continued)

Ref.	Year	Particle Type, Source, Delivery Mode	Model	Energy (MeV)	Dose (Gy)	Delivery Time (s)	Pulse/ Bunch Count	Pulse/ Bunch Rate (Hz)	FLASH Dose Rate Average (Gy/s)	FLASH Instantaneous Dose Rate (Gy/s)	Low or CONV (Gy/s)	Outcome
[75]	2021	Proton, cyclotron: continuous	C57BL/6 and C3H/HeJ mice model: *LSL-Kras$^{G12D/wt}$;p53$^{FL/FL}$* derived fibrosarcoma and RIF mice sarcoma. Canine model, skin irradiation	230	30, 45	**0.24–0.65**	NM*	NM*	69–124	NM*	0.39–0.65	Mice exposed to 30 Gy FLASH irradiation had higher overall survival and protection from severe morbidities (mean survival > 249 days) compared to CONV irradiation (mean survival = 211 days). RNA-seq of FLASH irradiated murine skin displayed increased expression of genes responsible for vascular repair, contrasting CONV which displayed upregulation of apoptotic and keratin signalling. In skin irradiation studies of both mice and canine models, FLASH alleviated skin damage and inflammation and reduced TGFβ1 expression compared to CONV. There was no dose rate dependence on tumour kill efficacy in the treatment of mice sarcomas.
[52]	2021	Proton, cyclotron: continuous	C57BL/6J mice, whole abdominal irradiation, MH641905 mouse pancreatic tumour cells	230	15 ± 0.1, 18 ± 0.1	**0.138–0.167**	NM*	NM*	108 ± 12.3	NM*	0.82 ± 0.196	15 Gy FLASH abdominal irradiations resulted in a higher percentage of EdU+ (marker of cell proliferation) cells per crypt and regenerated crypts compared to CONV. No statistically significant difference between utilisation of the SOPB*** or entry 'plateau' region of proton beam upon EdU + cells or crypt regeneration at FLASH or CONV dose rates. 18 Gy tumour irradiations resulted in similar tumour control between dose rates, however radiation lethality 20 days post irradiation was substantially decreased in FLASH SOBP*** treated mice (15%) vs. CONV (70%).

Table 3 (continued)

Ref.	Year	Particle Type, Source, Delivery Mode	Model	Energy (MeV)	Dose (Gy)	Delivery Time (s)	Pulse/ Bunch Count	Pulse/ Bunch Rate (Hz)	FLASH Dose Rate Average (Gy/s)	FLASH Instantaneous Dose Rate (Gy/s)	Low or CONV (Gy/s)	Outcome
[53]	2021	Proton, synchrocyclotron, pulsed	C57BL/6 mice, total abdominal irradiation	230	10–19	**0.1–0.2**	**80–152**	756	100	6200	0.1	Mice exposed to FLASH irradiation had a higher LD50 compared to those exposed to CONV at equivalent dosages. Survival was increased under FLASH conditions by between 10–20% depending upon dose administered.
[76]	2022	Carbon, synchrotron: pulsed	Chinese hamster ovary cells (CHO-K1)	280 ****	7.5	0.13	1	1.45×10^{10}	70	70	0.6	A statistically significant increase in cell survival was displayed for CHO-K1 cells exposed to FLASH vs. CONV irradiation at 0.5% and 4% oxygenation. No significant difference was observed between dose rates for cells exposed to 21% oxygenation.
[77]	2022	Proton, cyclotron: continuous	CDF1 mice, hind limb irradiation	244–250	23.2–39.2	0.35–0.73	NM*	NM*	65–92	NM*	0.35–0.40	After irradiation of hind limb skin, FLASH dose rates exhibited a normal tissue sparing effect in comparison to CONV, with a 44–58% higher dose required under FLASH to produce comparable tissue toxicities to CONV irradiation. This is consistent amongst all levels of acute skin damage (1.5–3.5), with the dose necessary to produce moist desquamation in 50% of mice (MDD_{50}) being higher in FLASH irradiated mice.

Table 3 (continued)

Ref.	Year	Particle Type, Source, Delivery Mode	Model	Energy (MeV)	Dose (Gy)	Delivery Time (s)	Pulse/ Bunch Count	Pulse/ Bunch Rate (Hz)	FLASH Dose Rate Average (Gy/s)	FLASH Instantaneous Dose Rate (Gy/s)	Low or CONV (Gy/s)	Outcome
[55]	2022	Carbon, synchrotron: pulsed	Human lung fibroblasts (HFL1) and human salivary gland tumour line (HSGc-C5)	290 ****	1, 2, 3	**0.005–0.031**	1	NM*	96–195	96–195	8–13	FLASH and CONV irradiation of HFL1 cells exhibited no significant difference in post-irradiation impediment of cell growth and induction of senescence. This applied when using the entrance plateau region (13 keV/µm) and Bragg peak region (50 keV/µm) of the carbon beam. In HSGc-C5 cells, no significant difference was observed in clonogenic survival when comparing either FLASH or CONV dose rates, or when utilising the plateau or Bragg peak region of the beam.
[56]	2022	Proton, LINAC: continuous	Normal human lung fibroblasts (IMR90)	4.5	1.5, 15	**0.015–0.15**	1	NM*	100	100	0.33	Clonogenic survival of IMR90 cells was improved under FLASH conditions compared to CONV. Radiation induced oxidative stress 40 min post-irradiation was also substantially lower in FLASH irradiated cells compared to CONV. In mitochondria, FLASH samples displayed similar morphology to unirradiated controls, whereas CONV samples showed morphological abnormalities. Expression of mitochondrial fission protein Drp1 was found to be higher in CONV irradiated cells versus FLASH, where there was no significant difference in Drp1 expression compared to control samples. CONV-IR also induced a significant decrease in mitochondrial copy number in comparison to FLASH.

Table 3 (continued)

Ref.	Year	Particle Type, Source, Delivery Mode	Model	Energy (MeV)	Dose (Gy)	Delivery Time (s)	Pulse/ Bunch Count	Pulse/ Bunch Rate (Hz)	FLASH Dose Rate Average (Gy/s)	FLASH Instantaneous Dose Rate (Gy/s)	Low or CONV (Gy/s)	Outcome
[57]	2022	Proton, synchrotron: pulsed	C57BL/6 mice, brain irradiation	146.6 ****	10	0.08	1	NM*	120	120	0.17	Under CONV, the fraction of γH2AX positive cells increased 10-fold compared to control, whereas under FLASH 2-fold increase was observed. In addition to significantly lower γH2AX radiation induced foci induction, FLASH conditions reduced the degree of inflammation associated with macrophage/microglia compared to CONV.
[78]	2022	Proton, cyclotron: continuous	Zebrafish embryos	224	32	0.115	1.2×10^{7}	1.06×10^{8}	300	1.5×10^{3}	0.15	FLASH irradiations exhibited reduced rates of pericardial edema at day 3 (FLASH: 54.3 ± 18.9%, CONV: 67.6 ± 20.6%) and day 4 (FLASH: 75.3 ± 13.1%, CONV: 90.1 ± 9.1%) post irradiation. The same was observed for spinal curvature at day 3 (FLASH: 15.4 ± 10.3, CONV: 27.2 ± 12.0) and day 4 (FLASH: 24.6 ± 11.5, CONV: 38.2 ± 15.5).
[79]	2022	Carbon, synchrotron: pulsed	C3H/He mice, LM8 osteosarcoma model	240 *****	18	0.15 ± 0.02	1	NM*	100	100	0.3	Under either FLASH or CONV dose rates, tumour control was achieved with similar efficacy. However, under FLASH dose rates, the proportion of mice with lung metastases was significantly lower than those irradiated under CONV (FLASH: ~10%, CONV: ~30%, Control: ~40%). Irradiated muscle tissues exhibited disorganized morphology under CONV irradiation, which was greatly reduced in FLASH irradiated mice.

Table 3 (continued)

Ref.	Year	Particle Type, Source, Delivery Mode	Model	Energy (MeV)	Dose (Gy)	Delivery Time (s)	Pulse/ Bunch Count	Pulse/ Bunch Rate (Hz)	FLASH Dose Rate Average (Gy/s)	FLASH Instantaneous Dose Rate (Gy/s)	Low or CONV (Gy/s)	Outcome
[80]	2022	Proton, cyclotron: continuous	CDF1 mice, CH3 mouse mammary sarcoma model	250	40–60	0.449–0.845	NM*	NM*	71–89	NM*	0.33–0.63	The total dose for 50% tumour control (TCD_{50}) for either dose rate was comparable, FLASH: 51.3 Gy, CONV: 49.1 Gy. For mice with tumour control, radiation induced fibrosis was mitigated in FLASH irradiated mice, with moist desquamation presenting in 50% of mice (MDD_{50}) at 52.3 Gy for FLASH versus < 40.1 Gy for CONV, and fibrosis presenting in 50% of mice (FD_{50}) at 55.6 Gy for FLASH versus 48.6 Gy for CONV.
[81]	2022	Proton, cyclotron: continuous	Zebrafish embryos	235	9–27	**0.007–0.3**	NM*	7.29×10^7	90, 1260	NM*	0.1, 0.9	In measuring radiolytic production of peroxide in a water phantom mimicking zebrafish physoxia (4% O_2), the overall yield of H_2O_2 was reduced under FLASH conditions regardless of dose administered. There was no substantial difference in zebrafish viability or fish length between FLASH and CONV irradiation modes, and both irradiation modes sparing zebrafish morphology compared to photon and electron irradiation at a dose of 10 Gy.
[82]	2022	Proton, LAP: pulsed	Prostate tumour cells PC3, normal prostate epithelial cells RWPE1	2	7.4–37.1	50–150	10–30	0.2	0.15–0.25	2.3×10^7 – 3.8×10^7	NM*	The surviving fraction of normal prostate RWPE1 cells irradiated by FLASH dose rate protons was greater than one order of magnitude higher than that of tumour prostate PC3 cells at a dose of 7 Gy. Increasing dose above approximately 15 Gy resulted in a small reduction of RWPE1 survival, whilst PC3 cells did not survive at any doses above this value.

* NM = Not mentioned, ** RBE = Relative Biological Effectiveness, *** SOBP = Spread-Out Bragg Peak, **** Units = MeV/u, ***** Units = MeV/n.

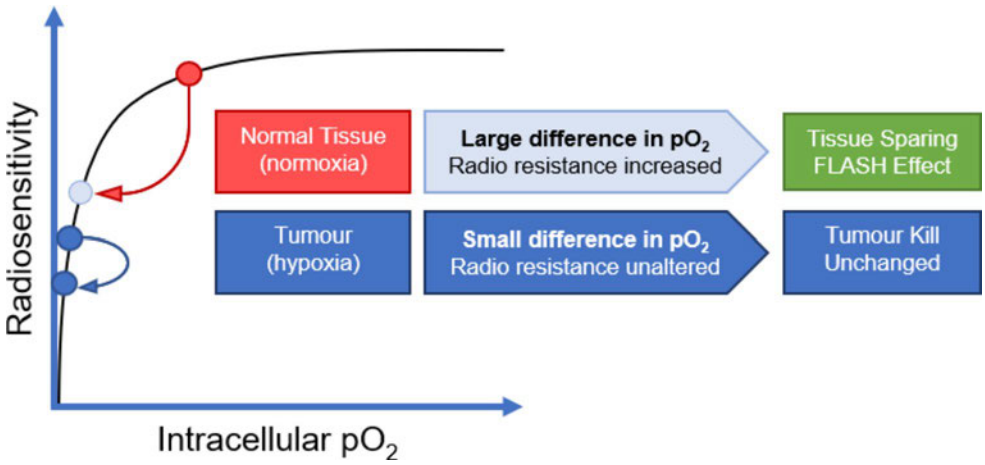


Fig. 3 Representation of the oxygen depletion hypothesis, depicting relative radiosensitivity of normal versus tumour tissues as a function of oxygen tension. Normal tissues see a more significant change in intracellular O_2 levels, affording a brief period of hypoxia which protects normal tissues from ROS related damage during FLASH irradiation. On average, cancerous cells are already relatively hypoxic, so radiation resistance is unchanged by O_2 consumption via FLASH. Permitted reprinting from Wilson et al. 2020 [87]

edema, erythema, fatigue, and puritus. One patient also experienced grade 2 extremity pain 1 month post treatment. FLASH was deemed clinically feasible in the palliative treatment of bone metastases, with the efficacy of treatment and the profile of adverse effects being analogous to conventional dose rate radiotherapies regimes [85].

Carbon-FLASH

The representation of experimental carbon-FLASH literature, in a radiobiological context, is sparse, with only six papers fitting the systematic criteria of this review. Two of these papers, authored by Zakaria et al. [12, 86], outline the potential anti-tumour benefits of carbon FLASH *in silico*. Monte Carlo simulations produced 3-dimensional track segments of low and high LET carbon ions to draw comparisons between their energy deposition profiles. High LET, 4.1 MeV/nucleon carbon ions (~330 keV/µm) exhibited a significant production of radiolytic oxygen after movement of the ions through water compared to lower LET carbon ions. As molecular oxygen can act as a radiosensitiser, they suggest that this radiolytic formation of oxygen at high LET (i.e., Bragg peak) may offer enhanced tumour control. Oxygenation remains relatively unchanged within the low LET, 'normal tissue' region in these simulations, also suggesting that the sparing capacity of carbon-FLASH would be unchanged [12]. In the first in vitro study by Tinganelli et al., CHO-K1 cells exposed to 7.5 Gy of 70 Gy/s carbon-ions had greater surviving fractions at 0.5% and 4% oxygenation (hypoxia) post-FLASH compared to CONV, but not at 21% O_2 (physoxia). These irradiations were performed within the plateau region of the dose-depth distribution (~13 keV/µm), with minimal sparing even at lower oxygen concentrations [76]. Following this, Tinganelli et al. published the first in vivo carbon FLASH study, analysing normal and tumour response in a C3H/He mouse model. Notable findings include comparable tumour control under either the FLASH (100 Gy/s) or CONV (0.3 Gy/s) dose rates, however there was a substantial reduction in the proportion of mice with lung metastases (~10% of mice under FLASH versus ~30% under CONV). In normal tissues, morphology was greatly spared under FLASH conditions compared to CONV, providing further evidence in support of a FLASH effect when applying carbon ions at ultra-high dose rates in vivo [79].

Additional simulation work explores the interaction of multiple interacting carbon ion tracks, instantaneous irradiations, and the effect these have upon radiolytic oxygen consumption and peroxide ion formation. At the highest dose rate utilised of approximately 10^{10} Gy/s, 300 MeV/nucleon (~11.6 keV/µm) carbon ions consumed 90% of oxygen present in solution, suggesting that carbon ions at FLASH dose rates are capable of inducing transient intracellular hypoxia [86]. Intriguingly, they also show that peroxide ion formation increases with increasing dose rate, and draw comparison to previous work conducted by Montay-Gruel et al. [36] where lower concentrations of H_2O_2 were produced at ~1000 Gy/s compared to ~0.1 Gy/s. However, as the dose rates and particles utilised (carbon ions vs. electrons) between these studies differ so greatly, it is very difficult for accurate comparisons to be drawn.

Mechanisms of the FLASH effect

Data from studies reviewed thus far collectively indicate three potential mechanisms for enhancing tumour control probability against the normal tissue complication probability during FLASH irradiation with particles. Specifically, normal tissue sparing effects due to rapid oxygen depletion; increased complexity in the nature of DNA damage that is more easily repaired by normal cells; and induction of antitumour immune response. Thus, the FLASH effect

may both reduce normal tissue toxicity as well as enhance tumour kill efficiency. While these mechanisms are the most frequently proposed and investigated [13, 87], data are not outright conclusive and, as is typical for radiobiology, likely to be highly convoluted and complex. Research captured by the systematic review specifically contributing to the discussion of these mechanisms are reviewed in the following sub-sections.

Oxygen depletion and reactive oxygen species

The cell killing capability of radiation therapy relies upon causing irreversible DNA damage to cancerous cells. When any cell is exposed to ionizing radiation (including protons) energy is transferred to intracellular chemical species upon physical interaction along its track. One of the sources of damage for particles is via direct collision and consequent ionization of DNA. Indirect DNA damage can also occur via the interaction of ionizing radiation with the intracellular species surrounding it, including oxygen and water [88]. Energetic charged particles can dissociate water and other molecules to form reactive oxygen species (ROS), DNA-damaging molecules which can disrupt DNA nucleotide sequences or the sugar-phosphate backbone [89]. It is suggested that the production of ROS is limited during FLASH irradiation, the hypothesis being that local oxygen is rapidly depleted at ultra-high dose rates, quicker than reoxygenation can occur. This means that any extra dose within the short timeframe does not contribute to further ROS production, thereby avoiding further damage to DNA due to this mechanism. With respect to normal tissues this leads to a state of radio-resistance. Within a hypoxic tumour environment however, then the change in radiosensitivity is less pronounced.

Solid tumours are often deficient in cellular oxygen due to poor vascularisation, meaning fewer ROS can be produced. As a result, hypoxic tumours are 2–3 times more radioresistant than under normoxic conditions [90]. By the oxygen-depletion theory, then the difference in intracellular O_2 is not as substantial for tumorigenic tissues (hypoxic à hypoxic) compared to normal tissues (physoxic à hypoxic) after FLASH exposure, meaning this protective effect is exacerbated in healthy tissue compared to cancerous tissue (Fig. 3).

Although this theory holds credence for in vitro models of oxygen depletion, there is debate in the radiobiology community as to the translation of this phenomena in vivo [91]. If a region of cancerous tissue has comparable levels of oxygenation to normal tissues, then would one not expect a tumour sparing effect as well? The controversy surrounding this theory suggests that transient oxygen depletion during FLASH is not the prime mechanism responsible for healthy tissue sparing, and that there are multiple other factors that contribute towards this radiobiological outcome [12, 92].

DNA damage: repair and response

The frequency of DSBs present within irradiated cells is one of the primary indicators of radiation induced DNA damage. Understanding the differences between how normal and tumour cells accumulate and respond to DSBs is therefore pivotal in defining the radiobiological characteristics of FLASH. Reports have indicated that ultra-high dose rates may reduce the number of γH2AX foci in both normal human fibroblasts and mice crypt base columnar cells, after administration of 20 Gy of 1000 Gy/s 4.5 MeV protons [63] or 14 Gy of 216 Gy/s 16 MeV electrons [43] respectively. This effect has also been illustrated in mouse Lewis lung carcinoma, observing a significantly higher number of γH2AX foci after 0.06 Gy/s versus 352 Gy/s 16 MeV electron irradiation [93]. However, clonogenic assays presented non-significant differences in cellular survival after 3 Gy irradiation. This appears contradictory to the equipotent antitumour effect ultra-high dose rates have in comparison to low dose rates; with present data, the implications of these findings are unclear.

Analysis and interpretation of γH2AX foci are fraught with challenges. One potential explanation for the differences between foci measurements and clonogenic survival is that although particle-FLASH reduces the total number of DSB foci observed in irradiated cells, the complexity of these DNA lesions increases with increasing dose rate [13, 94]. The pattern of DNA damage that FLASH irradiation produces compared to CONV has not yet been thoroughly analysed, and as such, there is difficulty in making conclusions concerning the degree of DNA damage that FLASH causes or prevents based upon clonogenic and γH2AX immunofluorescence assays alone. If under conventional irradiation conditions, DNA lesions are more broadly dispersed amongst foci, this would allow for resolving additional DNA DSBs during microscopic examination. Conversely, FLASH irradiation may produce clustered DSBs, where breakages occur within proximity to one another and are not discretely resolved. The initial conclusion for these observations would be that DNA damage appears to be of higher severity for CONV. Furthermore, γH2AX foci are indicators of the initiation of the DSB repair process, not of DSBs explicitly. If the nature of DNA damage between low and ultra-high dose rates differs, then these foci measurements are not directly comparable. This raises questions as to whether γH2AX foci assays can be presented as reliable predictors of cell death in this context.

Clustered DSBs are significantly more difficult for cells to repair than isolated lesions [95], and cancerous cells

often contain deleterious mutations within DNA damage repair (DDR) pathways. Particularly, defects in the non-homologous end joining (NHEJ) and homologous recombination (HR) repair pathways, responsible for DSB repair, result in increased radiosensitivity [96], an effect which is exacerbated for proton irradiation [97]. Initial observations show that the key radiobiological difference in response to particle-FLASH is that normal cells can better withstand ultra-high dose rates compared to cancerous cells. It is possible that tumour kill efficacy is maintained regardless of a reduction in γH2AX foci formation due to the inherent differences in DDR factor expression between normal and cancerous tissues. Normal cells may have a favourable predisposition for processing the pattern of DNA damage FLASH induces due to being more genetically stable, maintaining the NHEJ and HR repair mechanisms responsible for overcoming otherwise lethal DNA damage [13, 98]. Due to the inherent genomic instability of cancerous cells, dysfunction of these mechanisms would prevent cell survival after exposure, as clustered DSBs would be accumulated almost instantaneously at multiple foci under particle-FLASH conditions. Therefore, the differential effect within normal and tumorigenic tissues may lie within their respective abilities to resolve DNA damage of increasing complexity. Characterising the activation of the DNA repair factors expressed in each cell type post-FLASH would aid in determining which pathways drive FLASH's normal tissue sparing capabilities and provide explanations for FLASH's unchanged tumour kill efficacy.

Immune modulation: oncolytic and anti-inflammatory

Pathways involved in immune response are also thought to play a major role in both the enhancement of tumour control and reduction of inflammation during FLASH. It has been previously shown that ionizing radiation stimulates anti-tumour responses via expression of damage-associated molecular pattern (DAMP) molecules, consequently recruiting dendritic and cytotoxic T cells to neutralise tumour bodies [99, 100]. Indeed, the abscopal effect would be a prime example of radiation induced immune response, hypothesised to act via anti-tumour specific T-cells [101]. Yet, not much is understood concerning the implications of how FLASH interferes with the immune response in normal cells. Computational models predict that ultra-high dose rates may spare circulating immune cells, showing a reduction in immune cell death from 90 to 100% at conventional dose rates to 5–10% for dose rates greater than 40 Gy/s [102]. There is also evidence that TGFβ1, a pro-inflammatory cytokine, may be modulated during FLASH. After administration of 20 Gy at 1000 Gy/s (FLASH) or 0.2 Gy/s (CONV) protons to in vitro lung fibroblasts, Buonanno et al. observed a 4.7-fold reduced TGFβ1 induction during FLASH compared to CONV, suggesting that higher dose rates may be able to substantially reduce the degree of chronic inflammation in normal tissues [63]. Other factors, including modulation of the tumour microenvironment [70, 93], differential cytokine expression [74], and sparing of stem cell niches [44, 103] are also thought to contribute towards the FLASH effect, with further preclinical studies required to substantiate these observations.

Discussion

Whilst current literature appears to be explicit in biological methodology and outcomes of particle-FLASH experiments, the reporting of dosimetry and beam parameters are often not as thorough. To draw more accurate comparisons and conclusions between different FLASH studies, there is a necessity for both more stringent quality control and detailed descriptions of the irradiation characteristics used in these experiments. Particle- and electron-FLASH papers cite usage of substantially high dose rates, with average and/or instantaneous dose rates on the order of 1×10^6 Gy/s or higher [38, 41, 59–61, 65, 66, 68, 104]. This is potentially a considerable source of error in delivered dose as delivery of a conventional clinical dose (e.g., 50 Gy) in a matter of microseconds could have a significant degree of variability if FLASH pulses are not time gated with extreme precision, this being exacerbated at lower doses used experimentally. As this often appears to be neglected, there may be data which incorrectly correlates radiobiological effects to a predicted 'dose' for which there is substantial degrees of error. More thorough documentation of the methodology utilised to measure dosimetry needs to be provided, as it is intrinsically linked to the radiobiological data presented.

In considering the literature on potential therapeutic benefit of particle-FLASH, the data reviewed here illustrate differences in radiobiological responses compared to conventional irradiation dose rates. Although the effectiveness of particle-FLASH to eradicate tumours in vivo appears to be comparable to current clinical strategies, the outstanding result to date appears to be that the differential effect between normal and healthy tissues is increased considerably. Diffenderfer et al. [72] address these points effectively in their study, providing good justifications from past proton and electron-FLASH literature to form the basis of their experiments. One of the main limitations is that whilst protons are used for tumour irradiations instead of photons, their energy deposition profile is not taken advantage of, i.e. protons are transmitted through target volumes and rather than stopping as would be conducted clinically. Of these

34 particle-FLASH papers, only 6 utilise the Bragg peak for irradiations, the remaining employing the initial plateau region. Modulation of the Bragg peak and analysis of the damage that might be spared if FLASH dosage was conformed to the tumour volume is lacking in the proton studies mentioned, which is not reflective of clinical treatments using particle therapy that do employ this. For this technique to translate accurately from the preclinical phase to clinical use, it is vitally important that experiments mimic current clinical treatment methods as closely as possible. Ideally, this would include performing 3-dimensional dosimetry and conformation of the proton beam to a xenografted, orthotopic or spontaneous tumour volume. Nevertheless, this is not always feasible due to the limitations of the equipment used for irradiation or the scope of the experiments being performed (in vivo mice models for instance). This does not negate the value of transmission particle-FLASH experiments such as these, as they are invaluable in identifying how particle-FLASH affects healthy tissue proliferation and survival, as well as providing a general overview of which biological pathways respond to irradiation and in what manner. However, it should still be kept in mind that LET of the protons used in these studies and clinical practice differ substantially, and as such conclusions drawn from preclinical data should be taken with caution when attempting to translate them into clinical trials.

As mentioned previously, there is debate concerning which mechanisms contribute towards the particle-FLASH effect. Specifically, clinical scientists and some academics are uncertain whether the oxygen depletion hypothesis is valid, and if its contribution to normal tissue sparing in vivo is overstated compared to other hypothesised mechanisms. Alongside a multitude of studies conducted in vitro and in vivo, Monte Carlo computational modelling has been applied in attempts to validate this theory, aiming to identify the chemical interactions that occur along a single particle's trajectory during FLASH to determine the reaction kinetics and redox chemistry during radiolysis [92, 105, 106]. During conventional fractionated therapy at low dose rates, interactions between incoming ionised particles and intracellular species may occur, but the products of these reactions are unlikely to react with one another due to existing up to minutes apart. Therefore, the chance of ROS produced from each fraction interacting with each other is negligible. Under FLASH conditions, higher dose rates are used that are many orders of magnitude higher than conventional dose rates (> 40 Gy/s vs. 0.03 Gy/s), with ionizing radiation assumed to be evenly distributed almost instantaneously over the entire tumour volume. As such, spurs and tracks interact and overlap at a higher frequency, thereby increasing the initial concentration of e^-_{eq}, H^* and $^*OH$ radicals after radiation absorption. These radicals are at a concentration equal to or higher than intracellular O_2, and as there is a much shorter timeframe between radiation pulses, the chance of radical-radical combination increases. With H_2O_2, H_2O and H_2 being the major products of these interactions, it is hypothesised that cellular O_2 is consumed throughout the process, hence explaining why the FLASH effect induces radiolytic oxygen depletion. This also explains why normal tissues are protected during FLASH radiotherapy, as a lack of reactive oxygen species prevents DNA damage in irradiated cells. The duration over which radiation is delivered may also correlate with this. Zlobinskaya presented FLASH instantaneous dose rates of 2×10^{10}, however irradiation pulses were delivered over 35 min, resulting in a low average dose rate of 0.009 Gy/s [54]. Pulses at ultra-high dose rates, however at a lower frequency and as a result, a longer total irradiation time, may help elucidate mechanisms such as reoxygenation which could occur between pulses if the duration is long enough. Alternative FLASH mechanisms could dominate depending on the total duration of irradiation and instantaneous dose rates used, and not be entirely dependent upon the average dose rate administered.

These predictions outlined by Koch [107] and Spitz et al. [108] lay the foundation for Abolfath et al. [109] and their simulation-based study to test this hypothesis of oxygen depletion. Via analysis of sub-picosecond timescale interactions with Geant4-DNA Monte Carlo modelling, they aimed to perform a molecular dynamics simulation to help explain tissue damage mitigation observed during FLASH irradiation. They simulated damage to a confined portion of DNA irradiated with protons and measured how the molecules surrounding it (including protein, H_2O and O_2 molecules) interacted. Conclusions included an increase in ROS with increasing radiation dose, a decrease in ROS with an increase in dose rate, and that under physoxia conditions (4–5% O_2) the radioprotection of FLASH is maximised. In this instance, Abolfath et al. present that ROS interact through a vast series of hydrogen bonds, preventing ROS diffusion around DNA and reducing the chance of DNA damage. Modelling conducted by Zhu et al. [106] and Zakaria et al. [12] also support these findings. On the contrary, Labarbe et al. [110] present that transient oxygen depletion is not the prime mechanism for the FLASH effect; their model suggesting that a reduction of peroxyl radicals during FLASH is the prime mechanism by which normoxic tissues are protected.

Whilst the majority of simulation work appears to be in support of the oxygen effect and its influence upon particle-FLASH sparing, the translation and application of these results in experimental work is mixed. Beyreuther et al. [69] and their study analysing the effect of 224 MeV proton-FLASH irradiations upon zebrafish morphology depicted minimal differences in pericardial edema and spinal

curvature in comparison to CONV treatments. A similar study was conducted by Pawelke et al. [48], instead using 20 MeV electrons, observed reduced incidence of pericardial edema and spinal curvature under low pO_2 conditions after FLASH irradiations compared to high pO_2 conditions. This suggests that local oxygen concentration may have an impact upon the effectiveness of FLASH, where high pO_2 irradiations masked a potential FLASH effect and zebrafish morphology exhibited minimal differences compared to CONV. This also aligns with whole brain irradiation studies in mice, where Montay-Gruel et al. [36] displayed that the neurocognitive benefits of electron-FLASH were lost when brain tissue pO_2 was artificially doubled via carbogen breathing.

Water phantom studies, such as those conducted by Jansen et al. [111], seem to oppose these conclusions. Contrary to previously mentioned modelling studies, they state that for 10 Gy FLASH irradiations, oxygen consumption decreases with increasing dose rate nonlinearly due to lower steady state values of e^-_{aq} radicals, contradicting the apparent sparing effect of FLASH at low pO_2. Bovine serum albumin irradiations with electron-FLASH conducted by Cao et al. [46] also support these findings (Table 2), although in vivo measurements failed to achieve oxygen depletion under CONV conditions due to reoxygenation from vasculature. However, additional analogous experiments performed in vivo are required to further link oxygen depletion to the FLASH effect and to identify alternative biological explanations. Interestingly, the increased normal tissue sparing effect of FLASH at low pO_2 levels also appears contradictory to previous claims hypothesising that this effect would be inconsequential in comparable treatments of hypoxic tumourigenic tissues. An in vitro study by Adrian et al. [40] aligns with this, showing a FLASH tissue sparing effect in hypoxic prostate cancer cells. Spitz et al. [108] postulate that normal tissues can limit Fenton type reactions that yield ROS, thereby providing a potential explanation for this discrepancy. Regardless, translation of this sparing effect on in vivo, hypoxic tumourigenic models is yet to be thoroughly explored.

From these experimental data, the consensus appears to be that oxygen depletion does contribute towards healthy tissue sparing, this effect being greater at low pO_2 levels. Modelling of oxygen kinetics [105] and experiments utilising multicellular spheroids [112] suggest that FLASH depletion has negligible impact upon antitumour efficacy in already highly hypoxic tumour cores. Regardless, these data present multiple avenues for future work in addressing key questions concerning the feasibility of FLASH, limited not only to the oxygen effect but also other unknown biochemical mechanisms of the FLASH effect.

Conclusion

Particle therapy delivered in a particle-FLASH context appears to hold much potential in discovery of beneficial radiobiological response in both normal tissues and tumours. However, there are several areas which must be understood before this treatment modality can be translated safely in clinical settings. Many current data appear to present experimental artefacts and limitations. A major omission in many publications is a solid reporting on dosimetry and quality control. For ultra-high dose rates, the errors in dose are much more prone to significantly deviate from quoted doses compared to low dose rates. The impacts due to irradiation within the Bragg peak compared to the plateau region also remain to be identified. Key limitations of currently published literature stem from a lack of resolving the precise biological processes and mechanisms responsible for the normal tissue sparing effect, leaving much to be addressed in future preclinical work. Whilst the oxygen depletion hypothesis appears to be a compelling explanation to these underlying questions, there should be more emphasis on experiments which accurately represent in vivo conditions during oxygen depletion that are truly reflective of the tumour microenvironment. Along with this, whilst analysing DSB formation under FLASH irradiation conditions is valuable, more rigorous reporting of beam characteristics, doses administered, and DSB quantification techniques are also required to draw more accurate comparisons of the biological outcomes between experiments. Producing stricter, better-defined characteristics of "FLASH" or "continuous" beams of set dose rates is also of relevance, for instance there is evidence that quasi-continuous beams with a relatively low instantaneous dose rate (5×10^4 Gy/s) may contribute to not observing a FLASH effect [69]. Factors such as pulse structure, time between pulses and instantaneous versus average dose rate further complicate the biological impact of FLASH. Quantifying gene and protein expression under FLASH is also necessary to determine the differential action of DNA repair pathways between cancer and normal cells, as well as determining differences in cell cycle regulation, immune system modulation, and inflammation. Future work focusing on which dose rates, irradiation times, reactive species, and biochemical conditions optimally promote a beneficial particle-FLASH effect will contribute greatly towards progression of this phenomenon into clinical application.

Funding Open Access funding enabled and organized by CAUL and its Member Institutions

Open Access This article is licensed under a Creative Commons Attribution 4.0 International License, which permits use, sharing, adaptation, distribution and reproduction in any medium or format, as long as you give appropriate credit to the original author(s) and the

source, provide a link to the Creative Commons licence, and indicate if changes were made. The images or other third party material in this article are included in the article's Creative Commons licence, unless indicated otherwise in a credit line to the material. If material is not included in the article's Creative Commons licence and your intended use is not permitted by statutory regulation or exceeds the permitted use, you will need to obtain permission directly from the copyright holder. To view a copy of this licence, visit http://creativecommons.org/licenses/by/4.0/.

Reference list

1. Baskar R, Lee KA, Yeo R, Yeoh K-W (2012) Cancer and Radiation Therapy: current advances and future directions. Int J Med Sci 9(3):193–199. https://doi.org/10.7150/ijms.3635
2. Barnett GC, West CML, Dunning AM, Elliott RM, Coles CE, Pharoah PDP et al (2009) Normal tissue reactions to radiotherapy: towards tailoring treatment dose by genotype. Nat Rev Cancer 9(2):134–142. https://doi.org/10.1038/nrc2587
3. Paganetti H, Beltran C, Both S, Dong L, Flanz J, Furutani K et al (2021) Roadmap: proton therapy physics and biology. Phys Med Biol 66(5). https://doi.org/10.1088/1361-6560/abcd16
4. Giuranno L, Ient J, De Ruysscher D, Vooijs MA (2019) Radiation-Induced Lung Injury (RILI). Front Oncol 9. https://doi.org/10.3389/fonc.2019.00877
5. Palmer SL, Goloubeva O, Reddick WE, Glass JO, Gajjar A, Kun L et al (2001) Patterns of Intellectual Development among Survivors of Pediatric Medulloblastoma: a longitudinal analysis. J Clin Oncol 19(8):2302–2308. https://doi.org/10.1200/jco.2001.19.8.2302
6. Mostoufi-Moab S, Grimberg A (2010) Pediatric brain tumor treatment: growth consequences and their management. Pediatr Endocrinol Rev 8(1):6–17
7. Dracham CB, Shankar A, Madan R (2018) Radiation induced secondary malignancies: a review article. Radiation Oncol J 36(2):85–94. https://doi.org/10.3857/roj.2018.00290
8. De Ruysscher D, Niedermann G, Burnet NG, Siva S, Lee AWM, Hegi-Johnson F (2019) Radiotherapy toxicity. Nat Reviews Disease Primers 5(1). https://doi.org/10.1038/s41572-019-0064-5
9. Moreno AC, Frank SJ, Garden AS, Rosenthal DI, Fuller CD, Gunn GB et al (2019) Intensity modulated proton therapy (IMPT) – the future of IMRT for head and neck cancer. Oral Oncol 88:66–74. https://doi.org/10.1016/j.oraloncology.2018.11.015
10. Ohno T (2013) Particle radiotherapy with carbon ion beams. EPMA J 4(1). https://doi.org/10.1186/1878-5085-4-9
11. Soto LA, Casey KM, Wang J, Blaney A, Manjappa R, Breitkreutz D et al (2020) FLASH irradiation results in reduced severe skin toxicity compared to conventional-dose-rate irradiation. Radiat Res 194(6). https://doi.org/10.1667/rade-20-00090
12. Zakaria AM, Colangelo NW, Meesungnoen J, Azzam EI, Plourde M-É, Jay-Gerin J-P (2020) Ultra-High Dose-Rate, Pulsed (FLASH) Radiotherapy with Carbon Ions: Generation of early, transient, highly oxygenated Conditions in the Tumor Environment. Radiat Res 194(6). https://doi.org/10.1667/rade-19-00015.1
13. Zhou G (2020) Mechanisms underlying FLASH radiotherapy, a novel way to enlarge the differential responses to ionizing radiation between normal and tumor tissues. Radiation Med Prot 1(1):35–40. https://doi.org/10.1016/j.radmp.2020.02.002
14. Gao F, Yang Y, Zhu H, Wang J, Xiao D, Zhou Z et al (2022) First demonstration of the FLASH effect with ultrahigh dose rate high-energy X-rays. Radiother Oncol 166:44–50. https://doi.org/10.1016/j.radonc.2021.11.004
15. Shi X, Yang Y, Zhang W, Wang J, Xiao D, Ren H et al (2022) FLASH X-ray spares intestinal crypts from pyroptosis initiated by cGAS-STING activation upon radioimmunotherapy. Proc Natl Acad Sci 119(43):e2208506119. https://doi.org/10.1073/pnas.2208506119
16. Montay-Gruel P, Bouchet A, Jaccard M, Patin D, Serduc R, Aim W et al (2018) X-rays can trigger the FLASH effect: ultra-high dose-rate synchrotron light source prevents normal brain injury after whole brain irradiation in mice. Radiother Oncol 129(3):582–588. https://doi.org/10.1016/j.radonc.2018.08.016
17. Moher D, Liberati A, Tetzlaff J, Altman DG (2009) Preferred reporting items for systematic reviews and Meta-analyses: the PRISMA Statement. PLoS Med 6(7). https://doi.org/10.1371/journal.pmed.1000097
18. Favaudon V, Caplier L, Monceau V, Pouzoulet F, Sayarath M, Fouillade C et al (2014) Ultrahigh dose-rate FLASH irradiation increases the differential response between normal and tumor tissue in mice. Sci Transl Med 6(245). https://doi.org/10.1126/scitranslmed.3008973
19. Kirby-Smith JS, Dolphin GW (1958) Chromosome breakage at High Radiation Dose-Rates. Nature 182(4630):270–271. https://doi.org/10.1038/182270a0
20. Dewey DL, Boag JW (1959) Modification of the Oxygen Effect when Bacteria are given large pulses of Radiation. Nature 183(4673):1450–1451. https://doi.org/10.1038/1831450a0
21. Sutton HC, Rotblat J (1957) Dose-rate Effects in Radiation-Induced Chemical reactions. Nature 180(4598):1332–1333. https://doi.org/10.1038/1801332a0
22. Epp ER, Weiss H, Santomasso A (1968) The Oxygen Effect in bacterial cells irradiated with high-intensity pulsed Electrons. Radiat Res 34(2). https://doi.org/10.2307/3572557
23. Town CD (1967) Effect of high dose rates on survival of mammalian cells. Nature 215(5103):847–848. https://doi.org/10.1038/215847a0
24. Straub JM, New J, Hamilton CD, Lominska C, Shnayder Y, Thomas SM (2015) Radiation-induced fibrosis: mechanisms and implications for therapy. J Cancer Res Clin Oncol 141(11):1985–1994. https://doi.org/10.1007/s00432-015-1974-6
25. Kim H, Pyo H, Noh JM, Lee W, Park B, Park HY et al (2019) Preliminary result of definitive radiotherapy in patients with non-small cell lung cancer who have underlying idiopathic pulmonary fibrosis: comparison between X-ray and proton therapy. Radiat Oncol 14(1). https://doi.org/10.1186/s13014-019-1221-4
26. Hornsey S, Bewley DK (1971) Hypoxia in Mouse Intestine Induced by Electron Irradiation at High Dose-rates. Int J Radiation Biology Relat Stud Phys Chem Med 19(5):479–483. https://doi.org/10.1080/09553007114550611
27. Field SB, Bewley DK (1974) Effects of dose-rate on the Radiation response of rat skin. International Journal of Radiation Biology and Related Studies in Physics. Chem Med 26(3):259–267. https://doi.org/10.1080/09553007414551221
28. Purrott RJ, Reeder EJ, Lovell S (1977) Chromosome aberration yields Induced in Human Lymphocytes by 15 MeV electrons given at a conventional dose-rate and in Microsecond Pulses. Int J Radiation Biology Relat Stud Phys Chem Med 31(3):251–256. https://doi.org/10.1080/09553007714550291
29. Beyreuther E, Karsch L, Laschinsky L, Leßmann E, Naumburger D, Oppelt M et al (2015) Radiobiological response to ultra-short pulsed megavoltage electron beams of ultra-high pulse dose rate. Int J Radiat Biol 91(8):643–652. https://doi.org/10.3109/09553002.2015.1043755
30. Laschinsky L, Karsch L, Leßmann E, Oppelt M, Pawelke J, Richter C et al (2016) Radiobiological influence of megavoltage electron pulses of ultra-high pulse dose rate on normal tissue cells. Radiat Environ Biophys 55(3):381–391. https://doi.org/10.1007/s00411-016-0652-7
31. Montay-Gruel P, Petersson K, Jaccard M, Boivin G, Germond J-F, Petit B et al (2017) Irradiation in a flash: unique sparing of

memory in mice after whole brain irradiation with dose rates above 100 Gy/s. Radiother Oncol 124(3):365–369. https://doi.org/10.1016/j.radonc.2017.05.003
32. Loo BW, Schuler E, Lartey FM, Rafat M, King GJ, Trovati S et al (2017) (P003) Delivery of ultra-rapid flash radiation therapy and demonstration of normal tissue sparing after abdominal irradiation of mice. Int J Radiat Oncol Biol Phys 98(2). https://doi.org/10.1016/j.ijrobp.2017.02.101
33. Vozenin M-C, De Fornel P, Petersson K, Favaudon V, Jaccard M, Germond J-F et al (2019) The advantage of FLASH Radiotherapy confirmed in mini-pig and cat-cancer patients. Clin Cancer Res 25(1):35–42. https://doi.org/10.1158/1078-0432.Ccr-17-3375
34. Bourhis J, Sozzi WJ, Jorge PG, Gaide O, Bailat C, Duclos F et al (2019) Treatment of a first patient with FLASH-radiotherapy. Radiother Oncol 139:18–22. https://doi.org/10.1016/j.radonc.2019.06.019
35. Venkatesulu BP, Sharma A, Pollard-Larkin JM, Sadagopan R, Symons J, Neri S et al (2019) Ultra high dose rate (35 Gy/sec) radiation does not spare the normal tissue in cardiac and splenic models of lymphopenia and gastrointestinal syndrome. Sci Rep 9(1). https://doi.org/10.1038/s41598-019-53562-y
36. Montay-Gruel P, Acharya MM, Petersson K, Alikhani L, Yakkala C, Allen BD et al (2019) Long-term neurocognitive benefits of FLASH radiotherapy driven by reduced reactive oxygen species. Proc Natl Acad Sci 116(22):10943–10951. https://doi.org/10.1073/pnas.1901777116
37. Simmons DA, Lartey FM, Schüler E, Rafat M, King G, Kim A et al (2019) Reduced cognitive deficits after FLASH irradiation of whole mouse brain are associated with less hippocampal dendritic spine loss and neuroinflammation. Radiother Oncol 139:4–10. https://doi.org/10.1016/j.radonc.2019.06.006
38. Alaghband Y, Cheeks SN, Allen BD, Montay-Gruel P, Doan N-L, Petit B et al (2020) Neuroprotection of Radiosensitive Juvenile mice by Ultra-High Dose Rate FLASH Irradiation. Cancers 12(6). https://doi.org/10.3390/cancers12061671
39. Montay-Gruel P, Markarian M, Allen BD, Baddour JD, Giedzinski E, Jorge PG et al (2020) Ultra-High-Dose-Rate FLASH irradiation limits reactive gliosis in the brain. Radiat Res 194(6). https://doi.org/10.1667/rade-20-00067.1
40. Adrian G, Konradsson E, Lempart M, Bäck S, Ceberg C, Petersson K (2020) The FLASH effect depends on oxygen concentration. Br J Radiol 93(1106). https://doi.org/10.1259/bjr.20190702
41. Allen BD, Acharya MM, Montay-Gruel P, Jorge PG, Bailat C, Petit B et al (2020) Maintenance of tight Junction Integrity in the absence of vascular dilation in the brain of mice exposed to Ultra-High-Dose-Rate FLASH Irradiation. Radiat Res 194(6):625–635. https://doi.org/10.1667/RADE-20-00060.1
42. Breitkreutz DY, Shumail M, Bush KK, Tantawi SG, Maxime PG, Loo BW (2020) Initial steps towards a clinical FLASH Radiotherapy System: Pediatric Whole Brain irradiation with 40 MeV electrons at FLASH Dose Rates. Radiat Res 194(6). https://doi.org/10.1667/rade-20-00069.1
43. Levy K, Natarajan S, Wang J, Chow S, Eggold JT, Loo PE et al (2020) Abdominal FLASH irradiation reduces radiation-induced gastrointestinal toxicity for the treatment of ovarian cancer in mice. Sci Rep 10(1). https://doi.org/10.1038/s41598-020-78017-7
44. Fouillade C, Curras-Alonso S, Giuranno L, Quelennec E, Heinrich S, Bonnet-Boissinot S et al (2020) FLASH irradiation spares lung progenitor cells and limits the incidence of radio-induced senescence. Clin Cancer Res 26(6):1497–1506. https://doi.org/10.1158/1078-0432.Ccr-19-1440
45. Chabi S, To THV, Leavitt R, Poglio S, Jorge PG, Jaccard M et al (2021) Ultra-high-dose-rate FLASH and conventional-dose-rate irradiation differentially affect human acute lymphoblastic leukemia and normal hematopoiesis. Int J Radiat Oncol Biol Phys 109(3):819–829. https://doi.org/10.1016/j.ijrobp.2020.10.012
46. Cao X, Zhang R, Esipova TV, Allu SR, Ashraf R, Rahman M et al (2021) Quantification of Oxygen Depletion during FLASH Irradiation in Vitro and in vivo. Int J Radiation Oncology*Biology*Physics 111(1):240–248. https://doi.org/10.1016/j.ijrobp.2021.03.056
47. Montay-Gruel P, Acharya MM, Gonçalves Jorge P, Petit B, Petridis IG, Fuchs P et al (2021) Hypofractionated FLASH-RT as an effective treatment against Glioblastoma that reduces Neurocognitive Side Effects in mice. Clin Cancer Res 27(3):775–784. https://doi.org/10.1158/1078-0432.CCR-20-0894
48. Pawelke J, Brand M, Hans S, Hideghéty K, Karsch L, Lessmann E et al (2021) Electron dose rate and oxygen depletion protect zebrafish embryos from radiation damage. Radiother Oncol 158:7–12. https://doi.org/10.1016/j.radonc.2021.02.003
49. Gasymova E, Meier V, Guscetti F, Cancedda S, Roos M, Rohrer Bley C (2017) Retrospective clinical study on outcome in cats with nasal planum squamous cell carcinoma treated with an accelerated radiation protocol. BMC Vet Res 13(1). https://doi.org/10.1186/s12917-017-1018-3
50. Konradsson E, Arendt ML, Bastholm Jensen K, Børresen B, Hansen AE, Bäck S et al (2021) Establishment and initial experience of clinical FLASH Radiotherapy in Canine Cancer Patients. Front Oncol 11. https://doi.org/10.3389/fonc.2021.658004
51. Wei S, Lin H, Choi JI, Simone CB, Kang M (2021) A Novel Proton Pencil Beam scanning FLASH RT Delivery Method enables optimal OAR sparing and Ultra-High Dose Rate Delivery: a Comprehensive Dosimetry Study for Lung Tumors. Cancers 13(22). https://doi.org/10.3390/cancers13225790
52. Kim MM, Verginadis II, Goia D, Haertter A, Shoniyozov K, Zou W et al (2021) Comparison of FLASH Proton Entrance and the spread-out Bragg Peak Dose Regions in the sparing of mouse intestinal crypts and in a pancreatic tumor model. Cancers 13(16). https://doi.org/10.3390/cancers13164244
53. Evans T, Cooley J, Wagner M, Yu T, Zwart T (2021) Demonstration of the FLASH Effect within the spread-out Bragg Peak after Abdominal Irradiation of mice. Int J Part Therapy. https://doi.org/10.14338/ijpt-20-00095
54. Zlobinskaya O, Siebenwirth C, Greubel C, Hable V, Hertenberger R, Humble N et al (2014) The Effects of Ultra-High Dose Rate Proton Irradiation on Growth Delay in the treatment of human tumor xenografts in Nude mice. Radiat Res 181(2):177–183. https://doi.org/10.1667/rr13464.1
55. TASHIRO M, YOSHIDA Y, OIKE T, NAKAO M, YUSA K, HIROTA Y et al (2022) First human cell experiments with FLASH Carbon Ions. Anticancer Res 42(5):2469–2477. https://doi.org/10.21873/anticanres.15725
56. Guo Z, Buonanno M, Harken A, Zhou G, Hei TK (2022) Mitochondrial damage response and fate of normal cells exposed to FLASH Irradiation with Protons. Radiat Res 197(6):569–582
57. Dokic I, Meister S, Bojcevski J, Tessonnier T, Walsh D, Knoll M et al (2022) Neuroprotective Effects of Ultra-High Dose Rate FLASH Bragg Peak Proton Irradiation. Int J Radiat Oncol Biol Phys 113(3):614–623. https://doi.org/10.1016/j.ijrobp.2022.02.020
58. Manti L, Perozziello FM, Borghesi M, Candiano G, Chaudhary P, Cirrone GAP et al (2017) The radiobiology of laser-driven particle beams: focus on sub-lethal responses of normal human cells. J Instrum 12(03):C03084–C. https://doi.org/10.1088/1748-0221/12/03/c03084
59. Doria D, Kakolee KF, Kar S, Litt SK, Fiorini F, Ahmed H et al (2012) Biological effectiveness on live cells of laser driven protons at dose rates exceeding 109Gy/s. AIP Adv 2(1). https://doi.org/10.1063/1.3699063
60. Schmid TE, Dollinger G, Hable V, Greubel C, Zlobinskaya O, Michalski D et al (2011) The effectiveness of 20 MeV protons at Nanosecond Pulse Lengths in Producing chromosome aberrations

in human-Hamster hybrid cells. Radiat Res 175(6):719–727. https://doi.org/10.1667/rr2465.1
61. Auer S, Hable V, Greubel C, Drexler GA, Schmid TE, Belka C et al (2011) Survival of tumor cells after proton irradiation with ultra-high dose rates. Radiat Oncol 6(1). https://doi.org/10.1186/1748-717x-6-139
62. Schmid TE, Dollinger G, Hauptner A, Hable V, Greubel C, Auer S et al (2009) No evidence for a different RBE between Pulsed and continuous 20 MeV protons. Radiat Res 172(5):567–574. https://doi.org/10.1667/rr1539.1
63. Buonanno M, Grilj V, Brenner DJ (2019) Biological effects in normal cells exposed to FLASH dose rate protons. Radiother Oncol 139:51–55. https://doi.org/10.1016/j.radonc.2019.02.009
64. Rogakou EP, Pilch DR, Orr AH, Ivanova VS, Bonner WM (1998) DNA double-stranded breaks induce histone H2AX phosphorylation on serine 139. J Biol Chem 273(10):5858–5868. https://doi.org/10.1074/jbc.273.10.5858
65. Bayart E, Flacco A, Delmas O, Pommarel L, Levy D, Cavallone M et al (2019) Fast dose fractionation using ultra-short laser accelerated proton pulses can increase cancer cell mortality, which relies on functional PARP1 protein. Sci Rep 9(1). https://doi.org/10.1038/s41598-019-46512-1
66. Raschke S, Spickermann S, Toncian T, Swantusch M, Boeker J, Giesen U et al (2016) Ultra-short laser-accelerated proton pulses have similar DNA-damaging effectiveness but produce less immediate nitroxidative stress than conventional proton beams. Sci Rep 6(1). https://doi.org/10.1038/srep32441
67. Zlobinskaya O, Dollinger G, Michalski D, Hable V, Greubel C, Du G et al (2012) Induction and repair of DNA double-strand breaks assessed by gamma-H2AX foci after irradiation with pulsed or continuous proton beams. Radiat Environ Biophys 51(1):23–32. https://doi.org/10.1007/s00411-011-0398-1
68. Hanton F, Chaudhary P, Doria D, Gwynne D, Maiorino C, Scullion C et al (2019) DNA DSB Repair Dynamics following irradiation with laser-driven protons at Ultra-High Dose Rates. Sci Rep 9(1). https://doi.org/10.1038/s41598-019-40339-6
69. Beyreuther E, Brand M, Hans S, Hideghéty K, Karsch L, Leßmann E et al (2019) Feasibility of proton FLASH effect tested by zebrafish embryo irradiation. Radiother Oncol 139:46–50. https://doi.org/10.1016/j.radonc.2019.06.024
70. Rama N, Saha T, Shukla S, Goda C, Milewski D, Mascia AE et al (2019) Improved tumor control through T-cell infiltration modulated by ultra-high dose rate proton FLASH using a clinical pencil beam scanning proton system. Int J Radiat Oncol Biol Phys 105(1):S164–S5. https://doi.org/10.1016/j.ijrobp.2019.06.187
71. Abel E, Girdhani S, Jackson I, Eley J, Katsis A, Marshall A et al (2019) Characterization of radiation-induced lung fibrosis and mode of cell death using single and multi-pulsed proton flash irradiation. Int J Radiat Oncol Biol Phys 105(1):E652–E653. https://doi.org/10.1016/j.ijrobp.2019.06.1033
72. Diffenderfer ES, Verginadis II, Kim MM, Shoniyozov K, Velalopoulou A, Goia D et al (2020) Design, implementation, and in vivo validation of a novel proton FLASH radiation therapy system. Int J Radiat Oncol Biol Phys 106(2):440–448. https://doi.org/10.1016/j.ijrobp.2019.10.049
73. Zhang Q, Cascio E, Li C, Yang Q, Gerweck LE, Huang P et al (2020) FLASH investigations using protons: design of Delivery System, preclinical setup and confirmation of FLASH Effect with Protons in Animal Systems. Radiat Res 194(6). https://doi.org/10.1667/rade-20-00068.1
74. Cunningham S, McCauley S, Vairamani K, Speth J, Girdhani S, Abel E et al (2021) FLASH Proton Pencil Beam scanning irradiation minimizes Radiation-Induced Leg contracture and skin toxicity in mice. Cancers 13(5). https://doi.org/10.3390/cancers13051012
75. Velalopoulou A, Karagounis IV, Cramer GM, Kim MM, Skoufos G, Goia D et al (2021) FLASH Proton Radiotherapy spares normal epithelial and mesenchymal tissues while preserving Sarcoma Response. Cancer Res 81(18):4808–4821. https://doi.org/10.1158/0008-5472.Can-21-1500
76. Tinganelli W, Sokol O, Quartieri M, Puspitasari A, Dokic I, Abdollahi A et al (2022) Ultra-high dose rate (FLASH) carbon ion irradiation: Dosimetry and first cell experiments. Int J Radiat Oncol Biol Phys 112(4):1012–1022. https://doi.org/10.1016/j.ijrobp.2021.11.020
77. Singers Sørensen B, Krzysztof Sitarz M, Ankjærgaard C, Johansen J, Andersen CE, Kanouta E et al (2022) In vivo validation and tissue sparing factor for acute damage of pencil beam scanning proton FLASH. Radiother Oncol 167:109–115. https://doi.org/10.1016/j.radonc.2021.12.022
78. Karsch L, Pawelke J, Brand M, Hans S, Hideghéty K, Jansen J et al (2022) Beam pulse structure and dose rate as determinants for the flash effect observed in zebrafish embryo. Radiother Oncol 173:49–54. https://doi.org/10.1016/j.radonc.2022.05.025
79. Tinganelli W, Weber U, Puspitasari A, Simoniello P, Abdollahi A, Oppermann J et al (2022) FLASH with carbon ions: tumor control, normal tissue sparing, and distal metastasis in a mouse osteosarcoma model. Radiother Oncol 175:185–190. https://doi.org/10.1016/j.radonc.2022.05.003
80. Sørensen BS, Sitarz MK, Ankjærgaard C, Johansen JG, Andersen CE, Kanouta E et al (2022) Pencil beam scanning proton FLASH maintains tumor control while normal tissue damage is reduced in a mouse model. Radiother Oncol 175:178–184. https://doi.org/10.1016/j.radonc.2022.05.014
81. Kacem H, Psoroulas S, Boivin G, Folkerts M, Grilj V, Lomax T et al (2022) Comparing radiolytic production of H < sub > 2 O < sub > 2 and development of zebrafish embryos after ultra high dose rate exposure with electron and transmission proton beams. Radiother Oncol 175:197–202. https://doi.org/10.1016/j.radonc.2022.07.011
82. Bin J, Obst-Huebl L, Mao J-H, Nakamura K, Geulig LD, Chang H et al (2022) A new platform for ultra-high dose rate radiobiological research using the BELLA PW laser proton beamline. Sci Rep 12(1):1484. https://doi.org/10.1038/s41598-022-05181-3
83. Varian, aSHC (2022) : Feasibility Study of FLASH Radiotherapy for the Treatment of Symptomatic Bone Metastases. https://ClinicalTrials.gov/show/NCT04592887 Accessed
84. Chow R, Kang M, Wei S, Choi JI, Press RH, Hasan S et al (2021) FLASH radiation therapy: review of the literature and considerations for future research and proton therapy FLASH trials. Appl Radiat Oncol 10(2):15–21
85. Mascia AE, Daugherty EC, Zhang Y, Lee E, Xiao Z, Sertorio M et al (2022) Proton FLASH Radiotherapy for the treatment of symptomatic bone metastases: the FAST-01 Nonrandomized Trial. JAMA Oncol. https://doi.org/10.1001/jamaoncol.2022.5843
86. Zakaria AM, Colangelo NW, Meesungnoen J, Jay-Gerin J-P (2021) Transient hypoxia in water irradiated by swift carbon ions at ultra-high dose rates: implication for FLASH carbon-ion therapy. Can J Chem 99(10):842–849. https://doi.org/10.1139/cjc-2021-0110
87. Wilson JD, Hammond EM, Higgins GS, Petersson K (2020) Ultra-High Dose Rate (FLASH) Radiotherapy: silver bullet or Fool's gold? Front Oncol 9. https://doi.org/10.3389/fonc.2019.01563
88. Alizadeh E, Sanz AG, García G, Sanche L (2013) Radiation damage to DNA: the Indirect Effect of Low-Energy Electrons. J Phys Chem Lett 4(5):820–825. https://doi.org/10.1021/jz4000998
89. Srinivas US, Tan BWQ, Vellayappan BA, Jeyasekharan AD (2019) ROS and the DNA damage response in cancer. Redox Biol 25. https://doi.org/10.1016/j.redox.2018.101084
90. Maier P, Hartmann L, Wenz F, Herskind C (2016) Cellular Pathways in response to Ionizing Radiation and their targetability

for Tumor Radiosensitization. Int J Mol Sci 17(1). https://doi.org/10.3390/ijms17010102
91. Durante M, Vozenin M-C, Breneman J, Dong L, Scifoni E (2021) Panel discussion – FLASH therapy. Particle Therapy Co-Operative Group (PTCOG), Online
92. Boscolo D, Scifoni E, Durante M, Kramer M, Fuss MC (2021) May oxygen depletion explain the FLASH effect? A chemical track structure analysis. Radiother Oncol 162:68–75. https://doi.org/10.1016/j.radonc.2021.06.031
93. Kim Y-E, Gwak S-H, Hong B-J, Oh J-M, Choi H-S, Kim MS et al (2021) Effects of Ultra-high doserate FLASH irradiation on the Tumor Microenvironment in Lewis Lung Carcinoma: role of myosin light chain. Int J Radiation Oncology*Biology*Physics 109(5):1440–1453. https://doi.org/10.1016/j.ijrobp.2020.11.012
94. Ilicic K, Combs SE, Schmid TE (2018) New insights in the relative radiobiological effectiveness of proton irradiation. Radiat Oncol 13(1). https://doi.org/10.1186/s13014-018-0954-9
95. Nickoloff JA, Sharma N, Taylor L, Clustered DNA, Double-Strand (2020) Breaks: Biological Effects and Relevance to Cancer Radiotherapy. Genes 11(1). https://doi.org/10.3390/genes11010099
96. Alhmoud JF, Woolley JF, Al Moustafa A-E, Malki MI (2020) DNA Damage/Repair management in cancers. Cancers 12(4). https://doi.org/10.3390/cancers12041050
97. Szymonowicz K, Krysztofiak A, van der Linden J, Kern A, Deycmar S, Oeck S et al (2020) Proton Irradiation increases the necessity for homologous recombination repair along with the indispensability of non-homologous end joining. Cells 9(4). https://doi.org/10.3390/cells9040889
98. Konopacka M, Rogoliński J, Sochanik A, Ślosarek K (2016) Can high dose rates used in cancer radiotherapy change therapeutic effectiveness? Współczesna Onkologia 6:449–452. https://doi.org/10.5114/wo.2016.65603
99. Jeong H, Bok S, Hong B-J, Choi H-S, Ahn GO (2016) Radiation-induced immune responses: mechanisms and therapeutic perspectives. Blood Res 51(3). https://doi.org/10.5045/br.2016.51.3.157
100. Takahashi J, Nagasawa S (2020) Immunostimulatory Effects of Radiotherapy for local and systemic control of Melanoma: a review. Int J Mol Sci 21(23). https://doi.org/10.3390/ijms21239324
101. Demaria S, Formenti SC (2016) Can abscopal effects of local radiotherapy be predicted by modeling T cell trafficking? J Immunother Cancer 4(1). https://doi.org/10.1186/s40425-016-0133-1
102. Jin JY, Gu A, Wang W, Oleinick NL, Machtay M, Kong FM (2020) FLASH dose rate effect on circulating immune cells: a potential mechanism for FLASH-RT? Int J Radiat Oncol Biol Phys 108(3). https://doi.org/10.1016/j.ijrobp.2020.07.2079
103. Pratx G, Kapp DS (2019) A computational model of radiolytic oxygen depletion during FLASH irradiation and its effect on the oxygen enhancement ratio. Phys Med Biol 64(18):185005. https://doi.org/10.1088/1361-6560/ab3769
104. Chaudhary P, Milluzzo G, Ahmed H, Odlozilik B, McMurray A, Prise KM et al (2021) Radiobiology experiments with Ultra-high Dose Rate Laser-Driven Protons: Methodology and State-of-the-art. Front Phys 9. https://doi.org/10.3389/fphy.2021.624963
105. Petersson K, Adrian G, Butterworth K, McMahon SJ (2020) A quantitative analysis of the role of oxygen tension in FLASH radiation therapy. Int J Radiat Oncol Biol Phys 107(3):539–547. https://doi.org/10.1016/j.ijrobp.2020.02.634
106. Zhu H, Li J, Deng X, Qiu R, Wu Z, Zhang H (2021) Modeling of cellular response after FLASH irradiation: a quantitative analysis based on the radiolytic oxygen depletion hypothesis. Phys Med Biol 66(18). https://doi.org/10.1088/1361-6560/ac226d
107. Koch CJ, Re (2019) Differential impact of FLASH versus conventional dose rate irradiation: Spitz. Radiother Oncol 139:62–63. https://doi.org/10.1016/j.radonc.2019.07.004
108. Spitz DR, Buettner GR, Petronek MS, St-Aubin JJ, Flynn RT, Waldron TJ et al (2019) An integrated physico-chemical approach for explaining the differential impact of FLASH versus conventional dose rate irradiation on cancer and normal tissue responses. Radiother Oncol 139:23–27. https://doi.org/10.1016/j.radonc.2019.03.028
109. Abolfath R, Grosshans D, Mohan R (2020) Oxygen depletion in FLASH ultra-high-dose-rate radiotherapy: a molecular dynamics simulation. Med Phys 47(12):6551–6561. https://doi.org/10.1002/mp.14548
110. Labarbe R, Hotoiu L, Barbier J, Favaudon V (2020) A physicochemical model of reaction kinetics supports peroxyl radical recombination as the main determinant of the FLASH effect. Radiother Oncol 153:303–310. https://doi.org/10.1016/j.radonc.2020.06.001
111. Jansen J, Knoll J, Beyreuther E, Pawelke J, Skuza R, Hanley R et al (2021) Does FLASH deplete oxygen? Experimental evaluation for photons, protons, and carbon ions. Med Phys 48(7):3982–3990. https://doi.org/10.1002/mp.14917
112. Khan S, Bassenne M, Wang J, Manjappa R, Melemenidis S, Breitkreutz DY et al (2021) Multicellular spheroids as in vitro models of oxygen depletion during FLASH irradiation. Int J Radiat Oncol Biol Phys 110(3):833–844. https://doi.org/10.1016/j.ijrobp.2021.01.050

Publisher's Note Springer Nature remains neutral with regard to jurisdictional claims in published maps and institutional affiliations.

Springer Nature or its licensor (e.g. a society or other partner) holds exclusive rights to this article under a publishing agreement with the author(s) or other rightsholder(s); author self-archiving of the accepted manuscript version of this article is solely governed by the terms of such publishing agreement and applicable law.

3.4.3 Updated Systematic Search

Since the last literature search conducted on 8th of December 2022, there have been 114 particle-FLASH studies published based on the search terms used in the systematic review. Of these, 19 meet the criteria outlined in the systematic review, particularly pertaining to preclinical and clinical data concerning FLASH-induced radiobiological effects. This update adds to the content of the particle-FLASH systematic review with literature published in 2023 and 2024. The update was conducted on the 11th of December 2024.

Three *in vitro* studies were identified, all of which were proton-FLASH driven. Yagi *et al.* 2024 [87] irradiated human papillomavirus-related cervical adenocarcinoma cell line HSGc-C5 and human dermal fibroblasts (HDF) with 0 - 24 Gy of 230 MeV protons at both 250 Gy/s and 1 Gy/s (FLASH vs CONV), and with the center of the spread-out Bragg peak (SOBP). Under normoxic conditions, cell survival increased for both the tumour HSGc-C5 and normal HDF cell types at doses over 20 Gy, as well as showing increased γH2AX foci under CONV vs FLASH [87]. Similar findings were reported in A549 cells irradiated with 0 – 6 Gy 660 MeV protons at 70 Gy/s FLASH and 0.1 Gy/s CONV, where the fraction of surviving tumour cells increased at doses of 4 and 6 Gy [88]. Contrastingly, one of these studies determining the effects of hypoxia under FLASH and CONV conflicts with the findings of these previous two studies. Clonogenicity was measured in non-tumour (U-251) and tumourigenic (A549) cells irradiated with 0 – 18 Gy 230 MeV protons at > 50 Gy/s FLASH or 0.1 Gy/s CONV. No significant differences in cell survival were observed at FLASH dose rates under normoxia or hypoxia for both cell lines compared to CONV [89]. Even in this limited pool of *in vitro* studies, this is exemplary of conflicting evidence of a beneficial FLASH effect regarding cell clonogenicity, even when using identical cell lines as per the latter two studies discussed here irradiating A549 cells [88, 89].

In vivo publications predominated literature, with mice and zebrafish studies analysing the dependency of FLASH on tissue toxicity, inflammation in normal tissues and immune system infiltration into tumours, neurocognition, and overall animal survival. Findings from normal skin toxicity studies in mice possess a few key findings. The first of these is that using different fractionation schemes affects normal tissue sparing. Single-beam delivery at doses between 30 – 40 Gy at dose

rates of 80 – 100 Gy/s for FLASH showed a significant FLASH effect in hind leg irradiations of mice. However, when splitting the dose into 2 deliveries, this sparing reduced compared to a single delivery. When increasing to three or more separate deliveries of the same total dose, the benefits of FLASH were lost entirely compared to CONV [90, 91]. Another interesting insight is that there may be a tissue dependency on the threshold dose rate at which FLASH tissue sparing can be observed. More specifically, Sørensen *et al.* 2024 [90] displayed that radiosensitive tissues required higher dose rates to see reduced toxicity per a FLASH effect, whilst less sensitive tissues exhibited reduced toxicity at lower dose rates. One of the most interesting of these instances was that a sparing effect, comparable to FLASH, was observed when using 2 - 5.6 Gy/s [90], which is unexpected considering the definition of FLASH at > 40 Gy/s. This suggests that moderate increases in dose rate greater than typical Gy/min CONV dose rates used currently but less than the ultra-high dose rates used by FLASH could be equally effective in mitigating normal tissue toxicity. Other publications measuring mice skin toxicity show that SOBP proton-FLASH retains the normal tissue sparing effect of FLASH [92], and minimising the degree of radiation-induced inflammation including reducing epidermis thickness, collagen deposition or skin contraction compared to CONV [93]. An interesting finding relating to oxygen depletion in Zhang *et al.* 2023 [93] was that mice that that had their legs tied to limit blood flow or were breathing pure oxygen had a reversal of sparing in normal tissues under FLASH, with responses similar to CONV [93]. Oxygenation during anaesthesia also appears to eliminate the benefits of FLASH in irradiation of brain tissue in rats, with the neurocognitive benefits and anti-tumour modulation lost versus CONV [94]. Similar brain irradiation studies in normoxic conditions preserves the neurocognitive benefits FLASH confers and even enhances tumour control [95-97].

The effects of FLASH on mice survival were also determined for abdominal, heart and head and neck irradiation. Amongst these studies, most showed improved overall survival, functional capabilities of organs irradiated, and reduced expression of inflammatory factors under FLASH versus CONV [98-100]. However, findings from Bell *et al.* 2024 [101] show that mice lethality is actually increased when using proton-FLASH rather than CONV at a dose of 14 Gy 4

days post-irradiation [101], with no differences in intestinal cell proliferation between dose rates. In studies irradiating zebrafish embryos, one study displayed an improvement in zebrafish morphology and viability with increased FLASH dose rates compared to CONV post-irradiation [102] whilst another reported reduced impact of FLASH on body length and pericardial edema, but no differences observed for spinal curvature or viability between FLASH and CONV [103].

Finally, Varian have also started a second proton-FLASH clinical trial on the 8th of March 2023 (ClinicalTrials.gov: NCT05524064) called FAST-02. As per the FAST-01 clinical trial [104] for which a protocol has recently been published [105], the FAST-02 trial has been approved for > 40 Gy/s proton FLASH using 8 Gy in a single fraction, for 10 patients with 1 – 3 painful bone metastases in the thorax. Conducted at Cincinnati Children's Hospital Medical Center, it has been approved under the FDA Investigational Device Exemption. The primary endpoints of this study are determining FLASH's pain relief capabilities and safety for in-human treatments [106]. This study is expected to complete on the 1st of April 2025.

Most *in vitro* and *in vivo* FLASH studies detailed here appear to show benefits of ultra-high dose rate irradiations. Despite this, there is still a small proportion of publications which appear to conflict with these findings, reporting equivalent or enhanced toxicity of FLASH compared to CONV. It is also encouraging to see more emphasis placed on dosimetric validation of FLASH delivery through a combination of more rigorous dose measurement and simulation work [107-115], as well as use of the Bragg peak for irradiations [87, 92]. Akin to the findings of the systematic review, although key hypotheses of FLASH are implied from the data here such as oxygen depletion and immune modulation, there is still no established mechanism for the positive (or negative) effects observed.

3.5 Conclusion

These literature reviews encompass several key aspects of DNA damage and repair research to further the development of experimental therapeutics. They explore novel DSB detection assays through immunofluorescence techniques, which offer enhanced sensitivity and specificity compared to traditional methods,

allowing for more accurate detection of DNA damage in various experimental settings. The reviews also delved into the essential components of the DNA damage repair response, detailing the activation timeframes of key DDR proteins and the regulatory mechanisms involved in their recruitment and function. In addition, an overview of FLASH radiotherapy was presented, discussing its historical use with X-rays and the subsequent expansion of this research to proton and carbon ion experiments, which offer distinct advantages in terms of precision and tissue sparing. Together, these reviews established a solid framework for the experimental work in this PhD project, particularly in optimising STRIDE as a reliable DSB detection marker. Furthermore, they provided insights that informed the verification of STRIDE's ability to detect DNA damage induced by treatments such as AuNPs, ATMi, and FLASH radiotherapy, thus setting the stage for subsequent experimental investigations and enhancing knowledge of DNA repair mechanisms in the context of novel therapeutic approaches.

4 Quantification of DNA double-strand break damage and repair kinetics using novel IHC markers

4.1 Introduction

Reviewing literature about double-stranded breaks (DSBs) and DNA damage response (DDR) detection techniques through immunofluorescence microscopy revealed the most established of these techniques. For DSB detection this was SensiTive Recognition of Individual DNA Ends (STRIDE), and for the DDR this was γH2AX. γH2AX has been frequently used as a measure of genotoxicity [25, 30, 116], often conflated for DSB presence as previously discussed in Chapter 3.2 and 3.3. Although developed relatively recently, the STRIDE protocol is the most published DSB detection method compared to similar DSB techniques [37, 117-120]. It is also appropriate regarding its lack of reliance on endogenous regulation for its activity, which allows for direct detection of DSBs without variability in DDR expression affecting quantification. However, multiple steps throughout the STRIDE protocol, which has added complexity compared to DDR detection protocols, needed thorough optimisation throughout all steps of the methodology. After validating STRIDE and co-staining with γH2AX, it was then applied to characterise radiation induced DNA damage from X-rays, as well as radiosensitisers. This included 2 Gy X-rays alone and in combination with either gold nanoparticles (AuNPs) or ATM inhibitor (ATMi) AZD1390, both of which have been shown to have DDR suppressive capabilities [10, 48, 72, 121].

4.2 Immunofluorescence Staining Optimisations

4.2.1 γH2AX Response to Neocarzinostatin

Prior to optimising the intricate STRIDE protocol, a preliminary experiment was first conducted to test whether the immunofluorescence staining protocol of γH2AX was appropriate. To achieve this, 4T1 cells were exposed to varying concentrations of neocarzinostatin (NCS). NCS is an antitumour radiomimetic drug that when introduced into the cellular environment, causes the production of ROS that damage DNA and promotes activation of the DDR [122-124]. Cells were fixed 1 hour after exposure to 0 µg/mL, 1 µg/mL or 10 µg/mL of NCS (Figure 8).

Apart from the presence of a few pan-stained cells in the negative control 0 µg/mL condition, the intensity of γH2AX signal amongst the cell population increases as the dosage of NCS increases (Figure 8). This result is expected as when NCS is introduced, the production of ROS will consequently induce DSBs that will activate the DDR, including γH2AX. With this incremental increase in γH2AX signal for increasing NCS doses, this therefore was sufficient to validate the γH2AX staining protocol.

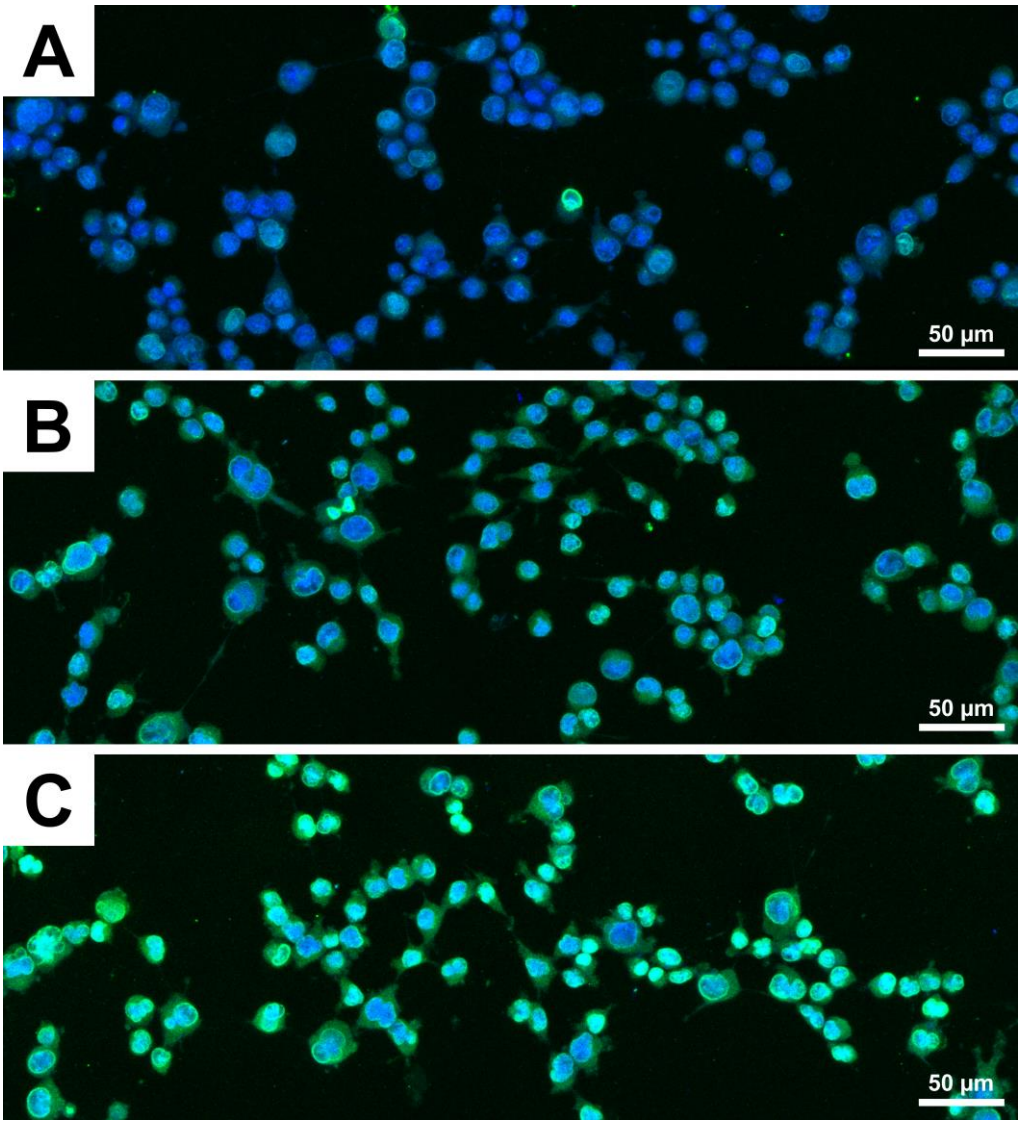


Figure 8: 20x immunofluorescence images of 4T1 cells stained with anti-γH2AX Alexa 488 conjugate (green) representing phosphorylated histone 2AX, and DAPI (blue) representing nuclei. Each condition was treated with varying concentrations of neocarzinostatin for 1 hour and then fixed simultaneously. A.) Negative control, 0 µg/mL NCS., B.) 'Low' dose, 1 µg/mL NCS, and C.) 'High' dose, 10 µg/mL NCS.

4.2.2 STRIDE Validation in Response to Hydrogen Peroxide

After verifying the γH2AX staining protocol, optimisations progressed to validating each step of the STRIDE protocol, which has much greater technical complexity compared to the γH2AX staining protocol. The STRIDE process involves the use of a combination of TUNEL assay reagents to conjugate BrdUTP to DNA ends, followed by addition of two primary and two secondary antibodies against BrdU, and finally amplification of the fluorescence signal through a proximity ligation reaction between the two Duolink secondary antibodies. To validate STRIDE, preliminary experiments were conducted with hydrogen peroxide (H_2O_2) at varying exposure times to determine whether increases in H_2O_2 exposure time correlated with an increase in the frequency of DNA DSBs, represented by STRIDE foci. A concentration of 20 mM was selected to induce a high degree of toxicity [125], to make the induction of DSBs more frequent and to provide high contrast against control conditions where spontaneous DSBs may have been detected. The first of these experiments was performed with 4T1 cells with H_2O_2 exposure times of 0 (no H_2O_2 exposure, negative control), 15, 30 and 60 minutes (Figure 9).

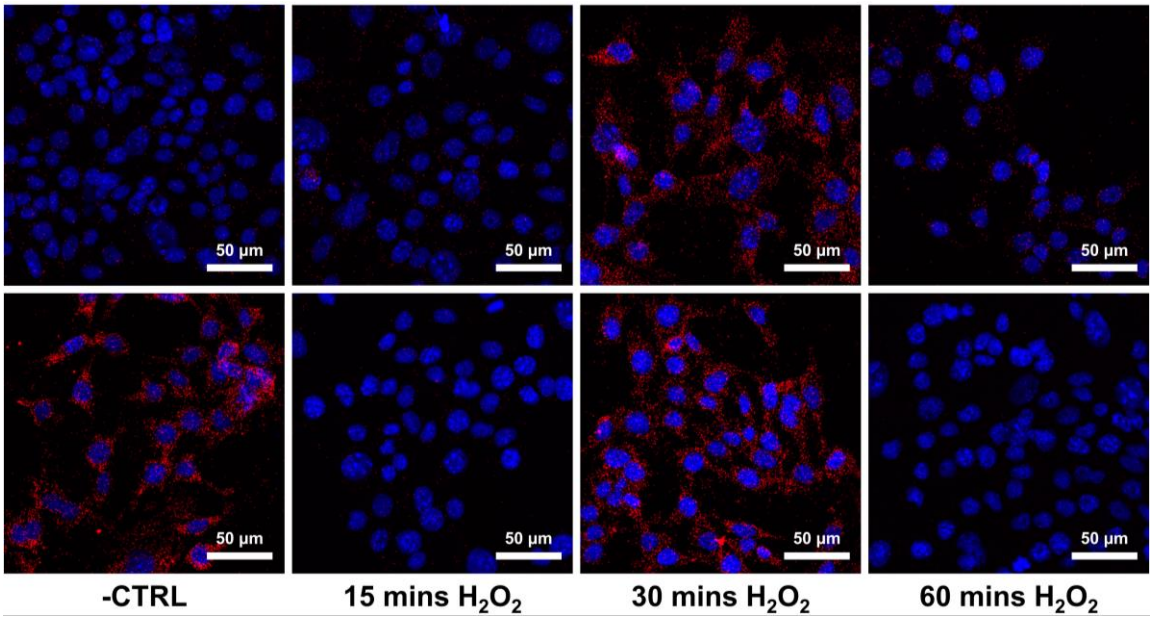


Figure 9: 4T1 cells stained with DAPI (blue) and STRIDE (red) exposed to 20 mM H_2O_2 for different exposure times and fixed immediately after. Duplicates are represented in each column (top row = first duplicate, bottom row = second duplicate), with negative control (-CTRL) representing no H_2O_2 exposure, and 15, 30 and 60 minutes H_2O_2 exposure times respectively. Images were captured at 20x magnification.

Here it appears that 30 minutes H_2O_2 has the most STRIDE foci, compared to 15 or 60 minutes H_2O_2. The second replicate of the negative control also appears to possess STRIDE staining. These findings were unexpected given that the 30 minutes exposure condition apparently induced a higher STRIDE signal compared to 60 minutes exposure. The signal present in one of the negative control replicates suggested that there may be non-specific or off-target antibody binding, as these wells should have minimal DSBs without peroxide exposure. To diagnose the source of this issue, multiple troubleshooting experiments were conducted, the first of these being to determine whether any components of the STRIDE protocol are binding within cells non-specifically. The first optimization displayed in Figure 10 tested whether off-target binding may be caused by the secondary antibodies or in the TUNEL step of the protocol.

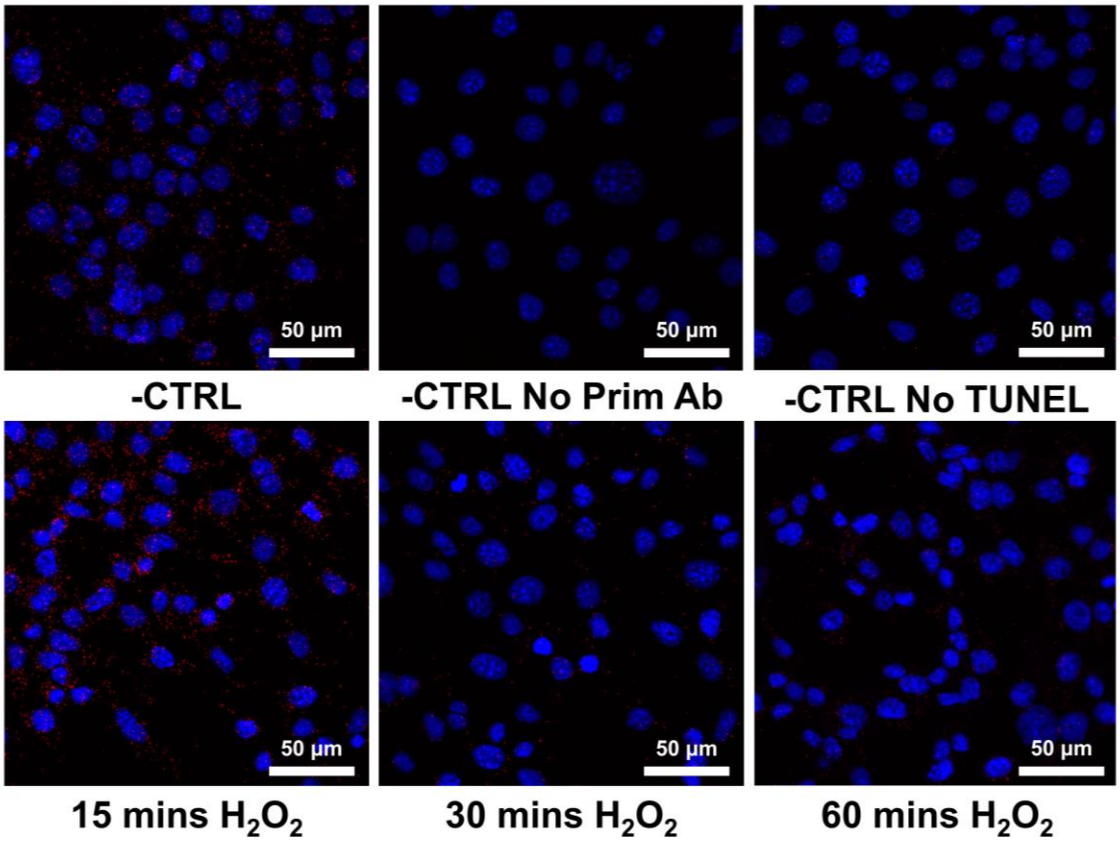


Figure 10: 4T1 cells stained with DAPI (blue) and STRIDE (red) exposed to 20 mM H_2O_2 for different exposure times followed by fixation. Cells were either not treated with H_2O_2 as a negative control (-CTRL), negative control and stained with STRIDE without the primary antibodies (-CTRL No Prim Ab), negative control stained with STRIDE without the TUNEL reagents of the STRIDE protocol (-CRL No TUNEL), and treated with H_2O_2 for 15, 30 and 60 minutes. Images were captured at 20x magnification.

As shown in the -CTRL sample (Figure 10), it appears there were still either low levels of spontaneous DSB formation or some degree of non-specificity causing STRIDE signal to be present. When removing the primary antibodies or TUNEL reagents however, it appeared that there were nearly no foci formed as expected. Red foci appeared in some cells for these samples, but it was difficult to conclude whether they were a result of applying STRIDE or background signal/debris since they are so few and do not appear in every cell. Overall, it appeared that without the TUNEL (-CTRL No TUNEL) or primary antibody (-CTRL No Prim Ab) steps of the STRIDE protocol, that foci were unable to form as per the H_2O_2 exposure or -CTRL conditions. The STRIDE signal at 15 minutes H_2O_2 exposure appears higher than that of both 30 and 60 minutes, which was another point of confusion as per similar findings in Figure 9. As some foci were still detected in the -CTRL conditions, the steps that these negative controls tested were verified further (Figure 11).

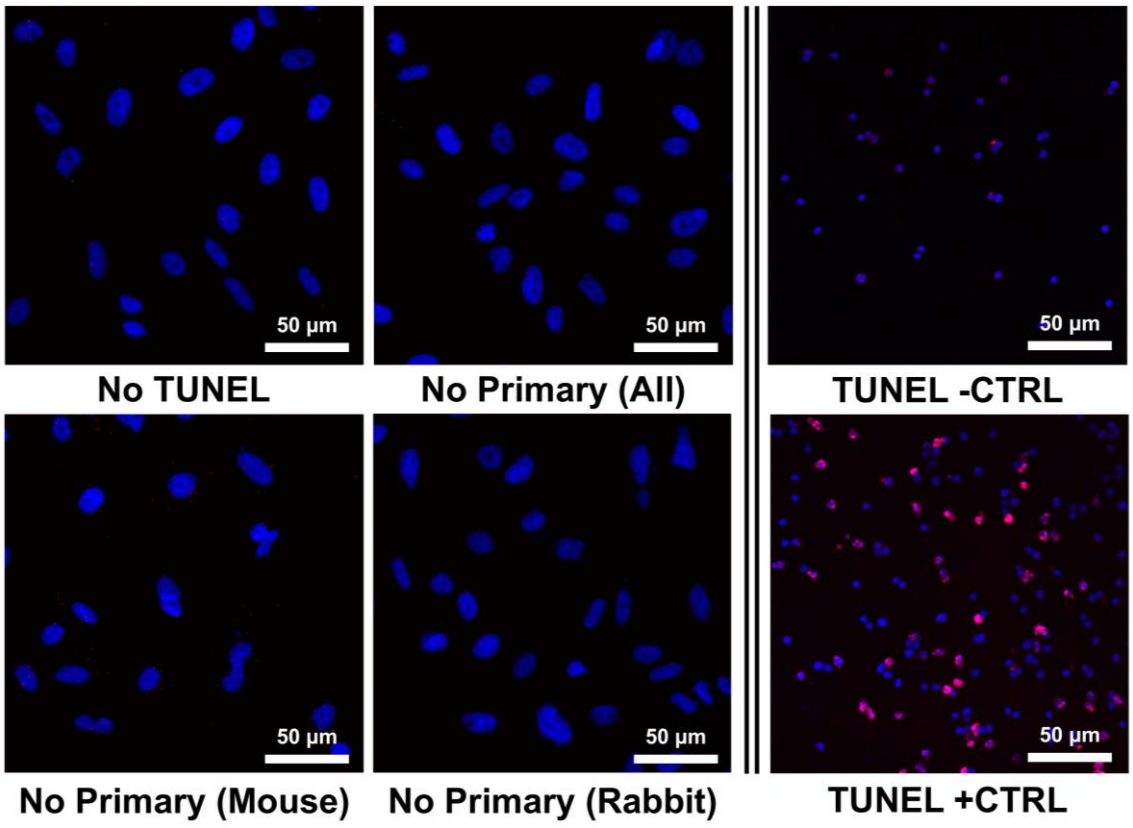


Figure 11: 4T1 cells stained with DAPI (blue) and STRIDE (red) with no TUNEL (top row, left), no primary antibodies (top row, middle), no mouse primary antibody (bottom row, left), or no rabbit primary antibody (bottom row, middle). Negative and positive control samples of HL-60 were also stained with DAPI (blue) and anti-BrdU antibody (red), represented by TUNEL -CTRL (top row,

right) and TUNEL +CTRL (bottom row, right) respectively. Images were captured at 20x magnification.

One out of the two primary antibodies used for STRIDE staining may have been responsible for the small degree of off-target staining in the -CTRL samples in Figure 10. As such, STRIDE staining was conducted with only one out of the two antibodies (i.e., the entire STRIDE protocol but with no mouse or no rabbit primary antibody). Positive and negative control cells within the TUNEL assay kit itself were also tested to determine whether applying TUNEL staining alone revealed a degree of non-specificity. From Figure 11, it appears that when key components of the STRIDE protocol are removed, including TUNEL, both primary antibodies, or one of the mouse or rabbit primary antibodies, that no STRIDE foci form. Furthermore, it appears that the function of TUNEL assay, which detects cell fragmentation through BrdU conjugation to DNA ends [126], also works as intended, with an increased TUNEL signal for the positive control cells and minimal TUNEL signal in negative control cells (Figure 11). Background STRIDE foci formation observed in negative controls was therefore unlikely to be due to off-target binding of either of the primary antibodies. When BrdU conjugation is removed from the STRIDE protocol, thereby removing the anti-BrdU primary antibody binding site, a loss of STRIDE signal is also observed. Therefore, there other aspects of the protocol were optimised to minimise background STRIDE signals in the negative control samples where cells were not purposefully exposed to genotoxicity. This included testing blocking buffers (Figure 12), wash frequency (

Figure 13), and fixative (Figure 14).

The blocking buffer serves two purposes in the STRIDE protocol: to block the cells prior to antibody incubation, and to act as a diluent for primary and secondary antibodies. A Duolink blocking solution/antibody diluent was used in all optimisation steps until this stage. However, given that there was background signal in the negative controls that could not be explained by off-target primary antibody binding in the negative controls, then inadequate blocking may have been responsible. This was tested by applying both the Duolink blocking buffer and a mixture of Phosphate Buffered Saline (PBS), Tween-20 and Bovine Serum Albumin (BSA), a widespread antibody blocking solution [127].

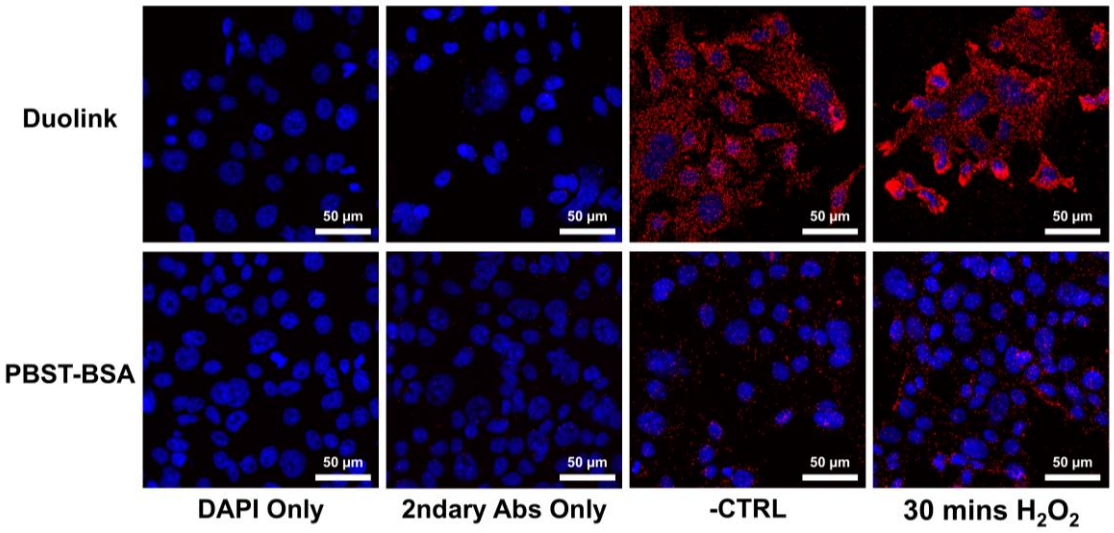


Figure 12: 4T1 cells stained with DAPI (blue) and STRIDE (red), blocked (and antibodies diluted) with either Duolink blocking buffer (top row) or PBST-BSA (bottom row). For either of these blocking buffers, a DAPI only stain was applied (without STRIDE), the secondary antibodies + fluorophore (2ndary Abs Only), -CTRL (0 minutes H_2O_2 exposure), and 30 minutes 20 mM H_2O_2 exposure. Images captured at 20x magnification.

Figure 12 shows that, at least for these samples and the fields of view imaged, that PBST-BSA reduces the degree of background signal in negative control compared to the Duolink blocking buffer. When Duolink blocking was utilised, it seems that STRIDE staining had minimal differences between negative control and 30 minutes H_2O_2 exposure. DAPI and secondary antibody only samples do not present background STRIDE foci for either blocking buffer used. However, even in the negative control sample with PBST-BSA blocking, background foci are still present. This led to attempting to increase the frequency of washing throughout the protocol, incorporating the change in blocking buffer to PBST-BSA. Figure 13 shows that when washing was increased from three times per washing step with washing buffer to five times, that background STRIDE foci formation was reduced. Here, there was still a discrepancy where foci under the 60-minute H_2O_2 exposure time were fewer than 15- or 30-minutes exposure for 5 times washed samples (Figure 13). The reason for this occurring is uncertain, however it could be due to either variations in the staining of STRIDE throughout each well, which would be difficult to validate without whole-well imaging, or even variations in how H_2O_2 is perfused within the intracellular environment of cells in each well, potentially leading to changes in DSB formation.

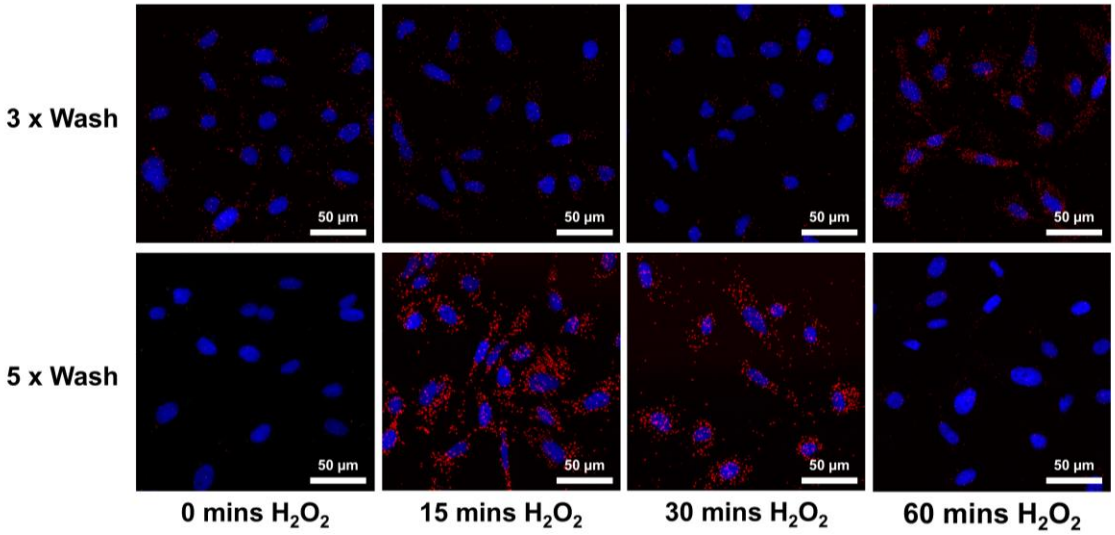


Figure 13: PC-3 cells stained with DAPI (blue) and STRIDE (red) washed either three (top row) or five (bottom row) times with wash buffer between STRIDE protocol steps. Cells were also exposed to 20 mM H_2O_2 for 0 (negative control), 15, 30 and 60 minutes and fixed immediately after. Images captured at 20x magnification.

The final stage of STRIDE optimisation was to determine the best method for cell fixation. Paraformaldehyde (PFA) and Ethanol (EtOH) fixatives were compared (Figure 14). Either fixative was equally efficient after exposure of cells to no H_2O_2 or 60 minutes H_2O_2, evidenced at both 20x and 63x magnifications. It appeared that there was an increase in STRIDE foci for cells exposed to H_2O_2, with a small degree of background in negative controls.

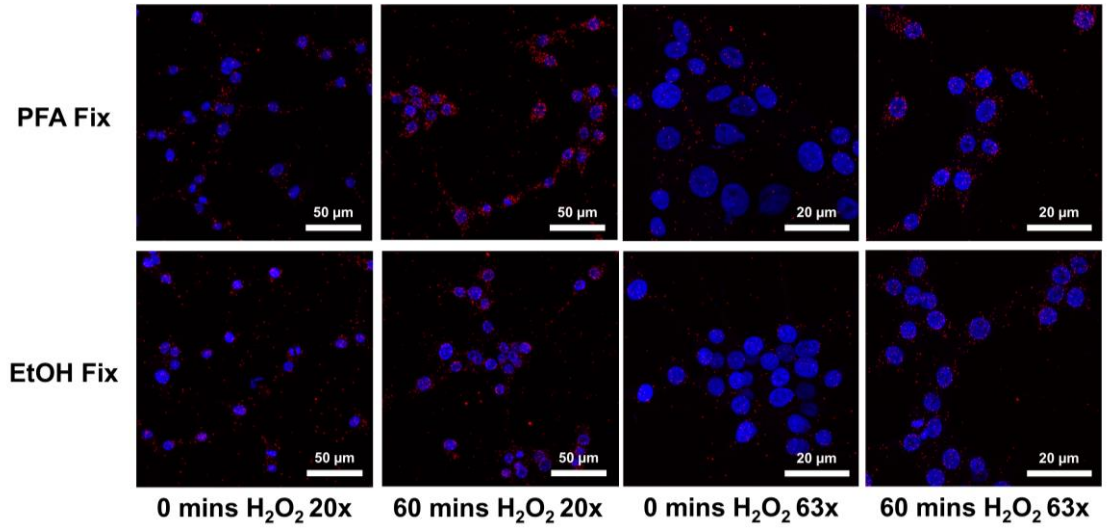


Figure 14: U87 cells stained with DAPI (blue) and STRIDE (red) and fixed with either 4% paraformaldehyde (PFA) or 95% EtOH + 5% glacial acetic acid. Cells were either exposed to no

H_2O_2 (0 mins H_2O_2) or H_2O_2 for 60 minutes. Images were captured at both 20x and 63x magnification for all conditions.

At this stage, small numbers of STRIDE foci were accepted as spontaneous DNA damage, representative of the ~50 endogenous DSBs that occur per cell cycle [128], considering that foci formation in negative controls is far fewer compared to H_2O_2 treated samples. STRIDE was then applied in combination with γH2AX staining. The STRIDE protocol was applied first, followed by γH2AX immunostaining, and finally a DAPI counterstain. An ATMi was also tested to determine whether it was capable of inhibiting γH2AX foci formation with and without H_2O_2 inducing DSBs. Figure 15 highlights this experiment, where PC-3 cells were treated with AZD1390 1 hour prior to exposure to H_2O_2. STRIDE co-stained with γH2AX appeared to work well, with both markers presenting foci when exposed to H_2O_2 exclusively (Figure 15).

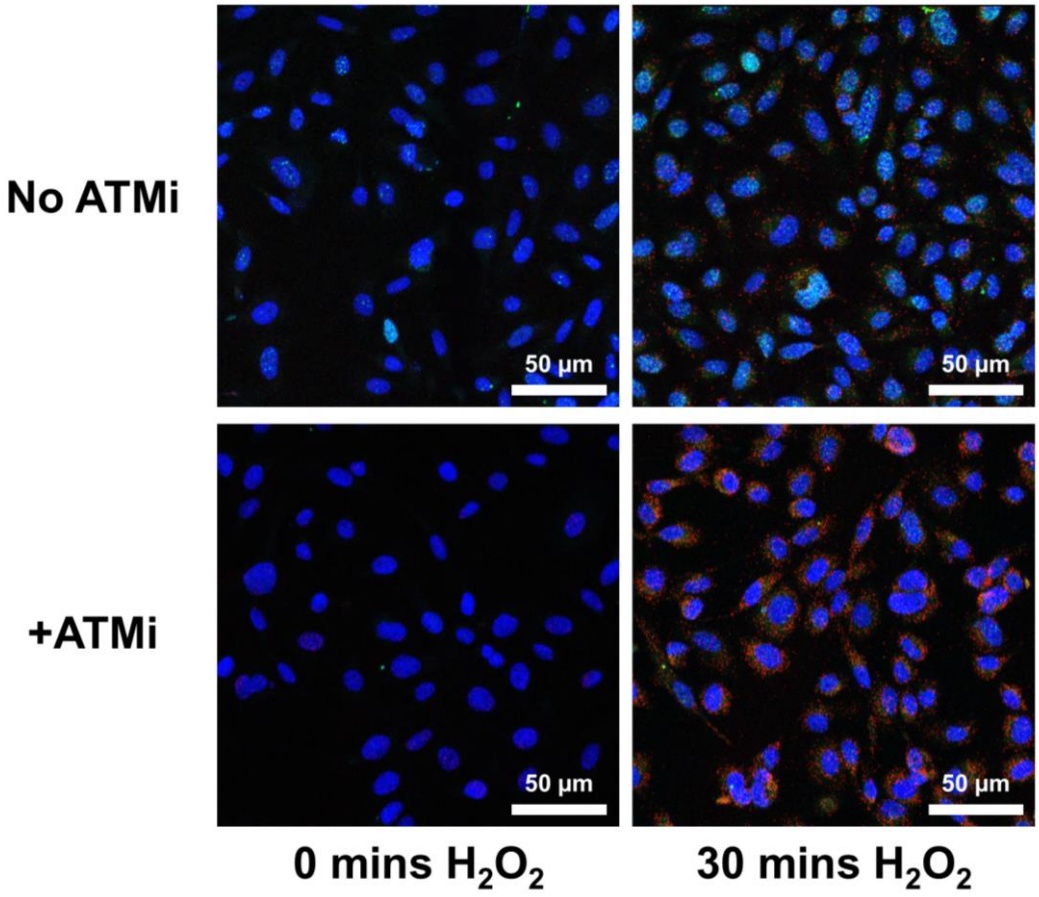


Figure 15: PC-3 cells stained with DAPI (blue), STRIDE (red) and anti-γH2AX Alexa 488 (green). Cells were exposed to either: no ATMi or H_2O_2 (top left), no ATMi and H_2O_2 for 30 minutes (top right), ATM inhibitor and no H_2O_2 (bottom left), and ATM inhibitor and H_2O_2 (bottom right). ATMi

AZD1390 was prepared to a final dilution of 30 nM, and H_2O_2 to a final concentration of 20 mM in wells where appropriate.

Furthermore, AZD1390 inhibition of γH2AX phosphorylation also appeared successful, eliminating any γH2AX signal in the 0 minutes H_2O_2 sample in addition to the 30 minutes sample. STRIDE foci formation at these timepoints did not appear to be affected by ATMi pre-treatment, strongly supporting that the DSB detection capabilities of STRIDE are independent of activity of γH2AX. Incorporating all previous optimisations into this final preliminary experiment enabled us to validate not only the action of STRIDE versus γH2AX, but also AZD1390 as an ATMi capable of suppressing γH2AX activity. All these optimisation steps then carried onto every experiment with STRIDE and γH2AX staining following this, including in vitro irradiations with X-rays and protons in combination with AuNPs and ATMi.

4.3 Gold Nanoparticles Cause Radiosensitization in 4T1 Cells by Inhibiting DNA Double Strand Break Repair: Single Cell Comparisons of DSB Formation and γH2AX Expression

4.3.1 Summary

Leading on from the preliminary experiments validating the use of STRIDE against peroxide and optimising the variables within its extensive protocol, experiments progressed to X-ray irradiations in combination with radiosensitisers. The first of these analysed was AuNPs. Historically, hypotheses surrounding nanoparticle radiosensitisation focused on the enhancement of physical dose deposition as a driving factor, however this has shifted towards emphasis on the physicochemical, chemical and biological effects of AuNPs [9, 42, 43]. This publication explores the application of STRIDE to determine whether physical dose enhancement is achieved through introduction of AuNPs into the cellular environment, and to determine how AuNPs affect DDR repair kinetics when combined with X-rays.

Check for updates

ChemPhysChem

Research Article
doi.org/10.1002/cphc.202400764

Chemistry Europe
European Chemical Societies Publishing

www.chemphyschem.org

Gold Nanoparticles Cause Radiosensitization in 4T1 Cells by Inhibiting DNA Double Strand Break Repair: Single Cell Comparisons of DSB Formation and γH2AX Expression

Jake Atkinson,[a] Joshua Chopin,[b] Eva Bezak,[c, d] Hien Le,[c, e] and Ivan Kempson*[a]

Metal nanoparticles sensitize cancers to radiotherapy however their mechanisms of action are complex. The conceptual inspiration arose from theories of physical dose deposition however various chemical and biological factors have also been identified. Interpretation of data has been limited by challenges in measuring true DNA damage compared to DNA damage repair factors. Here, we applied a new assay, STRIDE, for the first time to measure DNA double strand breaks (DSBs) in 4T1 cells as a model of triple negative breast cancer exposed to gold nanoparticles and radiation, and compared this to the common γH2AX assay for DSB repair. The STRIDE assay showed no increase in DSB detection 15 mins after irradiation for cells containing nanoparticles compared to cells without. Gold nanoparticles led to prolonged detection of DSBs after irradiation and delayed the DSB repair. The data show no evidence of increased radiation dose deposition with nanoparticles, but rather enhanced radiobiological effects resulting from nanoparticles which includes disruption of the recruitment of essential DDR machinery, thereby impairing DNA repair processes.

Introduction

X-ray radiotherapy has long been a cornerstone in the treatment of various cancers, particularly effective in targeting solid tumours. This technique leverages high-energy ionising radiation against cancers through damaging DNA directly via ionisation or indirectly through the production of reactive oxygen species (ROS). Both forms of damage result in the formation of DNA double-stranded breaks (DSBs), ultimately leading to the induction of apoptosis.[1] It is prescribed for a broad range of cancers, such as breast, prostate, lung, and head and neck cancers due to its precision and ability to target specific volumes noninvasively with minimal impact on surrounding healthy tissues.[2] Although treatments aim to minimise damage to surrounding organs at risk, exposure of healthy tissue is often necessary to deliver a substantial dose to the tumour volume in curative regimen. This places a limit on the total dose that can be safely delivered to the tumour site and as such, the effectiveness of utilising X-rays as a standalone treatment has all but plateaued. This has promoted a growing interest in adjuvant regimen that produce enhanced tumouricidal effects whilst reducing normal tissue complications even further. Combining radiotherapy with chemo and radiopharmaceuticals,[3] immunotherapies,[4] and metal nanoparticles,[5] holds promise in further sensitizing tumourigenic cells and thus improving patient outcomes.[6]

Amongst these metals, gold nanoparticles (AuNPs) rose to popularity as a radiosensitizer in preclinical studies due to being chemically inert, biocompatible and capable of functionalisation with various molecules to deliver drug payloads or increase their specificity to cancerous cells.[7] Early hypotheses on the use of AuNPs in cancer treatment focused on their ability to increase the physical dose of radiation delivered to cancer cells. AuNPs interact with X-rays and can lead to localised dose enhancement through producing secondary electrons, X-ray fluorescence, Compton scattering, Auger electron emission, and pair production, depending on X-ray energy. These interactions can increase the lethality of radiation to cancer cells through increasing the DNA DSBs.[8] However, it has become evident that the physical interaction of nanoparticles with incident X-rays alone does not fully explain the observed biological outcomes.[9] These enhanced therapeutic effects are more likely a combination of these physical processes, physicochemical process and complex biological mechanisms, including the induction of oxidative stress through reactive oxygen species, modulation of cellular signalling pathways, and effects on the tumour microenvironment.[9] Never-the-less, there are notable accomplishments for a number of nanoparticles receiving market approval or entering clinical trials to enhance radiotherapeutic effects.[10]

[a] J. Atkinson, I. Kempson
Future Industries Institute, University of South Australia, Mawson Lakes, SA 5095, Australia
E-mail: Ivan.Kempson@unisa.edu.au

[b] J. Chopin
Industrial AI Research Centre, University of South Australia, Mawson Lakes, SA 5095, Australia

[c] E. Bezak, H. Le
UniSA Allied Health and Human Performance, University of South Australia, Adelaide, SA 5095, Australia

[d] E. Bezak
Department of Physics, University of Adelaide, North Terrace, Adelaide, SA 5005, Australia

[e] H. Le
Department of Radiation Oncology, Royal Adelaide Hospital, Adelaide, SA 5000, Australia

Supporting information for this article is available on the WWW under https://doi.org/10.1002/cphc.202400764

© 2024 Wiley-VCH GmbH

For instance, Turnbull et al. (2019) showed evidence of AuNPs producing a bottleneck in DNA damage repair pathways through the downregulation of thymidylate synthase (TS).[5a] This is the only enzyme capable of de novo thymidine monophosphate synthesis, which is further phosphorylated to thymidine triphosphate, one of the four nucleoside triphosphates necessary for DNA replication and repair.[11,12] Downregulation of TS thereby impairs the ability to repair damaged DNA, contributing towards the radiosensitization effect observed. AuNP internalisation also increased the degree of DSB repair foci, as indicated by γH2AX foci formation, suggesting that the stalling of DNA repair by inhibiting critical repair components may contribute to an increase in the repair burden on the cell. Moreover, the study highlighted a preferential sensitization of S-phase cells to radiation in the presence of AuNPs. S-phase cells, actively replicating their DNA, are typically more resistant to radiation due to heightened DNA repair activities, but AuNPs disrupt this repair proficiency, increasing their vulnerability to radiation-induced stress.[5a]

Genotoxic insults require better diagnostic tools which are currently limited in their design. Previously, assays used to measure the severity of a genotoxic insult quantify the activation of DNA repair factors, notably γH2AX, ATM, and 53BP1. It is important to recognise these assays are a measure of DSB repair and not actual DSBs themselves. γH2AX has been correlated with DSB formation, as have other components of the DNA damage response (DDR). However, they are prone to inconsistencies because of numerous confounding factors. In cases where radiation causes catastrophic damage to genes encoding DDR proteins, normal regulation of these proteins' expression will be severely disrupted, causing variability in their activation. The activation of these factors may also differ between cell types, making direct comparison between normal and cancerous cell types inconclusive.[13] Therefore, although endogenous repair factors can be correlated with genotoxicity, and by extension the presence of DSBs under specific circumstances, they cannot directly represent DSB counts.[14] This is a pertinent issue in quantifying and characterising genotoxicity currently, as this places limits on our interpretation of the biological mechanisms that drive nanoparticle radiosensitization with and without radiation.

Novel immunofluorescence assays are capable of visualising sites of DNA damage and repair factors in situ. Recently developed techniques are even capable of resolving individual DSBs on a single-cell level. SensiTive Recognition of Individual DNA Ends (STRIDE) by Kordon et al. 2020 is one such technique, which uses a combination of BrdU conjugation, anti-BrdU antibodies, and a proximity ligation assay to mark DSB ends.[15] By analysing the formation of DSBs with STRIDE and pairing this with co-stain for a marker of DSB repair activation, such as γH2AX, we can compare DSB formation with repair factor kinetics. This is invaluable to conclude whether the internalisation of nanoparticles influences DSB formation, and whether this is the cause of the downregulation of factors required for DNA repair. We hypothesised that if the physical dose deposition appreciably increases with nanoparticles, we should observe an increase in DSB formation through the STRIDE assay. Here we used a gold nanoparticle stabilised with polyethyleneglycol (PEG) and functionalised with transferrin to target a receptor commonly overexpressed on cancer cells. We have previously validated that these particles have a radiosensitization effect both in vitro.[5a,16] and in vivo (unpublished). Understanding the interplay between DNA damage and repair is crucial for shaping our understanding of the use of radiosensitizers and we believe this to be the first report comparing kinetics of DSB formation and repair with nanoparticle radiosensitizers.

Materials and Methods

Cell Culture and Pre-Treatment

Mouse derived 4T1 (American Type Culture Collection, CRL-2539) cells were cultured with RPMI (Thermo Fisher: 11875093) in a 37 °C incubator at 95% relative humidity and 5% CO_2. 12 hours before irradiation, cells were seeded into Ibidi μ-Slide 8 Well chambered coverslips (Ibidi, 80826) at a density of 40,000 cells per well. 2 hours prior to irradiation, AuNPs were introduced to select conditions at a final concentration of 1 nM. The Turkevich method was used to synthesise AuNPs of size 16–18 nm[17] which were PEGylated and functionalised with transferrin as we have reported extensively previously.[5a,16,18] Conditions were performed in duplicate.

X-Ray Irradiation

X-ray irradiation was performed with a 160 kV RadSource 2000 Small Animal Irradiator located at the South Australian Health and Medical Research Institute (SAHMRI), Adelaide, Australia. Cells were irradiated for 45 seconds with a total dose delivered of approximately 1.93 Gy (0.0429 Gy/s). Cells were fixed incrementally at 15-, 30-, 45-, 60-, 120-, 240-, and 1440- minutes post-irradiation with 4% paraformaldehyde for 10 minutes at room temperature.

STRIDE Assay

Following fixation, cells were permeabilised in PBS/0.5%Triton X-100 for 10 min and subsequently incubated with 0.5–10 mM EDTA/PBS for 10 min at room temperature. Cells were washed with 100 μL of TUNEL kit Wash Buffer at room temperature. BrdUTP conjugation to DSB ends was performed with the APO-BrdU Kit (BD Biosciences, Cat No. 556405). A master mix of TdT enzyme, TdT reaction buffer, BrdUTP and ddH_2O was made according to the manufacturer's instructions. 50 uL of the BrdUTP conjugation master mix was added per well and incubated for 1 hour at 37 °C in a humidified incubator, followed by a wash with 100 μL of Rinse Buffer at room temperature. Each well was then blocked with 200 μL 3% BSA for 1 hour at 37 °C, then incubated with 40 μL of both Mouse MoBu-1 anti-BrdU (Abcam, 8039, 1:500) and Rabbit Polyclonal anti-BrdU (Abcam, ab152095, 1:200) antibodies in 3% BSA overnight at 4°C. Wells were then thoroughly washed with Duolink® In Situ Wash Buffers, Fluorescence, 1X Wash Buffer A (Sigma Aldrich, DUO82049) and incubated with 40 μL of Duolink® In Situ PLA® Probe Anti-Rabbit PLUS (Sigma Aldrich, DUO92002–100RXN) and Anti-Mouse MINUS (Sigma Aldrich, DUO92004–100RXN) master mixed in 3% BSA for 1 h in a 37 °C humidified incubator. Wells were then washed with 1X Wash Buffer A and incubated with 40 μL of ligation mix (Sigma Aldrich, DUO92013) for 30 minutes at 37 °C. Wells were washed with 1X Wash Buffer A and subsequently incubated with 40 μL polymerase mix (Sigma Aldrich,

© 2024 Wiley-VCH GmbH

14397641, 0, Downloaded from https://chemistry-europe.onlinelibrary.wiley.com/doi/10.1002/cphc.202400764 by University Of South Australia, Wiley Online Library on [25/11/2024]. See the Terms and Conditions (https://onlinelibrary.wiley.com/terms-and-conditions) on Wiley Online Library for rules of use; OA articles are governed by the applicable Creative Commons License

DUO92013) for 100 minutes at 37 °C. Finally, wells were washed for 10 minutes with 1X Wash Buffer B (Sigma Aldrich, DUO82049) at room temperature, and then 0.01X Wash Buffer B for 1 min.

γH2AX Assay

Cells were blocked with 3% BSA for 1 hour at 37 °C, followed by incubation with anti-phospho-histone H2 A.X (Ser139) (20E3) Rabbit mAb conjugated with Alexa Fluor 488 (Cell Signaling Technology, #9719). Finally, nuclear staining of the cells was performed with 1 mg/mL DAPI solution (Thermo Fisher, Cat No. 62248).

Confocal Imaging

The Zeiss LSM 710 and LSM 980 laser scanning confocal microscopes (Carl Zeiss, Germany) were used to acquire fluorescent images of cells with a Plan-Apochromat 20x/0.8 M27 lens. A total of 4 fields of view were acquired with a 10% overlap as well as multiple z-slices, to a final image size for each condition of 1950×1950 pixels. Laser excitation and emission spectra used for acquisition are as follows: STRIDE: λ_{ex} 644 nm; λ_{em} 669 nm (Cyanine 5, Zeiss Filter set 50); γH2AX: λ_{ex} 488 nm; λe_m 496 nm (Alexa 488); DAPI: λ_{ex} 350 nm; λ_{em} 470 nm.

Image Analysis

Acquired confocal images were stitched and z-stack maximum projections produced in ZEN (black edition) 3.0 SR and exported in .TIF format. Maximum projection images were then subsequently processed in CellProfiler 4.2.6. For γH2AX acquisition, images obtained from the confocal possessed bands of low brightness throughout each tile acquired. These patterns were identical for each tile within the entire image and represented an imaging artefact. Each image in this dataset was edited in Paint.net to remove these low/inconsistent brightness regions. When the borders between low and high brightness regions were not well defined, these were accentuated by adjusting the luminosity curves to better define regions of inconsistent brightness. These low brightness regions were then manually cropped, excluding them from downstream processing.

CellProfiler has several modules that perform different operations on a set of input images. The 'analysis pipeline' is summarised in Figure 1. Modules can be added, removed, or re-ordered depending on the needs of each experimental run. Our process to identify objects within nuclei follows the format of splitting each RGB image into their grayscale constituents, classifying and identifying nuclei, and then measuring the signal from the red or green channels within each nucleus to obtain values of integrated intensity. Data was then exported to an Excel spreadsheet, integrated intensity values for STRIDE or γH2AX were divided by integrated intensity of DAPI and transferred to GraphPad Prism 10 for further graphing and statistical analysis. As this data is non-parametric, p-values were obtained by performing a Mann-Whitney U test for STRIDE and γH2AX data at the 15-, 60- and 1440- minute timepoints comparing irradiated cells with or without AuNPs. Final figures were edited with ImageJ 1.54f and Canva.

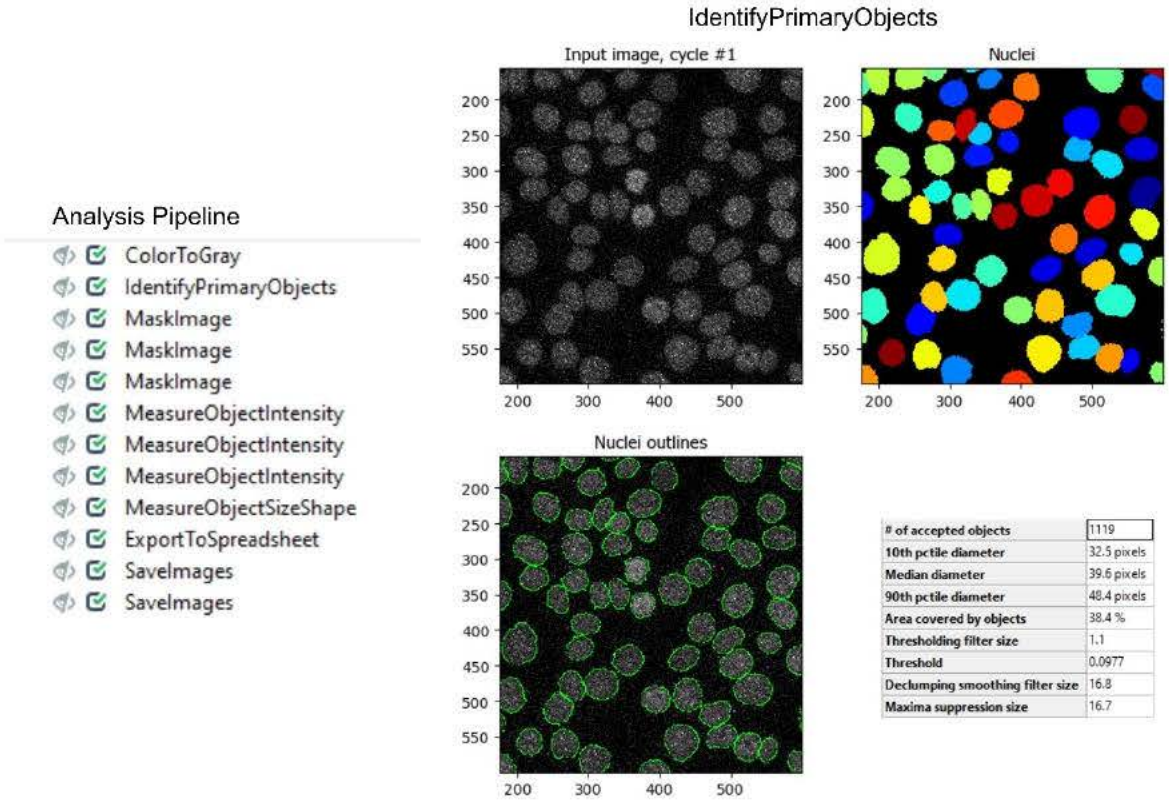


Figure 1. (Left) Analysis pipeline within CellProfiler 4.2.6. Each RGB image was separated into its constituent channels with ColourToGray. Nuclei were identified based on the blue channel with IdentifyPrimaryObjects (Right). Each channel was then masked based on the objects (nuclei) identified, and the values of integrated intensity measured for each nucleus with MeasureObjectIntensity.

© 2024 Wiley-VCH GmbH

14397641, 0, Downloaded from https://chemistry-europe.onlinelibrary.wiley.com/doi/10.1002/cphc.202400764 by University Of South Australia, Wiley Online Library on [25/11/2024]. See the Terms and Conditions (https://onlinelibrary.wiley.com/terms-and-conditions) on Wiley Online Library for rules of use; OA articles are governed by the applicable Creative Commons License

Results and Discussion

Confocal Images

For this study of DNA DSB formation and repair kinetics, 2 hours prior to irradiation (T = −120 minutes), cells were treated with or without 1 nM AuNPs and then returned for incubation at 37 °C. The X-ray dose of 2 Gy was chosen as it represents a typical clinical radiation dose fraction for many cancer treatments and results in an approximate 50 % clonogenic capacity for 4T1 cells (data not shown). Thus, the X-ray dose was sufficient to result in substantial impact on cell's proliferative capacity without substantially inducing rapid cell necrosis, allowing for effective measurement with STRIDE and γH2AX immunostaining. As nanoparticles can interfere with cell cycle progression, leading to arrest,[19] cell phase redistribution,[20] and/or apparent nanoparticle interphase redistribution,[21] we were cautious to ensure that the same quantity of DNA was distributed across the cell populations for the initial exposure to radiation in comparison to controls. As G_2/M phase cells contain double the DNA as G_1 phase cells we constrained any possibility of the cell populations arresting or accumulating in cell phases by having a short incubation time of 2 hours with nanoparticles before irradiation. We have also shown this time frame is sufficient to result in sensitization.[16] As shown here, indeed, despite the low nanoparticle concentration, at longer time points we reveal a genotoxic stress is exerted on the cells by the nanoparticles.

The timepoints cited in the figures below (T = 15, 30, 45 minutes etc.) are the cell fixation times post-irradiation with irradiation time at T = 0. Timepoints ranged from within an hour of insult up to 24 hours. This allowed us to identify the initial physical DNA damage (i.e. DSBs) to be reported by STRIDE, and the subsequent widespread activation of the DNA damage response (DDR) with γH2AX. From this, a profile of the DNA DSB and repair kinetics across each condition was recorded, and thus the times at which DSBs are repaired or whether repair is stalled could be observed. Figure 2 presents representative confocal microscopy images.

Negative Controls

Due to the magnification used to capture these images, both STRIDE and gamma H2AX foci are difficult to accurately resolve. As such, we did not quantify discrete foci but rather integrated intensity, i.e., the summed pixel intensities within each nucleus was measured. The integrated intensity of the blue channel (DAPI) corresponds with the total DNA content of each nucleus.[22] DNA content of cells is highly variable across a population (e.g. G_2/M phase cells have double the DNA content in preparation for cell division compared to G_1 cells). STRIDE and γH2AX intensities are inherently affected by this, as higher DNA content within a cell corresponds with an increased capacity for DNA breakages after an insult, and consequently additional repair signalling. To account for this, each individual cell's integrated intensity value for either STRIDE or γH2AX was normalised (divided) by the integrated intensity value of DAPI. In doing so, this minimises one potential source of variability in the data regarding the heterogenous nature of each cell population and allows for interpretation of STRIDE and γH2AX

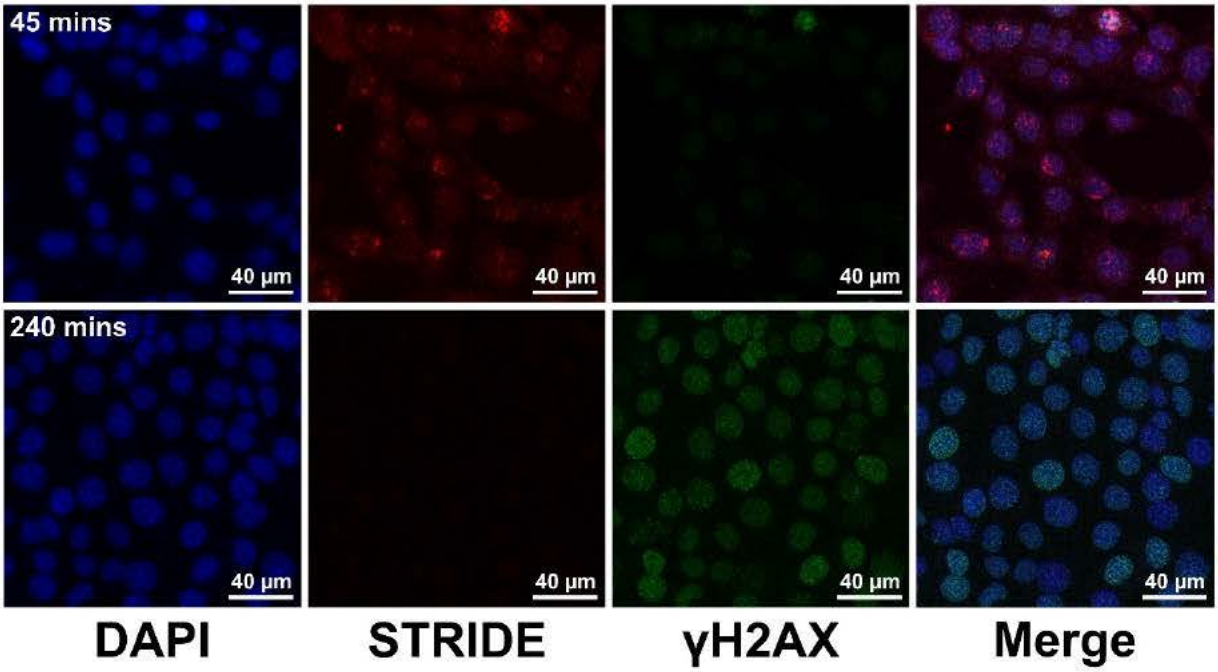


Figure 2. Confocal acquisition at 20x magnification of 4T1 cells irradiated with 160 kV, 1.93 Gy X-rays + 1 nM AuNPs. Cells were stained with Duolink In Situ Detection Reagents FarRed (Cy5) against STRIDE, anti-phospho-histone H2AX conjugated with Alexa 488 against γH2AX, and DAPI. Top row, X-rays + AuNPs, 45 mins post-irradiation. Bottom row, X-rays + AuNPs, 240 minutes post-irradiation.

© 2024 Wiley-VCH GmbH

14397641, 0, Downloaded from https://chemistry-europe.onlinelibrary.wiley.com/doi/10.1002/cphc.202400764 by University Of South Australia, Wiley Online Library on [25/11/2024]. See the Terms and Conditions (https://onlinelibrary.wiley.com/terms-and-conditions) on Wiley Online Library for rules of use; OA articles are governed by the applicable Creative Commons License

signals on a single-cell level without cell phase interfering as a confounding variable.

Data from the non-treated negative controls (Figure 3) present a roughly constant trend across all timepoints up to 1440 minutes, with median values ranging from 0.31–0.43 arbitrary units for STRIDE and 0.23–0.34 for γH2AX. However, the degree of variability in values for integrated intensity across each cell population is notable and is typical of cell population heterogeneity.[16,22] Such heterogeneity is not apparent in bulk assays. Respective plots of averaged data are provided in supporting information (Figure S1). Heterogeneity in γH2AX expression is particularly obvious in terms of the interquartile ranges for each condition. Such heterogeneity is a common feature for endogenous markers, where the baseline expression can vary widely even in the absence of experimental treatments.

Figure 4 shows that after 4T1 cells are treated with 1 nM AuNPs there is a trend in increasing DNA damage formation and repair. STRIDE presents a baseline level of integrated intensity at the 15- and 30- minute timepoints sitting at approximately 0.40, which then gradually increases incrementally from 45 minutes onwards. This is suggestive of a time dependent accumulation of DSBs due to the intracellular presence of AuNPs, with the median STRIDE signal peaking at 1440 minutes, reaching 0.81. There are multiple potential mechanisms which support this observed cumulative buildup of DSBs, particularly, the generation of ROS. Multiple factors have been proposed to drive ROS generation by AuNPs, including interfacial catalysis, dissolution of ions and interruption of cellular homeostasis.[5b]

The γH2AX signal is also supportive of the accumulation of DSBs, with increased levels of repair activation observed at 60 (0.35) and 120 (0.48) minutes, and a gradual decline in

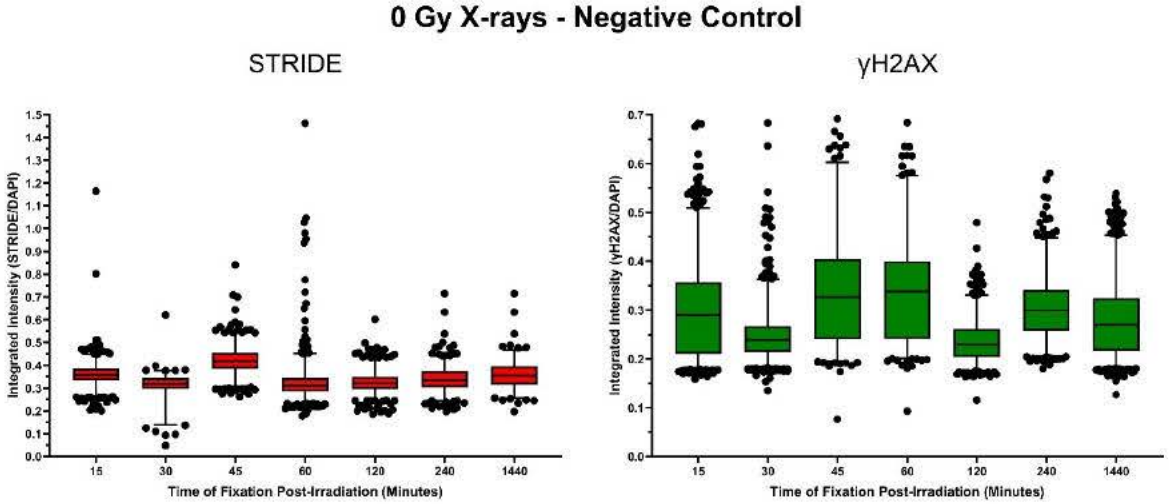


Figure 3. Non-irradiated 4T1 cells without AuNPs treatment (negative control). Integrated intensity values for STRIDE, γH2AX, and DAPI from single cells were measured. STRIDE and γH2AX values were normalised to DAPI. Data show the median value within the 25th and 75th percentile data points (box). Whiskers show the 2.5–97.5 percentile, and dots represent data points outside the range represented by whiskers.

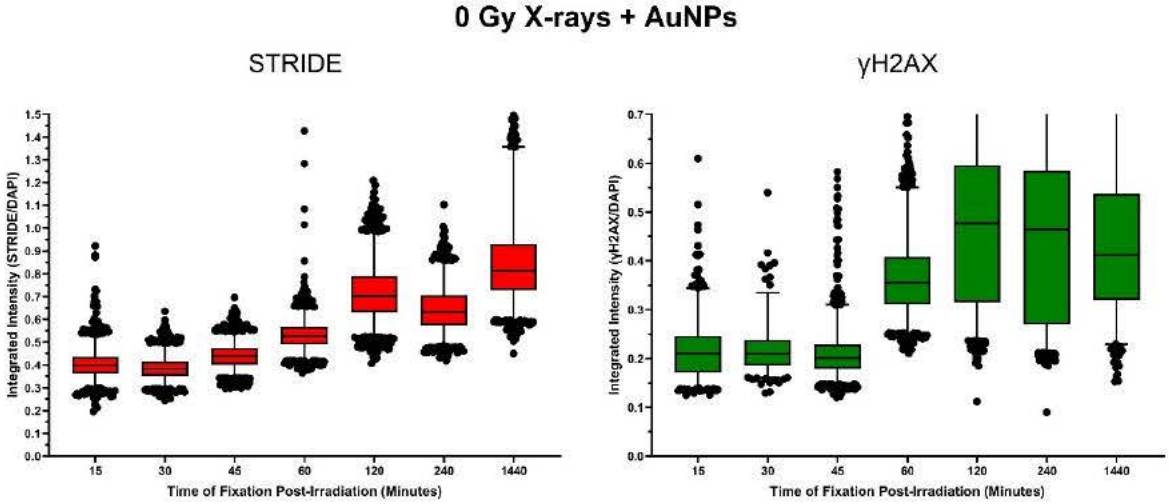


Figure 4. Nanoparticle exposure leads to formation of DNA damage and repair. Non-irradiated 4T1 cells treated with 1 nM AuNPs. Integrated intensity values for STRIDE, γH2AX, and DAPI were measured for individual nuclei, and STRIDE and γH2AX values normalised to DAPI.

© 2024 Wiley-VCH GmbH

14397641, 0, Downloaded from https://chemistry-europe.onlinelibrary.wiley.com/doi/10.1002/cphc.202400764 by University Of South Australia, Wiley Online Library on [25/11/2024]. See the Terms and Conditions (https://onlinelibrary.wiley.com/terms-and-conditions) on Wiley Online Library for rules of use; OA articles are governed by the applicable Creative Commons License

phosphorylation observed at 240 (0.46) and 1440 minutes (0.41). Initially, it appears that the homeostatic expression of γH2AX is suppressed at 15, 30 and 45 minutes with addition of AuNPs in comparison to the negative control; median γH2AX levels being approximately 0.21 with AuNPs and 0.23–0.34 without. While only subtle, this does suggest that AuNPs may interfere with the phosphorylation of H2AX at these earlier timepoints and delay the repair of low levels of DNA damage. This phenomenon has been previously observed by Turnbull et al. 2019, wherein downregulation of thymidylate synthase was observed for PC-3 cells that internalised the same AuNPs[5a].

DNA Damage and Repair Kinetics After X-Ray Irradiation

The kinetics of the DNA damage after X-ray irradiation is revealed by STRIDE. Initially, STRIDE is elevated at 15 minutes post irradiation (0.7) followed by a sharp decrease at the 30 minute timepoint (0.47) and a consequent return to baseline at later timepoints. The disappearance of DSBs at the 30 minute timepoint cannot be taken as successful DSB repair. Our interpretation of this data is that initiation of DSB identification and repair has commenced, and hence the recruitment of DDR factors to the breakage site obscures the DSB ends. Protein complexes responsible for the initiation and progression of repair through the non-homologous end joining (NHEJ) and homologous recombination (HR) are bound in proximity to the ends of DSBs from approximately 10 minutes post-insult onwards. This may result in the obstruction of the once free DNA ends and thus prevent STRIDE from binding to these breakage sites.[14] This is supported by the opposite trend observed for γH2AX, where expression is low at 15 minutes (0.26) followed by an increase in γH2AX signal at 30 minutes (0.36). This indicates the initiation of DSB repair is well underway, with it essentially reaching a peak at 60 minutes (0.43). The data at 1440 minutes (0.40) shows a slight decrease indicating DSB repair resolving.

DNA Damage and Repair Kinetics After AuNP Internalisation and X-Ray Irradiation

Different trends in the detection of DSBs and their repair were observed when cells were irradiated alone (Figure 5) compared to when they had internalized AuNPs prior to irradiation (Figure 6). We first sought to test our hypothesis that the STRIDE assay could reveal an increase in DSBs for cells with AuNPs prior to irradiation, compared to irradiation alone. If the nanoparticles caused an increase in localised dose deposition due to X-ray interactions with the AuNPs we expected this to present an increase in the STRIDE signal. In comparing the STRIDE data sets at 15 mins, no difference was observed ($p = 0.8340$, Mann-Whitney U test). This is an important result as it provides a direct measurement showing that the physical dose enhancement theory is not evidenced, i.e. there is no evidence of AuNPs causing an increase in DSBs. Other interesting trends of DNA damage and repair that differed to irradiation alone were observed, however. Starting with STRIDE, DNA damage appears to continue to persist at 30, and 45 minutes post-irradiation, both with p values of < 0.0001 when compared to radiation alone (Mann-Whitney U test). At 60 minutes, STRIDE sensitivity disappears (Figure 6), contrasting STRIDE without AuNPs where its signal disappears after 30 minutes. This delay in DSB detection alludes that AuNPs impede the repair of DSBs without contributing to the overall repair burden by generating additional DSBs. This is presumably due to DDR machinery obscuring the DSB only at later time points when nanoparticles are present. STRIDE then gradually increases again at 120, 240 and 1440 minutes, at which point the signal reaches a second peak. This mirrors the cumulative increase in DSBs observed in the 0 Gy + AuNPs condition (Figure 4), where STRIDE also reaches a peak at 1440 minutes. This has implications when conducting clonogenic assays where the data obtained depends upon longer timepoints with this chronic stress present and may not be directed purely by the acute irradiation exposure causing the DSBs as observed from 15–45 minutes.

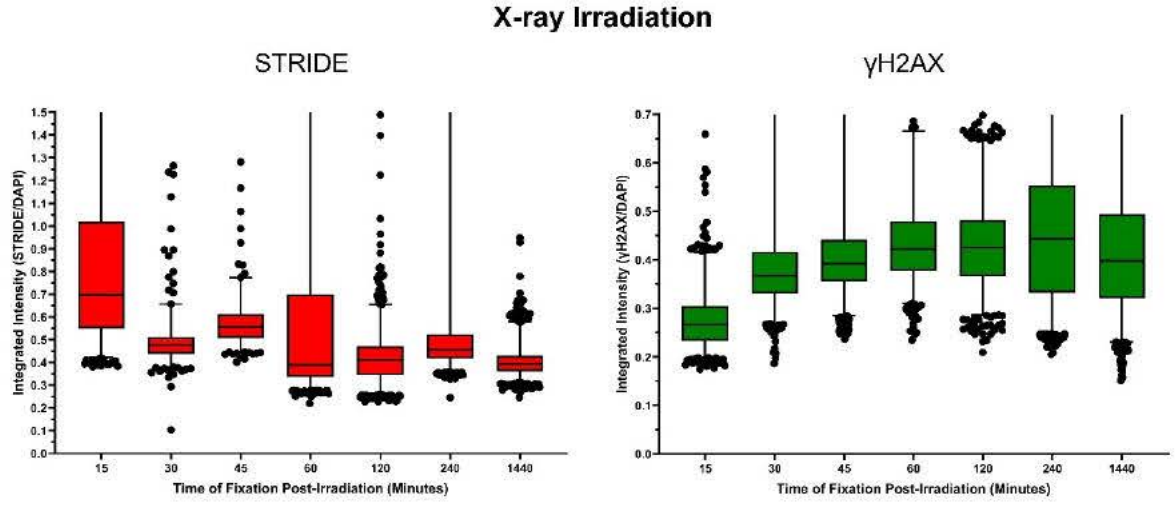


Figure 5. X-ray irradiation causes DNA DSBs followed by repair. 4T1 cells irradiated with 1.93 Gy X-rays without AuNP treatment. Integrated intensity values for STRIDE, γH2AX, and DAPI were measured for individual nuclei, and STRIDE and γH2AX values normalised to DAPI.

© 2024 Wiley-VCH GmbH

14397641, 0, Downloaded from https://chemistry-europe.onlinelibrary.wiley.com/doi/10.1002/cphc.202400764 by University Of South Australia, Wiley Online Library on [25/11/2024]. See the Terms and Conditions (https://onlinelibrary.wiley.com/terms-and-conditions) on Wiley Online Library for rules of use; OA articles are governed by the applicable Creative Commons License

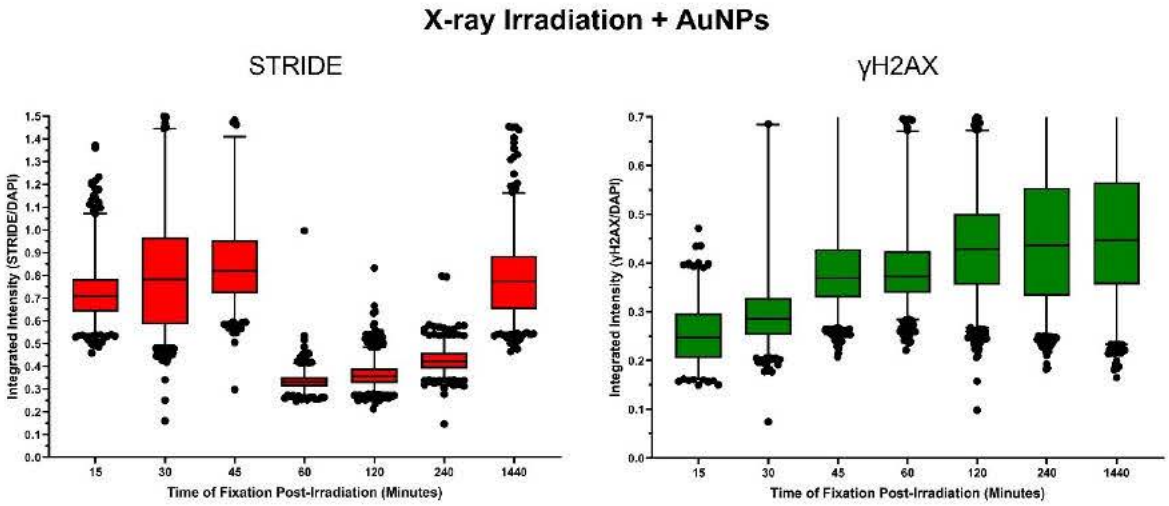


Figure 6. 4T1 cells irradiated with 1.93 Gy X-rays and pre-treated with 1 nM AuNPs. Integrated intensity values for STRIDE, γH2AX, and DAPI were measured for individual nuclei, and STRIDE and γH2AX values normalised to DAPI.

As with X-ray irradiation without AuNPs, γH2AX levels begin at baseline levels at 15 minutes (0.25), however at 30 minutes instead of a dramatic increase in signal indicating repair initiation seen in Figure 5, only a slight increase is observed when AuNPs are present (0.29), suggesting repair has not been initiated entirely ($p < 0.0001$, Mann-Whitney U test). The delayed onset of DSB repair observed in this condition, also reflected by the persistence of STRIDE at 45 minutes post-irradiation, suggests that AuNPs interfere with the recruitment of critical DDR machinery. In response to X-ray irradiation only, the proteins that are relevant at these timepoints include γH2AX, ATM, BRCA1, and 53BP1, all pivotal in both widespread chromatin remodelling and choosing whether NHEJ or HR will be used to repair the breakage site.[14] Hence, delaying the activation of these proteins through interaction with AuNPs would consequently stall the repair process,[14] and would likely have an additive effect in combination with the inhibition of bottleneck enzymes such as thymidylate synthase.[5a]

Median values then increase incrementally from 45 minutes (0.37) onwards all the way through to 1440 minutes (0.45). For these later timepoints (120, 240 and 1440 mins, $p = 0.7838$, 0.6691 and < 0.0001 respectively compared to radiation alone; Mann-Whitney U test) γH2AX signal increases and persists at this high level, whereas without AuNPs there is a gradual decrease (Figure 5). What may be observed here as 'persistent foci', presumably from X-ray induced damage, may not just be present from a limitation in DNA repair. These damage and repair foci at later timepoints likely include DSBs caused by cumulative AuNP induced stress, evidenced by the initial resolution of DSBs at 60 minutes indicated by STRIDE. We anticipate that the majority of internalised AuNPs are contained within vesicles in the cytoplasm as observed in our own work in vitro[18] and ex vivo[23] and commonly presented in literature[18,24] and may accumulate in proximity to the nucleus.[25] Proteomics of PC-3 cells using the same AuNPs showed downregulation of glutathione thioredoxin and peroxiredoxin antioxidant pathways after 2-hour and 24-hour exposure respectively, these enzymes reduce ROS burden and thus enhance cancer cell survival.[18] Internalisation in vesicles is unlikely to contribute towards the physical dose deposition by AuNPs, i.e. causing nuclear DSBs directly, but rather through the inhibition of antioxidants and preventing ROS scavenging[18] and DDR mechanisms.[5a] This highlights there should be caution interpreting longer time points in terms of these foci being 'persistent' DSBs carried over from X-ray irradiation, but instead induced independently because of a combination of physico-chemical, chemical and biological responses to AuNP internalisation.

Conclusions

The inclusion of AuNPs in irradiated 4T1 cells substantially alters the kinetics of DNA double-strand breaks formation and subsequent repair processes to resolve them. A few key conclusions result from this data being that whilst there is no evidence that AuNPs directly increase the generation of DSBs at the time of irradiation, their presence within the cell delays the repair of existing DSBs. This is evidenced by the persistence of STRIDE signals and the delayed activation and resolution of γH2AX when cells were co-cultured with AuNPs prior to irradiation. This suggests that AuNPs also interfere with the recruitment of DDR proteins responsible for progression towards NHEJ and HR repair pathways. This highlights the potential of AuNPs to modulate cellular responses to DNA damage, which has significant implications for their future use in cancer therapies, particularly in enhancing the efficacy of radiotherapy by inhibiting DNA repair. Future work is required to identify the mechanisms that drive the ability of AuNPs to perturb DSB repair pathways, as well as how internalisation can produce cumulative DSBs over prolonged exposure times.

© 2024 Wiley-VCH GmbH

14397641, 0, Downloaded from https://chemistry-europe.onlinelibrary.wiley.com/doi/10.1002/cphc.202400764 by University Of South Australia, Wiley Online Library on [25/11/2024]. See the Terms and Conditions (https://onlinelibrary.wiley.com/terms-and-conditions) on Wiley Online Library for rules of use; OA articles are governed by the applicable Creative Commons License

Acknowledgements

This research was funded by the Tour de Cure PhD Scholarship, grant ID number RSP-641-FY2023. We acknowledge Tour de Cure's contribution towards the preparation of this manuscript through the Tour de Cure Scholarship Grant and appreciate their continued support for this work. We acknowledge Microscopy Australia (ROR: 042 mm0k03) at the Future Industries Institute, University of South Australia, enabled by NCRIS. Thanks to Dr. Alex Cavallaro for assistance with operation of the Zeiss LSM 710 confocal microscope. Many thanks to Dr. Ali Nazarizadeh-Khangheshlaghi for assisting with the 4T1 cell culture, Dr. Sonia Theresa Sebastian for synthesis of the gold nanoparticles, and Dr. Bill Liapis for assisting with the operation of the X-ray irradiator.

Conflict of Interests

The authors declare no conflict of interest.

Data Availability Statement

The data that support the findings of this study are available from the corresponding author upon reasonable request.

Keywords: Double-stranded breaks · DNA repair · DDR kinetics · STRIDE · γH2AX

[1] G. Borrego-Soto, R. Ortiz-López, A. Rojas-Martínez, *Genet. Mol. Biol.* **2015**, *38*, 420–432.
[2] D. Y. Breitkreutz, M. D. Weil, M. Bazalova-Carter, *Phys. Medica* **2020**, *79*, 103–112.
[3] S. Dhoundiyal, S. Srivastava, S. Kumar, G. Singh, S. Ashique, R. Pal, N. Mishra, F. Taghizadeh-Hesary, *Eur. J. Med. Res.* **2024**, *29*, 26.
[4] X. Ge, H. Zhu, W. Dai, X. Sun, *J. Thorac. Dis.* **2016**, *8*, 2968–2970.
[5] a) T. Turnbull, M. Douglass, N. H. Williamson, D. Howard, R. Bhardwaj, M. Lawrence, D. J. Paterson, E. Bezak, B. Thierry, I. M. Kempson, *ACS Nano* **2019**, *13*, 5077–5090; b) D. Howard, S. Sebastian, Q. V.-C. Le, B. Thierry, I. Kempson, *Int. J. Mol. Sci.* **2020**, *21*, 579.
[6] E. J. Moding, M. B. Kastan, D. G. Kirsch, *Nat. Rev. Drug Discov.* **2013**, *12*, 526–542.
[7] I. Munaweera, B. Koneru, Y. Shi, A. J. Di Pasqua, J. Balkus, J. Kenneth, *APL Mater.* **2014**, *2*, 113315.
[8] S. J. McMahon, W. B. Hyland, M. F. Muir, J. A. Coulter, S. Jain, K. T. Butterworth, G. Schettino, G. R. Dickson, A. R. Hounsell, J. M. O'Sullivan, K. M. Prise, D. G. Hirst, F. J. Currell, *Sci. Rep.* **2011**, *1*, 18.
[9] I. Kempson, *WIREs Nanomed. Nanobiotechnol.* **2021**, *13*, e1656.
[10] a) C. L. Tourneau, X. Liem, T. V. F. Nguyen, S. E. Bedoui, S. Salas, M. P. Serrahima, X. Mirabel, S. W. H. Kam, L. Houdas, A. Debard, O. I. Vivar, L. A. Farber, J. O. Thariat, M. Lesnik, F. Helferich, A. Herczeg, Z. Papai, J. Fijuth, Z. Takacsi-Nagy, *Int. J. Radiat. Oncol. Biol. Phys.* **2024**, *118*, e6; b) C. Shen, K. Jameson, J. Weiss, T. Hackman, D. Corum, J. A. Akulian, R. Dixon, A. Pearson, J. Frakes, P. Said, H. Miraoui, E. Baskin-Bey, T. Seiwert, *Annal. Oncol.* **2019**, *30*, xi46; c) C. Verry, S. Dufort, B. Lemasson, S. Grand, J. Pietras, I. Troprès, Y. Crémillieux, F. Lux, S. Mériaux, B. Larrat, J. Balosso, G. Le Duc, E. L. Barbier, O. Tillement, *Sci. Adv.* **2020**, *6*, eaay5279; d) S. K. Libutti, G. F. Paciotti, A. A. Byrnes, H. R. Alexander, Jr., W. E. Gannon, M. Walker, G. D. Seidel, N. Yuldasheva, L. Tamarkin, *Clin. Cancer Res.* **2010**, *16*, 6139–6149; e) C. Chargari, P. Maury, M. Texier, C. Genestie, P. Morice, S. Bockel, S. Gouy, M. Ba, S. Achkar, F. Lux, O. Tillement, S. Dufort, G. L. E. Duc, O. Debeaumont, C. Massard, A. Maulard, E. Porcel, R. Bahleda, S. Ammari, D. Morel, S. Espenel, P. Pautier, C. Robert, E. Deutsch, *ACS Nano* **2024**, *18*, 16516–16529.
[11] B. G. Le François, J. A. Maroun, H. C. Birnboim, *Br. J. Cancer* **2007**, *97*, 1242–1250.
[12] E. T. McKinley, G. D. Ayers, R. A. Smith, S. A. Saleh, P. Zhao, M. K. Washington, R. J. Coffey, H. C. Manning, *PlOS One* **2013**, *8*, e58938.
[13] J. Atkinson, E. Bezak, I. Kempson, *Nat. Rev. Mol. Cell Biol.* **2022**, *23*, 579–580.
[14] J. Atkinson, E. Bezak, H. Le, I. Kempson, *Int. J. Mol. Sci.* **2024**, *25*, 2227.
[15] M. M. Kordon, M. Zarębski, K. Solarczyk, H. Ma, T. Pederson, J. W. Dobrucki, *Nucleic Acids Res.* **2019**, *48*, e14–e14.
[16] D. Howard, T. Turnbull, P. Wilson, D. J. Paterson, V. Milanova, B. Thierry, I. Kempson, *Small Sci.* **2024**, *n/a*, 2400053.
[17] J. Kimling, M. Maier, B. Okenve, V. Kotaidis, H. Ballot, A. Plech, *J. Phys. Chem. B* **2006**, *110*, 15700–15707.
[18] S. Sebastian, M. K. Hoffmann, D. Howard, C. Young, J. Washington, H. Unterweger, C. Alexiou, T. Turnbull, R. D'Andrea, P. Hoffmann, I. Kempson, *Antioxidants (Basel)* **2023**, *12*, 1617.
[19] W. Roa, X. Zhang, L. Guo, A. Shaw, X. Hu, Y. Xiong, S. Gulavita, S. Patel, X. Sun, J. Chen, R. Moore, J. Z. Xing, *Nanotechnology* **2009**, *20*, 375101.
[20] X. Zhang, X. Chen, Y. W. Jiang, N. Ma, L. Y. Xia, X. Cheng, H. R. Jia, P. Liu, N. Gu, Z. Chen, F. G. Wu, *ACS Appl. Mater. Interfaces* **2018**, *10*, 10601–10606.
[21] J. A. Kim, C. Åberg, A. Salvati, K. A. Dawson, *Nat. Nanotechnol.* **2012**, *7*, 62–68.
[22] G. Gruel, C. Villagrasa, P. Voisin, I. Clairand, M. Benderitter, J.-F. Bottollier-Depois, J. F. Barquinero, *PlOS One* **2016**, *11*, e0145786.
[23] C.-H. Wang, C.-J. Liu, C.-C. Chien, H.-T. Chen, T.-E. Hua, W.-H. Leng, H.-H. Chen, I. M. Kempson, Y. Hwu, M. Hsiao, T.-C. Lai, J. L. Wang, C.-S. Yang, H.-M. Lin, Y.-J. Chen, G. Margaritondo, *Mater. Chem. Phys.* **2011**, *126*, 352–356.
[24] a) D. B. Peckys, N. de Jonge, *Micros. Microanal.* **2014**, *20*, 189–197; b) M. Liu, Q. Li, L. Liang, J. Li, K. Wang, J. Li, M. Lv, N. Chen, H. Song, J. Lee, J. Shi, L. Wang, R. Lal, C. Fan, *Nat. Commun.* **2017**, *8*, 15646; c) C.-T. Ng, J. J. E. Li, R. L. Gurung, M. P. Hande, C.-N. Ong, B.-H. Bay, L.-Y. L. Yung, *Experiment. Biol. Med.* **2013**, *238*, 1355–1361; d) B. D. Chithrani, A. A. Ghazani, W. C. W. Chan, *Nano Lett.* **2006**, *6*, 662–668; e) C. Brandenberger, C. Mühlfeld, Z. Ali, A.-G. Lenz, O. Schmid, W. J. Parak, P. Gehr, B. Rothen-Rutishauser, *Small* **2010**, *6*, 1669–1678.
[25] J. J. Li, L. Zou, D. Hartono, C. N. Ong, B. H. Bay, L. Y. L. Yung, *Adv. Mater.* **2008**, *20*, 138-++.

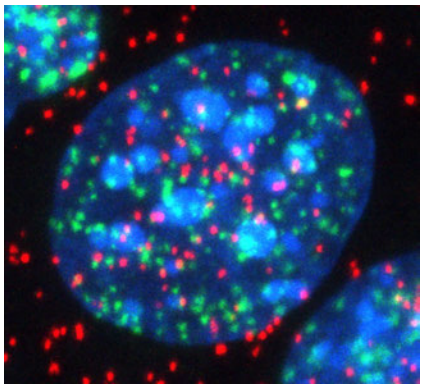
Manuscript received: July 31, 2024
Revised manuscript received: October 23, 2024
Accepted manuscript online: October 30, 2024
Version of record online: ■■, ■■

© 2024 Wiley-VCH GmbH

14397641, 0, Downloaded from https://chemistry-europe.onlinelibrary.wiley.com/doi/10.1002/cphc.202400764 by University Of South Australia, Wiley Online Library on [25/11/2024]. See the Terms and Conditions (https://onlinelibrary.wiley.com/terms-and-conditions) on Wiley Online Library for rules of use; OA articles are governed by the applicable Creative Commons License

RESEARCH ARTICLE

This study applies the STRIDE assay to assess DNA double strand breaks (DSBs) in 4T1 breast cancer cells treated with gold nanoparticles (AuNPs) and radiation. Findings reveal that AuNPs do not increase radiation dose deposition but delay DSB repair through DNA damage repair machinery disruption. Comparison is made to γH2AX on a single-cell level.



*J. Atkinson, J. Chopin, E. Bezak, H. Le, I. Kempson**

1 – 9

Gold Nanoparticles Cause Radiosensitization in 4T1 Cells by Inhibiting DNA Double Strand Break Repair: Single Cell Comparisons of DSB Formation and γH2AX Expression

14397641, 0, Downloaded from https://chemistry-europe.onlinelibrary.wiley.com/doi/10.1002/cptc.202400764 by University Of South Australia, Wiley Online Library on [25/11/2024]. See the Terms and Conditions (https://onlinelibrary.wiley.com/terms-and-conditions) on Wiley Online Library for rules of use; OA articles are governed by the applicable Creative Commons License

ChemPhysChem

Supporting Information

Gold Nanoparticles Cause Radiosensitization in 4T1 Cells by Inhibiting DNA Double Strand Break Repair: Single Cell Comparisons of DSB Formation and γH2AX Expression

Jake Atkinson, Joshua Chopin, Eva Bezak, Hien Le, and Ivan Kempson*

Supporting Information:

Gold nanoparticles cause radiosensitization in 4T1 cells by inhibiting DNA double strand break repair: Single cell comparisons of DSB formation and γH2AX expression.

Authors: Jake Atkinson[1], Joshua Chopin[2], Eva Bezak[3,4], Hien Le[3,5], Ivan Kempson[1,*]

Affiliations

[1] Future Industries Institute, University of South Australia, Mawson Lakes, SA 5095, Australia

[2] Industrial AI Research Centre, University of South Australia, Mawson Lakes, SA 5095, Australia

[3] UniSA Allied Health and Human Performance, University of South Australia, Adelaide, SA 5095, Australia

[4] Department of Physics, University of Adelaide, North Terrace, Adelaide, SA 5005, Australia

[5] Department of Radiation Oncology, Royal Adelaide Hospital, Adelaide, SA 5000, Australia

[*]Author to whom correspondence should be addressed. Ivan.Kempson@unisa.edu.au

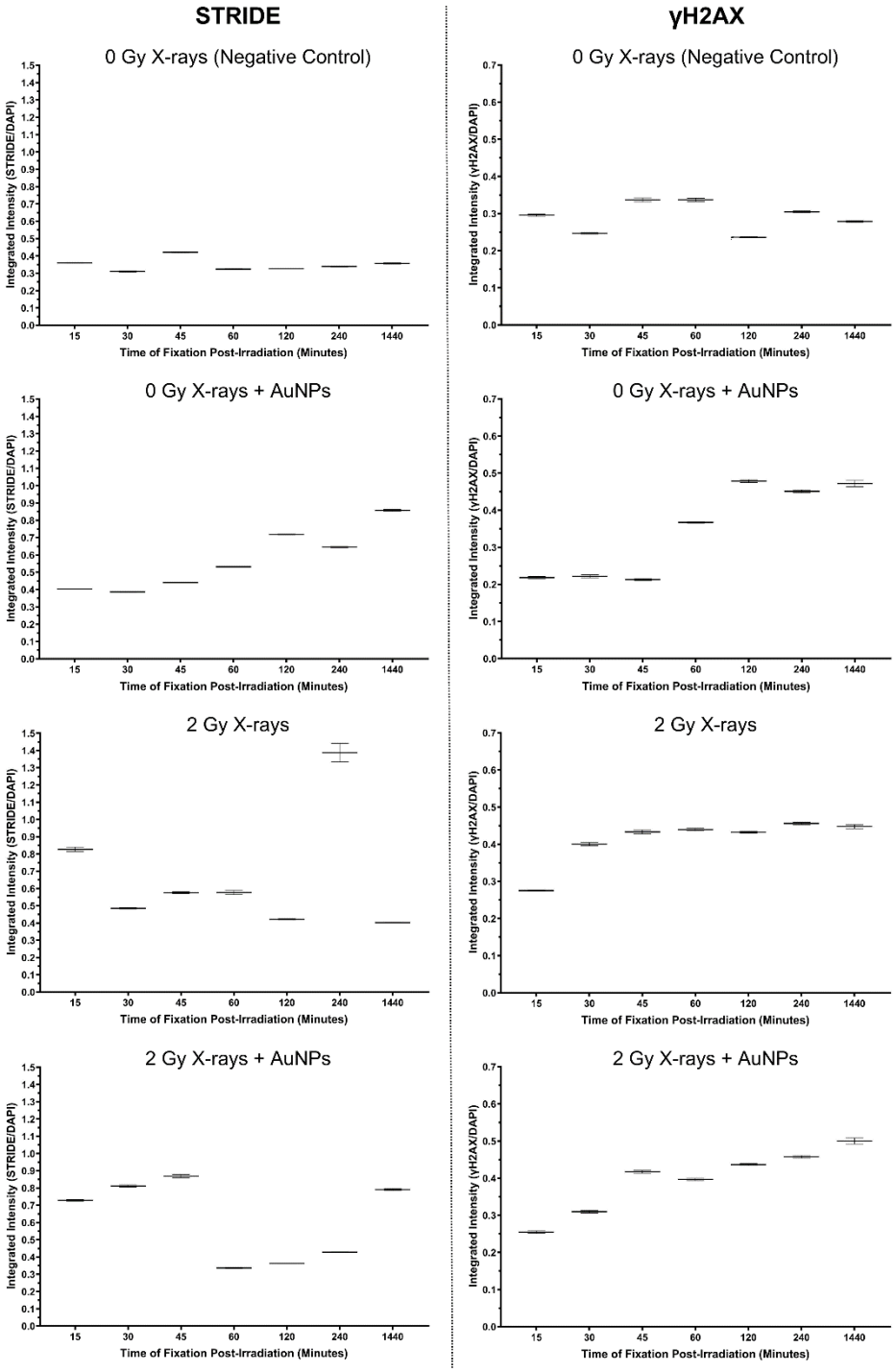


Figure S1: Plots of the integrated intensity of STRIDE/γH2AX divided by DAPI, with horizontal lines representing the mean of each population for each timepoint, and error bars denote the standard error of the mean.

Table S1: Descriptive statistics for each dataset for STRIDE and γH2AX across all timepoints. Values recorded include the number of values in each population (n), mean, median, standard deviation, standard error of the mean, range (defined by Prism as the difference in the minimum and maximum values), and 25th and 75th percentiles.

		0 Gy X-rays (Negative Control)		0 Gy X-rays + AuNPs		X-ray Irradiation		X-ray Irradiation + AuNPs	
		STRIDE	**γH2AX**	**STRIDE**	**γH2AX**	**STRIDE**	**γH2AX**	**STRIDE**	**γH2AX**
15 minutes	Number of values	834	1016	1528	922	820	945	832	390
	Minimum	0.2003	0.1587	0.1961	0.1243	0.3813	0.1748	0.4597	0.149
	25% Percentile	0.3334	0.2105	0.3622	0.1705	0.5505	0.233	0.6402	0.205
	Median	0.3582	0.2891	0.3983	0.2103	0.6968	0.2672	0.7089	0.2468
	75% Percentile	0.3857	0.3567	0.4361	0.2469	1.02	0.3043	0.7844	0.2967
	Maximum	1.165	0.6819	0.9228	2.192	2.319	0.659	1.859	0.4717
	Range	0.9649	0.5232	0.7267	2.068	1.938	0.4841	1.399	0.3227
	Mean	0.3598	0.2957	0.4024	0.2182	0.8273	0.2753	0.7285	0.2545
	Std. Deviation	0.05408	0.09374	0.06214	0.08687	0.3694	0.05748	0.1375	0.06172
	Std. Error of Mean	0.001873	0.002941	0.00159	0.002861	0.0129	0.00187	0.004767	0.003125
30 minutes	Number of values	258	1005	1630	515	560	1214	1768	904
	Minimum	0.04873	0.1353	0.2442	0.1294	0.1036	0.1864	0.1603	0.07444
	25% Percentile	0.2973	0.2139	0.352	0.1857	0.4389	0.3305	0.5845	0.2525
	Median	0.3184	0.2382	0.3818	0.2095	0.4762	0.3679	0.7832	0.2862
	75% Percentile	0.3438	0.2672	0.4166	0.2382	0.5115	0.4172	0.9662	0.3291
	Maximum	0.6202	0.7909	0.6357	1.768	1.266	1.563	2.291	1.076
	Range	0.5714	0.6556	0.3915	1.639	1.162	1.376	2.13	1.002
	Mean	0.3107	0.2466	0.386	0.2217	0.485	0.4003	0.8109	0.3095
	Std. Deviation	0.05535	0.05275	0.05036	0.08991	0.09348	0.1486	0.2796	0.106
	Std. Error of Mean	0.003446	0.001664	0.001247	0.003962	0.00395	0.004266	0.006649	0.003524
45 minutes	Number of values	712	413	1894	2395	484	1483	704	2471
	Minimum	0.2608	0.07638	0.2976	0.12	0.4013	0.2367	0.2976	0.2073
	25% Percentile	0.3851	0.2399	0.4022	0.1784	0.5077	0.3554	0.7202	0.3292
	Median	0.4184	0.3263	0.4387	0.2011	0.5576	0.392	0.8206	0.3694
	75% Percentile	0.4543	0.4046	0.4749	0.2281	0.612	0.4415	0.9541	0.4291
	Maximum	0.8405	0.7305	0.6963	3.142	1.619	2.142	3.096	2.79
	Range	0.5798	0.6541	0.3988	3.022	1.217	1.905	2.799	2.583
	Mean	0.4213	0.3368	0.4402	0.213	0.5751	0.433	0.8682	0.4169
	Std. Deviation	0.05985	0.1132	0.0536	0.1131	0.1205	0.1921	0.2411	0.1911
	Std. Error of Mean	0.002243	0.005571	0.001232	0.002312	0.005477	0.004988	0.009085	0.003844
60 minutes	Number of values	1000	509	1811	1803	1099	733	602	810
	Minimum	0.1786	0.093	0.3649	0.2108	0.2189	0.2343	0.2464	0.2216
	25% Percentile	0.2858	0.2407	0.4894	0.3111	0.3363	0.3771	0.3089	0.3385
	Median	0.3126	0.338	0.5263	0.3553	0.3883	0.4226	0.3301	0.3726
	75% Percentile	0.3439	0.3999	0.5671	0.4081	0.6996	0.4799	0.3527	0.4243
	Maximum	1.462	0.9488	1.428	1.109	3.19	1.217	1.99	0.8387
	Range	1.284	0.8558	1.063	0.8984	2.971	0.9829	1.744	0.6171
	Mean	0.3231	0.337	0.5311	0.3668	0.5767	0.4393	0.3365	0.3965
	Std. Deviation	0.0805	0.103	0.06727	0.08077	0.3929	0.09411	0.08114	0.09302
	Std. Error of Mean	0.002546	0.004565	0.001581	0.001902	0.01185	0.003476	0.003307	0.003268
120 minutes	Number of values	847	972	2113	2080	1701	1127	1335	1691
	Minimum	0.1862	0.1153	0.4063	0.1116	0.2267	0.2095	0.212	0.09791
	25% Percentile	0.2967	0.2038	0.6302	0.3153	0.3444	0.3662	0.3254	0.3547
	Median	0.3222	0.2292	0.7032	0.4772	0.4103	0.4258	0.356	0.4288
	75% Percentile	0.3496	0.2617	0.7905	0.5966	0.4716	0.4824	0.3914	0.5012
	Maximum	0.6014	0.4794	2.433	1.288	2.062	1.042	0.8326	1.014
	Range	0.4152	0.3641	2.027	1.176	1.835	0.8329	0.6206	0.9156
	Mean	0.3262	0.2358	0.7179	0.4785	0.4209	0.4322	0.3622	0.4363
	Std. Deviation	0.04578	0.04228	0.1245	0.1731	0.1294	0.09185	0.05449	0.1103
	Std. Error of Mean	0.001573	0.001356	0.002708	0.003795	0.003138	0.002736	0.001491	0.002682
240 minutes	Number of values	611	664	1346	2100	1251	2238	806	2138
	Minimum	0.1974	0.1795	0.4199	0.09006	0.2458	0.2051	0.1466	0.1823
	25% Percentile	0.3041	0.2579	0.5741	0.2695	0.4163	0.3327	0.3908	0.3324
	Median	0.3349	0.299	0.632	0.4645	0.4562	0.4433	0.4215	0.4369
	75% Percentile	0.3742	0.3415	0.7061	0.5841	0.5234	0.5535	0.4602	0.5545
	Maximum	0.7149	0.5802	2.713	1.88	7.995	1.179	0.7979	1.407
	Range	0.5174	0.4006	2.293	1.79	7.749	0.9741	0.6513	1.225
	Mean	0.3391	0.3046	0.645	0.4511	1.387	0.456	0.4273	0.4573
	Std. Deviation	0.05396	0.06293	0.1122	0.1799	1.902	0.1447	0.0536	0.1529
	Std. Error of Mean	0.002183	0.002442	0.003058	0.003926	0.05379	0.003059	0.001888	0.003307
1440 minutes	Number of values	294	1258	1890	890	1779	1663	866	1002
	Minimum	0.1974	0.1267	0.4498	0.1528	0.2469	0.1512	0.4656	0.1651
	25% Percentile	0.3159	0.2166	0.7267	0.3204	0.3608	0.3207	0.6503	0.3558
	Median	0.3537	0.27	0.8141	0.4117	0.3936	0.3977	0.7735	0.447
	75% Percentile	0.395	0.3248	0.9318	0.5382	0.4288	0.4943	0.8861	0.5657
	Maximum	0.7149	1.181	3.814	2.69	0.9478	2.172	1.844	3.5
	Range	0.5174	1.054	3.364	2.537	0.7009	2.021	1.378	3.334
	Mean	0.3563	0.2785	0.857	0.4718	0.4022	0.4475	0.7903	0.5001
	Std. Deviation	0.05835	0.07592	0.2211	0.2538	0.06439	0.2207	0.1756	0.2576
	Std. Error of Mean	0.003403	0.00214	0.005086	0.008508	0.001527	0.005411	0.005968	0.008139

4.4 Mechanisms of ATM Inhibitor AZD1390-Mediated Radiosensitization by Comparing DNA DSB Formation and Repair in 4T1 Cells

4.4.1 Summary

Following the established DDR perturbing and radiosensitising effects of AuNPs, attention then shifted to investigating the combination of X-rays with an ATM inhibitor (ATMi). This publication focuses on using STRIDE to quantify genotoxicity and measure DSBs in the context of when ATMis are applied, an approach not previously possible using conventional DDR markers. DDR inhibitors including ATMis function by inhibiting DNA repair factors such as γH2AX, which complicates their use as direct indicators of genotoxicity. While these DDR markers can confirm whether ATM inhibition has occurred, they do not provide a quantifiable measure of how much DNA repair is actually being blocked. In contrast, STRIDE offers a direct means of assessing DSBs, allowing for a more accurate analysis of the impact of ATMis on DNA repair kinetics and its potential role in enhancing radiosensitisation when combined with X-ray irradiation.

4.4.2 Authors and Affiliations

Jake Atkinson[1], Joshua Chopin[2], Eva Bezak[3,4], Hien Le[3,5], Ivan Kempson[1]*

[1] Future Industries Institute, University of South Australia, Mawson Lakes, SA 5095, Australia

[2] Industrial AI Research Centre, University of South Australia, Mawson Lakes, SA 5095, Australia

[3] UniSA Allied Health and Human Performance, University of South Australia, Adelaide, SA 5095, Australia

[4] Department of Physics, University of Adelaide, North Terrace, Adelaide, SA 5005, Australia

[5] Department of Radiation Oncology, Royal Adelaide Hospital, Adelaide, SA 5000, Australia

*Author to whom correspondence should be addressed.

4.4.3 Abstract

Radioresistant cancers often exhibit upregulated DNA damage response (DDR) proteins including ataxia telangiectasia mutated (ATM), recovering more readily from radiation-induced DNA double-strand breaks (DSBs). ATM inhibitors (ATMi) are therefore being explored as adjuvants in radiotherapy to both enhance radiosensitivity and minimise normal tissue complications. The molecule AZD1390 has been developed as an inhibitor of ATM and is undergoing assessment in clinical trials. However, traditional markers of DNA DSB repair, such as γH2AX, represent stages of DDR downstream from the action of ATM. The ATMi AZD1390, developed by AstraZeneca, ultimately prevents phosphorylation of the H2AX histone variant. In order to quantify ATMi AZD1390 action, the novel and highly complementary assay SensiTive Recognition of Individual DNA Ends (STRIDE) was employed to directly quantify DSBs in comparison to γH2AX after X-ray irradiation of 4T1 cells. Findings revealed that ATM inhibition via AZD1390 delays DSB repair initiation and appears to play a greater role in suppressing DDR beyond ATM inhibition alone. In X-ray irradiated conditions, obfuscation of DSBs commenced between 30- to 45-minutes post-irradiation without AZD1390 versus 45 to 60-minutes for cells pretreated with AZD1390 and entirely prevented γH2AX in the majority of cells. STRIDE and γH2AX exhibited almost no co-localization indicating that they provide distinct and complementary information. DSB formation was also assessed in cells fixed pre-insult to minimise any biological response, providing unprecedented assessment of DSB formation. These results highlight the potential of STRIDE to accurately measure DNA damage response kinetics, paving the way for more precise mechanistic studies into the role of ATM in radiotherapy.

Key words: Double-strand breaks, DNA repair, ATM inhibition, Radiosensitization, Radiotherapy, Cancer

4.4.4 Introduction

During X-ray radiotherapy, one of the principal modes of cell death is the induction of DNA double-stranded breaks (DSBs). These occur through either direct ionization of DNA or indirectly via ionization of surrounding water molecules, generating cytotoxic reactive oxygen species (ROS) which

subsequently interact with DNA. If unrepaired, DSBs lead to mutations, chromosomal aberrations, or cell death, making efficient detection and repair critical for maintaining genomic integrity [129]. As such, cells constantly monitor DNA damage through activation of key signalling molecules within the DNA damage response (DDR). This includes ATM (ataxia telangiectasia mutated), ATR (ATM and Rad3-related), and γH2AX, which enable the recruitment of factors that initiate DSB repair pathways. ATM plays an intricate role in regulating the DDR, being recruited to DNA breakage sites by the DSB tethering MRE11-RAD50-NBS1 (MRN) complex, and subsequently undergoing autophosphorylation at Ser1981 [130]. This active form of ATM is then able to phosphorylate Ser139 of histone variant H2AX (γH2AX), which allows for widespread chromatin remodelling and accumulation of proteins within the homologous recombination (HR) or non-homologous end joining (NHEJ) pathways at DSB sites [6].

In clinical situations, the effectiveness of single modality radiation or chemotherapy is often constrained by the risk of normal tissue complications. Therefore, a combination of surgery, radiotherapy, and chemotherapy is often prescribed in advanced cancers to enhance the likelihood of tumour control and eliminate microscopic disease [131]. Dysregulation of the DDR often leads to radioresistance, making proteins within this pathway candidates for targeted chemotherapies [132]. Development of ATM inhibitors (ATMi) therefore holds great potential in increasing the vulnerability of radio- and chemo-resistant tumours. Inhibiting ATM can enhance the sensitivity of cancer cells to radiotherapy by interrupting the DDR and preventing cancerous cells from surviving otherwise lethal damage [133, 134]. AZD1390, developed by AstraZeneca, is one such inhibitor highly selective against ATM with a half-maximal inhibitory concentration (IC50) of 0.78 nM [48]. It possesses an advantage over similar ATMi, including the previously developed AZD0156, due to its ability to penetrate the blood-brain barrier (BBB). The BBB prevents many widely used anti-cancer pharmaceuticals from entering the brain [135], and even if penetrance is possible, intratumoural drug concentration may not exceed the cytotoxic threshold required to eliminate the tumour entirely [136]. Therefore, the combination of both AZD1390's selectivity and BBB penetrance is highly

desirable for treatment of radioresistant brain tumours such as glioblastoma multiforme (GBM) [135, 137-139]. This capability was validated in a study using 11C-labelled AZD1390 and positron emission topography (PET) imaging in cynomolgus monkey brains [48], and a phase I clinical trial (ClinicalTrials.gov ID: NCT03423628) has also commenced to determine the tolerability of administering AZD1390 in combination with radiotherapy in GBM patients [135].

ATMi have also been investigated for their role in enhancing the radiosensitivity of breast cancers (BC). As the most commonly diagnosed cancer in women [140], BC commonly shows abnormalities in the ATM gene, which is a contributing risk factor in both its development [141, 142] and cancer-specific survival [143]. Inhibition of ATM has been shown to reduce the degree of cell invasion, migration and metastasis in both MDA-MB-231 and MCF-7 cells [144]. AZD1390 has been tested in mice against patient derived xenografts of HER2+ and triple-negative breast cancer, with pre-treatment sensitizing these cancer types to radiation in orthotopic models [121]. AZD1390-induced ATMi has also been shown to delay growth in 4T1 tumour models, and activate the cGAS/STING pathway, enhancing the type 1 interferon response and increasing the effectiveness of anti-PD-1 immunotherapy [145]. These findings highlight the potential of ATM inhibitors to broaden the therapeutic window and improve adjuvant therapies in BC treatment.

There is a need for more sensitive and precise techniques to assess DNA damage and repair, particularly within the realm of drug development and mechanistic studies. A major limitation in the characterization of ATMi function currently is the inability to accurately quantify their impact on DNA damage and repair. Conventional immunofluorescence-based methods typically rely on the detection of DNA repair markers, yet these assays do not directly quantify DSBs [36] and are prone to biases [33, 116]. For instance, using markers such as ATM or γH2AX, which signal downstream DNA damage response molecules to initiate repair, becomes problematic when DDR inhibitors are applied. Inhibition of ATM leads to reduced phosphorylation of γH2AX [53], which diminishes its detection via immunofluorescence and, as a result, compromises the reliability of these markers as indicators of DNA damage. γH2AX is the most conventional proxy for DSBs, however this signal is not expressed when ATMis are used [36]. Therefore, no published studies have been able to describe the exact impact of ATMi on the

formation and repair of DSBs by the DDR with immunofluorescent approaches. The effectiveness of ATMis in modulating DSB repair cannot be fully understood using current assays, impeding efforts to assess their role in enhancing genotoxicity.

There are significant gaps in understanding how ATMis affect DSB repair kinetics. Novel immunofluorescence assay STRIDE (SensiTive Recognition of Individual DNA Ends) offers a highly sensitive approach to address this challenge by detecting DSBs at single-break resolution [37]. This enables a precise analysis of the effects of ATM inhibition on DNA repair processes, particularly in the context of radiation-induced DNA damage. As STRIDE can bind to free DSB ends [37], this allows the ability to quantify the physical DNA breakages caused by X-rays and provide a comparison to biological signals activated in response. By leveraging the sensitivity of STRIDE, the primary aim of this study was to characterize the role AZD1390 plays in influencing the repair of DSBs. Internalization of AZD1390 was anticipated to inhibit activity of γH2AX, and consequently perturb DSB repair. Immunofluorescence stains for both STRIDE and γH2AX were used to quantify DSB formation and repair in 4T1 cells, a murine model of triple-negative BC, exposed to ATM inhibitor AZD1390, X-rays, and their combination. Capturing these changes in DSB and repair dynamics presents a powerful tool to provide insight into how DDR inhibitors modulate the DNA damage repair landscape, especially in the context of radiosensitization strategies. This study presents a proof-of-concept protocol developed to evaluate DNA damage and repair mechanisms in the context of DDR inhibitors such as AZD1390, providing insights into the impact of ATMis on DNA repair processes. While the experiments conducted using 4T1 cells provide a model for these mechanisms, the results may not fully represent the complexities inherent in different normal and malignant cell types. These findings establish a foundation for further investigations into the broader applicability of DDR inhibitors in diverse cellular contexts, with the aim of better informing drug development.

4.4.5 Methods

4.4.5.1 Cell Culture and Pre-treatment

Mouse-derived 4T1 cells (ATCC, CRL-2539) were cultured in RPMI medium (Thermo Fisher, 11875093) in a 37°C incubator with 95% relative humidity and 5% CO_2. Cells were seeded at a density of 40,000 cells per well into Ibidi µ-Slide 8 Well chambered coverslips (Ibidi, 80826) 12 hours before irradiation. Two hours prior to irradiation, AZD1390 (MedChemExpress, HY-109566) was added to specific conditions at a final concentration of 30 nM. All conditions were conducted in duplicate.

4.4.5.2 X-ray Irradiation

X-ray irradiation was performed using a 160 kV RadSource 2000 Small Animal Irradiator at the South Australian Health and Medical Research Institute (SAHMRI) in Adelaide, Australia. Cells immersed in 200 µL culture medium were irradiated for 45 seconds, delivering a total dose measured to be approximately 1.93 Gy (0.0429 Gy/s) with a Radcal Accu-Dose+ probe positioned in air adjacent to the slides. The exact dose received by the cells is dependent on surrounding scattering materials, volume of PBS above the cells and back-scattering material. Consequently, the measured dose from the probe, 1.93 Gy, is provided only as an estimate of the dose received by the cells, but anticipate this to be within 10% of the true dose. Fixation occurred pre-irradiation, denoted as the 0-minute timepoint, and at 15-, 30-, 45-, 60-, 120-, 240-, and 1440-minutes post-irradiation (post-IR) using 4% paraformaldehyde for 10 minutes at room temperature.

4.4.5.3 STRIDE Assay

Following fixation, cells were permeabilized in PBS with 0.5% Triton X-100 for 10 minutes and incubated with 0.5–10 mM EDTA/PBS at room temperature for another 10 minutes. Cells were then washed with 100 µL of TUNEL kit Wash Buffer. BrdUTP labelling of DSB ends was performed using the APO-BrdU Kit (BD Biosciences, Cat No. 556405), following the manufacturer's instructions. A 50 µL master mix, containing TdT enzyme, TdT reaction buffer, BrdUTP, and ddH_2O, was added to each well and incubated for 1 hour at 37°C. Wells were then washed with 100 µL of Rinse Buffer and blocked with 200 µL of 3% BSA for 1 hour at 37°C. Mouse MoBu-1 anti-BrdU (Abcam, 8039, 1:500) and Rabbit

Polyclonal anti-BrdU (Abcam, ab152095, 1:200) antibodies were incubated overnight at 4°C in 3% BSA. After thorough washing with Duolink® In Situ Wash Buffers, the Duolink® PLA® Probes Anti-Rabbit PLUS (Sigma Aldrich, DUO92002) and Anti-Mouse MINUS (Sigma Aldrich, DUO92004) were added for 1 hour at 37°C. Subsequent incubations included a 30-minute ligation at 37°C, followed by a 100-minute polymerase incubation, with washes between each step. Final washes were performed using 1X and 0.01X Wash Buffer B.

4.4.5.4 γH2AX Assay

Cells were blocked in 3% BSA for 1 hour at 37°C, followed by incubation with anti-phospho-H2A.X (Ser139) Rabbit mAb conjugated with Alexa Fluor 488 (Cell Signaling Technology, #9719). Nuclear staining was performed using 1 mg/mL DAPI solution (Thermo Fisher, Cat No. 62248).

4.4.5.5 Confocal Imaging

Fluorescent images were acquired using Zeiss LSM 710 confocal microscope (Carl Zeiss, Germany) with a Plan-Apochromat 20x/0.8 M27 lens. Four fields of view, including approx. 24 z-slices (2 µm) with 10% overlap between fields of view, were collected for each condition, resulting in 1950 x 1950 pixel images and a size of x: 807.68 µm, y: 807.68 µm, z: 48.00 µm. The excitation and emission spectra used were as follows: STRIDE (λex 644 nm; λem 669 nm), γH2AX (λex 488 nm; λem 496 nm), and DAPI (λex 350 nm; λem 470 nm).

4.4.5.6 Image Analysis

Acquired confocal images were stitched and z-stack maximum projections produced in ZEN (black edition) 3.0 SR and exported in .TIF format. Maximum projection images were then subsequently processed in CellProfiler 4.2.6 [146]. CellProfiler has several modules to perform batch operations on a set of input images. Modules can be added, removed, or re-ordered depending on the needs of each experimental run. The process to identify objects (foci) within nuclei follows the format of splitting each RGB image into their grayscale constituents, classifying and identifying nuclei based on the blue channel (DAPI), and then measuring the signal from the red, green, and blue channels within each nucleus to obtain values of integrated intensity. For 63x images, thresholds were defined to produce masks of individual STRIDE and γH2AX foci and consequently allow

for quantification per nucleus. Data was then exported to Excel, integrated intensity values for STRIDE or γH2AX were normalized to the integrated intensity of DAPI and transferred to GraphPad Prism 10 for further graphing and statistical analysis. As this data is non-parametric, p-values were obtained by performing a Mann-Whitney U test for STRIDE and γH2AX data at select timepoints comparing irradiated cells with or without AZD1390. Final figures were edited with ImageJ 1.54f to add scale bars and Photopea to produce collages of confocal images.

4.4.6 Results and Discussion

4.4.6.1 Confocal Imaging

Two-hours prior to irradiation (T = -120 minutes), cells were treated with or without 30 nM AZD1390 and then returned to a 37°C humidified incubator. Wells were then fixed at a 0-minutes timepoint, that is at the 2-hour exposure point for the AZD1390 pre-treatment and just prior to X-ray irradiation. The rationale was to obtain a measure of the physical damage caused by X-rays without initiation of the biological DDR. As of the time of writing and to the best of our knowledge, this is the first report of such a procedure prior to irradiation to determine DSB counts *in vitro*. After irradiation, cells were also fixed incrementally from 15 to 1440 minutes post-insult to compare both STRIDE and γH2AX kinetics in single cells. Confocal imaging was performed at 20x to obtain integrated intensity values for all experimental conditions and timepoints, and at 63x for foci quantification of the 15-, 30- and 45-mintutes post-IR 'X-ray irradiation only' conditions (Figure 16, Figure 21).

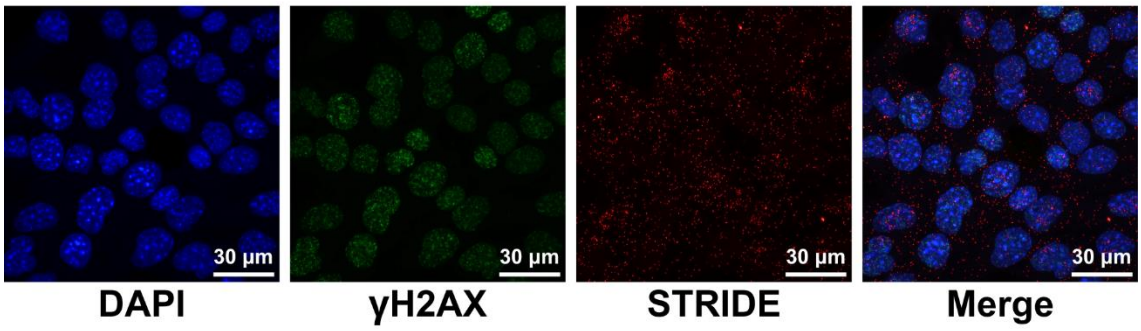


Figure 16: Confocal images at 63x magnification of 4T1 cells irradiated with 1.93 Gy of 160 keV X-rays and fixed 30-minutes post-IR. Cells were co-stained to identify DSBs (red) and γH2AX (green) with STRIDE (Duolink In Situ Detection Reagents FarRed (Cy5)), and anti-phospho-histone H2AX conjugated with Alexa 488 respectively. DAPI was used to label individual nuclei.

4.4.6.2 0 Gy X-rays Negative Controls

For the negative control with no radiation and no ATMi (Figure 17), little to no STRIDE foci were expected to form as well as a relatively low, baseline level of H2AX phosphorylation across all timepoints. This is because STRIDE foci, representative of DSBs, should mainly occur due to X-ray irradiation of cells. As there was no irradiation of these samples, STRIDE fluorescence should not be abundant under this condition. Generally, the majority of conditions represent values from between ~700 - ~1,500 individual cells (Table 1). Data are also presented in terms of the mean values in Figure 22, which is useful for easier visualization of the data trends. Potential sources of STRIDE foci formation in this negative control include spontaneous DSBs during DNA replication, cytosolic DNA fragments or damaged mitochondrial DNA. Immunofluorescence imaging of these control samples does not suggest that these sources of STRIDE foci exist in high numbers, however. Since cells were not cell phase synchronized, the DNA content (and hence DAPI signal) between cells in different phases would vary. STRIDE and γH2AX signals could also present artefacts due to this, as differences in DNA content may correlate with additional DSBs and H2AX phosphorylation events. To minimize this, the integrated intensities of STRIDE and γH2AX were divided by the integrated intensity of DAPI to express these signals as a proportion of DAPI per cell.

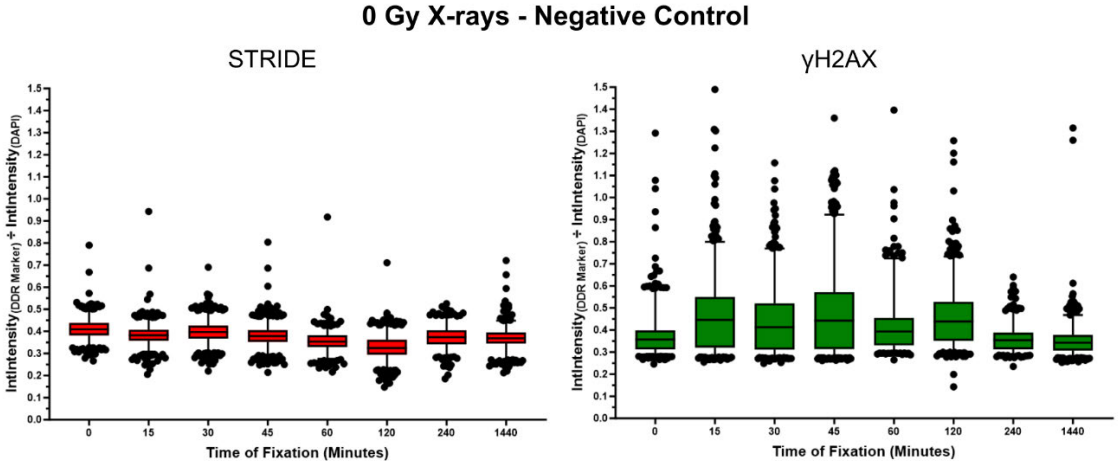


Figure 17: Negative control condition of 4T1 cells without X-ray or ATM inhibitor AZD1390 treatment (negative control). Integrated intensity values for STRIDE, γH2AX, and DAPI from single cells were measured. STRIDE and γH2AX values were normalised to DAPI. Data show the

median value within the 25th and 75th percentile data points (box). Whiskers show the 2.5 - 97.5 percentile, and dots represent data points outside the range represented by whiskers.

When observing normalized integrated intensity values, both STRIDE and γH2AX reflected a low level of genotoxic stress within these cell populations. For the sake of this experiment, it can be considered the 'baseline' level of damage and repair respectively for 4T1 cells. Median intensities range from 0.32 - 0.41 for STRIDE and 0.34 – 0.45 for γH2AX, with the latter marker's signal appearing to increase slightly between the 0- (0.36) and 15-minute (0.45) timepoints and then plateaus at the majority of timepoints afterwards. This could be due to the minute level of stress these cells were placed under on the trip to and from the irradiator lab. Measures were taken to ensure cells were temperature controlled by using heat packs surrounding the culture plates in their transport container, although it did not permit for maintenance of optimal oxygen and carbon dioxide levels (~20% and 5% respectively). Additionally, as the containers the well plates were carried in were not sterile, and due to removing the lids from the Ibidi 8-well plates prior to irradiation to minimise attenuation, there was a potential window for infection although it is anticipated that over these time frames there would be negligible impact.

Data from cells which were cultured with the ATMi are provided in Figure 18. Like the negative control, there is minimal change in STRIDE signal across all timepoints. As ATM is an activator of γH2AX, inhibition of ATM through AZD1390 also results in a reduction in phosphorylation of γH2AX. AZD0156, another clinical-grade ATM inhibitor from the same family as AZD1390, was also established to suppress γH2AX in FaDu cells at a dose of 30 nM following 5 Gy irradiation [53]. Therefore, with AZD1390 being highly selective of ATM with an IC50 of 0.78 nM [48], and the dose utilised being far above this (30 nM), near-complete suppression of γH2AX signal was expected to be observed. Hence for this AZD1390 control, substantial changes in γH2AX fluorescence intensity across timepoints were not expected. Indeed, the median integrated intensities for this sample are lower across all timepoints (0.28 – 0.32) compared to cells without AZD1390. STRIDE foci exhibit comparable median intensities (0.24 – 0.34), compared to the negative control where there is also no X-ray treatment. These data indicate that there was still a low level of genotoxic stress to the cells

in this condition, but the resulting γH2AX formation which had been observed in Figure 17, has been suppressed in Figure 18 due to the ATMi.

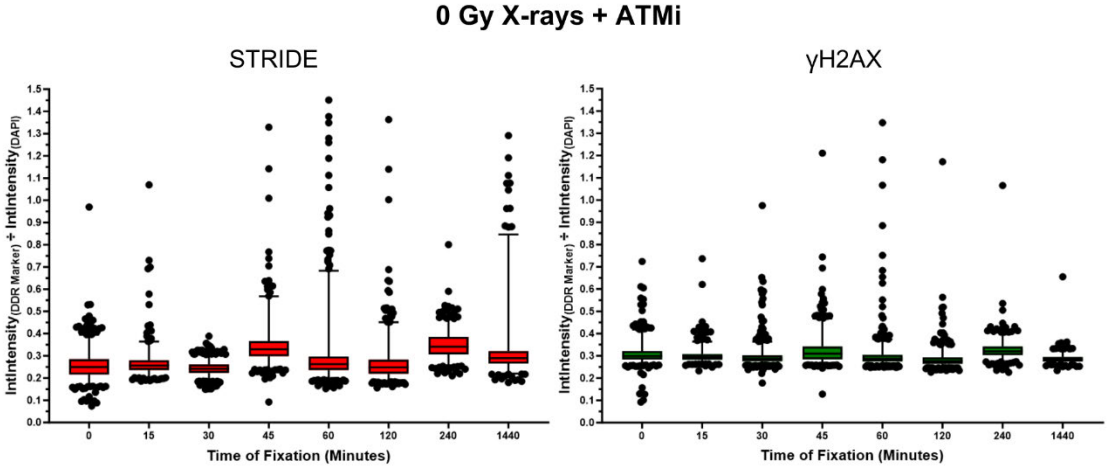


Figure 18: Non-irradiated 4T1 cells pre-treated with 30 nM AZD1390. Integrated intensity values for STRIDE, γH2AX, and DAPI from single cells were measured. STRIDE and γH2AX values were normalised to DAPI. Data show the median value within the 25th and 75th percentile data points (box). Whiskers show the 2.5 - 97.5 percentile, and dots represent data points outside the range represented by whiskers.

4.4.6.3 X-ray Irradiation Combined with AZD1390

Upon exposure to X-rays and the induction of physical DNA lesions, the DSB kinetics of STRIDE become apparent (Figure 19). Initially, STRIDE DSB foci are at their peak at the 0-minute timepoint (0.69 arbitrary units), wherein samples were fixed pre-irradiation. This is the first time DSB's have been measured in this way and provides a new approach to studying DNA damage in situ with no active DDR. The maximum number of DSB foci were expected to be observed at this timepoint, as the biological repair mechanisms do not yet have an opportunity to initiate repair post-IR. Therefore, it is an unambiguous representation of the exact number of DSBs that are occurring due to the physical dose administered. As time post-IR increases, STRIDE DSB intensity already decrease slightly at 15 minutes (0.59) and then maintained at 30 minutes (0.59) post-irradiation, after which there is a substantial decrease at the 45-minute (0.43) timepoint. This decrease in fluorescence then tapers off from 60 minutes (0.33) onwards with a return to baseline levels of STRIDE, akin to the negative control and ATMi only conditions. Conversely, γH2AX signal is at a minimum at the 0-minute timepoint (0.34), with increases at the 15- (0.40), 30- (0.54), and 45-minute (0.60)

timepoints. This signal then plateaus at the 60-minute timepoint (0.58), and then reduces slightly as activation persists at 120- (0.52), 240- (0.53) and 1440-minutes (0.43) post-IR. Noticeably, although the fluorescence intensity of STRIDE decreases back to baseline levels, γH2AX is still active through to 1440-minutes.

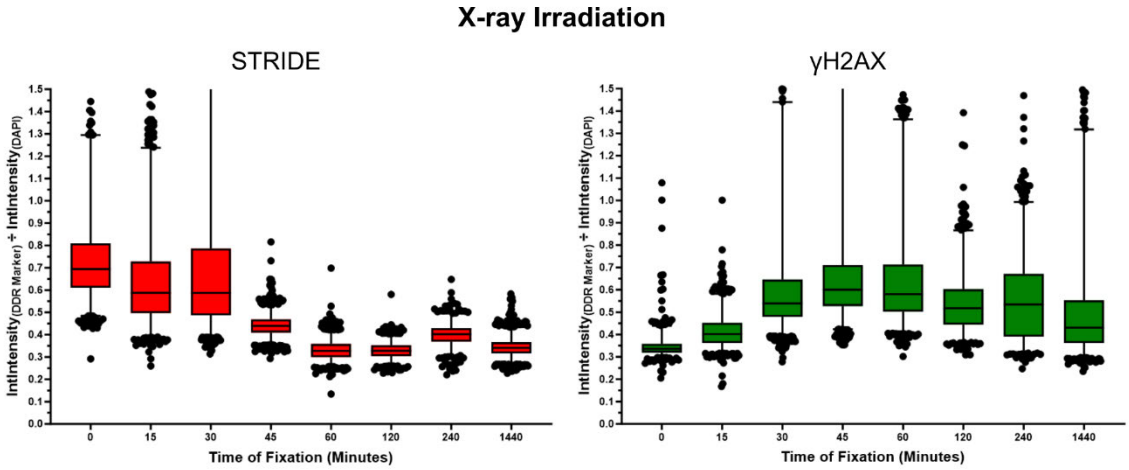


Figure 19: 4T1 cells irradiated with X-rays. Integrated intensity values for STRIDE, γH2AX, and DAPI from single cells were measured. STRIDE and γH2AX values were normalised to DAPI. Data show the median value within the 25th and 75th percentile data points (box). Whiskers show the 2.5 - 97.5 percentile, and dots represent data points outside the range represented by whiskers.

One trend that is immediately noticeable is the characteristic ‘crossing over’ of integrated intensity between STRIDE and γH2AX at the 30- and 45- minute timepoints. As repair signalling increases, represented by γH2AX, STRIDE intensity decreases as a function of time beginning at 30 minutes and continuing through to the 1440-minute timepoint. Conversely, γH2AX increases from the 30-minute timepoint and then reaches a peak at both 45- and 60-minutes post-IR. This suggests that initiation of DNA damage repair obscures the ability of STRIDE to detect DSBs, likely due to recruitment of proteins to DSB ends that prevent STRIDE from binding.

This study also investigated in whether there was a cell phase dependence on STRIDE vs γH2AX normalised intensities, aiming to determine whether DNA damage or repair are enhanced within certain subpopulations. Specifically, how radiosensitive (G2/M) versus more radioresistant (G1 and S) phases respond to

X-rays. By analysing the integrated intensities of DAPI and segmenting cell cycle phase, it appears that γH2AX is first active in G2/M phase cells at 30- and 45-minutes, with G1 cells lagging with elevated signals from 60-minutes onwards (Figure 23 to Figure 30). S phase cells remained relatively unchanged in terms of damage or repair accumulation. However, confocal microscopy provides limited fidelity in assessing DNA content across the cell cycle phase and these trends require high-throughput validation via flow cytometry.

Similarly to the AZD1390 only condition, inhibition of ATM with AZD1390 results in a low level of γH2AX phosphorylation across all timepoints (0.26 - 0.41), even when in combination with X-ray irradiation (Figure 20). This validates that even in the presence of radiation induced DSBs, that inhibition of ATM biological repair proteins will suppress the repair response. However, compared to irradiation alone, STRIDE intensities remain at their peak intensities at 0- (0.84), 15- (0.82) and 30-minutes (0.89) for a longer duration, and consequently decrease at later timepoints. Interestingly, the intensity of STRIDE signal across these timepoints is higher than with X-ray irradiation alone (Mann-Whitney $p < 0.0001$).

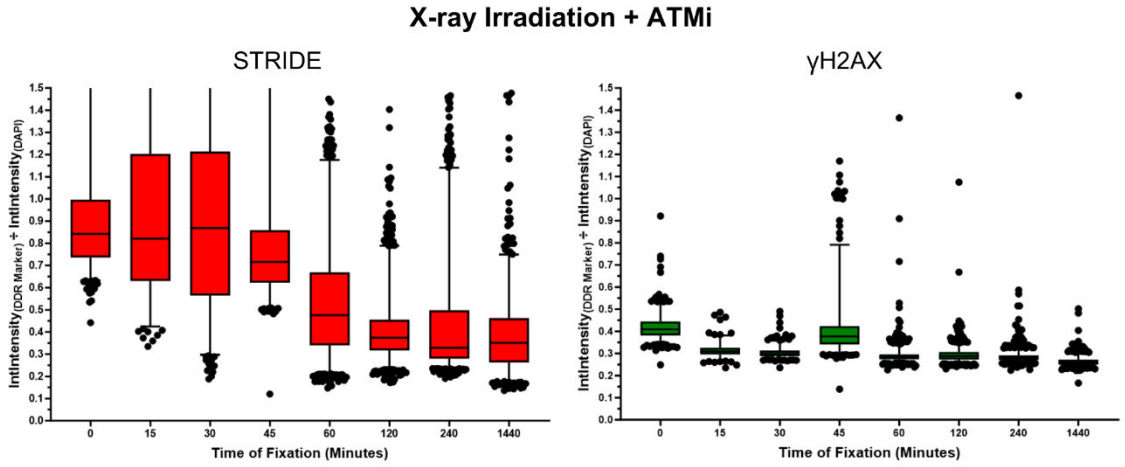


Figure 20: 4T1 cells irradiated with X-rays and pre-treated with 30 nM AZD1390. Integrated intensity values for STRIDE, γH2AX, and DAPI from single cells were measured. STRIDE and γH2AX values were normalised to DAPI. Data show the median value within the 25th and 75th percentile data points (box). Whiskers show the 2.5 - 97.5 percentile, and dots represent data points outside the range represented by whiskers.

STRIDE signal then begins decreasing at 45- (0.72) and more substantially at 60-minutes (0.48) post-IR. This is also distinct from X-ray irradiation only, where

STRIDE signal decreases substantially at the 45-minute (0.43) and 60-minute (0.33) timepoints, compared to when AZD1390 is added ($p < 0.0001$). One potential explanation for this delay in DNA damage repair is that upon addition of AZD1390, suppression of both ATM and γH2AX phosphorylation promotes alternate damage signalling molecules to compensate and commence accumulation of DDR proteins at DSB sites. These processes are likely less efficient than ATM or γH2AX, causing DSB repair proteins to take longer to accumulate at DSB sites, which delays their ability to obscure STRIDE detection.

4.4.6.4 Colocalization of STRIDE and γH2AX Foci

To further investigate the relationship between STRIDE and γH2AX, the spatiotemporal correlation between the two markers was then explored. Specifically, in determining whether a γH2AX focus appears at the same location as a STRIDE focus when it resolves. Literature indicates that γH2AX foci can form 200 – 400 kilobases away from the DSB site [13, 40], so assessing colocalization could determine if γH2AX foci align with individual DSBs. Whether the disappearance of a STRIDE focus coincides with the emergence of a γH2AX focus, or rather if DSB resolution and the initiation of γH2AX repair signalling are linked, was also investigated (Figure 21).

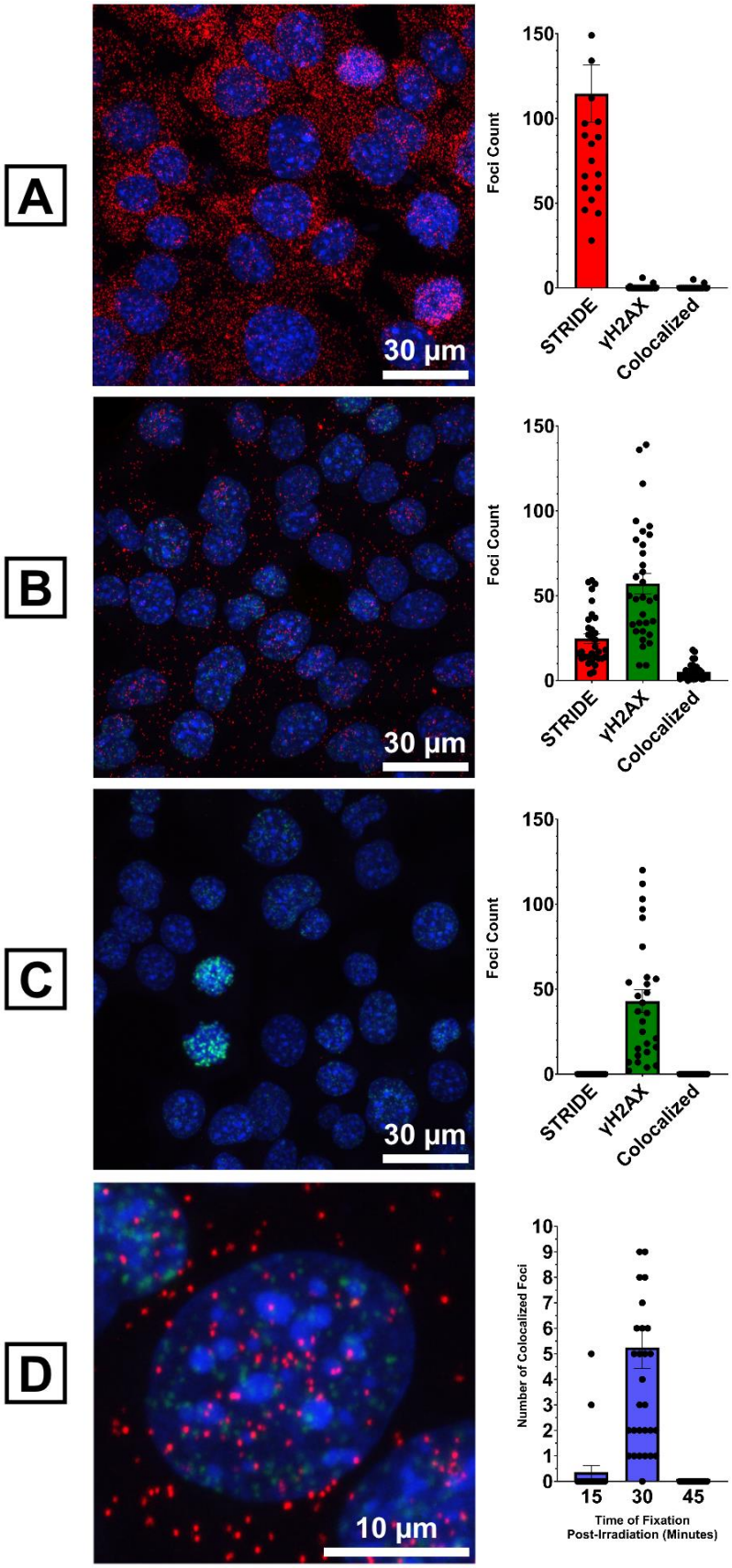


Figure 21: 63x magnification images of X-ray irradiated 4T1 cells stained with DAPI (nuclei), STRIDE (red) and anti-γH2AX Alexa 488 conjugate (green), as well as corresponding foci counts

at A.) 15-minutes post-IR, B.) 30-minutes post-IR, and C.) 45-minutes post-IR. Each image is representative of an independent well. D.) 30-minutes post-IR focusing on a single 4T1 cell. Mean + standard error of the mean values of colocalized foci identified across all three fixation timepoints.

From the images depicted in Figure 21, STRIDE and γH2AX foci generally do not colocalize, indicating that there may be proteins or other factors preventing STRIDE from binding to DSBs after their formation but before γH2AX foci are established (via H2AX phosphorylation). This is important as it identifies that the two markers represent distinctly different parts of the DSB formation and response pathways and are directly complementary. At the 30-minute timepoint there is a strong co-existence of STRIDE and γH2AX foci as STRIDE foci counts decrease, γH2AX counts increase. To confirm that the colocalization of foci at 30-minutes was not an artifact of the maximum intensity projection, individual z-slices were qualitatively analysed, showing fewer instances of colocalization across z-slices than with the maximum projection. This is indicative that that STRIDE and γH2AX markers do not frequently colocalize on the same z-plane.

4.4.7 Conclusion

This study supports the critical role of ATM in the repair of DSBs and highlights the potential of AZD1390 to enhance the radiosensitivity of cancerous cells. By employing STRIDE, the effect of AZD1390 on DNA repair kinetics within a 24-hour timeframe in 4T1 cells was successfully characterised. It was discovered that the physical presence of DNA breaks can still be detected using STRIDE when cells are treated with AZD1390, making it a superior tool for assessing DNA damage formation in scenarios where DDR markers like γH2AX are suppressed, and are hence unreliable indicators of genotoxicity. Moreover, STRIDE showed that treatment of cells with a combination of AZD1390 and X-rays delayed the onset of DSB resolution compared to X-rays alone. Obfuscation of the DSB to STRIDE due to DSB sensing is delayed in the presence of ATMi, indicating ATMis play a greater role in suppressing DDR beyond ATM inhibition alone. Consequently, ATM inhibition effectively prolongs the persistence of radiation-induced DNA damage, providing a potential therapeutic advantage by stalling DNA sensing and repair in radioresistant cell types and thereby extending the window during which they remain vulnerable to radiotherapy. In future studies,

testing of AZD1390 against multiple cancer cell types with varying radioresistance would provide valuable insights into whether its effectiveness in perturbing DSB repair is universal. Exploring combination therapies that pair AZD1390 with other DDR-targeting chemotherapeutics could also provide a more comprehensive strategy to both overcome radioresistance and enhance the DSB burden in aggressive or late-stage cancers.

4.4.8 Acknowledgements

This research was funded by the Tour de Cure PhD Scholarship, grant ID number RSP-641-FY2023. We acknowledge Tour de Cure's contribution towards the preparation of this manuscript through the Tour de Cure Scholarship Grant and appreciate their continued support for this work.

We acknowledge Microscopy Australia (ROR: 042mm0k03) at the Future Industries Institute, University of South Australia, enabled by NCRIS. Thanks to Dr. Alex Cavallaro for assistance with operation of the Zeiss LSM 710 confocal microscope.

Many thanks to Dr. Bill Liapis for assisting with the operation of the X-ray irradiator.

4.4.9 Supplementary Data

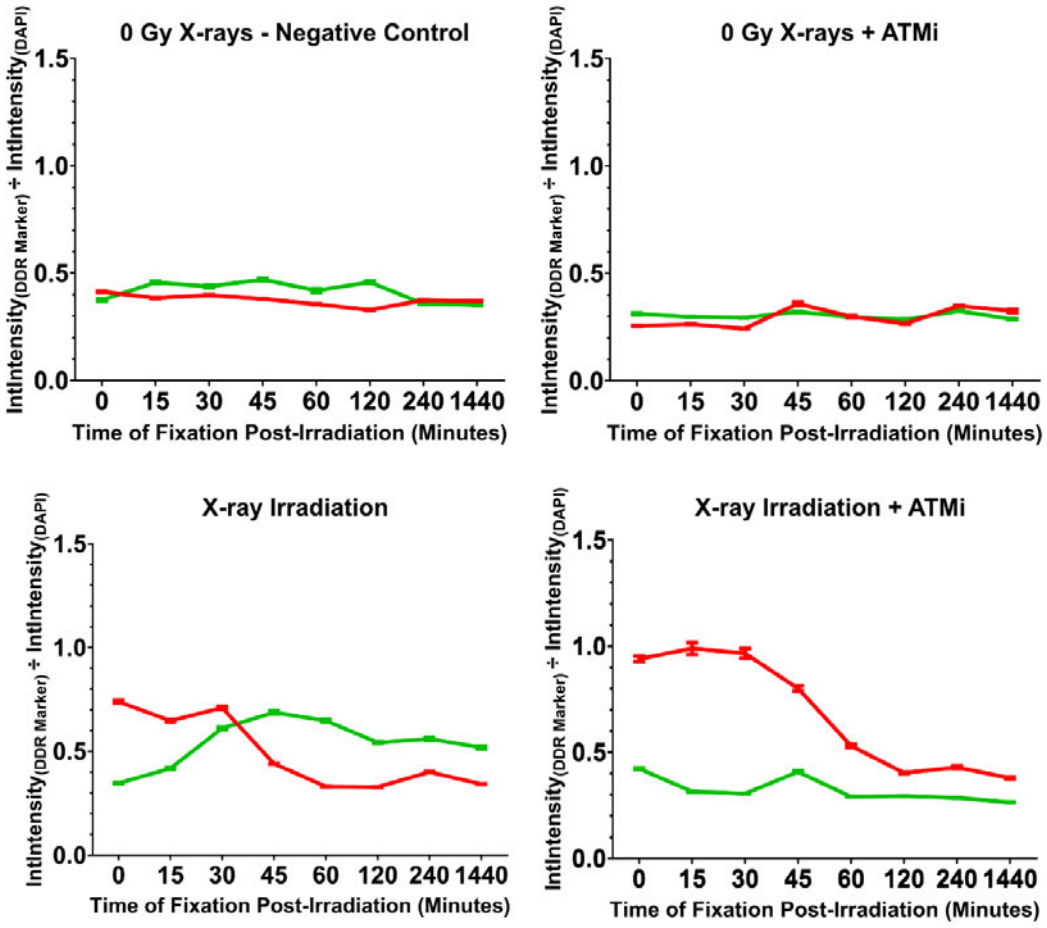


Figure 22: Mean and standard error of the mean (SEM) values of integrated intensity for STRIDE (red) and γH2AX (green) normalized to DAPI for 4T1 cells under various conditions. Top left: no X-ray irradiation or pre-treatment with AZD1390, top right: exclusively pre-treatment with 30 nM AZD1390, bottom left: exclusively X-ray irradiation, bottom right: X-ray irradiation in combination with 30 nM AZD1390 pre-treatment. Integrated intensity measurements were taken from individual nuclei across different fixation timepoints.

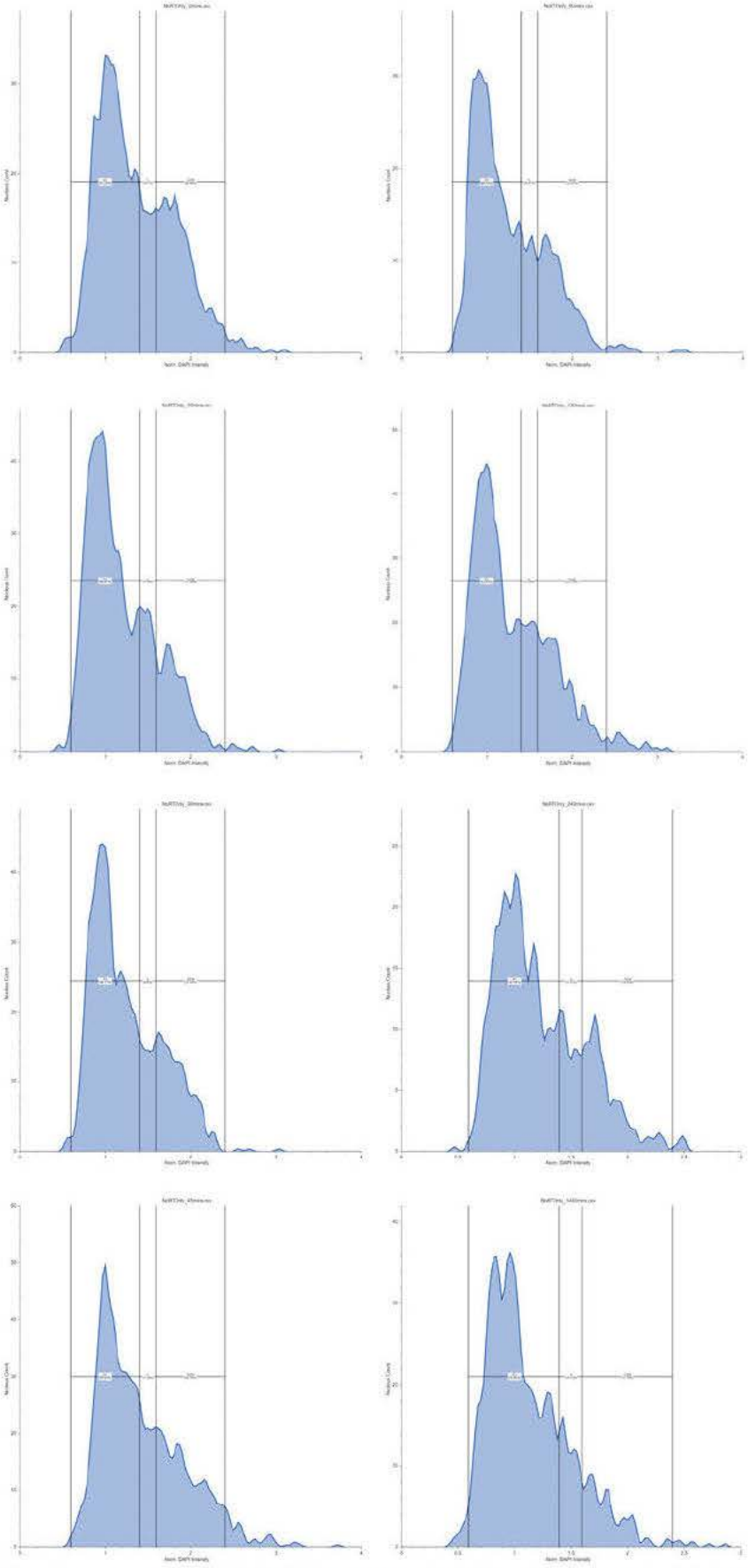


Figure 23: No X-rays or AZD1390. Histograms depicting the integrated intensity of DAPI normalized to the intensity of the 2N peak for each fixation timepoint. The gating of the G1 (0.6 – 1.4), S (1.4 – 1.6), and G2/M (1.6 – 2.4) phases are also displayed. Plots produced with Floreada.io.

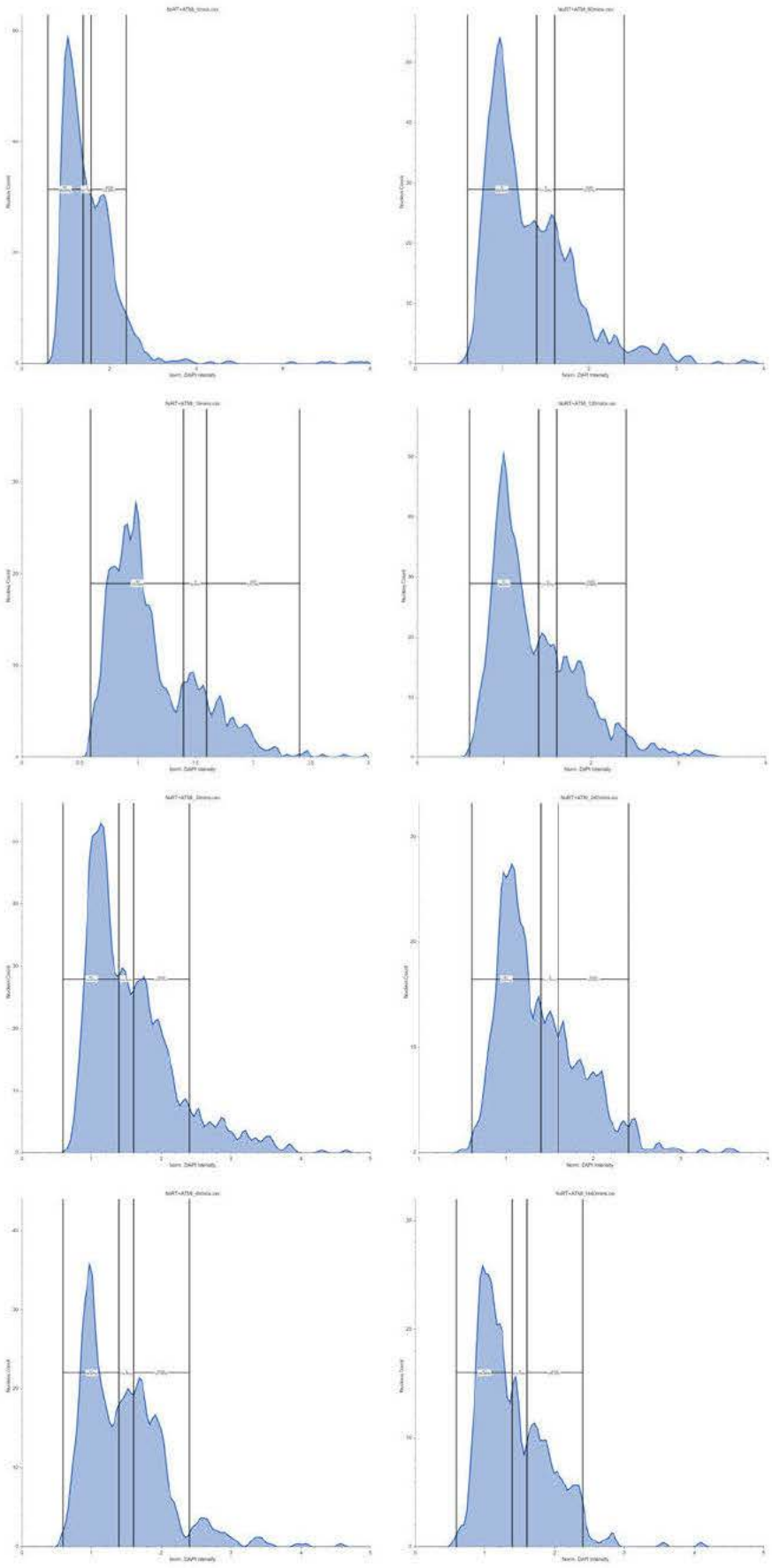


Figure 24: No X-rays + AZD1390. Histograms depicting the integrated intensity of DAPI normalized to the intensity of the 2N peak for each fixation timepoint. The gating of the G1 (0.6 – 1.4), S (1.4 – 1.6), and G2/M (1.6 – 2.4) phases are also displayed. Plots produced with Floreada.io.

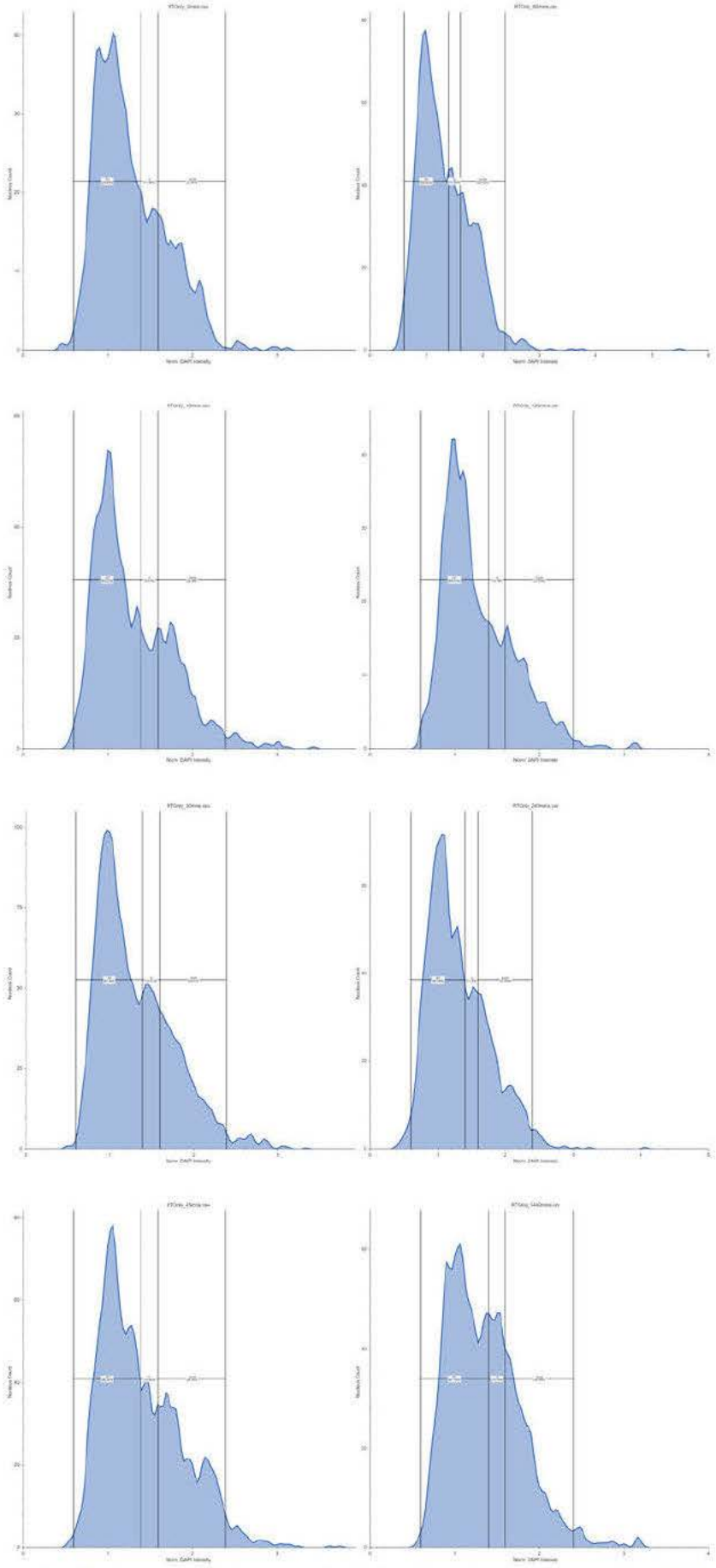


Figure 25: X-ray irradiation only. Histograms depicting the integrated intensity of DAPI normalized to the intensity of the 2N peak for each fixation timepoint. The gating of the G1 (0.6 – 1.4), S (1.4 – 1.6), and G2/M (1.6 – 2.4) phases are also displayed. Plots produced with Floreada.io.

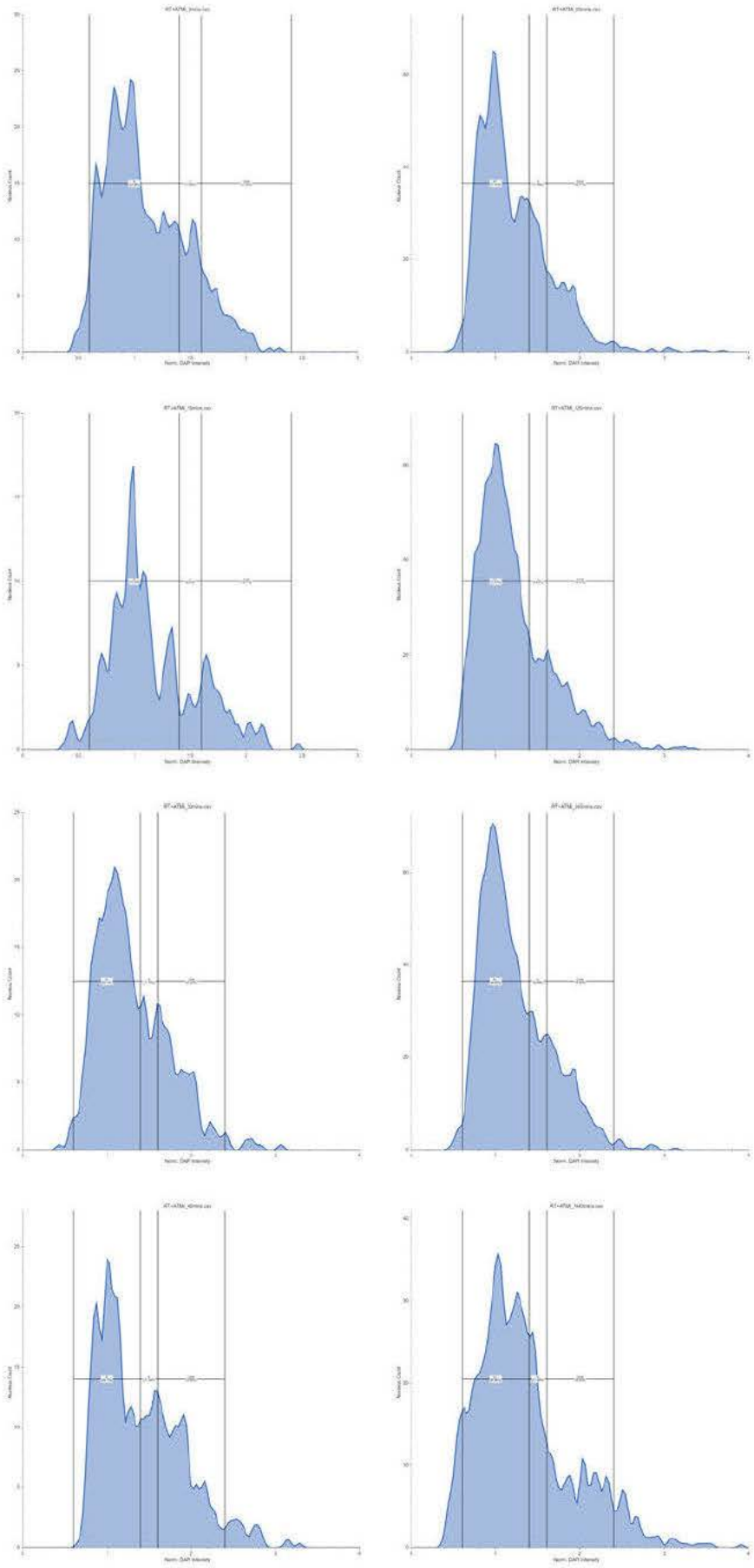


Figure 26: X-ray irradiation + AZD1390. Histograms depicting the integrated intensity of DAPI normalized to the intensity of the 2N peak for each fixation timepoint. The gating of G1 (0.6 – 1.4), S (1.4 – 1.6), and G2/M (1.6 – 2.4) phases are also displayed. Plots produced with Floreada.io.

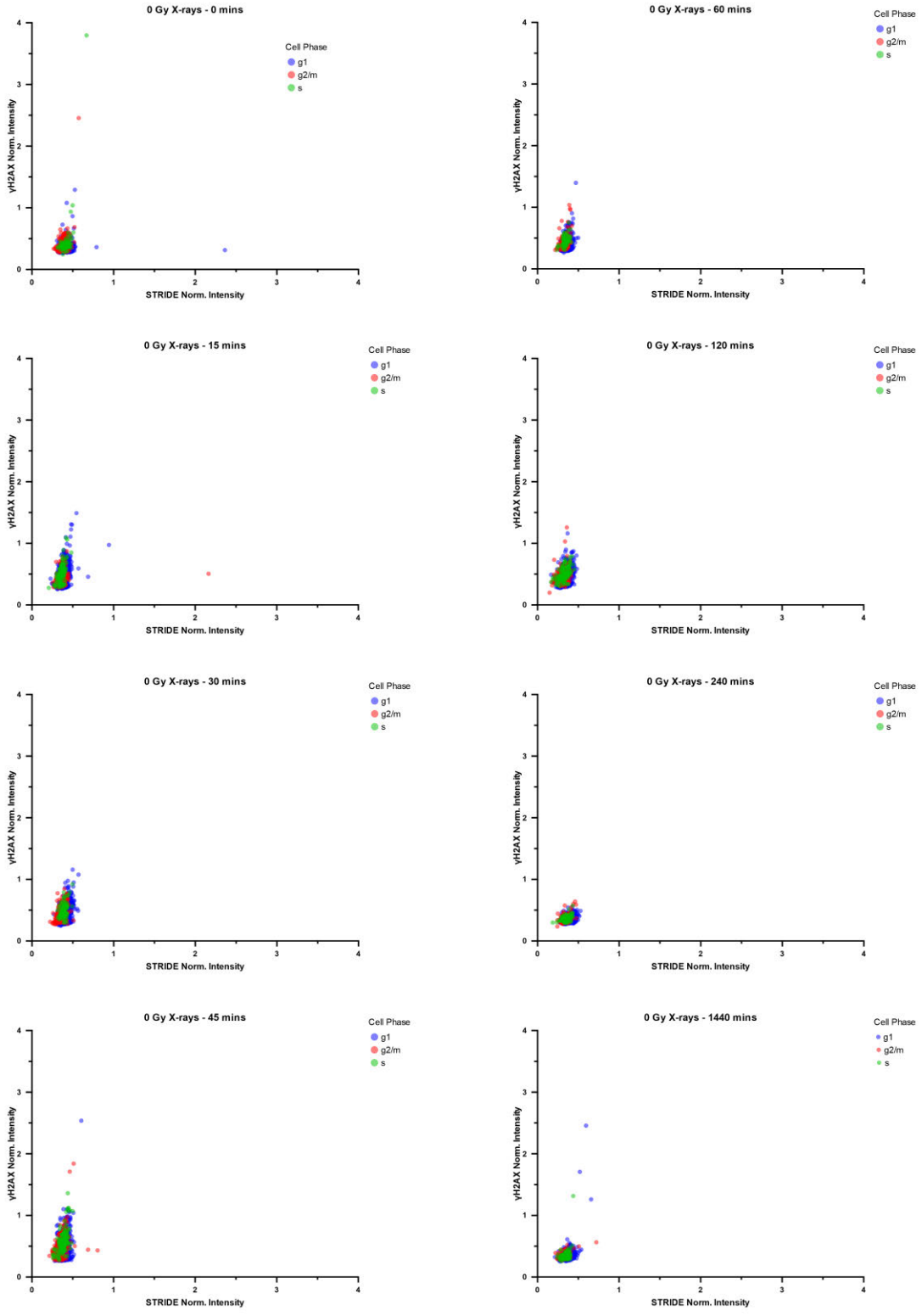


Figure 27: Normalized integrated intensities of STRIDE (x-axis) versus γH2AX (y-axis) for 4T1 cells with no X-ray or AZD1390 treatment. Intensities were gated (Figure 23) to determine the approximate proportion of cells in G1 (blue), S (green) and G2/M (red) phases.

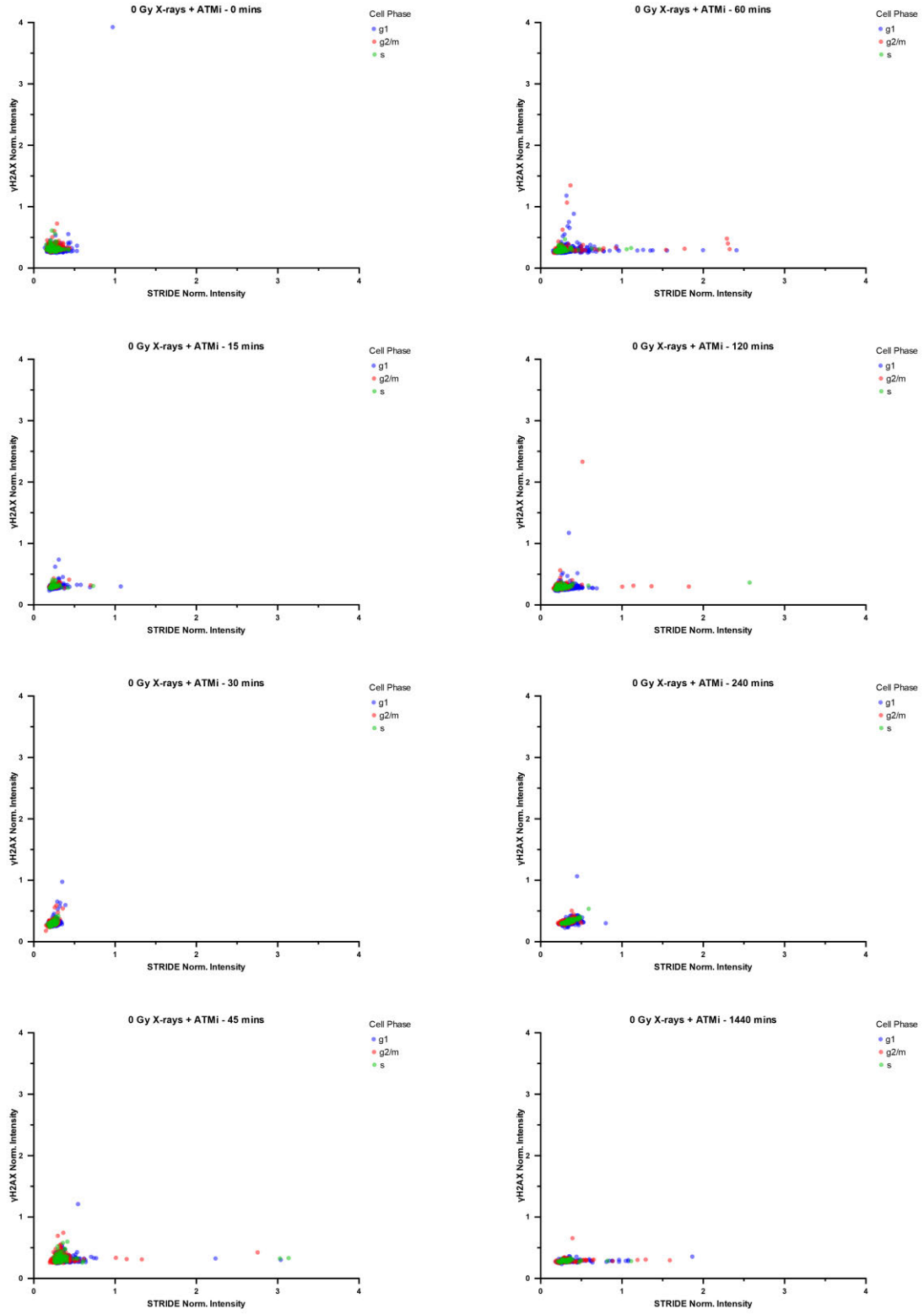


Figure 28: Normalized integrated intensities of STRIDE (x-axis) versus γH2AX (y-axis) for 4T1 cells pre-treated with 30 nM AZD1390 only. Intensities were gated (Figure 24) to determine the approximate proportion of cells in G1 (blue), S (green) and G2/M (red) phases.

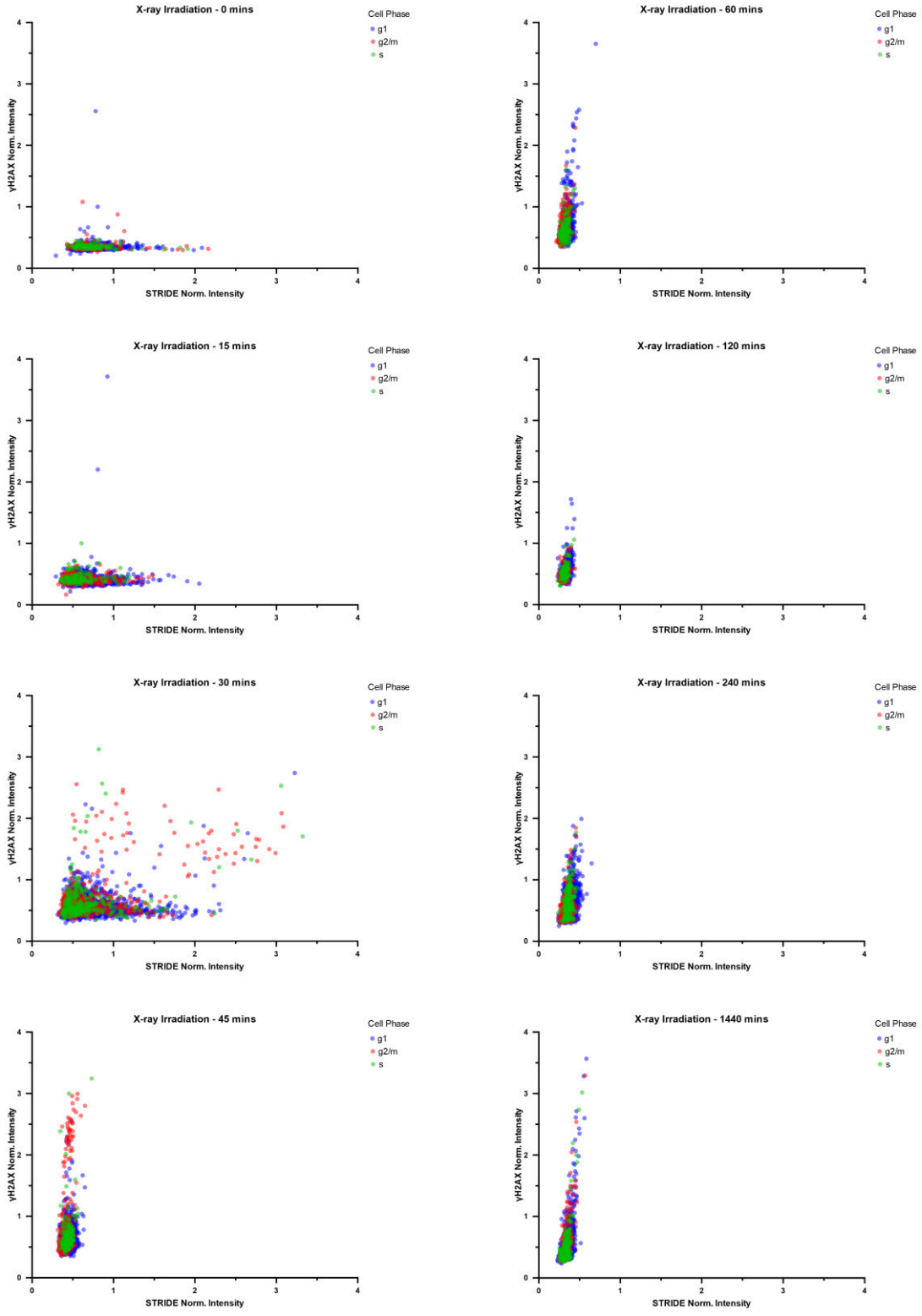


Figure 29: Normalized integrated intensities of STRIDE (x-axis) versus γH2AX (y-axis) for 4T1 cells treated with X-rays only. Intensities were gated (Figure 25) to determine the approximate proportion of cells in G1 (blue), S (green) and G2/M (red) phases.

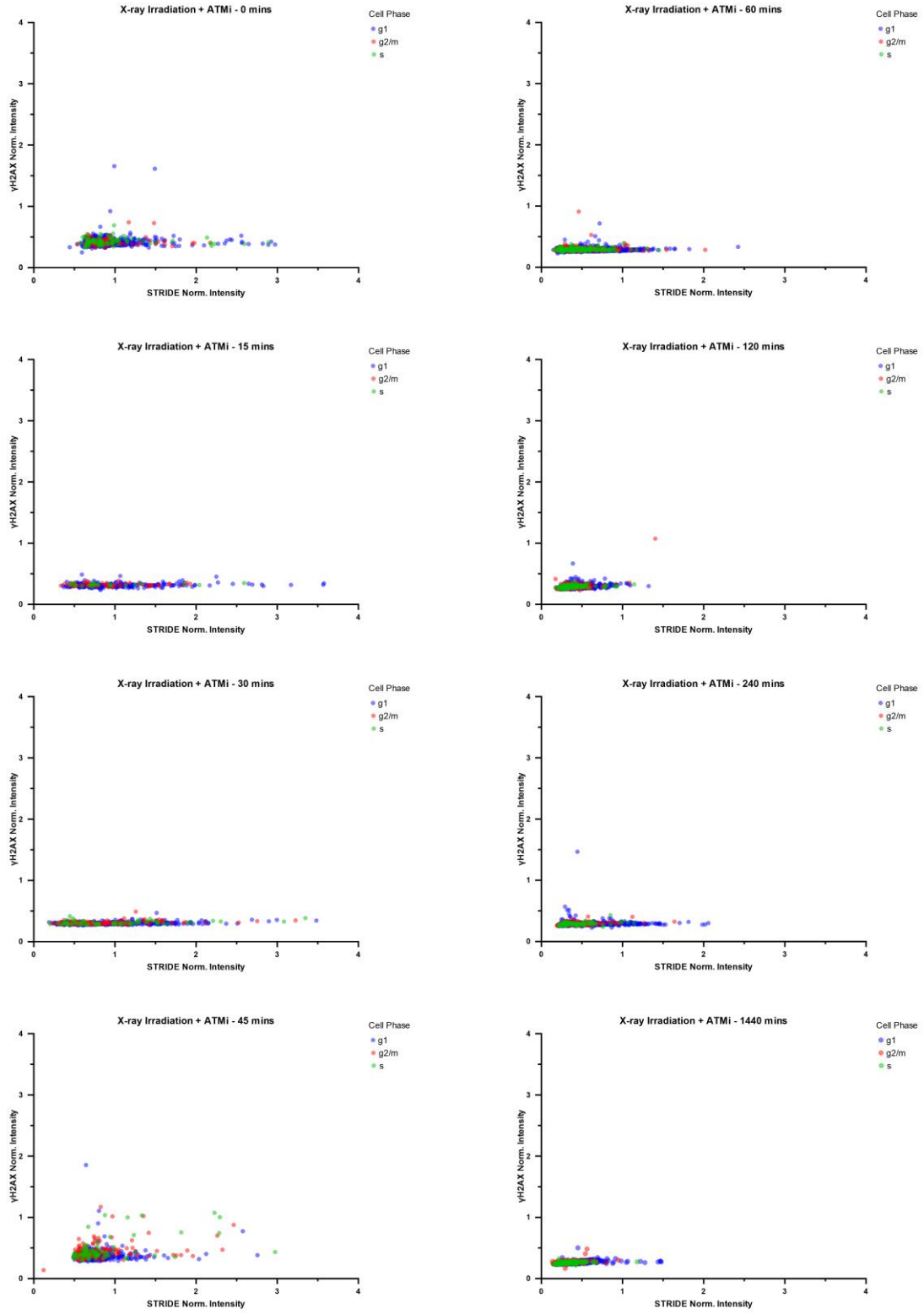


Figure 30: Normalized integrated intensities of STRIDE (x-axis) versus γH2AX (y-axis) for 4T1 cells treated with both X-rays and 30 nM AZD1390. Intensities were gated (Figure 26) to determine the approximate proportion of cells in G1 (blue), S (green) and G2/M (red) phases.

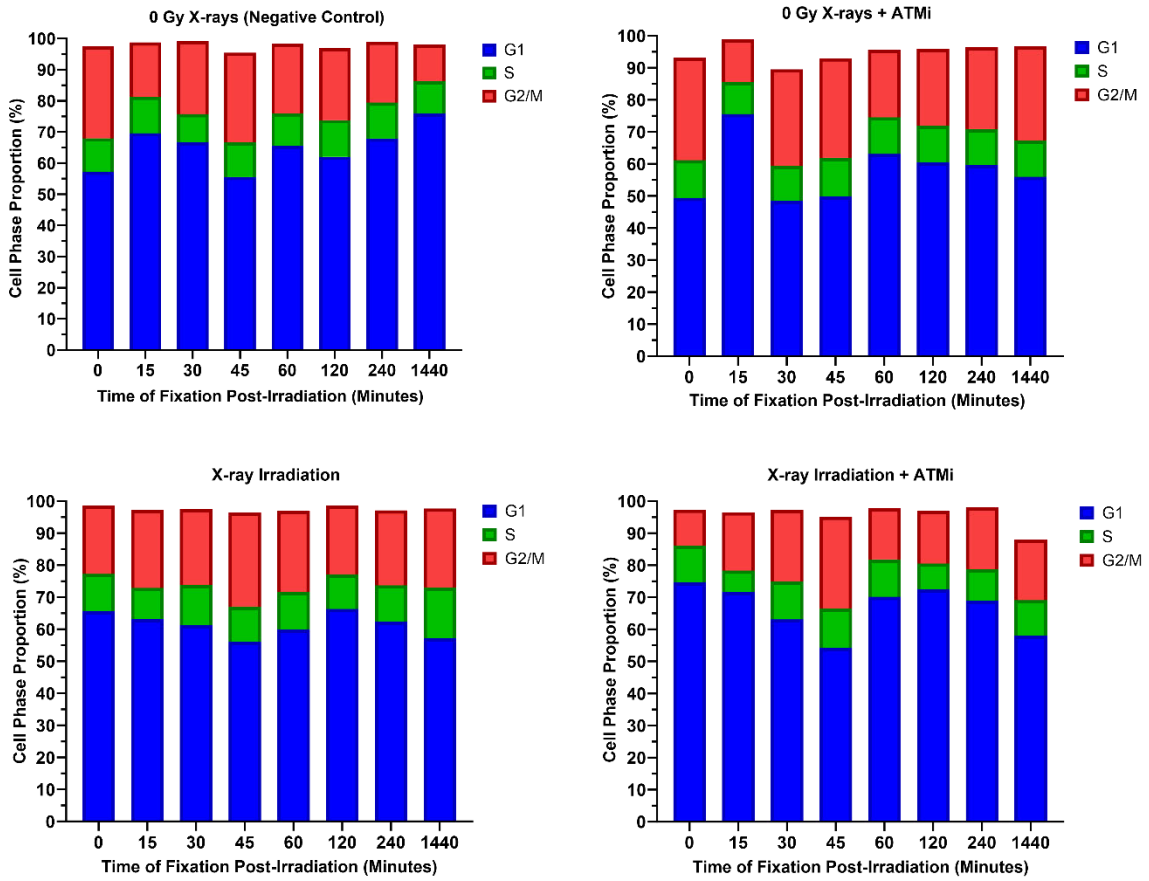


Figure 31: Stacked box plots depicting the percentage of 4T1 cells in each cell phase, G1 (blue), S (green), and G2/M (red) across fixation timepoints post-IR. Cells were gated based on the ranges defined in Figure 22-25.

Table 1: Descriptive statistics for each dataset for STRIDE and □H2AX across all timepoints. Values recorded include the number of values in each population (n), mean, median, standard deviation, standard error of the mean, range (defined by Prism as the difference in the minimum and maximum values), and 25th and 75th percentiles.

		0 Gy X-rays (Negative Control)		0 Gy X-rays + ATMi		X-ray Irradiation		X-ray Irradiation + ATMi	
		STRIDE	γH2AX	STRIDE	γH2AX	STRIDE	γH2AX	STRIDE	γH2AX
0 minutes	Number of values	924	924	880	880	1036	1036	724	724
	Minimum	0.266	0.2459	0.07408	0.09229	0.2921	0.2048	0.4421	0.2488
	25% Percentile	0.3818	0.3127	0.2163	0.2835	0.6104	0.3194	0.7365	0.382
	Median	0.4094	0.3571	0.2494	0.2994	0.6944	0.3362	0.8421	0.409
	75% Percentile	0.4382	0.3982	0.285	0.3219	0.8095	0.3579	0.996	0.444
	Maximum	2.364	3.795	0.9698	3.925	2.162	2.555	2.972	1.656
	Range	2.098	3.549	0.8958	3.832	1.87	2.351	2.53	1.407
	Mean	0.4136	0.3757	0.256	0.3119	0.7393	0.3465	0.9426	0.4209
	Std. Deviation	0.07846	0.1573	0.06317	0.1301	0.2092	0.08609	0.3564	0.08352
	Std. Error of Mean	0.002581	0.005175	0.002129	0.004387	0.006499	0.002675	0.01325	0.003104
15 minutes	Number of values	1030	1030	676	676	1259	1259	346	346
	Minimum	0.2049	0.2548	0.1865	0.2327	0.2601	0.1673	0.3348	0.2352
	25% Percentile	0.3578	0.3206	0.2364	0.2829	0.4973	0.3617	0.6304	0.2963
	Median	0.3823	0.4457	0.256	0.2942	0.5879	0.4022	0.821	0.3099
	75% Percentile	0.4075	0.5495	0.28	0.3072	0.7284	0.4521	1.203	0.3265
	Maximum	2.164	1.49	1.07	0.7368	2.052	3.714	3.575	0.4862
	Range	1.959	1.235	0.8833	0.504	1.791	3.547	3.24	0.251
	Mean	0.3842	0.4572	0.264	0.2986	0.6478	0.4175	0.9919	0.3133
	Std. Deviation	0.07114	0.1547	0.05799	0.03224	0.2182	0.1271	0.5212	0.02992
	Std. Error of Mean	0.002217	0.00482	0.002231	0.00124	0.00615	0.003581	0.02802	0.001608
30 minutes	Number of values	993	993	1266	1266	2495	2495	553	553
	Minimum	0.2203	0.2483	0.1488	0.1777	0.3138	0.2777	0.1883	0.2353
	25% Percentile	0.3669	0.3116	0.2237	0.2762	0.4864	0.4795	0.5646	0.2885
	Median	0.3969	0.4129	0.2419	0.2871	0.5872	0.5392	0.8684	0.2979
	75% Percentile	0.4259	0.5203	0.2611	0.3022	0.7866	0.6459	1.213	0.3132
	Maximum	0.6903	4.186	0.3887	0.9754	5.892	4.634	3.482	0.4902
	Range	0.4699	3.938	0.2399	0.7978	5.579	4.356	3.294	0.2549
	Mean	0.3968	0.4387	0.243	0.2944	0.7101	0.6107	0.9688	0.3034
	Std. Deviation	0.04678	0.1832	0.02909	0.03947	0.3828	0.274	0.5237	0.02406
	Std. Error of Mean	0.001484	0.005813	0.0008176	0.001109	0.007664	0.005486	0.02227	0.001023
45 minutes	Number of values	1221	1221	798	798	2092	2092	624	624
	Minimum	0.2141	0.2614	0.09228	0.1279	0.2928	0.3543	0.1206	0.1386
	25% Percentile	0.3524	0.314	0.2986	0.2847	0.41	0.5273	0.6221	0.3414
	Median	0.3786	0.4424	0.3294	0.3097	0.4394	0.6004	0.7155	0.3772
	75% Percentile	0.4054	0.5716	0.3663	0.3417	0.469	0.711	0.8588	0.4238
	Maximum	0.8042	2.537	3.134	1.211	0.8158	4.062	2.974	1.855
	Range	0.59	2.276	3.041	1.083	0.523	3.708	2.853	1.716
	Mean	0.3799	0.4708	0.3588	0.322	0.4407	0.6871	0.8033	0.406
	Std. Deviation	0.04619	0.1902	0.2166	0.06176	0.04647	0.3534	0.3195	0.1319
	Std. Error of Mean	0.001322	0.005444	0.007666	0.002186	0.001016	0.007726	0.01279	0.005279
60 minutes	Number of values	711	711	1234	1234	1471	1471	1437	1437
	Minimum	0.2161	0.2649	0.1522	0.2476	0.1342	0.3018	0.1475	0.2258
	25% Percentile	0.329	0.331	0.2364	0.2753	0.2991	0.5031	0.3408	0.274
	Median	0.3538	0.3933	0.2628	0.2873	0.3272	0.5809	0.4759	0.2837
	75% Percentile	0.3826	0.4549	0.2969	0.3044	0.3586	0.7132	0.6685	0.2958
	Maximum	0.9178	5.436	2.408	1.348	0.6985	3.652	2.424	1.365
	Range	0.7017	5.171	2.256	1.1	0.5643	3.35	2.277	1.139
	Mean	0.355	0.419	0.2993	0.2968	0.3308	0.6475	0.5327	0.2888
	Std. Deviation	0.04396	0.2181	0.1854	0.05986	0.04394	0.257	0.2598	0.04151
	Std. Error of Mean	0.001649	0.008178	0.005278	0.001704	0.001146	0.006701	0.006853	0.001095
120 minutes	Number of values	1106	1106	1098	1098	929	929	1533	1533
	Minimum	0.1473	0.1426	0.1561	0.2263	0.2279	0.3088	0.1712	0.2304
	25% Percentile	0.2948	0.3518	0.2199	0.264	0.3041	0.4449	0.3173	0.2724
	Median	0.3248	0.4388	0.2485	0.2767	0.328	0.5175	0.3741	0.2882
	75% Percentile	0.3618	0.5274	0.2821	0.2934	0.3525	0.6027	0.455	0.3056
	Maximum	0.7109	4.883	2.57	2.331	0.5809	1.717	1.403	1.074
	Range	0.5637	4.74	2.414	2.105	0.353	1.409	1.232	0.8438
	Mean	0.3284	0.4584	0.267	0.285	0.329	0.5422	0.4055	0.2917
	Std. Deviation	0.05026	0.185	0.1154	0.0736	0.03705	0.1399	0.1364	0.03347
	Std. Error of Mean	0.001511	0.005564	0.003483	0.002221	0.001215	0.004591	0.003484	0.0008548
240 minutes	Number of values	685	685	684	684	812	812	1669	1669
	Minimum	0.1852	0.2347	0.21	0.2258	0.2202	0.2472	0.1909	0.2242
	25% Percentile	0.3413	0.3134	0.3065	0.3037	0.369	0.3905	0.2804	0.2714
	Median	0.3738	0.3539	0.3409	0.3202	0.402	0.5346	0.3292	0.2801
	75% Percentile	0.4045	0.388	0.3854	0.342	0.43	0.6716	0.4981	0.2908
	Maximum	0.5257	0.6405	0.8005	1.065	0.648	1.544	2.057	1.466
	Range	0.3405	0.4058	0.5905	0.8396	0.4279	1.297	1.866	1.242
	Mean	0.3734	0.3578	0.3488	0.3258	0.4004	0.5594	0.4319	0.2839
	Std. Deviation	0.04721	0.05448	0.05967	0.04324	0.04933	0.1953	0.246	0.03665
	Std. Error of Mean	0.001804	0.002081	0.002281	0.001653	0.001731	0.006852	0.006021	0.0008971
1440 minutes	Number of values	1038	1038	556	556	1851	1851	1145	1145
	Minimum	0.2128	0.2537	0.1797	0.2341	0.2272	0.2349	0.1361	0.1662
	25% Percentile	0.3449	0.3071	0.2649	0.2748	0.3164	0.3621	0.2635	0.2501
	Median	0.369	0.3425	0.2895	0.2845	0.341	0.4306	0.3507	0.2594
	75% Percentile	0.3949	0.3776	0.3209	0.2948	0.3661	0.5532	0.4617	0.2722
	Maximum	0.7205	2.457	1.865	0.6555	0.5833	3.566	1.477	0.5021
	Range	0.5077	2.203	1.685	0.4214	0.356	3.331	1.341	0.336
	Mean	0.3693	0.353	0.3257	0.2873	0.3428	0.5181	0.3804	0.2628
	Std. Deviation	0.0451	0.1014	0.1544	0.023	0.04092	0.301	0.161	0.02019
	Std. Error of Mean	0.0014	0.003147	0.006548	0.0009755	0.000951	0.006997	0.004759	0.0005968

5 Establishment of in vitro experiments at the proton-FLASH beamline at Chang Gung Memorial Hospital

5.1 Introduction

Healthy tissue damage is the key limiting factor of radiotherapy (RT), which is employed in nearly half of all brain cancer treatments. In Australia, the five-year survival rate of brain malignancies stands at 23%, with 1579 deaths recorded in 2023, making it the 9th highest cause of cancer-related mortality [147]. Thus, there is demand for innovative treatment modalities for tumours adjacent to radiation-sensitive healthy tissues. Evidence suggests delivering radiation in less than 1 second (termed FLASH) rather than minutes (conventional, CONV) spares healthy tissues at equivalent doses. Proton therapy can be prescribed in the treatment of brain cancers and offers a significant improvement in sparing healthy tissue since the treatment beam stops within the tumour. Combining proton therapy with FLASH could thus provide additional benefits by enhancing therapeutic responses and further reducing healthy tissue toxicity. As previously outlined in Chapter 3.4, although the underlying mechanisms responsible for the therapeutic benefits of FLASH have been hypothesised and preclinical data allude to certain radiobiological processes, none have been thoroughly validated. Predicted aspects of the FLASH effect, particularly differential DNA damage and response, could not be studied previously due to an inability to accurately measure DNA damage. With the establishment of STRIDE and its validation through both peroxide and X-ray based studies (Chapter 4), the analytical capability to characterise FLASH in terms of its DNA damaging capabilities is now possible. The overall aim of these experiments was to compare the radiobiological induction of double-strand breaks (DSBs) and repair foci in normal versus cancerous cells under proton-FLASH.

At the time of writing, no experimental beamlines in Australia have been established for preclinical FLASH irradiations, creating a significant limitation for conducting advanced radiobiological research domestically. To overcome this, a partnership was initiated with clinical researchers at Chang Gung Memorial Hospital (CGMH) radiotherapy clinic in Taiwan, which houses one of the most

advanced experimental proton-FLASH beamlines in the world. This collaboration, formalised through establishment of a memorandum of understanding (MoU), provided the opportunity to directly test hypotheses using purpose-built facilities. CGMH not only provides conventional X-ray treatments, but also the latest proton-FLASH therapy technologies, with one of the worlds-best developed dedicated proton-FLASH beamlines for experiments (Figure 32). Access to world-class proton therapy infrastructure under this MoU ensures any preclinical data collected are clinically relevant, particularly by delivering proton-FLASH irradiation with a clinical irradiator and analysing its effects on normal and cancerous cell types. This includes glioblastoma-derived cell line U87-MG and human-derived oral fibroblasts (OF).

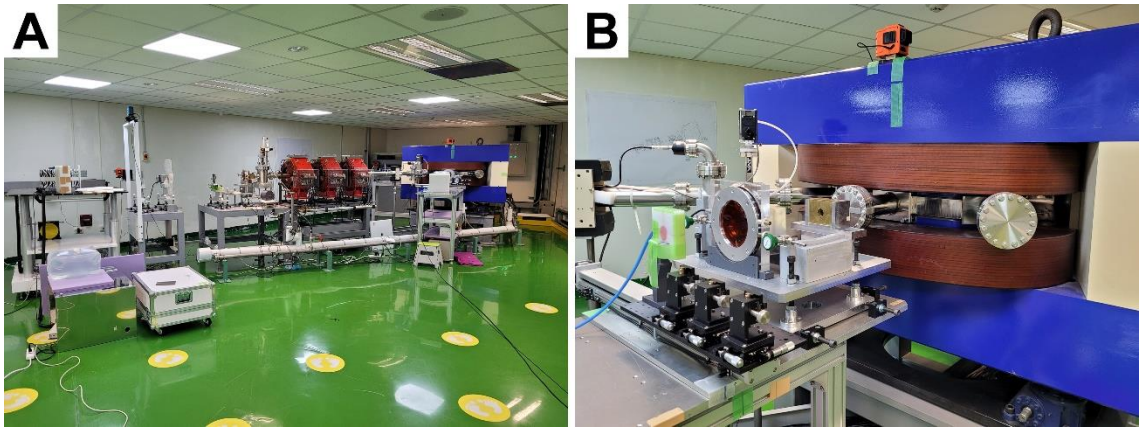


Figure 32: The CGMH Particle Physics and Beam Delivery Core Laboratory. A.) View of experimental beamlines capable of preclinical proton irradiations originating from the 230 MeV Sumitomo Heavy Industries cyclotron. Two discrete beamlines originate from the dipole magnet (blue) with separate beam ports. The longer beamline extending to the left is capable of spread-out Bragg peak (SOBP) irradiations at CONV dose rates, whilst the beamline to the right (highlighted in B) is capable of shoot-through FLASH irradiations in the plateau region. Photos: Jake Atkinson.

The radiation source for this clinical facility, a Sumitomo Heavy Industries 230 MeV cyclotron, treats over 1500 patients per year across four patient rooms, in addition to the dedicated preclinical experiment room dedicated for spread-out Bragg peak (SOBP) and FLASH experiments. Within this room there are two separate beamlines for proton irradiation. The leftmost beamline (Figure 32, A) for broad-field irradiation is equipped with a double scattering system, ensuring over 90% dose uniformity across a 10 cm diameter area, and includes a wheel

range modulator for generating a spread-out Bragg peak (SOBP) [148]. The rightmost beamline (Figure 32, B) possesses a collimator, followed by a transmission ionization chamber (TIC), an additional collimator, and finally the sample platform for pass-through irradiation. There is also scope for installation of an attenuator to produce SOBP proton-FLASH on this beamline in future work, however for the sake of establishing *in vitro* irradiations the shoot-through plateau region was utilised.

The CGMH radiation research team has previously established in vivo experiments using this FLASH beamline, recording dose rates as high as 100 Gy/s [148], far exceeding the 40 Gy/s approximated for FLASH to exhibit differential effects [84]. As also discussed in Chapter 3.4, similar preclinical proton studies using FLASH dose rates have lacked thorough dosimetry monitoring. Hsiao et al., 2024 [148] detail a dose monitoring system for this proton-FLASH beamline that incorporates a combination of the TIC, Poor Man's Faraday Cup, beam position monitor, and ETB3 films, able to provide real-time feedback on the irradiation time and dose rates per pulse [148]. With more confidence in how reliably proton dose can be delivered, researchers can more confidently compare the physical dose deposited to the radiobiological outcomes observed through immunofluorescence staining.

5.2 Experimental Setup

5.2.1 Proposed Irradiation Setup

The initial plan for proton irradiations was to utilise the FLASH beamline at CGMH in combination with a SOBP to characterise not only the differences in STRIDE and γH2AX foci formation in response to FLASH and CONV irradiation modes, but also differences in foci formation across the proton dose deposition curve. These are the entry or plateau, Bragg peak, and distal drop-off regions respectively, and there is evidence that there are differences in the frequency of DNA damage response (DDR) repair foci for each region [149-151]. As such, the initial experimental plan sought to characterise not only the differences in DSB/repair foci between FLASH and CONV in normal and cancerous cells, but also how foci formation changes along the radiation track (Figure 33). This would be of great interest to determine differences in normal versus cancerous cell

responses to exposure in each region of the SOBP, particularly in normal cells where the distal region of the proton beam is relevant.

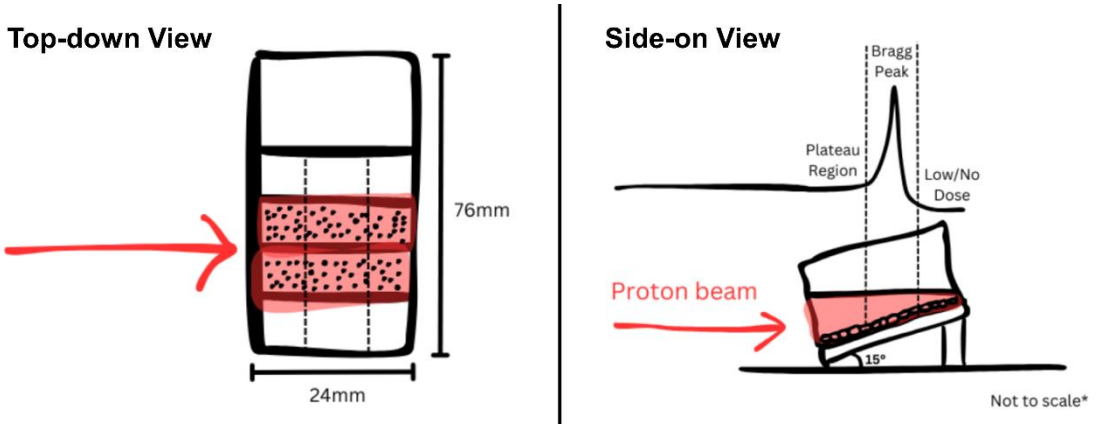


Figure 33: Outlines of the initial plan for proton irradiations at CGMH utilising SOBP FLASH. Ibidi or Sarstedt 4-well chamber slides (Ibidi, 80426. Sarstedt, 94,6170.402) would be irradiated where the proton beam is incident approximately perpendicular to the longest side of the plate, with the 2 centremost wells (2 and 3) being seeded with cells. The slight incline depicted in the side-on-view ensures the beam is directed to pass through a layer of culture media before reaching the cells to minimise variability in scatter and dose deposition. The Bragg peak is calibrated to deliver maximal dose in the centre of each well, enabling coverage of the dose plateau, Bragg peak, and low/no-dose drop-off regions within each well.

These cells would be irradiated with a total dose between 2 – 4 Gy maximum dose in the Bragg peak, with the risk of being incapable of resolving individual foci within cells if doses exceeded 4 Gy due to excessive DSBs and repair. Hsiao *et al.* (2024) [148], proposed use of the lowest possible FLASH dose rate measured in this study of 52.63 Gy/s and CONV dose rate of ~0.04 Gy/s, with a pulse width of ~40 ms delivered in a single proton pulse at a beam current of 100 nA. Minimising variability in dose delivery was also a focus. The CGMH team informed that there is a timing error of approximately 10%, which causes greater variability in the delivered dose as dose rate increases. To minimise this, the lowest possible dose rate that still exceeded the > 40 Gy/s required to qualify as FLASH was used. As previously discussed in Chapter 2.7.1, U87-MG and OFs were selected based on their clinical relevance to proton therapy, however 4T1 cells were also prepared as a backup cell type in case there were issues with U87-MG cell viability after transport to Taiwan. Ten plates were irradiated in total; five plates for FLASH and five for CONV, with three plates assigned as negative controls without irradiation (Table 2).

Table 2: Proposed experimental plate setups for SOBP proton-FLASH irradiations at CGMH. Overview of experimental conditions for FLASH and conventional irradiation (CONV) experiments, including variations with ATM inhibitor (ATMi), gold nanoparticles (AuNPs), and control conditions. Each condition specifies the cell type, fixation time, number of wells used, and the number of tests required for immunofluorescence staining (1 cm^2 = 1 test).

Plate #	Condition Description	Plate Type	# of Wells	# of 'Tests' (1 cm^2 = 1 test)
1	FLASH +ATMi: U87 and OFs – 15 mins fix	4 Well	2	4
2	FLASH +ATMi: U87 and OFs – 1 hour fix	4 Well	2	4
3	FLASH -ATMi: U87 and OFs – 15 mins fix	4 Well	2	4
4	FLASH -ATMi: U87 and OFs – 1 hour fix	4 Well	2	4
5	FLASH + AuNPs: U87 only – 15 min and 1 hour fix	4 Well	2	4
6	CONV +ATMi: U87 and OFs – 15 mins fix	4 Well	2	4
7	CONV +ATMi: U87 and OFs – 1 hour fix	4 Well	2	4
8	CONV -ATMi: U87 and OFs – 15 mins fix	4 Well	2	4
9	CONV -ATMi: U87 and OFs – 1 hour fix	4 Well	2	4
10	CONV + AuNPs: U87 only – 15 min and 1 hour fix	4 Well	2	4
11	No irradiation control: U87 + FBs + ATMi – 15 mins and 1 hour fix	8 Well	4	4
12	No irradiation control: U87 + FBs – 15 mins and 1 hour fix	8 Well	4	4
13	No irradiation control: U87 + AuNPs 15 mins and 1 hour fix	8 Well	2	2
	TOTAL			**50**

5.2.2 Revised Irradiation Setup

In preparing the experimental setup for proton irradiation studies, extensive engagement with the team at the Chang Gung Memorial Hospital (CGMH) Proton Beam Centre ensured alignment between the experimental requirements and the technical capabilities of their beamline. A crucial part of these discussions concerned the feasibility of switching between FLASH and conventional (CONV) irradiation modes within a single irradiation session. In the days leading up to a proposed irradiation day, cells need to be cultured, seeded into the well plates that will be used for irradiation, and then grown overnight to a specific confluency; for U87 and OF culture in a 1 cm^2 well exposed to 2 Gy protons, 15000 cells per well is suitable. Culturing cells in the same conditions and across the same timeframe is ideal to provide more consistent comparisons post-irradiation, as this minimises confounding variables that may be induced. For example, if cell

culture is staggered where two separate cultures are grown in preparation for a FLASH irradiation on Monday and CONV on Tuesday, the slight variations in temperature, cell phase, or AZD1390/AuNP pre-treatment duration may produce biases in data that are mistakenly interpreted as differences due to dose rate. As such, the CGMH team was consulted to determine the complexity of switching between FLASH and CONV modes, who advised that alternating between modes during one session would pose significant challenges, increasing the likelihood of technical issues. This was confirmed during the initial attempt to switch modes on the first day of irradiation on the 27th of November, where equipment problems necessitated rescheduling the CONV experiments to the 28th. However, this issue was rectified when performing irradiations on the 30th, and consecutive FLASH and CONV irradiations were successfully performed.

We also verified with the CGMH team whether the 52.63 Gy/s quoted in Hsiao *et al.* 2024 [148] was possible for *in vitro* irradiations. They confirmed that the lowest FLASH dose rate that the beamline can deliver is 40 Gy/s, which just meets the minimum requirements of FLASH irradiation. The dose rate calibration was conducted using ion chambers at a depth of 1 cm under water, employing a shoot-through plateau FLASH. It was emphasised that the dose rate error was approximately ±10%, so for the purposes of this study irradiations were conducted with an average dose rate of 48.2 Gy/s, ensuring that even when accounting for the error in dose rate, it still maintained the classification of 'FLASH'.

One of the more debated aspects of the setup involved positioning of the sample slides during irradiation. The cell monolayer was initially proposed to be positioned approximately parallel to the proton beam (Figure 33), allowing for irradiation with the plateau, SOBP, and drop-off regions within the proton track. The CGMH team expressed concerns that this added complexity to the setup and recommended performing shoot-though FLASH experiments with the monolayer perpendicular to the proton beam instead to reduce the complexity of the setup. It was also clarified that the beamline was only capable of plateau region FLASH, and that they had not yet validated Bragg peak FLASH. This necessitated adjustments in the protocol, including the choice of well plates and the orientation of dose delivery given Bragg peak FLASH was not feasible. They suggested

postponing the irradiation if analysing Bragg peak FLASH proved necessary, as custom modifications to the setup, including design of an attenuator, would require additional time and resources. Instead, the CGMH team prepared HDPE (High-Density Polyethylene) moulds to hold well plates with the monolayer positioned perpendicular to the proton beam. These moulds were specifically designed for Merck glass chambered slides, requiring us to adapt from using Ibidi and Sarstedt polymer-based well plates to Merck glass chambered slides (Figure 34).

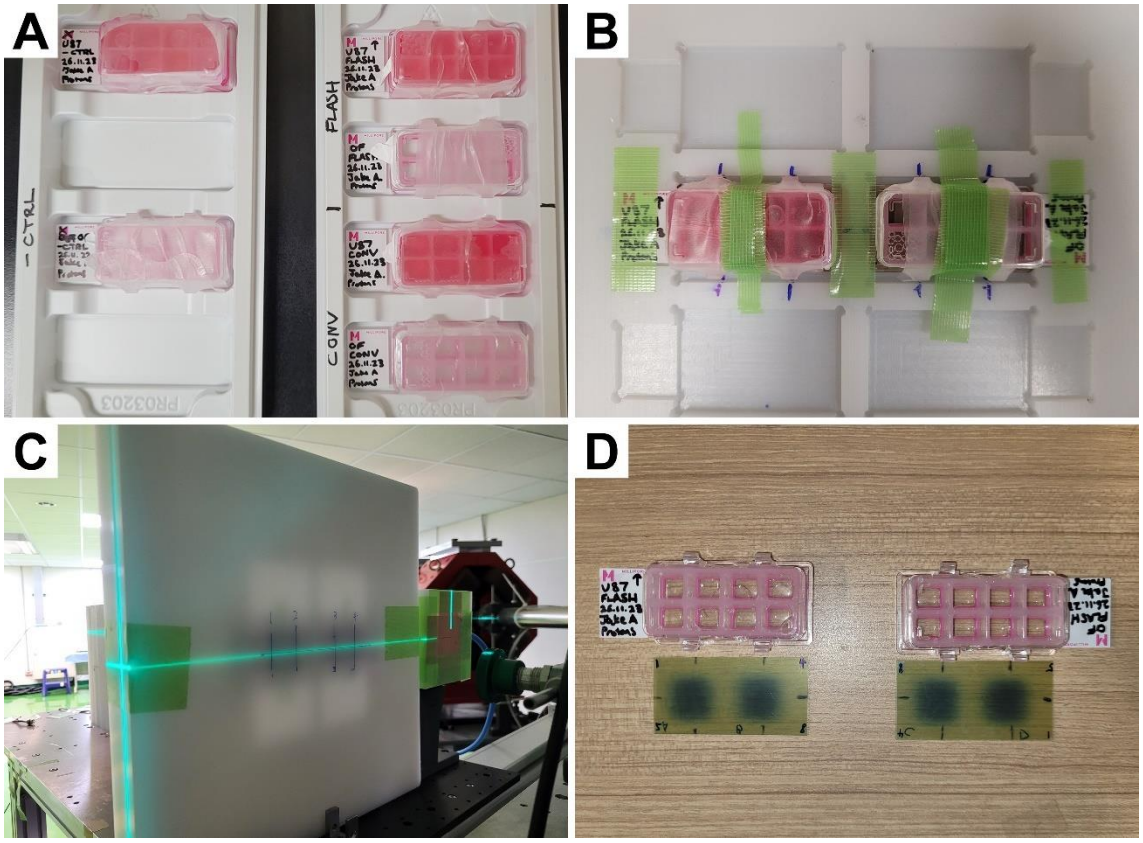


Figure 34: Well plate setup used for proton irradiations. A.) Millicell EZ SLIDE 8-well glass (Merck, PEZGS0896) were seeded with both U87 and OF cell lines and pretreated 2 hours before irradiation with 30 nM AZD1390 or 0.5 nM AuNPs. Immediately prior to irradiation, wells were filled (to capacity) with ~1 mL culture medium containing the appropriate pre-treatments to minimise both scatter and beam attenuation through air. To prevent culture medium from leaking from each plate, Teflon tape was wrapped around the outer walls of each 8-well plate, followed by followed by placing the lid on the well plate and wrapping the entire plate with paraffin. B.) Well plates taped to the HDPE moulds. Underneath each well plate, EBT3 film was adhered for dosimetry purposes to determine what area of each well was irradiated by protons. C.) HDPE mould in position ready for proton irradiation. Four irradiations were performed per run, with each irradiation delivering dose in a 1 cm^2 area to 4 wells. D.) FLASH-irradiated plates with their

corresponding EBT3 films. ‘A-D’ marked on the bottom of each film indicates the delivery of each 2 Gy dose, whilst the numbers represent the film’s orientation relative to the well plates, with ‘1’ corresponding to ‘well 1’ in the top left, and ‘8’ to ‘well 8’ in the bottom right of each plate.

Once prepared, the coverslips were secured in HDPE moulds to ensure consistent alignment throughout each irradiation. Protons were delivered in four sequential pulses across each plate, with a field size of approximately 1 cm^2. The proton beam was directed through the base of the coverslip (opposite the lid), ensuring uniform coverage across each sample (Figure 35). Finally, post-irradiation handling and analysis were meticulously planned to preserve the integrity of the samples and facilitate reliable data collection. The CGMH team provided guidance on the resting times required after irradiation to ensure the safety of experimenters when handling the cell plates due to material activation. Secondary particle emissions induced by relaxation of irradiated well plates, including neutrons and photons, need adequate time to dissipate. Lower doses, such as 2 Gy, require about 30 minutes for emissions to reach safe levels, while higher doses need up to 2 hours. As a fixation timepoint of 15 minutes post-irradiation was required, the experiment bunker contained a small benchtop with a ClearView Radiation Shield composed of clear polycarbonate. This was utilised to minimise user exposure to secondary reactions because of proton irradiation. They also assisted with maintaining samples at 37°C during fixation with an incubator prepared in the experimental beamline bunker, which was used prior to fixation to allow for optimal cell recovery conditions post-irradiation.

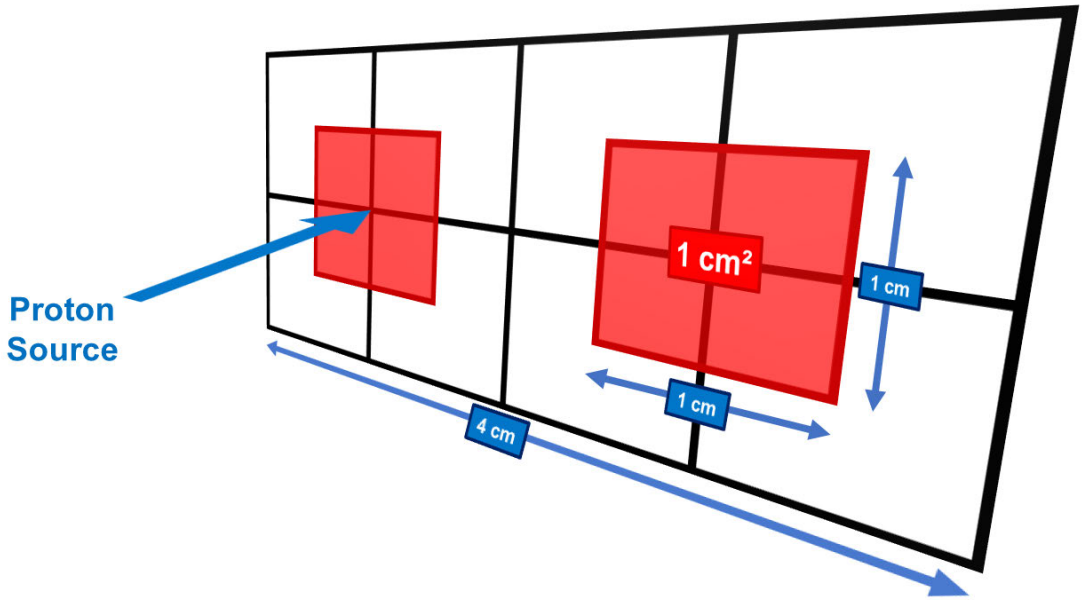


Figure 35: Schematic depicting the well plate irradiation setup with the proton-FLASH beamline at Chang Gung Memorial Hospital Proton Centre. Two 1 cm^2 field size proton irradiations were delivered through the underside of each plate, allowing for irradiation of all 8 wells in a single plate. Four irradiations were performed across two plates fields per CONV/FLASH run.

Our first FLASH dataset was collected on November 27 and 28, 2023, where eight Millipore 8-well plates were irradiated under various conditions to compare the effects of FLASH, conventional (CONV-1 and CONV-2), and control (CTRL) setups on U87 and OFs. Each irradiation exposure delivered approximately 2 Gy protons, with 30 nM of the ATM inhibitor AZD1390 applied two hours prior to irradiation to enhance radiosensitivity. For each cell type, four plates were prepared to represent the irradiation conditions. Samples were fixed using 4% paraformaldehyde at 15 minutes and 1 hour post-irradiation. The second proton-FLASH irradiation session was conducted on November 30, 2023, with six Millipore 8-well plates undergoing irradiation under revised conditions. Three plates each were prepared for U87 and OFs, covering FLASH, conventional (CONV), and control (CTRL) conditions. As per the previous run, each sample was exposed to approximately 2 Gy protons, with pre-irradiation treatments including either 30 nM AZD1390 or 0.5 nM AuNPs administered 2-hours pre-irradiation (Table 3). Fixation protocols remained consistent with 15-minutes and 1-hour timepoints post-irradiation. These experiments expanded on the initial studies by incorporating AuNPs, adding another variable for radiosensitization

effects. Together, these sessions provided a comprehensive dataset for comparing cellular responses to FLASH and conventional irradiation under diverse pre-treatment conditions. The irradiation parameters are outlined in Table 4.

Table 3: Arrangement of treatment conditions for each plate of the proton-FLASH irradiations. Each plate was divided into two halves, with pre-treatments repeated at 15-minute and 1-hour fixation timepoints. Each cell of this table that defines a pre-treatment condition: i.e., radiation only (RT), 30 nM AZD1390 (+ATMi), or 0.5 nM gold nanoparticles (+AuNPs), corresponds to a well of the negative control/no radiation (-CTRL), conventional (CONV) and FLASH irradiated samples. For each date, the top row corresponds to wells 1-4, and bottom row wells 5-8 (left to right).

	Treatment Conditions			
Date	**15 Minute Fixation**		**1 Hour Fixation**	
27/11/23, 28/11/23	RT	+ ATMi	RT	+ ATMi
	RT	+ ATMi	RT	+ ATMi
30/11/23	RT	+ ATMi	RT	+ ATMi
	+ AuNPs	-	+ AuNPs	-

Table 4: Summary of U87 and OF proton-FLASH irradiation conditions. Details of the date each irradiation was performed, the dose rate (FLASH vs CONV), cell type, fixation timepoint and EBT3 film position, as well as the dose delivered, pulse duration, and dose rate measured.

Date	**Mode**	**Cell Type and Fix Timepoint**	**EBT3 Position**	**Dose (Gy)**	**Pulse Time (ms)**	**Dose Rate (Gy/s)**
27/11/23	FLASH	U87 15 mins	A	2.21	43.06	51.22
		U87 1 hour	B	2.12	43.06	49.26
		OF 15 mins	D	1.99	43.06	47.67
		OF 1 hour	C	2.05	43.06	46.22
28/11/23	CONV	U87 15 mins	A	2.11	40	0.05286

		U87 1 hour	B	2.12	40	0.05389
		OF 15 mins	D	2.11	40	0.05272
		OF 1 hour	C	2.11	40	0.05278
30/11/23	FLASH	U87 15 mins	A	1.99	43.03	46.25
		U87 1 hour	B	2.10	43.03	48.80
		OF 15 mins	D	2.14	43.03	49.73
		OF 1 hour	C	2.00	43.03	46.48
30/11/23	CONV	U87 15 mins	A	2.12	40	0.53
		U87 1 hour	B	2.12	40	0.53
		OF 15 mins	D	2.12	40	0.53
		OF 1 hour	C	2.12	40	0.53

5.3 Results and Discussion

5.3.1 CLAHE Image Enhancement

There appeared to be issues with overall signal quality acquired from the red and green channels, which were used to resolve STRIDE and γH2AX signals respectively, using the ImageXpress Micro Confocal imaging system at CGMH in Taiwan. To address this, the images were processed in ImageJ to enhance contrast, utilising Contrast Limited Adaptive Histogram Equalization (CLAHE, Figure 36). This technique enhances contrast within an image whilst simultaneously preventing over-amplification of noise in localised regions. This was used to enhance the very low intensity signal of the red channel to identify STRIDE foci and enhance the contrast of the green channel to identify γH2AX foci. The parameters used in ImageJ were a block size of 127, 256 histogram bins, a maximum slope of 3.0, no mask applied, and the "Fast (less accurate)" option left unchecked. After CLAHE amplification, the STRIDE signal intensity within these images was still insufficient for successful quantification.

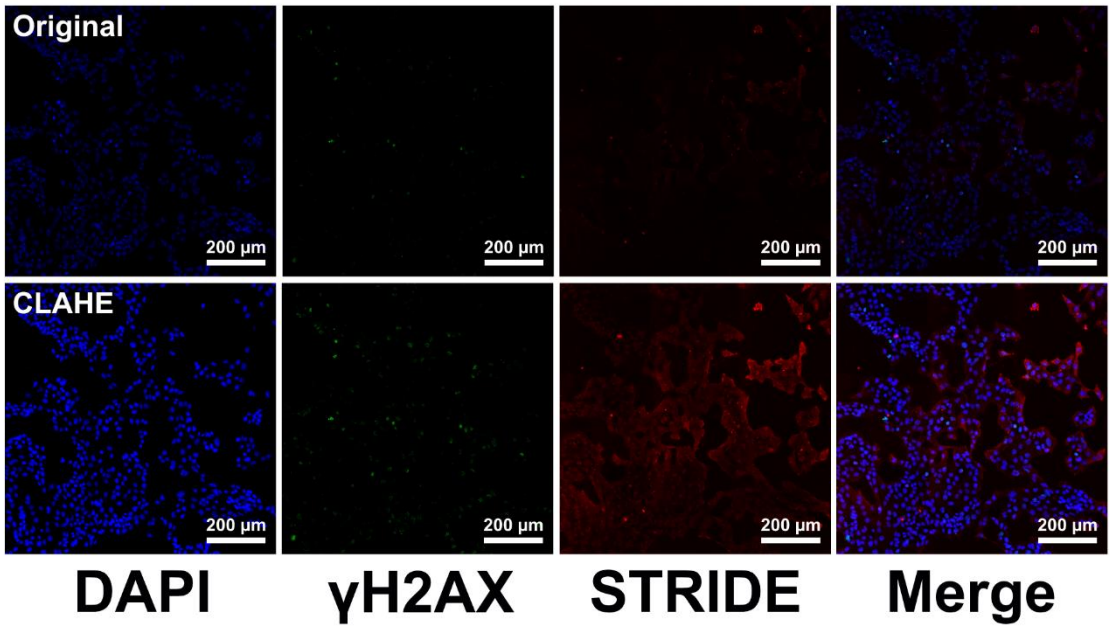


Figure 36: Confocal images of U87 cells irradiated with 2 Gy protons and fixed 15 minutes post-irradiation, captured on the ImageXpress Micro Confocal High-Content Imaging System at 40x magnification. The original acquisitions (top row) were enhanced with CLAHE in ImageJ 1.54f (bottom row).

One possible explanation is that the power of the light source was not calibrated to a sufficiently high intensity to achieve the necessary dynamic range across all images. Another notable feature of these images is that there are variations in pixel brightness across tiles in this image set. CLAHE processing was able to remove some of this variation, however re-imaging using light sources of increased power/brightness, or a different imaging would be required to rectify this entirely. Even when attempting manual brightness adjustment for these images, noise was produced which prevented differentiation of the authentic STRIDE signal obtained from the microscope acquisition and the amplified digital noise/artefacts. Thus, although throughout foci counts were obtained for both STRIDE and γH2AX, these technical issues impacted the quality of the data output after image analysis, and thus have opted to display only the most meaningful datasets throughout this chapter.

5.3.2 Results

After CLAHE enhancement of the images acquired in Taiwan, these were analysed with a CellProfiler pipeline as per X-ray experiments and detailed in Chapter 4.3 and 4.4. For the Taiwan image set acquired with the ImageXpress

Micro Confocal, foci analyses were performed for both STRIDE and γH2AX. Images were also re-acquired from the proton-FLASH plates transported back to the Future Industries Institute, Australia, with the Zeiss LSM 710, however γH2AX signal could no longer be acquired for this dataset, presumably due to fluorophore degradation. Despite these technical limitations, the following analysis explores how STRIDE and γH2AX foci formation diverges between FLASH and CONV irradiation, potentially reflecting differences in DNA damage repair mechanisms.

Figure 37 and Figure 38 present data from the proton irradiation alone and proton radiation with AuNPs pre-treatment conditions, respectively. Data for the ATMi condition and oral fibroblasts were also acquired but are excluded from discussion here as meaningful results could not be extracted. For the proton only condition (Figure 37), STRIDE appears to induce substantially more DSB foci under CONV (median = 40) irradiation compared to FLASH (median = 0) at 15 minutes ($p < 0.0001$, Mann-Whitney test). However, as STRIDE is a direct measurement of the number of DSBs, and hence a measure of the physical dose delivered to DNA, such substantial differences between the number of STRIDE foci are unexpected as the dose delivered was equivalent. From Chapter 3.4, it is expected that FLASH and CONV dose rates demonstrate isoefficient capacity to damage cancerous cells. Given that for this experimental setup cells were not fixed just prior to irradiation to determine the number of DSBs induced without the initiation of DSB repair, FLASH-induced DSBs could have been repaired by the 15-minute timepoint, although highly unlikely given the γH2AX response observed at both 15 and 60 minutes. DSBs appear to resolve at 60 minutes, also reflected in the increased activity of γH2AX at this timepoint. However, due to the lack of STRIDE foci in the FLASH condition at 15 minutes, it is difficult to conclude differences in DSB repair kinetics between CONV and FLASH. Slight differences are apparent between γH2AX foci formation for FLASH and CONV modes at 15 minutes post-irradiation; FLASH having median γH2AX foci count of 26 and CONV of 22 ($p = 0.0096$, Mann-Whitney test). At 15 minutes, the median γH2AX foci count for FLASH is higher than that of CONV, whereas at 60 minutes this trend inverts. Here, the median γH2AX foci count for FLASH (43) is lower than CONV (80), ($p < 0.0001$, Mann-Whitney test). This may be the result of a perturbed DDR under FLASH versus CONV irradiation. Although trends in

STRIDE appear inconclusive, γH2AX data here show discrete differences between γH2AX activation in response to FLASH versus CONV protons. This is emphasised at 60 minutes post-irradiation (Figure 37), however the mechanism responsible for this difference in foci formation cannot be confirmed. One potential explanation is the inability of U87 cells to repair complex FLASH-induced DNA damage. This may present as a delay in γH2AX phosphorylation, however additional fixation timepoints and reliable STRIDE data is required to confirm this.

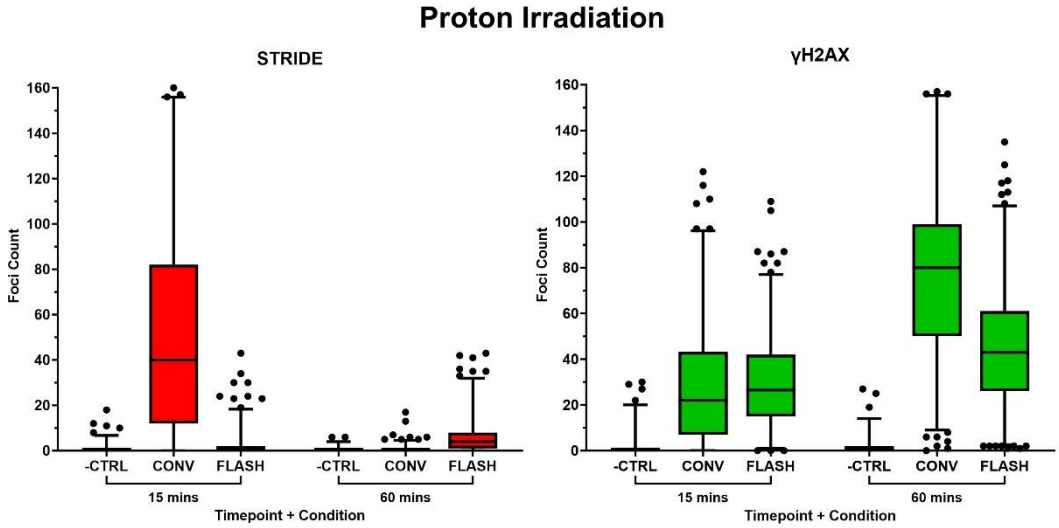


Figure 37: U87 cells fixed at 15- and 60-minute timepoints post-irradiation under the following conditions: negative control (-CTRL) cells exposed to 0 Gy protons, or 2 Gy protons delivered at a conventional (CONV) or ultra-high dose rate (FLASH) radiation. Foci counts for STRIDE and γH2AX from single cells were measured. Data show the median value within the 25th and 75th percentile data points (box). Whiskers show the 2.5 - 97.5 percentile, and dots represent data points outside the range represented by whiskers.

Upon addition of AuNPs 2-hours pre-irradiation (Figure 38), the kinetics observed for STRIDE samples become confusing to interpret. When compared to the median STRIDE foci with CONV irradiation alone of 40 (Figure 37), the STRIDE foci counts when proton irradiation is combined with AuNPs are lower than expected, these being 0 for CONV and 4 for FLASH (Figure 38). This is also unexpected as mentioned with the proton-irradiated only samples, since STRIDE foci should be at their maximum at this earliest timepoint. Moreover, STRIDE foci at 60 minutes for FLASH irradiation (29) are significantly greater than that of

CONV (3), ($p < 0.0001$, Mann-Whitney test). γH2AX foci formation for the negative control conditions (no proton irradiation with AuNP pre-treatment) show little to no induction of γH2AX signal. These findings appear consistent with X-ray + AuNP data presented in 4.4: X-ray + AuNP Publication. CONV and FLASH irradiated samples present maximum γH2AX signal 60 minutes post irradiation, these being 89 and 85 respectively ($p = 0.1513$, Mann-Whitney test). At 15 minutes, FLASH γH2AX foci counts are higher than those of CONV (34 vs 5, $p < 0.0001$, Mann-Whitney test). Also contrasting the radiation only samples, the kinetics of γH2AX upon AuNP addition appear similar between CONV and FLASH irradiations at 60 minutes.

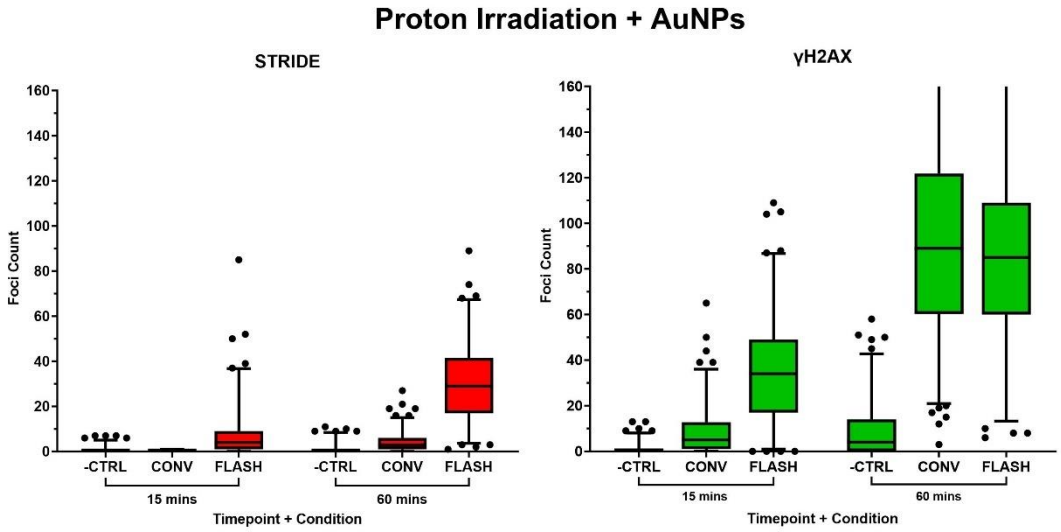


Figure 38: U87 cells were pretreated with 0.5 nM AuNPs 2 hours prior to irradiation and fixed at 15- and 60-minute timepoints post-irradiation. The irradiation conditions were as follows: negative control (-CTRL) with no radiation exposure + AuNPs, or exposure to 2 Gy protons delivered at either a conventional (CONV) or ultra-high dose rate (FLASH). Foci counts for STRIDE and γH2AX from single cells were measured. Data show the median value within the 25th and 75th percentile data points (box). Whiskers show the 2.5 - 97.5 percentile, and dots represent data points outside the range represented by whiskers.

Figure 39 presents the integrated intensity values of STRIDE normalised to DAPI taken from the experimental samples re-imaged at the Future Industries Institute. As per Figure 37 with proton irradiation only, in U87 cells at 15 minutes there are comparable integrated intensities between -CTRL (0.7159, arbitrary units) and FLASH (0.6961) samples ($p = 0.0026$, Mann-Whitney test), but higher STRIDE intensities under the CONV (0.8387) condition (FLASH vs CONV, $p < 0.0001$,

Mann-Whitney test). Upon pre-treatment of ATMi and AuNPs, the integrated intensities of the -CTRL and CONV samples exhibit minimal differences, with decreased intensities of STRIDE under FLASH. This observation is confusing, as STRIDE foci formation is expected to be minimal in non-irradiated cells. However, the data in Figure 39 indicates that STRIDE intensities are at their lowest in FLASH-irradiated samples.

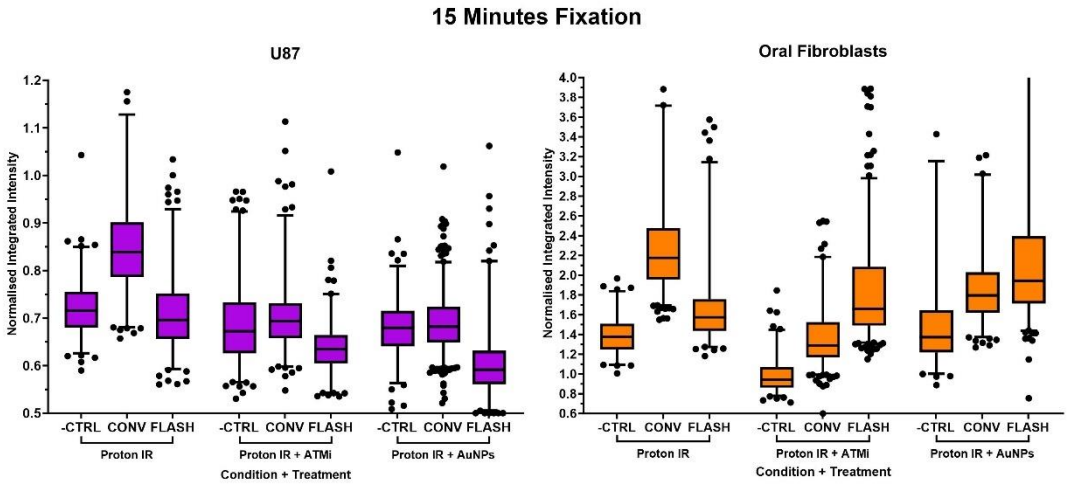


Figure 39: STRIDE normalised integrated intensity values obtained from U87 and oral fibroblast (OF) cells irradiated under three separate conditions. 1. Proton irradiation alone, 2. proton irradiation combined with 30 nM AZD1390, 3. proton irradiation combined with 0.5 nM AuNPs. Treatments were applied 2 hours prior to irradiation, and cells were fixed at 15- and 60-minute time points post-irradiation. The irradiation conditions were as follows: negative control (-CTRL) with no radiation exposure, or exposure to 2 Gy protons delivered at either a conventional (CONV) or ultra-high dose rate (FLASH). Integrated intensity values for STRIDE and DAPI from single cells were measured, with STRIDE values normalised to DAPI. Data show the median value within the 25th and 75th percentile data points (box). Whiskers show the 2.5 - 97.5 percentile, and dots represent data points outside the range represented by whiskers.

In OFs however, there appear to be some interesting trends when comparing CONV and FLASH STRIDE intensities. With proton irradiation only, the STRIDE intensities of CONV (2.176) are higher than that of FLASH (1.574) ($p < 0.0001$, Mann-Whitney test), which aligns with the hypothesis that FLASH mitigates damage to normal tissues. Protons combined with either ATMi or AuNPs in these cells show the opposite trend however, with FLASH enhancing the degree of damage when these adjuvants are added. CONV versus FLASH intensities for these pretreatments is equal to 1.290 vs 1.660 for ATMi ($p < 0.0001$, Mann-

Whitney test), and 1.795 versus 1.943 for AuNPs ($p < 0.0001$, Mann-Whitney test). From this, radiosensitisers appear to have an enhanced effect in normal tissues when combined with FLASH irradiation. However, across all U87 conditions, median STRIDE intensities for FLASH irradiated samples are lower than the median STRIDE intensities of both -CTRL and CONV samples. It is expected for the -CTRL samples to have the lowest median STRIDE intensities, as they are not exposed to radiation. Hence, this limits the overall reliability of the trends observed in the OF dataset.

5.3.3 Comparisons to Literature

Presently, there are no publications which have used STRIDE to measure DSBs induced by proton irradiation or FLASH. Previous work has shown that in comparison to X-ray irradiation at equivalent doses, protons both increase the amount of fragmented DNA (Comet assay) and exhibit delayed activation of γH2AX in glioma stem cells [152]. However, this contrasts analyses in normal tissue types, including hematopoietic stem cells, which exhibited no difference in the formation and disappearance of γH2AX foci between 1 Gy of 6 MV X-rays or protons. For proton irradiated samples, there was also no difference in γH2AX foci kinetics between mid-and distal region SOBP protons [151]. However, micronuclei production appeared to be elevated in both the SOBP and distal regions at 0.5 and 1 Gy proton exposures compared to X-rays irradiated with the same doses. Micronuclei are extranuclear bodies which are produced when acentric or whole chromosomes are not included in the daughter nuclei body in telophase, and are instead encapsulated in their own nuclear membrane in the cytoplasm [153]. They are often produced in response to genotoxic insults that induce DSBs, SSBs that are converted into DSBs after replication, or prevention of DNA synthesis [154]. This suggests that the intrinsic nature of protons may produce DNA DSBs in vastly different ways than compared to X-rays, potentially resulting in both an increase in the complexity of DNA damage through micronuclei induction, and a delay in DNA damage repair due to their higher LET and lower proton energies [150]. This has been shown indirectly in studies where increasing proton LET reduces cell survival [155] and delays the formation of 53BP1 foci [156]. Therefore, when comparing proton irradiated STRIDE and

γH2AX datasets to X-rays, these differences in the ability of protons to form DSBs need to be taken into consideration.

γH2AX signal intensities in response to FLASH have been explored in a few key publications. Buonanno *et al.* (2019) [67] measured the fold change of γH2AX fluorescence intensity in normal human lung fibroblasts exposed to 1, 2, 5, 10 and 20 Gy 4.5 MeV protons at 0.05, 100 and 1000 Gy/s. At the lower doses utilised (1, 2 and 5 Gy) and between 0.05 (CONV) and 100 Gy/s (FLASH), there appears to be minimal differences in γH2AX response, exhibiting similar intensities 30-minutes post irradiation [67]. Fouillade *et al*. (2020) [68] also showed similar findings in normal human lung cells (MRC5, IMR-90) and human lung epithelial carcinoma cells (A-549) exposed to 5.2 Gy 4.5 MeV electrons at 135 – 600 Gy/s, showing non-significant differences in γH2AX or 53BP1 foci counts [68]. Similar findings with non-significant difference in 53BP1 foci induction between CONV and FLASH were reported for FLASH irradiations in human skin fibroblasts [69] and time-dependent formation and loss of γH2AX in human derived cervical cancer cell line HeLa [70]. At earlier timepoints, it appears that γH2AX foci formation shows no differences between FLASH and CONV. γH2AX foci counts at 15 minutes post-irradiation with protons only (Figure 37), appear to show similar trends to previous studies of γH2AX foci formation at 30 minutes [67, 68]. However, these studies either did not analyse longer timepoints [67], or chose not to present this data [68]. Therefore, identifying differences in γH2AX foci formation at longer timepoints, as evidenced by the 60-minute timepoint in Figure 37, could reveal key differences in how cells respond to FLASH. Further study into whether FLASH delays the onset of the DDR, and whether proton-FLASH produces complex DSBs molecules cannot detect, will allow for confirmation of this potential mechanism.

5.4 Conclusion

The data presented in this chapter shows potential differences in DNA damage and repair kinetics between FLASH and CONV proton irradiation modes. While there are definite trends contrasting the two modalities, such as STRIDE showing a greater number of DNA DSB foci under CONV compared to FLASH at 15 minutes post-irradiation (Figure 37), several technical factors complicate

interpretation. Further experiments are required to determine if these differences are reflective of genuine variations in radiobiological responses or arise from unaccounted-for variables in the STRIDE assay. Although unlikely, there is a possibility that STRIDE interacts differently with proton-induced DSBs compared to X-ray-induced DSBs, given that most X-radiation-induced DNA damage stems from radiolytic ROS production rather than direct proton-DNA interactions. Alternatively, the results may reflect a distinct DNA repair response induced by proton-FLASH compared to CONV dose rates. If these findings are accurate, then this presents a unique vulnerability in the ability of cancerous cells to repair proton-FLASH DSBs. This contradicts previous findings that state FLASH is isoefficient at killing cancerous cells compared to CONV and brings into question whether normal tissues can respond to FLASH-induced DSBs more efficiently than cancers. This would strongly support the theory of a FLASH effect and address the lack of mechanistic understanding that exists currently. With a more comprehensive understanding of the mechanisms behind FLASH's normal tissue sparing (or conversely, enhanced cancer killing at equivalent doses), this would provide additional rationale to support further clinical trials and its eventual translation.

Conducting these experiments in Taiwan rather than locally presented logistical and technical challenges. The cost of transporting reagents to Taiwan was significant, and some equipment was not readily available. Adjustments to the irradiation setup added further complexity. The need to irradiate plates perpendicular to the beam axis necessitated the use of HDPE moulds and a shift from polymer-based Ibidi and Sarstedt plates to Merck glass chambered coverslips. While the decision to forgo irradiating slides parallel to the cell monolayer to investigate Bragg peak effects simplified the protocol, future studies should revisit this setup to fully characterise STRIDE and γH2AX foci formation under Bragg peak FLASH conditions. Imaging in Taiwan also presented challenges due to limited access to the confocal microscopy facilities at Chang Gung Memorial Hospital (CGMH). The ImageXpress Micro Confocal available to us was not optimised to acquire STRIDE and γH2AX signals with the desired brightness, nor were higher magnifications such as 63x available. Imaging was limited to standard 40x objectives, restricting the ability to perform meaningful foci

colocalisation analyses. In future studies, either extended access to microscopy facilities in Taiwan or transporting fixed samples back to Adelaide for reanalysis with confocal systems would enable higher-quality data acquisition and more flexibility in the experimental workflow. Transport of samples back to Australia would also benefit from use of polymer-based coverslips, as this would reduce the fragility of samples; one of the glass coverslips broke in transit on return to Australia for re-imaging, which impacted the ability to re-image specific conditions. Additionally, the thickness of the glass coverslip frames posed challenges for confocal imaging in Adelaide, as the microscope stage could not position the objective lens close enough for cells to be positioned within the focal plane. Removing the frame to mount the coverslip led to potential sample loss, particularly for the 60-minute fixation timepoints, limiting the STRIDE data acquired from these samples.

Despite the technical hurdles that complicated data interpretation, this study represents a step forward in optimising how proton-FLASH studies are conducted, offering valuable insights into logistical and technical considerations at the CGMH Proton Centre. The establishment of an MoU and collaboration between the team at CGMH and the University of South Australia will facilitate further radiobiological FLASH studies to be conducted. This experience will inform future experimental design, helping to address limitations in the protocols used, identify nuances in the STRIDE assay, and ultimately improve the reproducibility of this methodology and data derived from it. Whilst there are promising trends suggesting differences in DNA damage and repair kinetics between FLASH and CONV proton irradiation modes, the challenges encountered during these experiments limit the reliability of the conclusions. STRIDE data acquisition requires further refinement, particularly regarding its application in proton-FLASH studies. Regardless, this work establishes a strong foundation for the continued advancement of proton-FLASH radiotherapy research, and positions researchers at the University of South Australia to lead future preclinical work at the Australian Bragg Centre for Proton Therapy.

6 Attenuator design and modelling for adapting high current output from cyclotrons for preclinical proton irradiation studies

6.1 Introduction

The experiments conducted at Chang Gung Memorial Hospital in Taiwan used a purpose-built auxiliary beam line for proton FLASH irradiation from a 230 MeV Sumitomo Heavy Industries clinical cyclotron. No such beamline exists in Australia at the time of writing. In anticipation for the Australian Bragg Centre for Proton Therapy and installation of a clinical proton beamline, the establishment of a preclinical experimental setup for proton therapy is of interest. In addition to being pertinent to pursue future work based on the findings of this project, establishing FLASH dose rates in a setup within Australia is also essential to improve current and future clinical proton therapy technologies. In Adelaide, the South Australian Health and Medical Research Institute (SAHMRI) has a GE PETtrace 880 16.5 MeV cyclotron (GE Healthcare), which is managed and operated by the Molecular Imaging and Therapy Research Unit (MITRU). It is currently used to produce radioisotopes and radiopharmaceuticals, with a beam current in the range of 10–100 μA, translating to kGy/s dose rates and a minimum stable beam current of 40 nA. These specifications mean it produces FLASH dose rates [75]. The cyclotron is equipped with a solid beam line, making it possible to extract the proton beam for sample irradiations, including cell lines. Although capable of FLASH, to perform comparative irradiations at different CONV dose rates with the cyclotron a significant reduction of its normal operational dose rate is required. Rather than altering the beam current, as the lowest stable beam current is 40 nA which translates to a dose rate of 34 Gy/s (see section 6.2.1.1), the feasibility of producing a filter-like attenuator to reduce the rate of protons delivered to a target was explored. Attenuators are devices, often made from high-density metals, that may contain an array of holes or slits designed to selectively allow particles or radiation to pass through in a specific direction. Particles from a divergent source are blocked by the attenuator material, allowing only those that pass through the holes in the attenuator to reach the target. Filtering protons in this way reduces the total absorbed dose delivered

per unit time for a given beam current, thereby lowering the dose rate on the target. The attenuator described here was designed in the form of pitch metal collimator with drilled holes. This chapter provides an overview of the simulation work conducted in this thesis to calculate the specifications for an attenuator to be manufactured for the 16.5 MeV cyclotron at SAHMRI for use with a multi-target system and a beam size of 10 mm diameter. Design of an attenuator for existing hardware expands the capacity for radiobiological proton-FLASH research to be continued in Adelaide.

6.1.1 Material Properties

There are a few considerations in the manufacture of attenuators. The first of these are the melting point and rigidity of the material. Melting point is of utmost importance during these experiments, as accelerators such as the GE PETtrace 16.5 MeV cyclotron are primarily used to produce radioisotopes. It was not designed to accommodate radiobiological experiments and cannot be utilised for patient treatments. As such, the beam current, and hence the dose rate, that this cyclotron outputs is considerably higher than what would be used for radiobiological experiments simulating conventional clinical treatment conditions. To account for this high energy fluence output, the attenuator needs to withstand high temperatures. The material must also maintain its structural integrity under repeated handling to avoid deformation or misalignment that could impact dose consistency when changing between FLASH and CONV modes. Some degree of machinability is also required for attenuator manufacture, including rolling the material into thin sheets and drilling apertures with a picosecond laser. A picosecond laser is used because its extremely short pulse duration minimises heat transfer to the surrounding material during drilling, reducing the risk of thermal damage or distortion. This precision ensures clean, accurate apertures (on the order of 100 – 200 μm in size) in the sheets without compromising the structural integrity of the attenuator. Precision drilling is essential to create holes of exact dimensions, ensuring accurate modulation of the beam line and consistent dose delivery. Other factors include the metal being preferably non-toxic, affordable, and easy to obtain. Two metals were selected as candidates: brass and tungsten (Table 5).

Table 5: Mechanical properties of both brass [157] and tungsten [158], candidate metals to produce attenuators for FLASH experiments.

Material	**Brass**	**Tungsten**
Melting Point (°C)	900 - 940	3422
Density (g/cm^3)	8.4 - 8.73	19.3
Tensile Strength (MPa)	338 - 469	980

Brass and tungsten both share properties that make them suitable for attenuator manufacture. They are both relatively affordable (for a small component such as an attenuator) and have tensile strengths which allow for ease of machinability. However, the melting point and density of tungsten being much higher than brass means that it can withstand higher temperatures as well as absorb the same number of protons as a brass attenuator but with a reduced thickness. This is because tungsten's higher density allows it to absorb more protons per unit thickness, making it more effective at blocking radiation with less material.

6.1.2 Nuclear Reactions in the Attenuator Material

Most protons are stopped by the attenuator; these may, however, activate the material through secondary nuclear reactions within the attenuator material that subsequently emits nucleons. This is a concern when handling the attenuator during the switch between FLASH and CONV modes, as this potentially poses a hazard to users and contributes additional unwanted dose to biological specimens. One of the most significant of these activation products are neutrons, which are unfavourable as it adds a degree of ambiguity to the total dose delivered where neutrons will contribute in addition to protons. Although tungsten is optimal for its physical characteristics, availability, and ease of manufacture, it produces a higher proportion of neutrons compared to other attenuator materials, in order of decreasing activity by protons: Cerrobend, brass, iron, nickel, or high-density plastic (Figure 40, [159]).

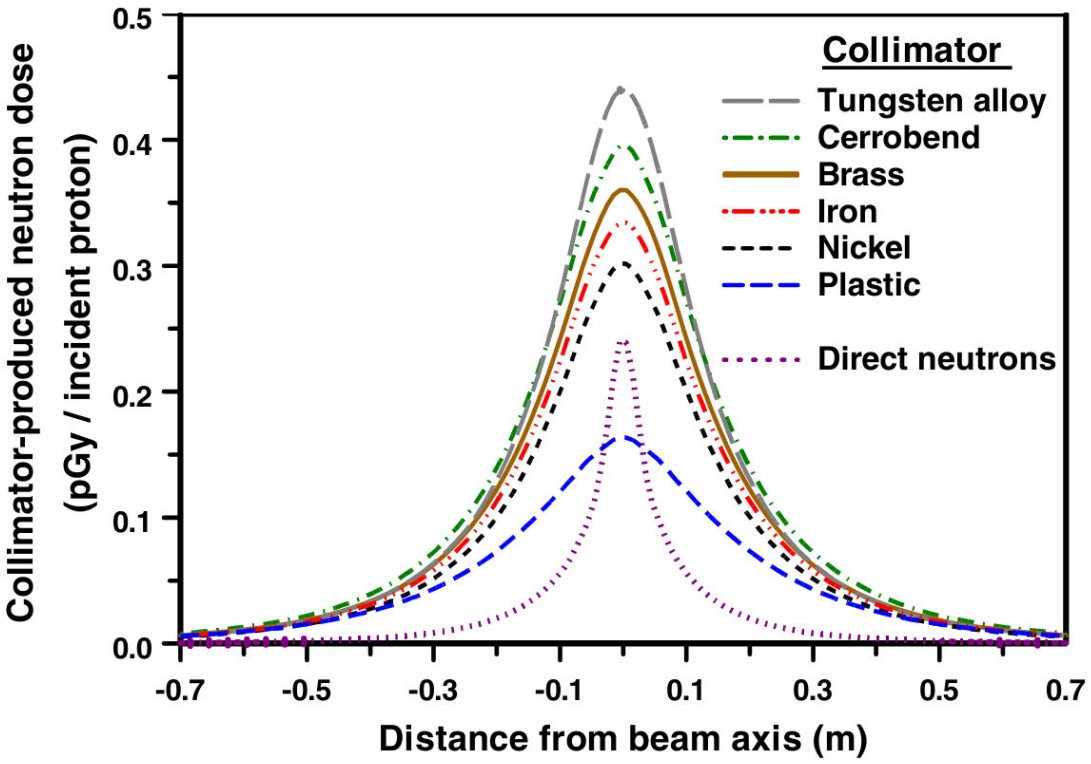


Figure 40: Dose of neutrons emitted per incident proton (pGy) on the attenuator face for different attenuator setups and materials delivered to a tissue phantom. 235 MeV protons were used, with the thickness for each attenuator listed corresponding to the range of the protons in each material. © Institute of Physics and Engineering in Medicine. Reproduced by permission of IOP Publishing Ltd. All rights reserved [159].

Figure 41 highlights that the neutron flux of tungsten is higher than that of brass for protons with energies less than 60 MeV [160]. For the SAHMRI cyclotron emitting 16.5 MeV protons, this translates to a neutron flux for brass of approximately 1 x 10^{-4} neutrons/MeV/cm^2/p and tungsten of approximately 1.1 x 10^{-4} neutrons/MeV/cm^2/p, resulting in a neutron flux ratio of 1 : 1.1, brass : tungsten at this energy [160]. Note that the proton energies and the thickness of the brass/tungsten blocks used to obtain these measurements in this study are both significantly greater than what would be used at SAHMRI, and thus have only been used as a guide to inform the selection of appropriate attenuator materials.

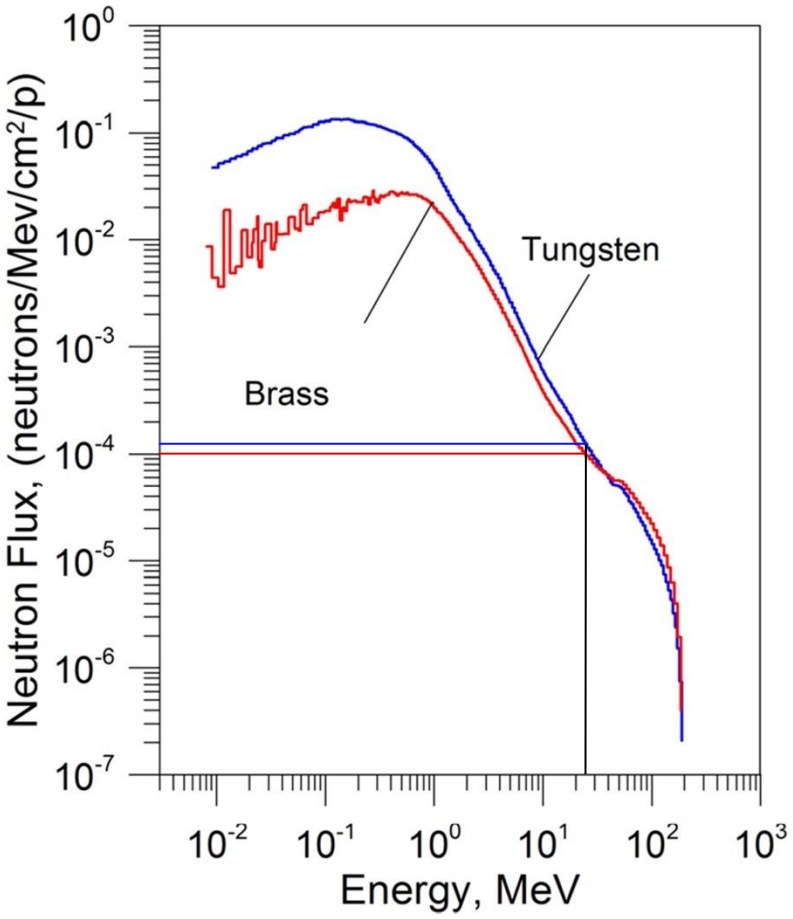


Figure 41: Neutron flux (neutrons/MeV/cm²/p) from a 6.5 cm thick brass aperture and tungsten multileaf collimator irradiated by 200 MeV protons [160]. The black line perpendicular to the x-axis indicates the operating MeV of the 16.5 MeV GE PETtrace cyclotron, and the red and blue lines perpendicular to the y-axis indicate the neutron flux values of brass and tungsten respectively. © 2011 American Association of Physicists in Medicine. Reproduced by permission of John Wiley and Sons [160].

The intention for future work is to modulate the dose rate for pre-clinical in vitro irradiations at relatively low doses (0 – 4 Gy), and thus the emission of neutrons under these circumstances, and the total dose they would deliver to the cells targeted, is expected to be negligible. However, this assumption is based on previous proton irradiation studies [161, 162] based on clinical setups, and should be verified with the GE PETtrace cyclotron. Quantitative results on neutron emission for this preclinical setup have not been performed, and further investigations are needed to confirm the extent of any secondary radiation effects under these conditions. To ensure the safety of personnel who handle the attenuator when switching from FLASH to CONV modes, then use of materials that emit a lower neutron flux post-irradiation should be a consideration for future

work [163, 164]. Moreover, experiments involving in vivo models necessitate the physical measurement of neutron production from attenuator materials with protons accelerated from the 16.5 MeV cyclotron. However, for the purpose of this work only in vitro experiments were considered and as such, the potential relevance of animal models was not a primary focus at this stage. As tungsten and brass were considered here, simulations based on the cyclotron dose rate determined the degree of attenuation required (i.e., number of holes) to reduce the proton flux to a CONV dose rate.

6.2 Attenuator Specifications

6.2.1 Dose Rate Calculations

6.2.1.1 40 nA Cyclotron Dose Rate

SAHMRI's GE Healthcare 16.5 MeV GE PETtrace cyclotron was previously modified by Asp et al. 2019 with the production of an 800 μm pitch brass collimator [75]. The main purpose of a collimator is to modify a beam source, such as a cyclotron, by filtering particles from a divergent source to produce a parallel, or collimated, beam. They are also capable of shielding unwanted particles from reaching the beam target. Asp et al. developed a collimator based on an array of pin holes. In this context, the pitch was defined as the distance between the centres of neighbouring holes in the collimator material. That publication included dosimetric readings obtained from external beam therapy 3 (EBT3) and HD-V2 gafchromic film. First, the average dose rate of the cyclotron without collimation from the gafchromic readings outlined in the publication [75] was calculated. This allowed us to determine whether the unmodified cyclotron is suitable for FLASH at this beam current and perform calculations to modify the beam current if necessary.

$$\mathrm{ETB3} \;=\; 0.61 \;\pm\; 0.06\ \mathrm{Gy/s}$$

$$\mathrm{HD\text{-}V2} \;=\; 0.75 \;\pm\; 0.05\ \mathrm{Gy/s}$$

$$\mathrm{Average} \;=\frac{\mathrm{EBT3} + \mathrm{HD\text{-}V2}}{2} = \frac{(0.61 \;\pm\; 0.06) + (0.75 \;\pm\; 0.05)}{2}$$

$$\mathrm{Average} = 0.68 \;\pm\; 0.11\ \mathrm{Gy/s}$$

The transmission of protons through a collimator of 800 μm pitch, and hole sizes of D1 = 100 μm and D2 = 150 μm, is 2%. From this, then determined the dose rate of protons reaching the beam target at 100% transmissibility, i.e. no attenuation, as dose rate is proportional to transmissibility.

$$\therefore \text{ At } 1\%, \frac{0.68}{2} = 0.34 \text{ Gy/s}$$

$$\therefore \text{At } 100\%, 0.34 \times 100 = 34 \text{ Gy/s}$$

$$\text{Beam on target nA for } 34 \text{ Gy/s} = 40.3 \pm 0.6 \text{ nA (from publication [75])}$$

The beam on target dose rate of 34 Gy/s is not sufficient to induce a FLASH effect, and thus an increase in beam current is needed to achieve a dose rate higher than 40 Gy/s.

6.2.1.2 55 nA Cyclotron Dose Rate

To meet the minimum threshold dose rate required for FLASH, the cyclotron's beam current was increased by 37.5%, corresponding with an increase in dose rate calculated below.

$$40 \text{ nA increased } 37.5\% \text{ to } 55 \text{ nA}, \frac{(55 - 40)}{40} \times 100 = 37.5\%$$

$$\therefore \text{Without attenuation, the dose rate of the } 55 \text{ nA proton beam will also increase by } 37.5\%:$$

$$34 \times 1.375 = 46.75 \text{ Gy/s } (100\% \text{ transmission})$$

Increasing the proton beam current from 40 nA (per Asp et al. 2019 [75]) to 55 nA will provide a dose rate of greater than 40 Gy/s, the minimum threshold for a FLASH irradiation. With this increased beam current, the dose rate will therefore also increase from 34 Gy/s to approximately 46.75 Gy/s. Without collimation, this beam current is appropriate for irradiations requiring FLASH irradiation conditions. To decrease the dose rate to an appropriate CONV dose rate on order of Gy/min, the design of an attenuator was required. This modification to the cyclotron was specifically designed to reduce transmission of protons and decrease flux, applying designs outlined in Asp et al. 2019 [75] to create a blocking material that will allow for CONV irradiations.

6.2.2 Dose Rate Calculations as a Function of Attenuator Pitch

The number of holes in the attenuator, or its transmissibility, directly relates to the number of protons that can reach the target per second. Based on the work conducted by Asp et al. 2020, an attenuator acts to reduce the beam current, and hence, the dose rate [165]. The greater the number or size of the holes in the attenuator, the higher the dose rate achieved on target and vice versa. The manufacture of three different attenuators was decided to achieve three distinct CONV dose rates, each possessing different pitches, these being 400 µm, 800 µm and 1400 µm.

Figure 42 depicts the relationship between the number of holes and attenuator pitch, which was used to determine the pitch required for each attenuator. For each 200 µm increase in attenuator pitch, the number of holes in the attenuator is reduced by half, starting from an initial value of 10000 holes. This gives the function $y = 10000 \times e^{(-0.003466)}$. Excel was used to derive this mathematical relationship from the data points in Figure 42.

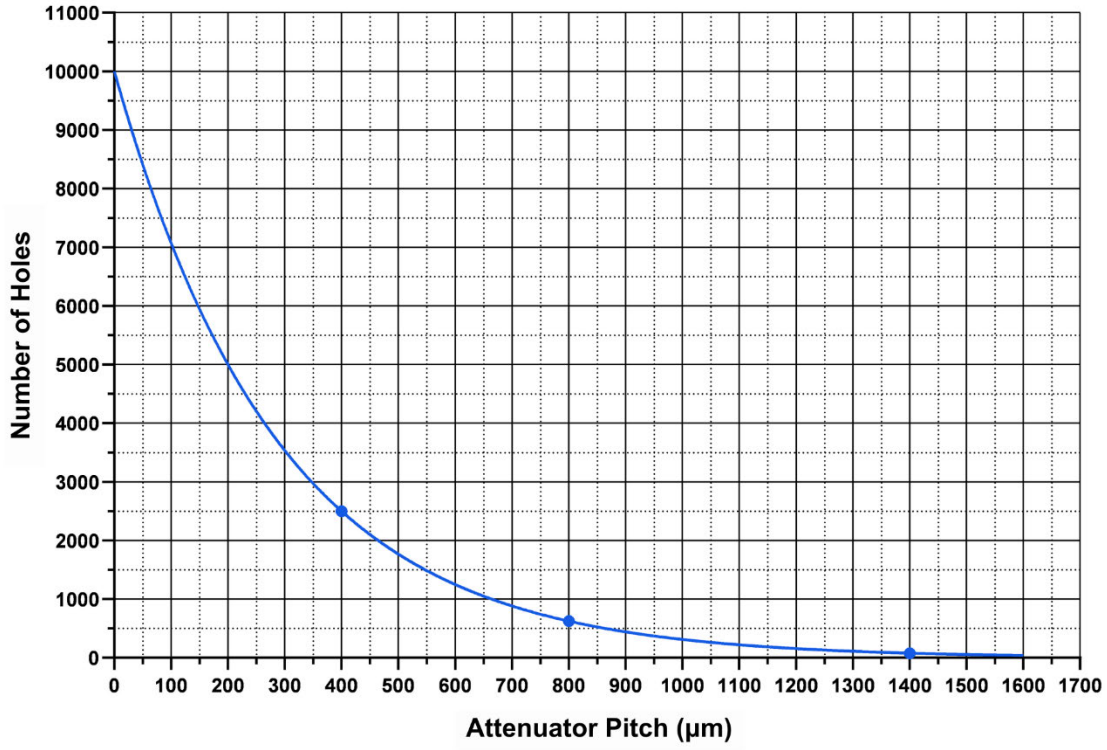


Figure 42: Graph depicting the exponential decay relationship $y = 10000 \times e^{(-0.003466)}$ between the number of attenuator holes versus attenuator pitch (µm). The three data points displayed:

(400, 2500), (800, 625) and (1400, 78) are the hole and pitch combinations to produce dose rates of 3.74 Gy/s, 0.935 Gy/s and 0.117 Gy/s respectively.

To calculate the dose rate of each attenuator, the dose rate per percentage of transmissibility was obtained based on the designs outlined in Asp et al. 2019. Using the dose rate calculated from the modified 55 nA proton beam of 46.75 Gy/s, the dose rates for attenuators with different transmissibility percentages were calculated.

$$\frac{46.75}{100} = 0.4675\ Gy/s\ (1\%\ \text{transmission of 55 nA proton beam})$$

$$\therefore 400\ \mu\text{m pitch attenuator dose rate (8\% transmission, 2500 holes)}$$

$$= 0.4675 \times 8$$

$$\underline{= 3.74\ \text{Gy/s}}$$

$$\therefore 800\ \mu\text{m pitch attenuator dose rate (2\% transmission, 625 holes)}$$

$$= 0.4675 \times 2$$

$$\underline{= 0.935\ \text{Gy/s}}$$

$$\therefore \text{Dose rate per hole} = \frac{0.935}{625} = 0.001496 = 1.45 \times 10^{-3}\ \text{Gy/s/hole}$$

As the transmissibility for a 1400 µm pitch attenuator was not recorded in the study, the dose rate per hole was utilised instead to obtain the final dose rate.

$$\therefore \text{For a } 1400\ \mu\text{m pitch attenuator with} \sim 78\ \text{holes}$$

$$1.45 \times 10^{-3} \times 78 = 0.117\ \text{Gy/s} = \sim 7\ \text{Gy/min}$$

6.2.3 SRIM and TRIM

With the number of holes and attenuator pitch determined, the required thickness of material needed to stop the protons with the attenuator was subsequently calculated. The first step was to obtain the ranges of 16.5 MeV protons in both brass and tungsten. The Monte Carlo package Stopping and Range of Ions in Matter (SRIM) by Ziegler et al. [74] was used to simulate the stopping power and the trajectory of the proton track through these materials. Table 6 depicts the

output for simulations regarding proton stopping power and range in brass and tungsten.

Table 6: SRIM output for calculating the stopping power of protons of energies up to 16.5 MeV in both brass and tungsten (units: MeV/mm). The projected range and longitudinal straggling of ions were primarily used to calculate optimal attenuator thickness for both metals.

Brass					
Ion Energy	**dE/dx Elect.**	**dE/dx Nuclear**	**Projected Range**	**Longitudinal Straggling**	**Lateral Straggling**
14.00 MeV	2.05E-02	9.81E-06	466.48 µm	22.27 µm	32.96 µm
15.00 MeV	1.95E-02	9.23E-06	524.72 µm	24.57 µm	36.83 µm
16.00 MeV	1.85E-02	8.72E-06	585.91 µm	26.92 µm	40.88 µm
16.50 MeV	1.81E-02	8.49E-06	617.6 µm	27.76 µm	42.97 µm
Tungsten					
14.00 MeV	2.864E+01	1.330E-02	290.56 µm	18.35 µm	32.76 µm
15.00 MeV	2.733E+01	1.253E-02	325.40 µm	20.20 µm	36.38 µm
16.00 MeV	2.614E+01	1.184E-02	361.90 µm	22.09 µm	40.15 µm
16.50 MeV	2.561E+01	1.153E-02	380.74 µm	22.91 µm	42.09 µm

From these stopping power tables, the total range of protons in these materials is the sum of their projected range at 16.5 MeV and longitudinal straggling. For each metal, the minimum thickness to stop all protons is:

$$\text{Brass: } 617.6 + 27.76 = 645.4\ \mu\text{m}$$

$$\text{Tungsten: } 380.74 + 22.91 = 403.7\ \mu\text{m}$$

These values were then used to inform the thickness of each metal for TRIM simulations, these being 650 µm brass and 400 µm tungsten. Under ‘Ion Data’, 1000 hydrogen ions with energies of 16.5 MeV were input. For ‘Target Data’, a single layer of either 650 µm brass or 400 µm tungsten was input, followed by 100 µm Lucite to simulate the wall of a cell culture well plate. Ion ranges, transmitted ions/recoils and collision details were recorded. The outputs below show the ionisation energies of these protons against target depth as they pass through brass/tungsten followed by Lucite (Figure 43) as well as visualisation of the proton tracks passing through these materials (Figure 44).

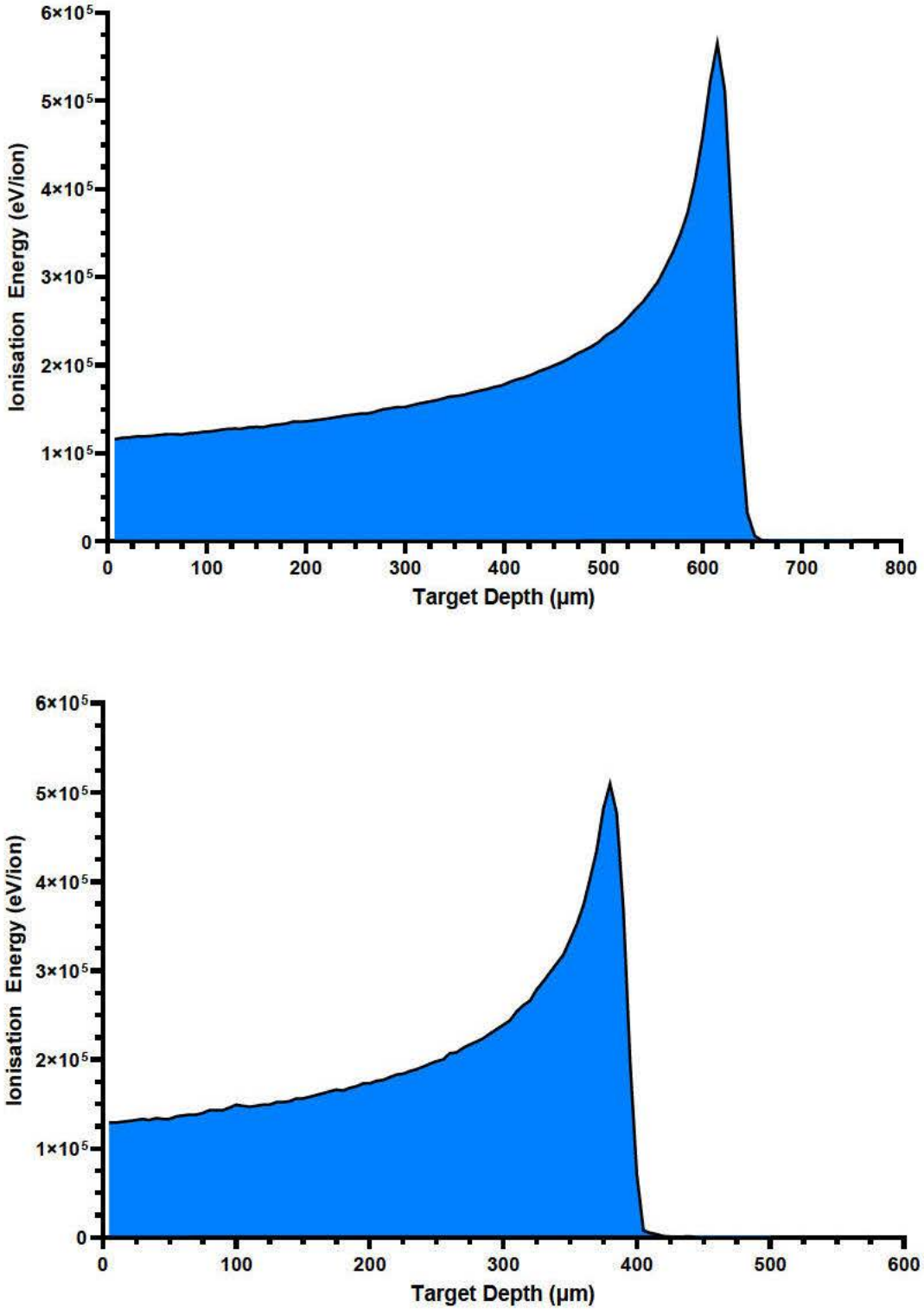
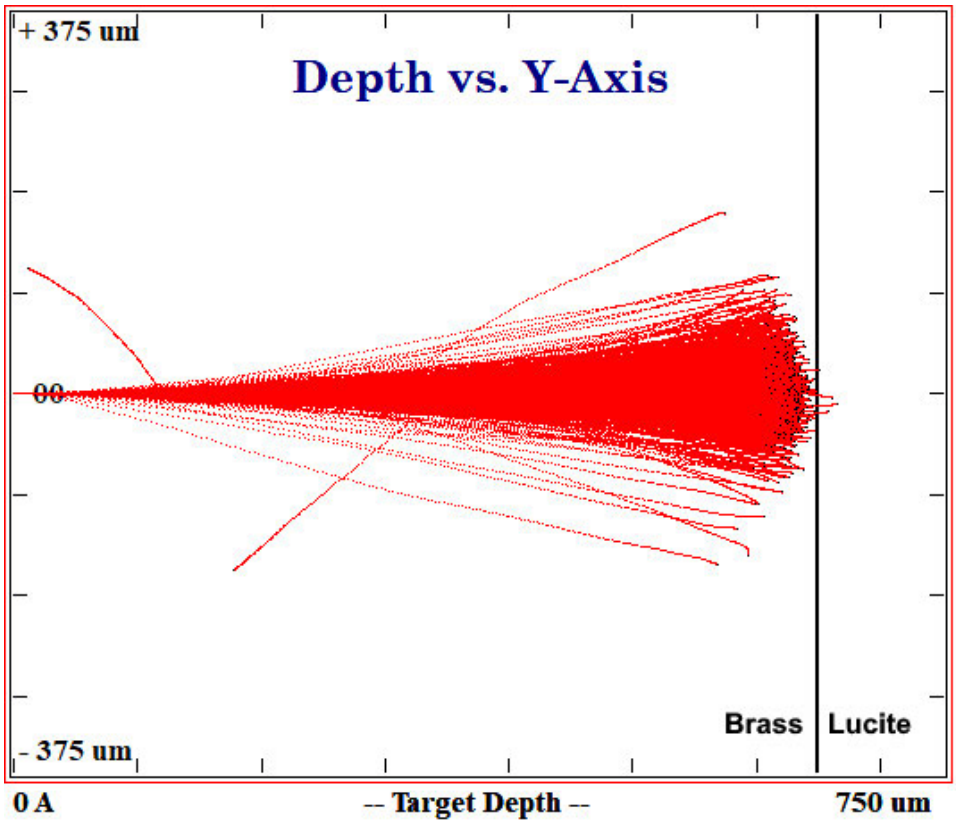


Figure 43: TRIM calculations representing target depth versus ionisation energy per ion utilising brass (top) and tungsten (bottom) with thicknesses of 650 µm and 400 µm respectively, followed by Lucite with a thickness of 100 µm. Appropriate values of thickness were determined from SRIM. Lucite was also incorporated in TRIM calculations to represent the material of the well plate wall.



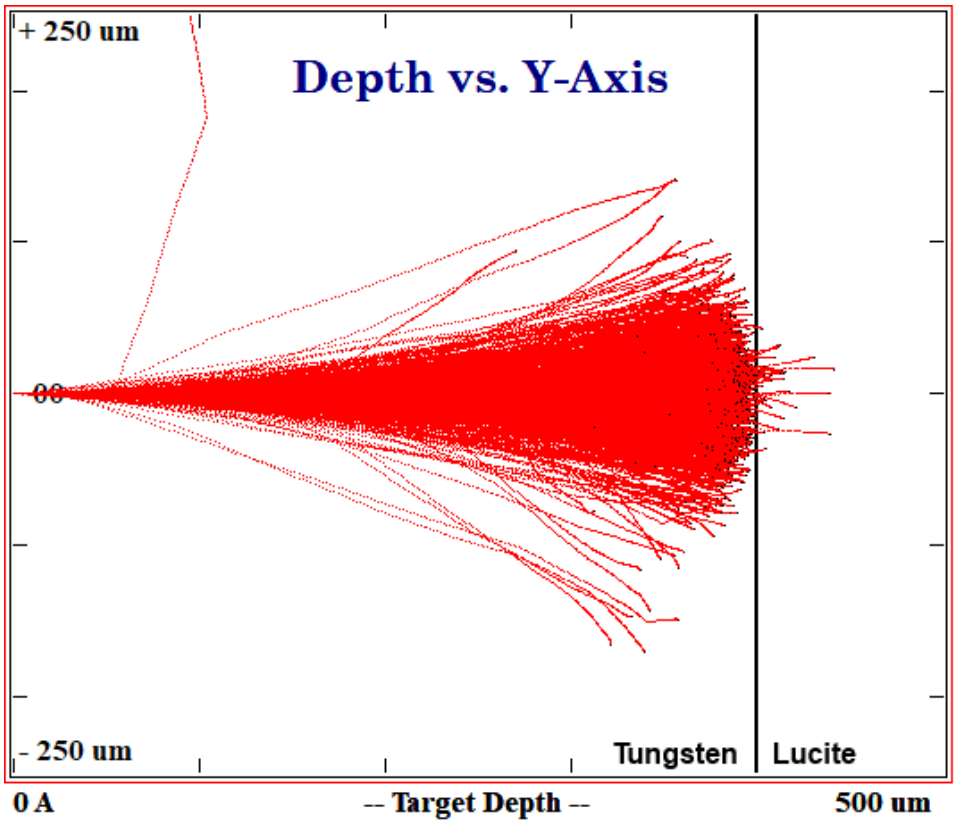


Figure 44: TRIM simulation output of target depth and individual proton tracks of 1000 16.5 MeV protons passing through 650 µm brass + 100 µm Lucite (top) and 400 µm tungsten + 100 µm Lucite (bottom).

As the longitudinal straggling values for protons entering the attenuator metals did not exceed the thickness of the Lucite well plate wall, the thicknesses of each attenuator material (in addition to Lucite) were sufficient to prevent their transmission (Figure 44). With this confirmed, this finalizes the specifications required to manufacture these attenuators. For brass, this is 25 x 0.65 x 25 mm (L x W x D), and for tungsten, 25 x 0.40 x 25 mm, with a 16 x 16 mm hexagonal array arrangement for the holes in their centres. The pitches of 400, 800 and 1400 µm translate to final dose rates of 3.74, 0.935 and 0.117 Gy/s for CONV irradiations, with 0.117 Gy/s being most representative of CONV as described in FLASH literature (Table 7, Figure 45 from [75]).

Table 7: Specifications of both brass and tungsten, candidate metals to produce attenuators for FLASH experiments, and the specifications for each material.

Material	Brass		Tungsten
Thickness (mm)	0.65		0.40
Length x Height (mm)	25 x 25		
Diameter D1 (µm)	100		
Diameter D2 (µm)	150		
Hole Configuration	16 x 16 hex array		
Pitch (µm)	400	800	1400
Number of Holes	2500	625	78
Dose Rate (Gy/s)	3.74	0.935	0.117

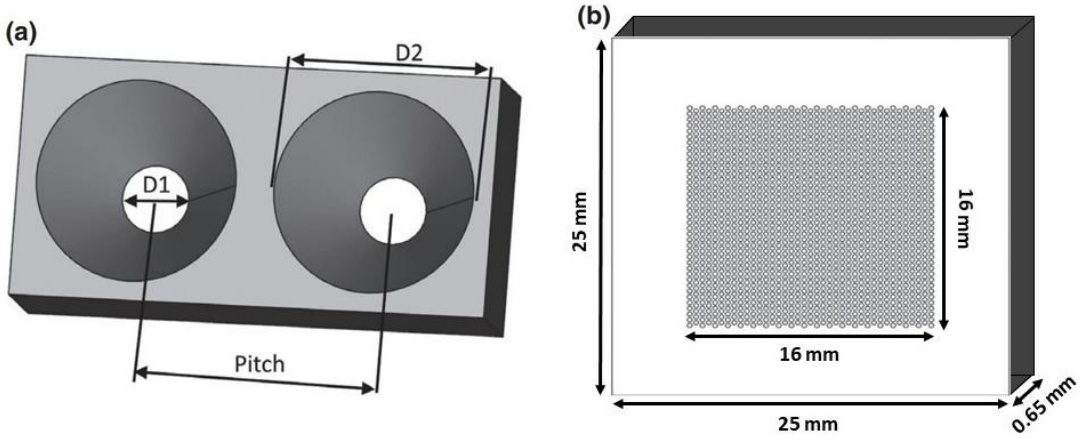


Figure 45: Schematic view of A.) Two of the attenuator holes showing the conical shape of the hole, where D1 = 0.1 mm, D2 = 0.15 mm and the 'Pitch' is varied for each of the three attenuators (0.4 mm, 0.8 mm and 1.4 mm respectively) B.) The 16 x 16 mm grid on the attenuator + dimensions of the brass attenuator with a thickness of 0.65 mm (not to scale). © 2019 American Association of Physicists in Medicine. Reproduced by permission of John Wiley and Sons [75].

6.3 Conclusion

This theoretical design lays the groundwork for future work in proton-FLASH to be conducted at SAHMRI's GE PETtrace cyclotron, or other accelerators that can emit 16.5 MeV protons. Current literature surrounding FLASH currently has significant shortfalls regarding rigorous dosimetry and an unknown mechanism for its healthy tissue sparing effects. To accelerate research in this field, the design and implementation of an attenuator for the GE PETtrace 16.5 MeV cyclotron provides a first step toward adapting non-clinical cyclotron setups for preclinical FLASH experiments. The modulation of the beam current from 40 nA [75] to 55 nA facilitates the greater than 40 Gy/s required for FLASH irradiation, with this modification translating to 46.75 Gy/s. The proposed attenuator will also enable researchers to modulate this ultra-high dose rate (without attenuation) to a CONV dose rate (with attenuation). This is crucial for comparing the effects of different dose rates in *in vitro* and *in vivo* mice models with controlled, reproducible modifications to the beamline and dose rates output. Findings from experiments conducted with this setup may also inform protocols for FLASH experiments at the Australian Bragg Centre for Proton Therapy, which will feature an advanced clinical proton beamline specifically designed for cancer treatments. By demonstrating that cyclotrons like the GE PETtrace 16.5 MeV system can be modified and utilised for preclinical FLASH irradiations, the findings from these experiments could influence its clinical adoption. Additionally, these modifications would allow for a more diverse range of research applications, including studies on the biological effects of radiation adjuvants and radioprotectants. This approach could facilitate proton-FLASH research in both Australia and Taiwan, specifically at SAHMRI (MITRU) and CGMH, and could provide a more accessible pathway for other institutions that lack dedicated FLASH beamlines. This work not only aids in developing a deeper understanding of FLASH's potential in cancer treatment but also demonstrates how non-clinical proton accelerators, typically used for radioisotope production, can be adapted for cutting-edge research applications, expanding the utility of such cyclotrons for future studies.

7 Discussion and Conclusion

7.1 Introduction

Overall, this thesis successfully validated STRIDE as an immunofluorescence-based technique capable of accurately characterizing DNA DSBs. STRIDE offers a robust and sensitive method to quantify the number of DSBs present in cells at a given time, enabling direct assessment of the extent of genotoxic insults. In comparison to traditional methods that rely on detecting cellular responses to DNA damage, such as the widespread activation of DNA damage repair proteins (e.g., γH2AX) or the recruitment of repair proteins to breakage sites (e.g., 53BP1, RAD51) STRIDE provides an exogenous measure of DNA breaks, independent of endogenous repair machinery. This feature is particularly significant, as it allows for an unambiguous quantification of DSBs, ensuring that damage assessment is not confounded by variations in the expression and activity of DDR repair factors. Additionally, STRIDE is not only limited to nuclear DNA but can also characterise DSBs in the cytoplasm, including mitochondrial DNA, cytosolic DNA fragments, and satellite micro-nuclei, meaning it is capable of also determining damage to extra-nuclear structures. By addressing limitations in current DSB detection techniques, STRIDE represents a significant advancement in the study of DNA damage and repair processes. The development of comparable DSB detection techniques, including DI-PLA and TUDEL, also shows promise in advancing this area of research. This unique capability positions STRIDE as a powerful tool for dissecting the molecular underpinnings of genotoxic stress and advancing understanding of cellular responses to DNA damage. This advancement is critical for fields such as radiobiology and cancer research, where the efficacy of treatments often hinges on their ability to induce lethal DNA damage in cancer cells while minimising harm to normal tissues. The severity of genotoxic insults, whether induced by ionising radiation, chemotherapeutics, or other DNA-damaging agents, can now be assessed.

The motivation for employing STRIDE originated from the systematic review of particle-FLASH radiotherapy in *Physical and Engineering Sciences in Medicine*, which highlighted immune system modulation, oxygen depletion, and DNA

damage repair and response as key mechanisms of the FLASH effect [84]. Existing studies lacked quantitative insights into formation of DSBs under FLASH irradiation, and indeed only analysed γH2AX or 53BP1 foci formation. The issue of a lack in thoroughly validated DSB detection techniques, and that DDR factors like γH2AX are often conflated as DSBs, was explored thoroughly in an authoritative Comment in *Nature Reviews Molecular Cell Biology* [36] and full-length review in the *International Journal of Molecular Sciences* [6]. Acceptance in these high-impact journals emphasises the importance of this current gap in knowledge, necessitating the validation of STRIDE. To achieve this, irradiations of 4T1 cells with X-rays were performed, facilitating the successful characterisation of the DSB and DDR repair kinetics of X-rays alone and in combination with either AZD1390 or AuNPs. By combining STRIDE with γH2AX immunostaining, the ability of AZD1390 and AuNPs to delay the onset of DNA repair was demonstrated. The X-ray and AuNP study was published in *ChemPhysChem* [73], whilst a manuscript for the ATMi data has been prepared and submitted for publication. These findings have significant implications for the treatment of cancers, as delaying DNA repair can sensitise tumours to radiation, enhancing the cytotoxic effect of specific doses, and thus reducing the overall dose required to eliminate tumours successfully. These findings contribute to the growing body of evidence supporting the use of ATMi and AuNPs as effective adjuvants in radiotherapy.

Applying the validation of the STRIDE assay in quantifying X-ray induced DNA damage, STRIDE was again applied in the collaboration with CGMH Proton Centre in Taiwan. Through this partnership, research capabilities were established that will benefit researchers at the University of South Australia by facilitating preclinical proton and FLASH radiotherapy studies. For the sake of addressing the DNA damage hypotheses proposed in papers summarised in Chapter 3.4, another aim was to validate DSB and DDR kinetics with STRIDE and γH2AX immunostaining as per the X-ray experiments conducted. Understanding the extent and nature of DNA damage induced under FLASH conditions is crucial for elucidating its underlying biological mechanisms and optimising its clinical application. *In vitro* proton-FLASH irradiations not only validated the feasibility of using STRIDE in this context, but also established a

workflow for future preclinical studies at this facility. While findings are inconclusive regarding the differential effects of proton-FLASH and conventional dose rates on DNA damage, they provide a solid foundation for future research. Further studies at CGMH will enable more thorough validation of FLASH versus CONV induced DSBs, and particularly whether there are key differences in how damage is formed under these conditions and whether cancerous and normal cell types respond to this damage differently. The establishment of STRIDE opens new avenues for studying DNA damage, placing the work of this thesis at the forefront of not only radiobiology, but cancer therapeutics as a whole. The following discussion highlights the novel findings obtained from STRIDE throughout this entire thesis, limitations of the protocol, and the overall validity of the data obtained. It also delves into how STRIDE can be applied in other experimental contexts, specifically its potential applications in clinical oncology, as well as how end-users may benefit from this technology.

7.2 Discussion

7.2.1 Novel Findings

Since STRIDE itself is a newly developed technique, the methodology of which was only published in 2020, the findings of the experiments within this thesis are highly novel. Therefore, STRIDE was tested against a variety of genotoxic insults to determine its overall sensitivity in marking DSB sites, as well as whether it is better at marking DSBs induced by specific insults. Previous publications utilising STRIDE established its capabilities in determining damage in spermatozoa after exposure to UVB and peroxide [117], CRISPR/Cas9-Induced breaks [166], and HeLa and U2OS cells exposed to peroxide, UV, photosensitized reactions, bleomycin, doxorubicin and topotecan [37]. More recent publications have utilised this technique against bone marrow derived macrophages treated with olaparib [118] and multiple HR-deficient cancer cell types in response to small molecule acylfulvene prodrugs [119, 120]. After scoping for DSB detection techniques in literature, STRIDE was selected due to it being the most established in terms of its use and validation. At the time of first utilising STRIDE for experimental work in 2022, cell exposure to peroxide was used as one of the most used methods to test the marking efficiency of STRIDE in response to damage. Thus, initial

experiments thoroughly used peroxide exposure against PC-3, 4T1, and U87 cancer cells. This allowed for the optimisation of primary and secondary antibody concentrations, determining whether off-target/non-specific binding was occurring, identifying the best antibody diluent and blocking buffer, optimising incubation times and temperatures, and the thoroughness of washing required throughout the protocol. Initial findings were confusing, as STRIDE presented high number of foci in the cytoplasm as well as the nucleus. This was unexpected as Kordon *et al.,* inventors of the STRIDE protocol emphasised in their Nucleic Acids Research publication that STRIDE foci would present in the nucleus [37]. They do not provide explanations for STRIDE foci that persist outside of the nucleus [37], but after conferring with one of the co-authors over email, they stated that extra-nuclear foci should not be considered 'off-target' and that mitochondrial DNA breaks and cytosolic DNA fragments should be expected.

After optimising the staining protocol, STRIDE was then applied to quantify DSBs after cell exposure to X-rays, AZD1390, AuNPs, and protons. DSB quantification was complemented with a stain for DNA repair, that being γH2AX. From this, several discoveries were made. Experiments with keV X-rays showed that STRIDE could label DSBs within 1-hour post-irradiation, after which DSB repair processes obscure the ability of STRIDE to bind to DSB ends. This was represented by a peak in γH2AX where STRIDE signals reached a minimum. It appears that with X-ray irradiation alone, γH2AX and STRIDE foci formation have an inverse relationship. The integrated intensity of γH2AX is at a minimum 0-minutes post-irradiation, whereas STRIDE is at its maximum. By fixing cells prior to irradiation, the number of DNA DSBs induced by radiation could be determined as repair processes would not have opportunity to initiate. This is incredibly valuable, as it shows STRIDE's ability to identify DSB damage within short timeframes post-irradiation, compared to historically where γH2AX signalling was only capable of identifying genotoxicity (through DSB repair) at approximately 30 minutes post-irradiation. Intensities between these two factors cross over at approximately 30 – 45 minutes post-irradiation, where STRIDE begins to substantially decrease and γH2AX increases. After 60 minutes, STRIDE returns to baseline values akin to negative controls without irradiation, whereas γH2AX

signal reaches a plateau and then gradually tapers off at longer timepoints (> 60 minutes).

Another prominent finding from this X-ray irradiation study was that both AuNPs and AZD1390 can delay the initiation of the DDR, and increase the time required for cells to repair DSBs. When AuNPs were combined with X-rays, it appeared that the overall DSB burden did not increase. This is an interesting finding as it supports previous work suggesting that mechanisms of AuNP radiosensitisation are biologically driven. The inhibition of thymidylate synthase supports findings of DDR delay [9]. In addition to impeding the ability of cancerous cells to repair DNA damaged by X-rays, AuNPs can induce cumulative DSB stress when incubated with cells for up to 24-hours. This stress can be observed in cells incubated with AuNPs alone or in combination with X-rays, also suggesting that the mere intracellular presence of AuNPs induces genotoxicity. This is particularly evident at 4- and 24-hours fixation timepoints, where the integrated intensities of STRIDE increase with a peak at 24-hours. Proteomics with incubation of the same AuNPs at these timepoints shows a marked downregulation in antioxidant pathways [72], potentially contributing towards this cumulation in DSBs seen at 24-hours. AZD1390 exhibited a similar capability to delay the onset of DSB repair. However, incubation up to 24-hours did not appear to induce any cumulative DSBs alone or in combination with X-rays.

Regarding proton-FLASH, although the reliability of the data extracted is mixed, a few potential trends are alluded to. Analysing γH2AX foci formation in U87 cells revealed that overall counts at the 15-minute fixation timepoint were similar between FLASH and CONV irradiated cells. This contrasts 60-minutes post-irradiation where CONV irradiation induced significantly more γH2AX foci than FLASH. STRIDE foci appeared to peak at 15 minutes for CONV and disappear at 60 minutes. STRIDE foci under FLASH at both 15 and 60 minutes were both near zero. Note that the reliability of STRIDE data presented here was impeded due to inadequate illumination, and hence excitation of STRIDE fluorophores, from the microscopy setup. When attempting re-imaging with the confocal at the Future Industries Institute, STRIDE measured in U87s did not have clearly discernible trends, whilst in OFs some potential trends emerged. In OFs irradiated with protons alone without pre-treatment with AZD1390 or AuNPs, STRIDE

integrated intensity values in FLASH-irradiated cells are lower than that of CONV. This would partially support the FLASH-effect hypotheses of differential DNA damage response, where DSBs form with different complexity under FLASH versus CONV, however the data acquired from U87s does not support this and ideally should be equivalent since the same physical dose is being delivered. Contrastingly, when ATMi or AuNPs are applied in combination with protons, STRIDE intensity is higher in FLASH irradiated samples versus CONV. This suggests that FLASH irradiation alone reduces the number of DSBs induced in normal cells, whilst enhancing radiosensitisation if ATMi or AuNPs are introduced. Due to the questionable reliability of this re-imaged dataset and sample degradation in transit from Taiwan, re-washing samples, and mounting with glass coverslips, ultimately these findings are inconclusive. Repetition of this set of proton-FLASH experiments would allow us to provide more meaningful comparisons between FLASH and CONV irradiation in normal and cancerous cell types and confirm whether the observations made from this data are valid.

7.2.2 Validity of Findings and Limitations

The validity of these experimental findings relies upon a few key assumptions, specifically in the capability of the STRIDE protocol. As immunofluorescent DSB detectors are a relatively new technology, there is not an abundance of literature to draw experience from. This is especially true in confirming its precise mechanism of action, potential off-target binding, or exactly what the ‘expected’ output of a DSB assay is. Other than comparison to γH2AX immunostaining, which is arguably the most established immunofluorescent method of measuring cellular responses to DNA damage, there are only a few comparable DSB detection techniques to compare STRIDE to [31, 38]. Different DSB assays also possess quirks that make one-to-one comparisons difficult. This includes differences in enzymatic components, oligonucleotide analogues bound to the DSB ends, reliance on endogenous factors, and the fluorescence signal conjugation and amplification methods used. However, from the few STRIDE studies experience was drawn from, [37, 117-120] the immunostaining presented in these publications was able to be reproduced.

For both the X-ray and proton irradiation experiments, each experimental condition was replicated in duplicate. Ideally, these conditions would be performed in triplicate at a minimum, in addition to conducting each experiment setup multiple times to ensure that the findings are reproducible. This is one limitation of these experimental findings due to a combination of time and resource limitations. As STRIDE is still in its infancy compared to other widespread assays, there are no kits available to purchase all the reagents required in one single package. Challenges were encountered in sourcing essential components of the staining protocol, with long lead times for delivery of up to 6 months in some cases, presumably due to limited stocks being produced and shipped incrementally each year. This includes the Duolink antibodies, fluorophores, and wash buffers, all of which cannot be sourced locally and require import from the United States. In addition to reagents having long lead times for delivery, the STRIDE methodology itself is also very lengthy, with multiple steps each with their own sources of potential error. Although the protocol was able to be optimised in cells exposed to peroxide, troubleshooting was very difficult because of this. This was compounded by the fact that all the reagents collectively had a cost of over 5000 AUD, and only allowed for 100 reactions, or staining of 100 $1cm^2$ wells. This greatly limited the number of replicates for each condition tested and repeats of entire experimental setups could only be conducted sparingly. Despite these limitations, validation of each step of the STRIDE protocol was successful prior to conducting tests with X-rays and protons.

Whilst conducting a narrative review on specific DNA DSB and repair immunofluorescent techniques [6], the exact method by which STRIDE can specifically target DSBs was explored. The STRIDE protocol dictates that terminal deoxynucleotidyl transferase (TdT) is required to conjugate BrdU to free DNA ends, thereby facilitating detection by two primary anti-BrdU antibodies, two secondary Duolink antibodies, and Duolink detection reagents to produce an immunofluorescent signal. One notable finding in analysing the function of TdT was its ability to conjugate nucleotides to the ends of single-stranded DNA as well as double-stranded DNA. Although this enzymatic function is supposed to occur at a much lower frequency at single-stranded ends compared to double-stranded

ends, considered ‘non-preferential’ activity, this means that single-stranded breaks (SSBs) could be labelled by STRIDE. SSBs occur at a much higher frequency than DSBs, on order of 10000 SSBs [167] to 50 DSBs [128] formed per day. From the data obtained from 2 Gy X-ray irradiation, the maximum number of STRIDE foci at 0 minutes post-irradiation and the maximum number of γH2AX foci between 30 - 60 minutes post-irradiation do not match. There are fewer X-ray-induced γH2AX foci when compared to STRIDE foci. This suggests that if DDR factors like γH2AX are used to estimate the number of DSBs, that the total number of DSBs would be underestimated. Considering though that due to the properties of TdT, it is possible that a small percentage of STRIDE foci presented are SSBs. Without a method to verify whether SSBs are tagged by STRIDE, it is difficult to discern whether a single DSB is responsible for a single γH2AX focus. When comparing the sensitivity of STRIDE to the TUNEL assay, the increased sensitivity of STRIDE is displayed in its capability to detect low level damage as individual, discrete foci [37] versus TUNEL which pan-stains the nucleus and is designed to detect SSBs as well as DSBs [126]. Therefore, based on previous estimates predicting DSB formation and current literature, it is very likely that the majority of fluorescent STRIDE foci mark, and are representative of, DNA DSBs.

7.2.3 Future Work

There are numerous directions for future research from the foundation laid by the data presented in this thesis. Since DSB detectors have not been used in literature, particularly in cancer therapeutics research where they hold immense value, characterisation of various radiotherapy modalities and chemo pharmaceuticals can be explored. The first of these would be to quantify the number of STRIDE foci that are produced per Gy of radiation. Quantitatively comparing STRIDE foci formation per Gy with the expected number of DSBs inferred from the γH2AX assay is essential to fully characterise DSB detectors. Ideally this would be performed with not only X-rays and protons as per the work conducted here, but multiple different sources of differing LET, energies, dose rates, and fractions. This could be achieved by irradiating cells with incrementally increasing dose (e.g., 0, 1, 2, 4, 8 Gy) as well as fixing cells at incremental timepoints post-irradiation. For instance, at shorter intervals post-irradiation and

at a higher temporal resolution, i.e., fixation every minute post-irradiation, would also be of immense value to discern clearer trends in STRIDE versus DDR factor kinetics. Insights into how each radiation type produces DSBs, the complexity of damage caused, and how cells repair this damage, would also be of interest. Previous publications have shown that γH2AX foci of differing complexities can be produced with particles of similar LET but differing particle type [168], and that differing LET affects γH2AX dephosphorylation rates [169]. If there is evidence that repair factors are recruited differently in response to different radiation types, then there is a potential difference in how the DSBs are formed to produce this response. Expanding comparative staining of STRIDE and γH2AX to other DDR factors, including 53BP1, RAD51, MRN, Ku70/80 or SIRT6, would allow for determination of the DSB versus DDR kinetics of not only proton-FLASH, but other genotoxic insults. These could also be readily applied against a multitude of DNA damage repair inhibitors or alternative nanoparticle formulations. This would provide a better understanding of the action/biases of each DDR marker recruited to the site of a DSB. Although in this thesis we found no evidence of colocalisation of STRIDE with γH2AX, future studies should explore more rigorous spatiotemporal single-cell analysis of where DSB and repair factors coincide through high resolution microscopy. All these comparisons would enable more definitive relationships to be drawn between radiation dose, DSB yield, and subsequent cellular responses.

Spatial arrangement of foci within the cytoplasm is also an area of further study. Determining damage to mitochondrial DNA [170-172], as well as in micronuclei [151, 153, 154] and cytoplasmic DNA fragments [173] would aid in the identification of potential vulnerabilities that therapeutics can target. As well as measuring DNA damage in different organelles, further validating and optimising the STRIDE assay to improve its resource efficiency and ease of use would also be highly beneficial. If STRIDE could be made widely available for researchers with purpose-made kits that were affordable and allowed for higher throughput than currently, then progression of DSB detection research would be greatly streamlined. Such improvements would address current limitations to STRIDE, allowing for enhanced accuracy in marking DSBs, reduced complexity regarding sourcing of reagents, and increasing cost efficiency. These optimisations would

ultimately support the generation of more robust experimental data. Extending the use of STRIDE to *in vivo* models is also of interest to potentially progress preclinical experiments to clinical trials.

Future proton-FLASH studies may utilise the 16.5 MeV GE PETtrace cyclotron at SAHMRI, which is conventionally used to produce radioisotopes for molecular imaging and therapeutic purposes. This beamline has potential for being adapted for *in vitro* and *in vivo* mice-based work, as outlined in Chapter 6. The 16.5 MeV GE PETtrace cyclotron is not purpose built for preclinical experiments and operates at insufficient energies to penetrate deep tissues. Thus, *in vivo* orthotopic or deep-seated brain tumour models would not be analysed in this study, as tissue penetration would be limited to a depth of only a few millimetres. To accommodate for this, mice xenografts would be injected subcutaneously. As proton therapies are also used to treat breast and bone cancers clinically, syngeneic mice models should be utilised to better mimic the the tumour microenvironment and immune interactions observed in human cancers. These models involve implanting tumour cells from the same genetic background as the host, preserving key features such as immune compatibility and tumour-host interactions. This approach allows for a more accurate evaluation of the therapeutic efficacy and biological responses to proton therapy, particularly in assessing immunological effects, tissue-specific microenvironments, and treatment-induced changes. Additionally, syngeneic models allow for further study of metastatic progression, which is relevant for breast and bone cancers frequently treated with proton therapy. Thus, the mouse strain utilised for these experiments should ideally be BALB/c, as they are immunocompetent and have a range of well-established cancerous cell lines available. These include 4T1, a mouse-derived triple-negative cell line that mimics stage IV human breast cancer, and K7M2, a mouse-derived osteosarcoma line. Prior to the commencement of *in vivo* experiments, clonogenicity assays using these cancerous cell lines would provide survival comparisons between FLASH or CONV dose rates. Addition of a non-cancerous cell line for comparison, such as the mouse-derived HC11 mammary epithelial cells, would provide valuable insights into the differential responses between normal and cancerous cells in response to FLASH. Plates

would be organised based upon cell type, dose, and dose rate with 3 experimental replicates for each dose applied (Figure 46).

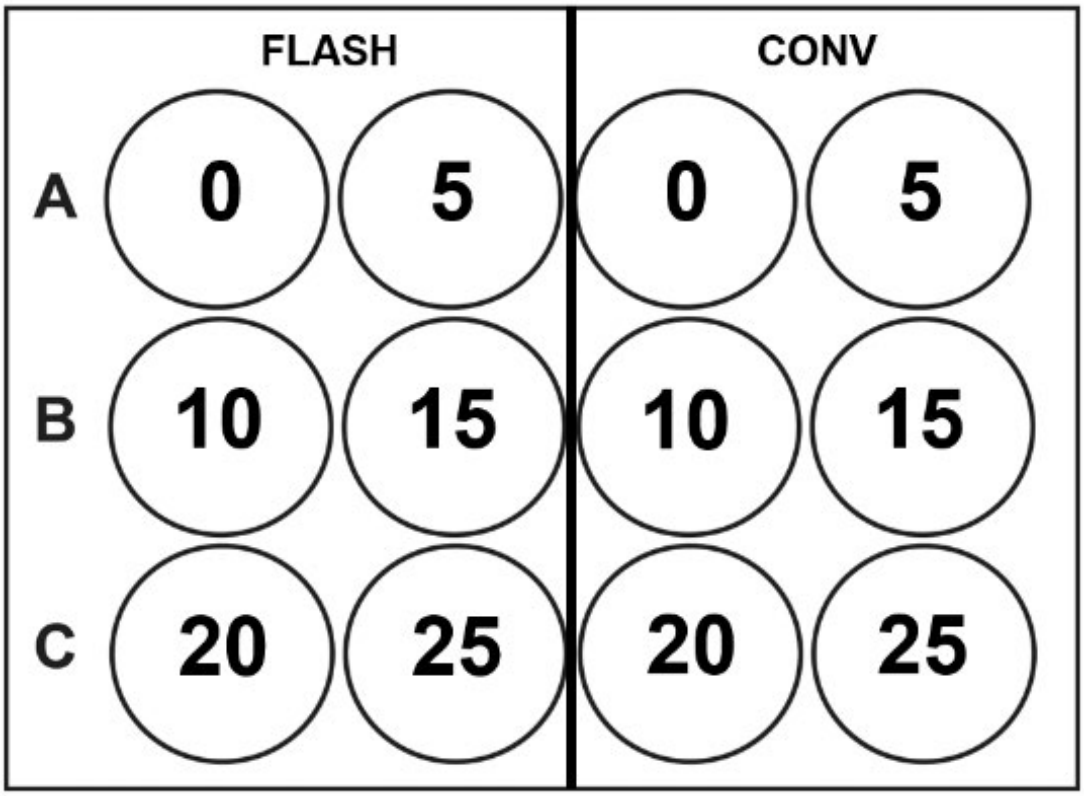


Figure 46: Plate layout for clonogenic and γH2AX 12-well plate assays under FLASH (40 Gy/s) and CONV (0.61 Gy/s) at different doses (units Gy). Layout replicated 3 times for 4T1, K7M2 and HC11 cell lines.

An ultra-high dose rate (FLASH, 46.75 Gy/s) and a low dose rate (CONV, 0.117Gy/s) should be employed, with external beam ports being used to modulate the dose rate, beam current, and proton fluence, in addition to a time-gated shutter to alter exposure time. A medical physicist and GE cyclotron engineer can assist with irradiations to ensure that the intended dose rates and doses are delivered. Following irradiation, cells would be cultured, fixed, and stained when cell colonies reached a suitable size for quantification. Determining how effective cancerous versus normal cells survive in response to either FLASH or CONV radiation damage would provide interesting results when compared to STRIDE foci formation. If STRIDE confirms that FLASH dose rates induce complex DNA damage at early timepoints, clonogenic assays can be used to assess whether this damage results in cell death at later timepoints. Additionally,

this would allow us to determine whether normal cells can recover more effectively than cancerous cells from this damage.

Progressing to *in vivo* studies with proton-FLASH is critical for translating *in vitro* findings into meaningful clinical applications, particularly in understanding the nuanced biological responses that underpin the FLASH effect. To characterise the FLASH effect to its fullest extent, avoiding alteration to the biological mechanisms that are predicted to influence radioprotection is essential. With evidence that the tumour microenvironment, immune and inflammatory response, stem cell niche, and metabolism have key roles in bolstering the FLASH effect, emulating these factors in mice models would provide data which will best translate clinically. Using mice which are immunodeficient or genetically modified would produce a poor model for analysis; therefore syngeneic models should be utilised in experiments quantifying tumour growth, expression of inflammatory cytokines (TGFβ, IL-1, IL-6, TNFα) [174], and immune cell lymphocyte infiltration. Skin irradiations can also be performed to gauge the differential response compared to cancerous tissues, particularly measuring whether FLASH mitigates normal tissue inflammation. With an *in vivo* platform for proton-FLASH also established at CGMH [148], modification of their clinical cyclotron with an attenuator could also facilitate Bragg peak FLASH *in vitro* and *in vivo* experiments, as well as repeating of *in vitro* experiments looking at proton-FLASH in combination with radiosensitisers.

7.3 Conclusion

This thesis establishes STRIDE as a groundbreaking tool in oncology, creating a new paradigm for characterising previously unobservable DNA damage. By combining STRIDE with γH2AX, this research has developed a novel framework to comprehensively study DNA DSBs and the associated DDR. This approach enables precise quantification of DSBs and monitoring of repair kinetics, offering insights into how the physical and biological mechanisms underlying genotoxic stress contrast each other on a single-cell level. Resolving cell-to-cell heterogeneity in DNA damage and repair capacity through per-cell foci quantification will allow for insights that would otherwise be masked in population-averaged data. Such advancements mark a significant step forward in

radiobiological research, with STRIDE also poised for widespread adoption in chemo- and nanotherapeutics. By accurately determining the effects of DSB-inducing insults, STRIDE can guide the development of anti-cancer therapies, optimise therapeutic protocols, and improve predictions of treatment outcomes.

Clinically, this project has focused on the application of STRIDE to advance the understanding and optimisation of X-ray and proton radiotherapy in combination with experimental treatment modalities including ATM inhibitors, AuNPs, and FLASH. These adjuvants/modalities have an emphasis on sensitising cancerous cells to radiation exposure, and in turn reducing the amount of radiation necessary for successful treatment. When applied to patients, this means that their prognosis is improved, whilst also minimising negative off-target side effects in normal tissues. The ability to quantify DNA damage with STRIDE allows us to accurately determine the degree of damage caused by a certain modality. While it may not be feasible for routine clinical implementation, STRIDE could be valuable in a research context to compare the number of DSBs present within tumours and peripheral normal tissue biopsies post-treatment. This approach could provide informative data for oncologists in understanding the differential effects of their treatment regimens on cancerous and normal tissues in patients. This could be complimented by genomic screening to identify appropriate DNA damage repair inhibitors or radiosensitisers against specific cancer subtypes. Its potential applications could also span to environmental studies and even space exploration, such as assessing radiation shielding and the effects of cosmic radiation. STRIDE can contribute to the development of radioprotectants for astronauts, or even radiation-resistant crops, ensuring genomic integrity is maintained for long voyages and reliable food production in extraterrestrial environments.

STRIDE’s ability to characterise phenomena such as the FLASH effect opens further opportunities for clinical translation. Determining the primary mechanism of action of FLASH is currently a hot topic in radiobiological research, with success in doing so potentially marking a new era in the radiotherapy landscape. Because of preferentially sparing normal tissue, hypofractionated FLASH may be beneficial which could increase the number of patients receiving radiotherapy that would otherwise be financially or logistically incapable of doing so. For example,

traditional fractionated radiotherapy regimens, delivered over several days, could be delivered in a hypofractionated scheme in less than a second. Administering higher doses within a shorter timeframe, both during irradiation and for each fraction, would reduce the number of days patients need to visit hospital to complete their treatment. This provides massive benefits for rural and remote individuals who struggle to spend extended periods of time away from home and work to receive treatment in major population centres. The insights gained from this work have the potential to drive dramatic improvements in cancer therapeutics, whether radiation- or pharmaceutical-based, ultimately contributing to better outcomes for patients. By bridging fundamental research with clinical applications, this thesis underscores the transformative potential of STRIDE in advancing understanding of DNA damage and repair in the context of cancer therapy and beyond.

Reference List

1. Aplan, P.D., *Causes of oncogenic chromosomal translocation.* Trends Genet, 2006. **22**(1): p. 46-55.
2. Mladenov, E., et al., *DNA double-strand break repair as determinant of cellular radiosensitivity to killing and target in radiation therapy.* Front Oncol, 2013. **3**: p. 113.
3. Barnett, G.C., et al., *Normal tissue reactions to radiotherapy: towards tailoring treatment dose by genotype.* Nat Rev Cancer, 2009. **9**(2): p. 134-42.
4. Kaina, B., L. Beltzig, and H. Strik, *Temozolomide – Just a Radiosensitizer?* Frontiers in Oncology, 2022. **12**.
5. Cheng, B., et al., *Recent advances in DDR (DNA damage response) inhibitors for cancer therapy.* European Journal of Medicinal Chemistry, 2022. **230**: p. 114109.
6. Atkinson, J., et al., *DNA Double Strand Break and Response Fluorescent Assays: Choices and Interpretation.* International Journal of Molecular Sciences, 2024. **25**(4): p. 2227.
7. Hopkins, J.L., L. Lan, and L. Zou, *DNA repair defects in cancer and therapeutic opportunities.* Genes Dev, 2022. **36**(5-6): p. 278-293.
8. Kantidze, O.L., et al., *Synthetically Lethal Interactions of ATM, ATR, and DNA-PKcs.* Trends in Cancer, 2018. **4**(11): p. 755-768.
9. Turnbull, T., et al., *Cross-Correlative Single-Cell Analysis Reveals Biological Mechanisms of Nanoparticle Radiosensitization.* ACS Nano, 2019. **13**(5): p. 5077-5090.
10. Howard, D., et al., *Quantitative Single-Cell Comparison of Sensitization to Radiation and a Radiomimetic Drug for Diverse Gold Nanoparticle Coatings.* Small Science, 2024. **n/a**(n/a): p. 2400053.
11. De Ruysscher, D., et al., *Radiotherapy toxicity.* Nature Reviews Disease Primers, 2019. **5**(1): p. 13.
12. Rogakou, E.P., et al., *Megabase chromatin domains involved in DNA double-strand breaks in vivo.* J. Cell Biol., 1999. **146**(5): p. 905-16.

13. Savic, V., et al., *Formation of dynamic gamma-H2AX domains along broken DNA strands is distinctly regulated by ATM and MDC1 and dependent upon H2AX densities in chromatin.* Mol Cell, 2009. **34**(3): p. 298-310.
14. Mah, L.J., A. El-Osta, and T.C. Karagiannis, *γH2AX: a sensitive molecular marker of DNA damage and repair.* Leukemia, 2010. **24**(4): p. 679-686.
15. Ray, A., et al., *ATR- and ATM-Mediated DNA Damage Response Is Dependent on Excision Repair Assembly during G1 but Not in S Phase of Cell Cycle.* PLoS ONE, 2016. **11**(7): p. e0159344.
16. Bakkenist, C.J. and M.B. Kastan, *DNA damage activates ATM through intermolecular autophosphorylation and dimer dissociation.* Nature, 2003. **421**(6922): p. 499-506.
17. Kitagawa, R. and M.B. Kastan, *The ATM-dependent DNA damage signaling pathway.* Cold Spring Harb. Symp. Quant. Biol., 2005. **70**: p. 99-109.
18. Schultz, L.B., et al., *P53 Binding Protein 1 (53bp1) Is an Early Participant in the Cellular Response to DNA Double-Strand Breaks.* Journal of Cell Biology, 2000. **151**(7): p. 1381-1390.
19. Escribano-Díaz, C., et al., *A Cell Cycle-Dependent Regulatory Circuit Composed of 53BP1-RIF1 and BRCA1-CtIP Controls DNA Repair Pathway Choice.* Mol. Cell, 2013. **49**(5): p. 872-883.
20. Mirman, Z. and T. de Lange, *53BP1: a DSB escort.* Genes Dev., 2020. **34**(1-2): p. 7-23.
21. Savic, V., et al., *Formation of Dynamic γ-H2AX Domains along Broken DNA Strands Is Distinctly Regulated by ATM and MDC1 and Dependent upon H2AX Densities in Chromatin.* Mol. Cell, 2009. **34**(3): p. 298-310.
22. Adams, B.R., et al., *Dynamic Dependence on ATR and ATM for Double-Strand Break Repair in Human Embryonic Stem Cells and Neural Descendants.* PLoS ONE, 2010. **5**(4): p. e10001.
23. Schütz, C.S., M.B. Stope, and S. Bekeschus, *H2A.X Phosphorylation in Oxidative Stress and Risk Assessment in Plasma Medicine.* Oxid Med Cell Longev, 2021. **2021**: p. 2060986.

24. Wanotayan, R., et al., *A deep learning model (FociRad) for automated detection of γ-H2AX foci and radiation dose estimation.* Scientific Reports, 2022. **12**(1): p. 5527.
25. Stenvall, A., et al., *Quantitative γ-H2AX immunofluorescence method for DNA double-strand break analysis in testis and liver after intravenous administration of 111InCl3.* EJNMMI Research, 2020. **10**(1): p. 22.
26. Curtin, N.J., *Inhibiting the DNA damage response as a therapeutic manoeuvre in cancer.* Br J Pharmacol, 2013. **169**(8): p. 1745-65.
27. Wang, M., S. Chen, and D. Ao, *Targeting DNA repair pathway in cancer: Mechanisms and clinical application.* MedComm, 2021. **2**(4): p. 654-691.
28. Zhu, Y., et al., *qDSB-Seq is a general method for genome-wide quantification of DNA double-strand breaks using sequencing.* Nat Commun, 2019. **10**(1): p. 2313.
29. Löbrich, M., et al., *gammaH2AX foci analysis for monitoring DNA double-strand break repair: strengths, limitations and optimization.* Cell Cycle, 2010. **9**(4): p. 662-9.
30. Mariotti, L.G., et al., *Use of the γ-H2AX Assay to Investigate DNA Repair Dynamics Following Multiple Radiation Exposures.* PLOS ONE, 2013. **8**(11): p. e79541.
31. Galbiati, A. and F. d'Adda di Fagagna, *DNA Damage In Situ Ligation Followed by Proximity Ligation Assay (DI-PLA).* Methods Mol Biol, 2019. **1896**: p. 11-20.
32. Tu, W.-Z., et al., *γH2AX foci formation in the absence of DNA damage: Mitotic H2AX phosphorylation is mediated by the DNA-PKcs/CHK2 pathway.* FEBS Lett., 2013. **587**(21): p. 3437-3443.
33. Granzotto, A., et al., *When Chromatin Decondensation Affects Nuclear γH2AX Foci Pattern and Kinetics and Biases the Assessment of DNA Double-Strand Breaks by Immunofluorescence.* Biomolecules, 2024. **14**(6): p. 703.
34. Müller, B., et al., *Detection of DNA Double Strand Breaks by γH2AX Does Not Result in 53bp1 Recruitment in Mouse Retinal Tissues.* Frontiers in Neuroscience, 2018. **12**.

35. Rybak, P., et al., *Low level phosphorylation of histone H2AX on serine 139 (γH2AX) is not associated with DNA double-strand breaks.* Oncotarget, 2016. **7**(31): p. 49574-49587.
36. Atkinson, J., E. Bezak, and I. Kempson, *Imaging DNA double-strand breaks — are we there yet?* Nature Reviews Molecular Cell Biology, 2022. **23**(9): p. 579-580.
37. Kordon, M.M., et al., *STRIDE—a fluorescence method for direct, specific in situ detection of individual single- or double-strand DNA breaks in fixed cells.* Nucleic Acids Research, 2019. **48**(3): p. e14-e14.
38. Lutze, J., S.E. Warrington, and S.J. Kron, *TdT-dUTP DSB End Labeling (TUDEL), for Specific, Direct In Situ Labeling of DNA Double Strand Breaks*, in *Biomedical Engineering Technologies*, A. Rasooly, H. Baker, and M.R. Ossandon, Editors. 2022, Springer US: New York, NY. p. 299-317.
39. Kinner, A., et al., *Gamma-H2AX in recognition and signaling of DNA double-strand breaks in the context of chromatin.* Nucleic Acids Res, 2008. **36**(17): p. 5678-94.
40. Rogakou, E.P., et al., *Megabase chromatin domains involved in DNA double-strand breaks in vivo.* J Cell Biol, 1999. **146**(5): p. 905-16.
41. Shroff, R., et al., *Distribution and dynamics of chromatin modification induced by a defined DNA double-strand break.* Curr. Biol., 2004. **14**(19): p. 1703-11.
42. Kempson, I., *Mechanisms of nanoparticle radiosensitization.* WIREs Nanomedicine and Nanobiotechnology, 2021. **13**(1): p. e1656.
43. Chen, Y., et al., *Gold Nanoparticles as Radiosensitizers in Cancer Radiotherapy.* Int J Nanomedicine, 2020. **15**: p. 9407-9430.
44. Roa, W., et al., *Gold nanoparticle sensitize radiotherapy of prostate cancer cells by regulation of the cell cycle.* Nanotechnology, 2009. **20**(37): p. 375101.
45. Carter, J.D., et al., *Nanoscale Energy Deposition by X-ray Absorbing Nanostructures.* The Journal of Physical Chemistry B, 2007. **111**(40): p. 11622-11625.

46. McMahon, S.J., et al., *Biological consequences of nanoscale energy deposition near irradiated heavy atom nanoparticles.* Sci Rep, 2011. **1**: p. 18.
47. Yokogawa, T., et al., *dUTPase inhibition confers susceptibility to a thymidylate synthase inhibitor in DNA-repair-defective human cancer cells.* Cancer Sci, 2021. **112**(1): p. 422-432.
48. Durant, S.T., et al., *The brain-penetrant clinical ATM inhibitor AZD1390 radiosensitizes and improves survival of preclinical brain tumor models.* Sci Adv, 2018. **4**(6): p. eaat1719.
49. Toulany, M., *Targeting DNA Double-Strand Break Repair Pathways to Improve Radiotherapy Response.* Genes (Basel), 2019. **10**(1).
50. Harris, B.R.E., et al., *ATM inhibitor KU-55933 induces apoptosis and inhibits motility by blocking GLUT1-mediated glucose uptake in aggressive cancer cells with sustained activation of Akt.* The FASEB Journal, 2021. **35**(4): p. e21264.
51. Wu, D., et al., *The blood–brain barrier: structure, regulation, and drug delivery.* Signal Transduction and Targeted Therapy, 2023. **8**(1): p. 217.
52. Jucaite, A., et al., *Brain exposure of the ATM inhibitor AZD1390 in humans—a positron emission tomography study.* Neuro-Oncology, 2020. **23**(4): p. 687-696.
53. Riches, L.C., et al., *Pharmacology of the ATM Inhibitor AZD0156: Potentiation of Irradiation and Olaparib Responses Preclinically.* Molecular Cancer Therapeutics, 2020. **19**(1): p. 13-25.
54. Mallick, S., *Proton Therapy*, in *Practical Radiation Oncology*, S. Mallick, G.K. Rath, and R. Benson, Editors. 2020, Springer Singapore: Singapore. p. 79-84.
55. De Simoni, M., et al., *FRED: a fast Monte Carlo code on GPU for quality control in Particle Therapy.* Journal of Physics: Conference Series, 2020. **1548**: p. 012020.
56. Prasanna, P.G., et al., *Normal Tissue Injury Induced by Photon and Proton Therapies: Gaps and Opportunities.* Int J Radiat Oncol Biol Phys, 2021. **110**(5): p. 1325-1340.
57. Loganovsky, K.N., et al., *Radiation-Induced Cerebro-Ophthalmic Effects in Humans.* Life (Basel), 2020. **10**(4).

58. Giuranno, L., et al., *Radiation-Induced Lung Injury (RILI).* Front Oncol, 2019. **9**: p. 877.
59. Palmer, S.L., et al., *Patterns of Intellectual Development Among Survivors of Pediatric Medulloblastoma: A Longitudinal Analysis.* Journal of Clinical Oncology, 2001. **19**(8): p. 2302-2308.
60. Mostoufi-Moab, S. and A. Grimberg, *Pediatric brain tumor treatment: growth consequences and their management.* Pediatr Endocrinol Rev, 2010. **8**(1): p. 6-17.
61. Moreno, A.C., et al., *Intensity modulated proton therapy (IMPT) - The future of IMRT for head and neck cancer.* Oral Oncol, 2019. **88**: p. 66-74.
62. Ohno, T., *Particle radiotherapy with carbon ion beams.* Epma j, 2013. **4**(1): p. 9.
63. Soto, L.A., et al., *FLASH Irradiation Results in Reduced Severe Skin Toxicity Compared to Conventional-Dose-Rate Irradiation.* Radiat Res, 2020. **194**(6): p. 618-624.
64. Montay-Gruel, P., et al., *Long-term neurocognitive benefits of FLASH radiotherapy driven by reduced reactive oxygen species.* Proc Natl Acad Sci U S A, 2019. **116**(22): p. 10943-10951.
65. Zhou, G., *Mechanisms underlying FLASH radiotherapy, a novel way to enlarge the differential responses to ionizing radiation between normal and tumor tissues.* Radiation Medicine and Protection, 2020. **1**(1): p. 35-40.
66. Nickoloff, J.A., N. Sharma, and L. Taylor, *Clustered DNA Double-Strand Breaks: Biological Effects and Relevance to Cancer Radiotherapy.* Genes, 2020. **11**(1).
67. Buonanno, M., V. Grilj, and D.J. Brenner, *Biological effects in normal cells exposed to FLASH dose rate protons.* Radiotherapy and Oncology, 2019. **139**: p. 51-55.
68. Fouillade, C., et al., *FLASH Irradiation Spares Lung Progenitor Cells and Limits the Incidence of Radio-induced Senescence.* Clinical Cancer Research, 2020. **26**(6): p. 1497-1506.
69. Hanton, F., et al., *DNA DSB Repair Dynamics following Irradiation with Laser-Driven Protons at Ultra-High Dose Rates.* Scientific Reports, 2019. **9**(1).

70. Zlobinskaya, O., et al., *Induction and repair of DNA double-strand breaks assessed by gamma-H2AX foci after irradiation with pulsed or continuous proton beams.* Radiation and Environmental Biophysics, 2012. **51**(1): p. 23-32.
71. Kimling, J., et al., *Turkevich Method for Gold Nanoparticle Synthesis Revisited.* The Journal of Physical Chemistry B, 2006. **110**(32): p. 15700-15707.
72. Sebastian, S., et al., *Kinetic Effects of Transferrin-Conjugated Gold Nanoparticles on the Antioxidant Glutathione-Thioredoxin Pathway.* Antioxidants, 2023. **12**(8): p. 1617.
73. Atkinson, J., et al., *Gold Nanoparticles Cause Radiosensitization in 4T1 Cells by Inhibiting DNA Double Strand Break Repair: Single Cell Comparisons of DSB Formation and γH2AX Expression.* ChemPhysChem, 2024. **n/a**(n/a): p. e202400764.
74. Ziegler, J.F., M.D. Ziegler, and J.P. Biersack, *SRIM – The stopping and range of ions in matter (2010).* Nuclear Instruments and Methods in Physics Research Section B: Beam Interactions with Materials and Atoms, 2010. **268**(11): p. 1818-1823.
75. Asp, J., et al., *Design and verification of an external radiobiological beam port on a 16.5 MeV GE PETtrace proton cyclotron.* Med Phys, 2019. **47**(2): p. 393-403.
76. Matsuda, M., et al., *High-dose proton beam therapy versus conventional fractionated radiation therapy for newly diagnosed glioblastoma: a propensity score matching analysis.* Radiation Oncology, 2023. **18**(1): p. 38.
77. Kovalchuk, A. and B. Kolb, *Low dose radiation effects on the brain - from mechanisms and behavioral outcomes to mitigation strategies.* Cell Cycle, 2017. **16**(13): p. 1266-1270.
78. Simmons, D.A., et al., *Reduced cognitive deficits after FLASH irradiation of whole mouse brain are associated with less hippocampal dendritic spine loss and neuroinflammation.* Radiotherapy and Oncology, 2019. **139**: p. 4-10.

79. Montay-Gruel, P., et al., *Hypofractionated FLASH-RT as an Effective Treatment against Glioblastoma that Reduces Neurocognitive Side Effects in Mice.* Clinical Cancer Research, 2021. **27**(3): p. 775-784.
80. Haussmann, J., et al., *Recent advances in radiotherapy of breast cancer.* Radiation Oncology, 2020. **15**(1): p. 71.
81. Schrörs, B., et al., *Multi-Omics Characterization of the 4T1 Murine Mammary Gland Tumor Model.* Frontiers in Oncology, 2020. **10**.
82. Naidu, M.D., et al., *Radiation Resistance in Glioma Cells Determined by DNA Damage Repair Activity of Ape1/Ref-1.* Journal of Radiation Research, 2010. **51**(4): p. 393-404.
83. Press, R.H., et al., *Clinical Review of Proton Therapy in the Treatment of Unilateral Head and Neck Cancers.* Int J Part Ther, 2021. **8**(1): p. 248-260.
84. Atkinson, J., et al., *The current status of FLASH particle therapy: a systematic review.* Physical and Engineering Sciences in Medicine, 2023.
85. Yao, L., D. Bojic, and M. Liu, *Applications and safety of gold nanoparticles as therapeutic devices in clinical trials.* J Pharm Anal, 2023. **13**(9): p. 960-967.
86. Sanai, N., et al., *CTNI-25. A PHASE 0/1B STUDY OF AZD1390 PLUS RADIOTHERAPY IN RECURRENT GLIOBLASTOMA PATIENTS.* Neuro-Oncology, 2023. **25**(Supplement_5): p. v79-v79.
87. Yagi, M., et al., *Sparing Effect on Cell Survival Under Normoxia Using Ultra-high Dose Rate Proton Beams from a Compact Superconducting AVF Cyclotron.* Anticancer Research, 2024. **44**(10): p. 4251-4260.
88. Rzyanina, A.V., et al., *A Study of the Survival of Tumor A549 Cells upon Proton Beam Irradiation in Flash and Standard Modes.* Biophysics (Russian Federation), 2024. **69**(2): p. 285-291.
89. Nomura, S., et al., *FLASH Effect Is Not Always Induced by Ultra-high Dose-rate Proton Irradiation Under Hypoxic Conditions.* Anticancer Research, 2024. **44**(7): p. 2973-2979.
90. Sørensen, B.S., et al., *Proton FLASH: Impact of Dose Rate and Split Dose on Acute Skin Toxicity in a Murine Model.* International Journal of Radiation Oncology Biology Physics, 2024. **120**(1): p. 265-275.

91. Mascia, A., et al., *Impact of Multiple Beams on the FLASH Effect in Soft Tissue and Skin in Mice.* International Journal of Radiation Oncology Biology Physics, 2024. **118**(1): p. 253-261.
92. Kristensen, L., et al., *Spread-out Bragg peak FLASH: quantifying normal tissue toxicity in a murine model.* Frontiers in Oncology, 2024. **14**.
93. Zhang, Q., et al., *Proton FLASH effects on mouse skin at different oxygen tensions.* Physics in Medicine and Biology, 2023. **68**(5).
94. Iturri, L., et al., *Oxygen supplementation in anesthesia can block FLASH effect and anti-tumor immunity in conventional proton therapy.* Communications Medicine, 2023. **3**(1).
95. Almeida, A., et al., *Dosimetric and biologic intercomparison between electron and proton FLASH beams.* Radiotherapy and Oncology, 2024. **190**.
96. Iturri, L., et al., *Proton FLASH Radiation Therapy and Immune Infiltration: Evaluation in an Orthotopic Glioma Rat Model.* International Journal of Radiation Oncology Biology Physics, 2023. **116**(3): p. 655-665.
97. Shukla, S., et al., *Ultra-high dose-rate proton FLASH improves tumor control.* Radiotherapy and Oncology, 2023. **186**.
98. Chowdhury, P., et al., *Proton FLASH Radiotherapy Ameliorates Radiation-induced Salivary Gland Dysfunction and Oral Mucositis and Increases Survival in a Mouse Model of Head and Neck Cancer.* Molecular Cancer Therapeutics, 2024. **23**(6): p. 877-889.
99. Cao, N., et al., *Preclinical Ultra-High Dose Rate (FLASH) Proton Radiation Therapy System for Small Animal Studies.* Advances in Radiation Oncology, 2024. **9**(3).
100. Kim, K., et al., *FLASH Proton Radiation Therapy Mitigates Inflammatory and Fibrotic Pathways and Preserves Cardiac Function in a Preclinical Mouse Model of Radiation-Induced Heart Disease.* International Journal of Radiation Oncology Biology Physics, 2024. **119**(4): p. 1234-1247.
101. Bell, B.I., et al., *Whole Abdominal Pencil Beam Scanned Proton FLASH Increases Acute Lethality.* International Journal of Radiation Oncology Biology Physics, 2024.

102. Horst, F., et al., *Dose and dose rate dependence of the tissue sparing effect at ultra-high dose rate studied for proton and electron beams using the zebrafish embryo model.* Radiotherapy and Oncology, 2024. **194**.
103. Saade, G., et al., *Ultrahigh-Dose-Rate Proton Irradiation Elicits Reduced Toxicity in Zebrafish Embryos.* Advances in Radiation Oncology, 2023. **8**(2).
104. Varian, a.S.H.C. *Feasibility Study of FLASH Radiotherapy for the Treatment of Symptomatic Bone Metastases*. 2022 December; Available from: https://ClinicalTrials.gov/show/NCT04592887.
105. Daugherty, E.C., et al., *FLASH Radiotherapy for the Treatment of Symptomatic Bone Metastases (FAST-01): Protocol for the First Prospective Feasibility Study.* JMIR Research Protocols, 2023. **12**.
106. Daugherty, E.C., et al., *FLASH radiotherapy for the treatment of symptomatic bone metastases in the thorax (FAST-02): protocol for a prospective study of a novel radiotherapy approach.* Radiation Oncology, 2024. **19**(1).
107. Zhao, X., et al., *A Novel Dose Rate Optimization Method to Maximize Ultrahigh-Dose-Rate Coverage of Critical Organs at Risk Without Compromising Dosimetry Metrics in Proton Pencil Beam Scanning FLASH Radiation Therapy.* International Journal of Radiation Oncology Biology Physics, 2024. **120**(4): p. 1181-1191.
108. Wyrsch, N., et al., *Amorphous silicon detectors for proton beam monitoring in FLASH radiotherapy.* Radiation Measurements, 2024. **177**.
109. Wang, S., et al., *Toward real-time, volumetric dosimetry for FLASH-capable clinical synchrocyclotrons using protoacoustic imaging.* Medical Physics, 2024. **51**(11): p. 8496-8505.
110. van Marlen, P., et al., *Technical note: Dosimetry and FLASH potential of UHDR proton PBS for small lung tumors: Bragg-peak-based delivery versus transmission beam and IMPT.* Medical Physics, 2024. **51**(10): p. 7580-7588.
111. Tsai, P., et al., *A comprehensive pre-clinical treatment quality assurance program using unique spot patterns for proton pencil beam scanning FLASH radiotherapy.* Journal of Applied Clinical Medical Physics, 2024. **25**(8).

112. Harrison, N., et al., *Characterizing devices for validation of dose, dose rate, and LET in ultra high dose rate proton irradiations.* Medical Physics, 2024. **51**(11): p. 8411-8422.
113. Fois, G.R., et al., *Monte Carlo simulations of microdosimetry and radiolytic species production at long time post proton irradiation using GATE and Geant4-DNA.* Medical Physics, 2024. **51**(10): p. 7500-7510.
114. Clark, M., et al., *Quantitative, real-time scintillation imaging for experimental comparison of different dose and dose rate estimations in UHDR proton pencil beams.* Medical Physics, 2024. **51**(9): p. 6402-6411.
115. Bookbinder, A., et al., *Validation and reproducibility of in vivo dosimetry for pencil beam scanned FLASH proton treatment in mice.* Radiotherapy and Oncology, 2024. **198**.
116. Cowell, I.G., et al., *γH2AX Foci Form Preferentially in Euchromatin after Ionising-Radiation.* PLOS ONE, 2007. **2**(10): p. e1057.
117. Halvorsen, P.S., *Establishment of a new quantitative method for in situ detection of DNA breaks in human spermatozoa*, in *Faculty of Health Sciences*. 2021, Oslo Metropolitan University: Oslo, Norway. p. 125.
118. Chauvin, S.D., et al., *Inherited C-terminal TREX1 variants disrupt homology-directed repair to cause senescence and DNA damage phenotypes in Drosophila, mice, and humans.* Nature Communications, 2024. **15**(1): p. 4696.
119. Zhou, J., et al., *LP-284, a small molecule acylfulvene, exerts potent antitumor activity in preclinical non-Hodgkin's lymphoma models and in cells deficient in DNA damage repair.* Oncotarget, 2023. **14**: p. 597-611.
120. Kulkarni, A., et al., *LP-184, a Novel Acylfulvene Molecule, Exhibits Anticancer Activity against Diverse Solid Tumors with Homologous Recombination Deficiency.* Cancer Res Commun, 2024. **4**(5): p. 1199-1210.
121. Tew, B.Y., et al., *ATM-Inhibitor AZD1390 Is a Radiosensitizer for Breast Cancer CNS Metastasis.* Clinical Cancer Research, 2023. **29**(21): p. 4492-4503.
122. Kang, M.A., et al., *DNA damage induces reactive oxygen species generation through the H2AX-Nox1/Rac1 pathway.* Cell Death & Disease, 2012. **3**(1): p. e249-e249.

123. Kang, Y., et al., *Protein phosphatase 5 regulates the function of 53BP1 after neocarzinostatin-induced DNA damage.* J Biol Chem, 2009. **284**(15): p. 9845-53.
124. Goldberg, I.H., *Free radical mechanisms in neocarzinostatin-induced DNA damage.* Free Radical Biology and Medicine, 1987. **3**(1): p. 41-54.
125. Nakamura, J., E.R. Purvis, and J.A. Swenberg, *Micromolar concentrations of hydrogen peroxide induce oxidative DNA lesions more efficiently than millimolar concentrations in mammalian cells.* Nucleic Acids Res, 2003. **31**(6): p. 1790-5.
126. Moore, C.L., A.V. Savenka, and A.G. Basnakian, *TUNEL Assay: A Powerful Tool for Kidney Injury Evaluation.* Int J Mol Sci, 2021. **22**(1).
127. Xiao, Y. and S.N. Isaacs, *Enzyme-linked immunosorbent assay (ELISA) and blocking with bovine serum albumin (BSA)--not all BSAs are alike.* J Immunol Methods, 2012. **384**(1-2): p. 148-51.
128. Vilenchik, M.M. and A.G. Knudson, *Endogenous DNA double-strand breaks: Production, fidelity of repair, and induction of cancer.* Proceedings of the National Academy of Sciences, 2003. **100**(22): p. 12871-12876.
129. Cannan, W.J. and D.S. Pederson, *Mechanisms and Consequences of Double-Strand DNA Break Formation in Chromatin.* Journal of Cellular Physiology, 2016. **231**(1): p. 3-14.
130. Jakob, B. and G. Taucher-Scholz, *Live Cell Imaging to Study Real-Time ATM-Mediated Recruitment of DNA Repair Complexes to Sites of Ionizing Radiation-Induced DNA Damage*, in *ATM Kinase: Methods and Protocols*, S.V. Kozlov, Editor. 2017, Springer New York: New York, NY. p. 287-302.
131. Wang, X., et al., *Combinatorial therapeutic strategies for enhanced delivery of therapeutics to brain cancer cells through nanocarriers: current trends and future perspectives.* Drug Deliv, 2022. **29**(1): p. 1370-1383.
132. Jurkovicova, D., et al., *DNA Damage Response in Cancer Therapy and Resistance: Challenges and Opportunities.* Int J Mol Sci, 2022. **23**(23).
133. García, M.E.G., D.G. Kirsch, and Z.J. Reitman, *Targeting the ATM Kinase to Enhance the Efficacy of Radiotherapy and Outcomes for Cancer Patients.* Semin Radiat Oncol, 2022. **32**(1): p. 3-14.

134. Terlizzi, C., et al., *ATM inhibition blocks glucose metabolism and amplifies the sensitivity of resistant lung cancer cell lines to oncogene driver inhibitors.* Cancer & Metabolism, 2023. **11**(1): p. 20.
135. AstraZeneca, *A Study to Assess the Safety and Tolerability of AZD1390 Given With Radiation Therapy in Patients With Brain Cancer*. 2018, National Library of Medicine: ClinicalTrials.gov.
136. Agarwal, S., et al., *Function of the Blood-Brain Barrier and Restriction of Drug Delivery to Invasive Glioma Cells: Findings in an Orthotopic Rat Xenograft Model of Glioma.* Drug Metabolism and Disposition, 2013. **41**(1): p. 33-39.
137. Ostrom, Q.T., et al., *CBTRUS Statistical Report: Primary Brain and Other Central Nervous System Tumors Diagnosed in the United States in 2016—2020.* Neuro-Oncology, 2023. **25**(Supplement_4): p. iv1-iv99.
138. Tran, B. and M.A. Rosenthal, *Survival comparison between glioblastoma multiforme and other incurable cancers.* Journal of Clinical Neuroscience, 2010. **17**(4): p. 417-421.
139. Ajaz, M., et al., *Current and Investigational Drug Strategies for Glioblastoma.* Clinical Oncology, 2014. **26**(7): p. 419-430.
140. Health, A.I.o. and Welfare, *Cancer data in Australia*. 2024, AIHW: Canberra.
141. Dorling, L., et al., *Breast Cancer Risk Genes - Association Analysis in More than 113,000 Women.* N Engl J Med, 2021. **384**(5): p. 428-439.
142. Moslemi, M., et al., *The association between ATM variants and risk of breast cancer: a systematic review and meta-analysis.* BMC Cancer, 2021. **21**(1): p. 27.
143. Laake, K., et al., *Loss of heterozygosity at 11q23.1 and survival in breast cancer: Results of a large European study.* Genes, Chromosomes and Cancer, 1999. **25**(3): p. 212-221.
144. Sun, M., et al., *Activation of the ATM-Snail pathway promotes breast cancer metastasis.* Journal of Molecular Cell Biology, 2012. **4**(5): p. 304-315.
145. Hu, M., et al., *ATM inhibition enhances cancer immunotherapy by promoting mtDNA leakage and cGAS/STING activation.* J Clin Invest, 2021. **131**(3).

146. Stirling, D.R., et al., *CellProfiler 4: improvements in speed, utility and usability.* BMC Bioinformatics, 2021. **22**(1): p. 433.
147. Australia, C. *Brain cancer in Australia statistics*. 2024 23/01/2024 [cited 2024 22/11/24]; Available from: https://www.canceraustralia.gov.au/cancer-types/brain-cancer/statistics.
148. Hsiao, T.Y., et al., *Proton FLASH Irradiation Platform for Small Animal Setup at Chang Gung Memorial Hospital.* IEEE Transactions on Radiation and Plasma Medical Sciences, 2024. **8**(1): p. 88-94.
149. Horendeck, D., et al., *High LET-Like Radiation Tracks at the Distal Side of Accelerated Proton Bragg Peak.* Front Oncol, 2021. **11**: p. 690042.
150. Carter, R.J., et al., *Complex DNA Damage Induced by High Linear Energy Transfer Alpha-Particles and Protons Triggers a Specific Cellular DNA Damage Response.* International Journal of Radiation Oncology*Biology*Physics, 2018. **100**(3): p. 776-784.
151. Sioen, S., et al., *Impact of proton therapy on the DNA damage induction and repair in hematopoietic stem and progenitor cells.* Sci Rep, 2023. **13**(1): p. 16995.
152. Alan Mitteer, R., et al., *Proton beam radiation induces DNA damage and cell apoptosis in glioma stem cells through reactive oxygen species.* Scientific Reports, 2015. **5**(1): p. 13961.
153. Luzhna, L., P. Kathiria, and O. Kovalchuk, *Micronuclei in genotoxicity assessment: from genetics to epigenetics and beyond.* Frontiers in Genetics, 2013. **4**.
154. Mateuca, R., et al., *Chromosomal changes: induction, detection methods and applicability in human biomonitoring.* Biochimie, 2006. **88**(11): p. 1515-1531.
155. Chaudhary, P., et al., *Relative Biological Effectiveness Variation Along Monoenergetic and Modulated Bragg Peaks of a 62-MeV Therapeutic Proton Beam: A Preclinical Assessment.* International Journal of Radiation Oncology*Biology*Physics, 2014. **90**(1): p. 27-35.
156. Chaudhary, P., et al., *Variations in the Processing of DNA Double-Strand Breaks Along 60-MeV Therapeutic Proton Beams.* International Journal of Radiation Oncology*Biology*Physics, 2016. **95**(1): p. 86-94.

157. *Brass Material Properties*. 2024 [cited 2024 13th May]; Available from: ezlock.com/brass-properties.
158. *Tungsten (W) - The Different Properties and Applications*. 2013 13th August 2013 [cited 2024 13th May]; Available from: https://www.azom.com/article.aspx?ArticleID=9119.
159. Brenner, D.J., et al., *Reduction of the secondary neutron dose in passively scattered proton radiotherapy, using an optimized pre-collimator/collimator.* Phys Med Biol, 2009. **54**(20): p. 6065-78.
160. Moskvin, V., C.-W. Cheng, and I.J. Das, *Pitfalls of tungsten multileaf collimator in proton beam therapy.* Medical Physics, 2011. **38**(12): p. 6395-6406.
161. Mares, V., et al., *Neutron Radiation Dose Measurements in a Scanning Proton Therapy Room: Can Parents Remain Near Their Children During Treatment?* Frontiers in Oncology, 2022. **12**.
162. Hälg, R.A. and U. Schneider, *Neutron dose and its measurement in proton therapy—current State of Knowledge.* British Journal of Radiology, 2020. **93**(1107).
163. Gustafsson, B., *Optimization of material in proton-therapy collimators with respect to neutron production*, in *UPTEC ES*. 2009. p. 32.
164. Hyer, D.E., et al., *Innovations and the Use of Collimators in the Delivery of Pencil Beam Scanning Proton Therapy.* International Journal of Particle Therapy, 2021. **8**(1): p. 73-83.
165. Asp, J., *Development of an external beam porton a 16.5 MeV proton cyclotron for radiobiological experiments*. 2020, Thesis (Masters by research(Applied Physics))--University of South Australia, 2020.
166. Rodriguez-Muñoz, M., et al., *Breakage of CRISPR/Cas9-Induced Chromosome Bridges in Mitotic Cells.* Front Cell Dev Biol, 2021. **9**: p. 745195.
167. Hossain, M.A., Y. Lin, and S. Yan, *Single-Strand Break End Resection in Genome Integrity: Mechanism and Regulation by APE2.* Int. J. Mol. Sci., 2018. **19**(8): p. 2389.
168. Jezkova, L., et al., *Particles with similar LET values generate DNA breaks of different complexity and reparability: a high-resolution microscopy analysis of γH2AX/53BP1 foci.* Nanoscale, 2018. **10**(3): p. 1162-1179.

169. Lee, U.-S., D.-H. Lee, and E.-H. Kim, *Characterization of γ-H2AX foci formation under alpha particle and X-ray exposures for dose estimation.* Scientific Reports, 2022. **12**(1): p. 3761.
170. Alexeyev, M., et al., *The maintenance of mitochondrial DNA integrity--critical analysis and update.* Cold Spring Harb. Perspect. Biol., 2013. **5**(5): p. a012641.
171. Pinto, M., et al., *Transient mitochondrial DNA double strand breaks in mice cause accelerated aging phenotypes in a ROS-dependent but p53/p21-independent manner.* Cell Death & Differentiation, 2017. **24**(2): p. 288-299.
172. Coffey, G., U. Lakshmipathy, and C. Campbell, *Mammalian mitochondrial extracts possess DNA end-binding activity.* Nucleic Acids Res., 1999. **27**(16): p. 3348-54.
173. Miller, K.N., et al., *Cytoplasmic DNA: sources, sensing, and role in aging and disease.* Cell, 2021. **184**(22): p. 5506-5526.
174. Okunieff, P., et al., *Molecular markers of radiation-related normal tissue toxicity.* Cancer Metastasis Rev, 2008. **27**(3): p. 363-74.

Appendices

PTCOG 61 Abstract

Author and co-author's details

Jake Atkinson[1,2], Eva Bezak[3,4], Hien Le[5], Chih-Tsung Yang[1], Zi-Xian Liao[6], Ching-Fang Yu[7,8], Tsi-Chian Chao[7], I-Chun Cho[7,8] and Ivan Kempson[1]

[1] Future Industries Institute, University of South Australia, Mawson Lakes, 5095, South Australia, Australia

[2] Author to whom any correspondence should be addressed.

[3] Cancer Research Institute, University of South Australia, Adelaide, South Australia, Australia

[4] Department of Physics, University of Adelaide, North Terrace, Adelaide, South Australia, Australia

[5] Department of Radiation Oncology, Royal Adelaide Hospital, Adelaide,

Australia

[6] Institute of Medical Science and Technology, National Sun Yat-Sen University, Kaohsiung, 80424, Taiwan

[7] Institute for Radiological Research, Chang Gung University, Taoyuan, Taiwan.

[8] Linkou Proton and Radiation Therapy Centre, Chang Gung Memorial Hospital, Taoyuan City, Taiwan.

Abstract Title: Characterising Proton-FLASH DNA Double-Strand Break Formation and Repair

Background and Aims: FLASH particle therapy is a promising treatment modality, yet the biological reasons underlying its ability to spare healthy tissue remain unclear. Our systematic review of FLASH particle therapy literature highlights three key mechanisms: transient oxygen depletion, immunomodulation, and complex DNA damage, including double-strand breaks (DSBs). Assessing the

nature and complexity of FLASH-induced DNA damage is pivotal in differentiating the genotoxic impact between normal and cancerous cells, the nature of which may contribute to the FLASH effect.

Methods: Through a systematic search of Scopus and MEDLINE databases, we identified 34 relevant studies on proton and carbon FLASH therapy, specifically targeting preclinical investigations exploring the radiobiological effects of ultra-high dose rates on both normal and cancerous cells. Additionally, we performed experiments to validate novel DSB marker 'STRIDE' and comparing foci formation to conventional DNA damage response marker γH2AX. Preliminary validation of STRIDE was performed with peroxide and x-rays in PC3 and 4T1 cells respectively. Comparative FLASH (~47 Gy/s) and conventional (~0.05 Gy/s) irradiation experiments were also performed in U87 and Human Oral Fibroblast cell lines at the CGMH Proton and Radiation Therapy Centre in Linkou, Taiwan.

Results: Our findings demonstrate a complementarity between STRIDE foci formation and γH2AX expression for quantifying DNA damage and subsequent repair, especially where DNA damage response (DDR) is impaired. STRIDE exhibits kinetics which are representative of the presence of DSBs immediately post-insult regardless of repair inhibition, and the progression of DNA repair thereafter. Conversely, γH2AX foci formation is impeded during DDR inhibition, and peaks 30 minutes post-insult with no inhibition.

Conclusion: The complementarity observed between STRIDE foci formation and γH2AX expression underscores the reliability of STRIDE in quantifying DNA damage, particularly in scenarios where the DDR is impaired. Does the tissue sparing effect of FLASH lie in a difference between how normal and cancerous cells resolve FLASH induced DNA damage? Characterising DSBs with STRIDE is key to answering this. This enhanced characterization of DNA double-strand breaks will not only further our understanding of FLASH particle therapy mechanisms but also facilitate a more precise assessment of radiobiological damage during the development of future cancer therapies.

Keywords: FLASH mechanisms, DNA damage repair, double-strand breaks, genotoxicity, immunofluorescence assays, differential effect

University of South Australia

Statement of Authorship

Title of Paper	Imaging DNA double-strand breaks — are we there yet?
Publication Status	■ Published ☐ Accepted for Publication ☐ Submitted for Publication ☐ Unpublished and Unsubmitted work written in manuscript style
Publication Details Relevant reference details	Atkinson, J., Bezak, E. & Kempson, I. Imaging DNA double-strand breaks — are we there yet?. Nat Rev Mol Cell Biol 23, 579–580 (2022). https://doi.org/10.1038/s41580-022-00513-7

PRINCIPAL AUTHOR

Name of Principal Author (Candidate)	Jake Atkinson
Contribution to the Paper Brief description of your work in this publication	In this comment, I was responsible for investigating and selecting literature on current and novel methods for detecting DNA double-strand breaks (DSBs), with a focus on quantifying these breaks more representatively. I authored each section of the manuscript, outlining the gaps in existing detection techniques and articulating the broader implications of DSB measurement for understanding cellular processes, genotoxicity, and advancements in gene-editing technologies. Following initial drafting, I worked closely with co-authors to refine and address feedback from reviewers.
Overall Percentage (%)	60
Certification	This paper reports on original research I conducted during the period of my Higher Degree by Research candidature and is not subject to any obligations or contractual agreements with a third party that would constrain its inclusion in this thesis. I am the primary author of this paper.
Signature *Signatures will be redacted by the Library at the time of publication*	[redacted] Date 20-Jun-24

CO-AUTHOR CONTRIBUTIONS

By signing the Statement of Authorship, each author certifies that:

I. the candidate's stated contribution to the publication is accurate (as detailed above);

II. permission is granted for the candidate in include the publication in the thesis; and

III. the sum of all co-author contribution is equal to 100% less the candidate's stated contribution.

Name of Co-Author 1	Ivan Kempson

University of South Australia

% Contribution to the Paper	20		
Signature *Signatures will be redacted by the Library at the time of publication*	Ivan Kempson	Digitally signed by Ivan Kempson Date: 2024.06.20 14:59:24 +09'30'	Date 20-Jun-24
Name of Co-Author 2	Eva Bezak		
% Contribution to the Paper	20		
Signature *Signatures will be redacted by the Library at the time of publication*	Eva Bezak	Digitally signed by Eva Bezak Date: 2024.06.21 10:29:19 +09'30'	Date 21-Jun-24
Name of Co-Author 3			
% Contribution to the Paper			
Signature *Signatures will be redacted by the Library at the time of publication*			Date
Name of Co-Author 4			
% Contribution to the Paper			
Signature *Signatures will be redacted by the Library at the time of publication*			Date
Name of Co-Author 5			
% Contribution to the Paper			
Signature *Signatures will be redacted by the Library at the time of publication*			Date
Name of Co-Author 6			
% Contribution to the Paper			
Signature *Signatures will be redacted by the Library at the time of publication*			Date
Name of Co-Author 7			
% Contribution to the Paper			

University of South Australia

Signature *Signatures will be redacted by the Library at the time of publication*		Date
Name of Co-Author 8		
% Contribution to the Paper		
Signature *Signatures will be redacted by the Library at the time of publication*		Date
Name of Co-Author 9		
% Contribution to the Paper		
Signature *Signatures will be redacted by the Library at the time of publication*		Date
Name of Co-Author 10		
% Contribution to the Paper		
Signature *Signatures will be redacted by the Library at the time of publication*		Date

University of South Australia

Statement of Authorship

Title of Paper	The current status of FLASH particle therapy: a systematic review
Publication Status	■ Published ☐ Accepted for Publication ☐ Submitted for Publication ☐ Unpublished and Unsubmitted work written in manuscript style
Publication Details Relevant reference details	Atkinson, J., Bezak, E., Le, H. et al. The current status of FLASH particle therapy: a systematic review. Phys Eng Sci Med 46, 529 560 (2023). https://doi.org/10.1007/s13246-023-01266-z

PRINCIPAL AUTHOR

Name of Principal Author (Candidate)	Jake Atkinson
Contribution to the Paper Brief description of your work in this publication	For this review, I designed and conducted a systematic search strategy, refining terms to capture relevant studies in the Scopus and Medline databases. I analysed each study's adherence to inclusion criteria, summarised pre-clinical and clinical data, and outlined the three predicted mechanisms of FLASH particle therapy. The key messages of this publication highlight the need for a cautious approach to clinical translation due to limitations in measuring FLASH in preclinical studies. Co-authors and I worked together to draft and refine the manuscript before submission and after receiving feedback from peer review.
Overall Percentage (%)	60
Certification	This paper reports on original research I conducted during the period of my Higher Degree by Research candidature and is not subject to any obligations or contractual agreements with a third party that would constrain its inclusion in this thesis. I am the primary author of this paper.
Signature *Signatures will be redacted by the Library at the time of publication*	[redacted] Date 20-Jun-24

CO-AUTHOR CONTRIBUTIONS

By signing the Statement of Authorship, each author certifies that:

I. the candidate's stated contribution to the publication is accurate (as detailed above);

II. permission is granted for the candidate in include the publication in the thesis; and

III. the sum of all co-author contribution is equal to 100% less the candidate's stated contribution.

Name of Co-Author 1	Ivan Kempson

University of South Australia

% Contribution to the Paper	20		
Signature *Signatures will be redacted by the Library at the time of publication*	Ivan Kempson	Digitally signed by Ivan Kempson Date: 2024.06.20 15:11:40 +09'30'	Date 20-Jun-24
Name of Co-Author 2	Eva Bezak		
% Contribution to the Paper	10		
Signature *Signatures will be redacted by the Library at the time of publication*	Eva Bezak	Digitally signed by Eva Bezak Date: 2024.06.20 15:59:05 +09'30'	Date 20-Jun-24
Name of Co-Author 3	Hien Le		
% Contribution to the Paper	10		
Signature *Signatures will be redacted by the Library at the time of publication*	Le, Hien (RAH)	Digitally signed by Le, Hien (RAH) Date: 2024.06.21 15:11:47 +09'30'	Date 21-Jun-24
Name of Co-Author 4			
% Contribution to the Paper			
Signature *Signatures will be redacted by the Library at the time of publication*			Date
Name of Co-Author 5			
% Contribution to the Paper			
Signature *Signatures will be redacted by the Library at the time of publication*			Date
Name of Co-Author 6			
% Contribution to the Paper			
Signature *Signatures will be redacted by the Library at the time of publication*			Date
Name of Co-Author 7			
% Contribution to the Paper			

University of South Australia

Signature *Signatures will be redacted by the Library at the time of publication*		Date
Name of Co-Author 8		
% Contribution to the Paper		
Signature *Signatures will be redacted by the Library at the time of publication*		Date
Name of Co-Author 9		
% Contribution to the Paper		
Signature *Signatures will be redacted by the Library at the time of publication*		Date
Name of Co-Author 10		
% Contribution to the Paper		
Signature *Signatures will be redacted by the Library at the time of publication*		Date

University of South Australia

Statement of Authorship

Title of Paper	DNA Double Strand Break and Response Fluorescent Assays: Choices and Interpretation
Publication Status	■ Published ☐ Accepted for Publication ☐ Submitted for Publication ☐ Unpublished and Unsubmitted work written in manuscript style
Publication Details Relevant reference details	Atkinson, J.; Bezak, E.; Le, H.; Kempson, I. DNA Double Strand Break and Response Fluorescent Assays: Choices and Interpretation. Int. J. Mol. Sci. 2024, 25, 2227. https://doi.org/10.3390/ijms25042227

PRINCIPAL AUTHOR

Name of Principal Author (Candidate)	Jake Atkinson
Contribution to the Paper Brief description of your work in this publication	As lead author, I expanded upon themes from my previous Nature Comment in this full-length review providing an overview of all the assays used to detect various points in the DNA damage response pathway, from DSB formation to repair. I synthesised and critiqued various immunofluorescence-based markers for DSB detection, providing detailed analysis and recommendations for researchers on selecting the appropriate markers to improve DSB quantification and data interpretation. I drafted the manuscript, later refining it with co-authors to ensure clarity.
Overall Percentage (%)	60
Certification	This paper reports on original research I conducted during the period of my Higher Degree by Research candidature and is not subject to any obligations or contractual agreements with a third party that would constrain its inclusion in this thesis. I am the primary author of this paper.
Signature *Signatures will be redacted by the Library at the time of publication*	[redacted] Date 20-Jun-24

CO-AUTHOR CONTRIBUTIONS

By signing the Statement of Authorship, each author certifies that:

I. the candidate's stated contribution to the publication is accurate (as detailed above);

II. permission is granted for the candidate in include the publication in the thesis; and

III. the sum of all co-author contribution is equal to 100% less the candidate's stated contribution.

Name of Co-Author 1	Ivan Kempson

University of South Australia

% Contribution to the Paper	20		
Signature *Signatures will be redacted by the Library at the time of publication*	Ivan Kempson	Digitally signed by Ivan Kempson Date: 2024.06.20 15:09:59 +09'30'	Date 20-Jun-24
Name of Co-Author 2	Eva Bezak		
% Contribution to the Paper	10		
Signature *Signatures will be redacted by the Library at the time of publication*	Eva Bezak	Digitally signed by Eva Bezak Date: 2024.06.20 15:59:57 +09'30'	Date 20-Jun-24
Name of Co-Author 3	Hien Le		
% Contribution to the Paper	10		
Signature *Signatures will be redacted by the Library at the time of publication*	Le, Hien (RAH)	Digitally signed by Le, Hien (RAH) Date: 2024.06.21 15:12:39 +09'30'	Date 21-Jun-24
Name of Co-Author 4			
% Contribution to the Paper			
Signature *Signatures will be redacted by the Library at the time of publication*			Date
Name of Co-Author 5			
% Contribution to the Paper			
Signature *Signatures will be redacted by the Library at the time of publication*			Date
Name of Co-Author 6			
% Contribution to the Paper			
Signature *Signatures will be redacted by the Library at the time of publication*			Date
Name of Co-Author 7			
% Contribution to the Paper			

University of South Australia

Signature *Signatures will be redacted by the Library at the time of publication*		Date
Name of Co-Author 8		
% Contribution to the Paper		
Signature *Signatures will be redacted by the Library at the time of publication*		Date
Name of Co-Author 9		
% Contribution to the Paper		
Signature *Signatures will be redacted by the Library at the time of publication*		Date
Name of Co-Author 10		
% Contribution to the Paper		
Signature *Signatures will be redacted by the Library at the time of publication*		Date

University of South Australia

Statement of Authorship

Title of Paper	Gold nanoparticles cause radiosensitization in 4T1 cells by inhibiting DNA double strand break repair: Single cell comparisons of DSB formation and γH2AX expression.
Publication Status	☐ Published ■ Accepted for Publication ☐ Submitted for Publication ☐ Unpublished and Unsubmitted work written in manuscript style
Publication Details Relevant reference details	

PRINCIPAL AUTHOR

Name of Principal Author (Candidate)	Jake Atkinson
Contribution to the Paper Brief description of your work in this publication	In this study, I conducted X-ray irradiations on 4T1 cells that were pre-treated with AZD1390, gold nanoparticles (AuNPs), or a combination of both with radiation. I performed all experimental aspects including sample preparation, staining each treatment group with STRIDE and γH2AX, confocal imaging and image analysis. I also authored the manuscript in full, presenting findings on how AuNPs disrupt the DNA repair machinery instead of increasing radiation dose deposition. I collaborated with co-authors for final revisions to ensure the study's insights were clearly articulated and ready for submission, and addressed peer reviewer's comments prior to publication.
Overall Percentage (%)	60
Certification	This paper reports on original research I conducted during the period of my Higher Degree by Research candidature and is not subject to any obligations or contractual agreements with a third party that would constrain its inclusion in this thesis. I am the primary author of this paper.
Signature *Signatures will be redacted by the Library at the time of publication*	[redacted] Date 6-Sep-24

CO-AUTHOR CONTRIBUTIONS

By signing the Statement of Authorship, each author certifies that:

I. the candidate's stated contribution to the publication is accurate (as detailed above);

II. permission is granted for the candidate in include the publication in the thesis; and

III. the sum of all co-author contribution is equal to 100% less the candidate's stated contribution.

Name of Co-Author 1	Ivan Kempson

University of South Australia

% Contribution to the Paper	10		
Signature *Signatures will be redacted by the Library at the time of publication*	Ivan Kempson	Digitally signed by Ivan Kempson Date: 2024.10.30 17:32:08 +10'30'	Date 30-Oct-24
Name of Co-Author 2	Eva Bezak		
% Contribution to the Paper	10		
Signature *Signatures will be redacted by the Library at the time of publication*	Eva Bezak	Digitally signed by Eva Bezak Date: 2024.11.08 15:13:53 +10'30'	Date 8/11/24
Name of Co-Author 3	Hien Le		
% Contribution to the Paper	10		
Signature *Signatures will be redacted by the Library at the time of publication*	Le, Hien (RAH)	Digitally signed by Le, Hien (RAH) Date: 2024.11.12 05:21:53 +10'30'	Date 12-Nov-24
Name of Co-Author 4	Joshua Chopin		
% Contribution to the Paper	10		
Signature *Signatures will be redacted by the Library at the time of publication*	Joshua Chopin	Digitally signed by Joshua Chopin Date: 2024.11.12 13:41:52 +10'30'	Date 12-Nov-24
Name of Co-Author 5			
% Contribution to the Paper			
Signature *Signatures will be redacted by the Library at the time of publication*			Date
Name of Co-Author 6			
% Contribution to the Paper			
Signature *Signatures will be redacted by the Library at the time of publication*			Date
Name of Co-Author 7			
% Contribution to the Paper			

University of South Australia

Signature *Signatures will be redacted by the Library at the time of publication*		Date
Name of Co-Author 8		
% Contribution to the Paper		
Signature *Signatures will be redacted by the Library at the time of publication*		Date
Name of Co-Author 9		
% Contribution to the Paper		
Signature *Signatures will be redacted by the Library at the time of publication*		Date
Name of Co-Author 10		
% Contribution to the Paper		
Signature *Signatures will be redacted by the Library at the time of publication*		Date

University of South Australia

Statement of Authorship

Title of Paper	Mechanisms of AZD1390-Mediated Radiosensitization by Comparing DNA DSB Formation and Repair in 4T1 Cells
Publication Status	☐ Published ☐ Accepted for Publication ☐ Submitted for Publication ■ Unpublished and Unsubmitted work written in manuscript style
Publication Details Relevant reference details	

PRINCIPAL AUTHOR

Name of Principal Author (Candidate)	Jake Atkinson
Contribution to the Paper Brief description of your work in this publication	In this study, I led experiments to investigate the effects of AZD1390, a potent ATM inhibitor, on DNA repair pathways in cancer cells subjected to x-ray irradiation. I treated cells with AZD1390 alone and in combination with radiation, then performed a series of x-ray irradiations to assess the compound's impact on DNA double-strand break formation and repair. Following treatment, I applied both STRIDE and γH2AX staining to visualize and quantify DNA damage/repair at the single-cell level, using confocal imaging and CellProfiler image analysis to evaluate repair inhibition. I drafted each section of the manuscript, detailing our findings on how AZD1390 sensitizes cells to radiation by impairing repair processes, and collaborated with co-authors to finalize the paper for submission.
Overall Percentage (%)	60
Certification	This paper reports on original research I conducted during the period of my Higher Degree by Research candidature and is not subject to any obligations or contractual agreements with a third party that would constrain its inclusion in this thesis. I am the primary author of this paper.
Signature *Signatures will be redacted by the Library at the time of publication*	[redacted] Date 21-Oct-24

CO-AUTHOR CONTRIBUTIONS

By signing the Statement of Authorship, each author certifies that:

I. the candidate's stated contribution to the publication is accurate (as detailed above);

II. permission is granted for the candidate in include the publication in the thesis; and

III. the sum of all co-author contribution is equal to 100% less the candidate's stated contribution.

Name of Co-Author 1	Ivan Kempson

University of South Australia

% Contribution to the Paper	10		
Signature *Signatures will be redacted by the Library at the time of publication*	Ivan Kempson	Digitally signed by Ivan Kempson Date: 2024.10.30 17:30:05 +10'30'	Date 30-Oct-24
Name of Co-Author 2	Eva Bezak		
% Contribution to the Paper	10		
Signature *Signatures will be redacted by the Library at the time of publication*	Eva Bezak	Digitally signed by Eva Bezak Date: 2024.11.08 15:15:31 +10'30'	Date 8/11/24
Name of Co-Author 3	Hien Le		
% Contribution to the Paper	10		
Signature *Signatures will be redacted by the Library at the time of publication*	Le, Hien (RAH)	Digitally signed by Le, Hien (RAH) Date: 2024.11.12 05:22:48 +10'30'	Date 12-Nov-24
Name of Co-Author 4	Joshua Chopin		
% Contribution to the Paper	10		
Signature *Signatures will be redacted by the Library at the time of publication*	Joshua Chopin	Digitally signed by Joshua Chopin Date: 2024.11.12 13:44:13 +10'30'	Date 12-Nov-24
Name of Co-Author 5			
% Contribution to the Paper			
Signature *Signatures will be redacted by the Library at the time of publication*			Date
Name of Co-Author 6			
% Contribution to the Paper			
Signature *Signatures will be redacted by the Library at the time of publication*			Date
Name of Co-Author 7			
% Contribution to the Paper			

University of South Australia

Signature *Signatures will be redacted by the Library at the time of publication*		Date
Name of Co-Author 8		
% Contribution to the Paper		
Signature *Signatures will be redacted by the Library at the time of publication*		Date
Name of Co-Author 9		
% Contribution to the Paper		
Signature *Signatures will be redacted by the Library at the time of publication*		Date
Name of Co-Author 10		
% Contribution to the Paper		
Signature *Signatures will be redacted by the Library at the time of publication*		Date